Scuola Internazionale Superiore di Studi Avanzati

Doctor of Philosophiae in Astrophysics

Radio - Loud Active Galactic Nuclei from parsec to Mega-parsec scales

The galaxy cluster environment of $z \sim 1 - 2$ FR I radio galaxies and properties of a complete sample of Flat Spectrum Radio Quasars

Trieste, October 30, 2014

Candidate: Gianluca Castignani

Supervisors: Annalisa Celotti
Marco Chiaberge
Gianfranco De Zotti

"Pija nomina e va' pe' strada."
Folk saying from Marche, Italy.

To my parents.
Ai miei genitori.

Abstract

The thesis covers two subjects of extra-galactic astrophysics that concern radio-loud active galactic nuclei (RLAGNs). We describe the two subjects separately, but there are deep connections between the two.

The first subject concerns the Mega-parsec scale environments of $z \sim 1-2$ radio galaxies. First, we describe a method (Poisson probability method, PPM) primarily introduced to search for dense Megaparsec-scale environments (i.e. galaxy clusters and groups) around a specific beacon using photometric redshifts and galaxy number counts on the basis of Poisson statistics.

We test the efficiency of our method of searching for cluster candidates against simulations. Two different approaches are adopted. (1) We use two $z \sim 1$ X-ray detected cluster candidates found in the Cosmic Evolution Survey (COSMOS) and we shift them to higher redshift up to $z = 2$. We find that the PPM detects the cluster candidates up to $z = 1.5$, and it correctly estimates both the redshift and size of the two clusters. (2) We simulate spherically symmetric clusters of different size and richness, and we locate them at different redshifts (i.e., $z = 1.0$, 1.5, and 2.0) in the COSMOS field. We find that the PPM detects the simulated clusters within the $z \sim 1-2$ range with a statistical 1-σ redshift accuracy of ~ 0.05.

The PPM naturally arises as an effective mean field theory defined on the ensemble of the photometric redshift realizations of the galaxies in the field. A differential argument embedded in the PPM theory shows that the PPM partially overcomes the limitations deriving from low number-count statistics and shot-noise fluctuations. This is ultimately achieved through the use of a solid positional prior and an accurate photometric redshift sampling. Therefore, the PPM is an efficient alternative method for high-redshift cluster searches that may also be applied to both present and future wide field surveys such as SDSS Stripe 82, Large Synoptic Survey Telescope (LSST), and *Euclid*. Accurate photometric redshifts and a survey depth similar or better than

that of COSMOS (e.g., $I < 25$) are required.

We also apply the PPM to search for high-redshift ($z \sim 1-2$) galaxy clusters around low power radio galaxies (FR I). We use a sample of 32 FR Is within the COSMOS field from the Chiaberge et al. catalog that we redefine on the basis of the radio power. The sample redefinition allows us to estimate the comoving space density of sources with $L_{1.4\ \mathrm{GHz}} \simeq 10^{32.3}$ erg s^{-1} Hz^{-1} at $z \simeq 1.1$, which strengthens the case for a strong cosmological evolution of these sources. Overdensities are found around $\sim 70\%$ of the FR Is. This rate is in agreement with the fraction found for low redshift FR Is and it is significantly higher than that for FR IIs at all redshifts. Cluster candidates found with our method are excellent targets for next generation space telescopes such as James Webb Space Telescope (JWST). The method reveals itself as a powerful tool to search for distant galaxy clusters.

The second subject that concerns RLAGNs is focused on blazars. We build a complete sample of flat-spectrum radio quasars (FSRQs) from the WMAP 7-yr catalog and compare black hole mass estimates based on fitting a standard accretion disk model to the 'blue bump' with those obtained from the commonly used single-epoch virial method. The sample comprises 80 objects flux limited at 1 Jy at 23 GHz, 55 of which (69%) have a clearly detected 'blue bump'. Thirty-three of the 55 FSRQs have, in the literature, black hole mass estimates obtained with the virial method. The mass estimates obtained from the two methods are well correlated. The fact that the two totally independent methods agree so closely in spite of all the potentially large uncertainties associated with each of them lends strong support to both of them.

We find evidence of mid-infrared (MIR) emitting active galactic nucleus (AGN) torus in the spectral energy distributions (SEDs) of seven of the 55 FSRQs with evidence of blue bump and an uncertain indication is found for one more. The fraction of FSRQs with evidence of AGN torus increases up to 39% if only the FSRQs at $z \leq 1$ and with evidence of blue bump are considered. Our results suggest that the detection of the AGN torus is favored in those FSRQs where the specific synchrotron flux at MIR wavelengths does not overwhelm the contribution from the torus. Conversely to BL Lac sources, which are known to lack much sign of gas, our results show that the AGN torus might be present in a large fraction of FSRQs.

Contents

Preface

The thesis covers two different subjects of extra-galactic astrophysics. They are considered separately, but there are deep connections between the two.

We exploit active galactic nuclei (AGNs), and in particular the subclass of low-power radio galaxies, to search for clusters of galaxies and groups at redshifts $z \sim 1-2$. Searching for high-redshift, i.e. $z \gtrsim 1$, clusters of galaxies represents a still open issue of modern astrophysics and observational cosmology. Finding high-redshift clusters is fundamental to understand how large scale structures form and evolve with cosmic time, especially in the exciting $z \sim 1-2$ redshift range, where the properties of both galaxies and the galaxy clusters significantly change.

We also statistically study a complete sample of blazars belonging to the flat-spectrum radio quasar class. In particular, by means of spectral energy distribution (SED) analysis we perform black hole mass estimates and search for evidence of AGN torus. AGN black hole mass estimates and the characterization and study of the AGN torus are key to understand the physics of active galaxies and the central engine, as well as the accretion processes and the emission mechanisms occurring in AGNs. Since they can reach extreme regimes, blazars represent spectacular laboratories to perform such studies.

The thesis is divided in four Parts and is structured as follows. In Part I we review the general properties of AGNs with particular emphasis on the radio-loud AGN subclass which blazars and radio galaxies belong to. In Chapter 1 we give a general overview of AGNs, with emphasis on the physics of accretion onto black holes, the AGN torus, and the different methods in estimating their black hole masses. In Chapter 2 we review the general properties of blazars mainly focusing on the emission mechanisms and the properties of the jets of these sources. In Chapter 3 we review the properties of the radio galaxies. We mainly focus on the radio galaxies at $z \gtrsim 1$, on their cosmological evolution, and on the interplay between the radio galaxies and their Mpc-scale environments.

In Part II we describe our work on $z \sim 1-2$ clusters of galaxies around low-power radio galaxies. We refer to Chapter 4 for an introduction to the problem. In Chapter 5 we introduce and characterize our sample. In Chapters 6, 7, and 8 we describe, test, and apply the Poisson Probability

Method (PPM), respectively, that we introduced to achieve our goal to find $z \sim 1-2$ galaxy clusters.

In Part III we describe our work on blazars. We refer to Chapter 9 for a brief introduction to the project. In Chapter 10 we introduce our blazar sample and perform the SED modeling. In Chapter 11 we describe our results. We refer to Chapter 12 for conclusions and future perspectives concerning both the projects on galaxy clusters and blazars.

Part IV includes additional material that is part of the present work. The PPM plots are reported in Appendix A and the SEDs of the blazars in our sample are reported in Appendix B.

A substantial part of the present thesis is reported in our recent work. "A New Method to Search for High-redshift Clusters Using Photometric Redshifts" (Castignani et al., 2014a) and "Cluster Candidates around Low-power Radio Galaxies at $z \sim 1-2$ in COSMOS" (Castignani et al., 2014b) refer to Part II and Appendix A. "Black-hole mass estimates for a homogeneous sample of bright flat-spectrum radio quasars" (Castignani et al., 2013) and "Active galactic nucleus torus emission for a homogeneous sample of bright flat-spectrum radio quasars" (Castignani & De Zotti, 2014) refer to Part III and Appendix B.

Ackowledgements

I warmly thank my supervisors: Annalisa, for her brilliant intuitions; Marco, for his constant mentoring in spite of the distance and for having included me in the project to search for high-redshift clusters using low power radio galaxies; Gianfranco, for his continuous mentoring and for having transmitted me part of his deep knowledge of physics. I thank Colin Norman, for his fundamental efforts in helping me to understand and clarify the theory the Poisson Probability Method is based on.

I thank Francesco Haardt, Andrea Lapi, and Luigi Danese for their contribution to the publications on which this thesis is based on. I thank Roberto Gilli, Joaquin Gonzalez-Nuevo, Paolo Tozzi, Eolo Di Casola, Domenico Monaco, and Matteo Casati for fruitful discussions. I thank the external examiners Alessandro Capetti and Gabriele Ghisellini for helpful comments to the thesis. I also thank SISSA and the Space Telescope Science Institute (STScI), where the work presented in this thesis was done.

The work presented in this thesis was partially supported by the STScI JDF account D0101.90157, the ASI/INAF agreement n. I/072/09/0, by INAF through the PRIN 2009 "New light on the early Universe with sub-mm spectroscopy" and (G.C.) by both the Internship Program ISSNAF-INAF 2010 and two of the Foundation Angelo Della Riccia fellowships both in 2012 and in 2013.

The research presented in this thesis has made use of data products

from the Wide-field Infrared Survey Explorer, which is a joint project of the University of California, Los Angeles, and the Jet Propulsion Laboratory/California Institute of Technology, funded by the National Aeronautics and Space Administration, and of the NASA/IPAC Extragalactic Database (NED) which is operated by the Jet Propulsion Laboratory, California Institute of Technology, under contract with the National Aeronautics and Space Administration.

Notations and conventions

Physical conventions

Throughout this work we adopt a flat ΛCDM cosmology with matter density $\Omega_{\rm m} = 0.32$, dark energy density $\Omega_\Lambda = 0.68$ and Hubble constant $h = H_0/100\,{\rm km\,s^{-1}\,Mpc^{-1}} = 0.67$ (Planck Collaboration XVI, 2013).

Acronyms and symbols

Table 1: Table of frequently used symbols, acronyms, and abbreviations

ACS	Advanced Camera for Surveys
ACT	Atacama Cosmology Telescope
AGN	Active Galactic Nucleus
ASKAP	Australian Square Kilometre Array Pathfinder
BCG	Brightest Cluster Galaxy
BH	Black Hole
BLR	Broad Line Region
BLRG	Broad Line Radio Galaxy
BMS	Blazar Main Sequence
CFHTLS	Canada-France-Hawaii Telescope Legacy Survey
CMB	Cosmic Microwave Background
COSMOS	Cosmic Evolution Survey
CSS	Compact Steep Spectrum
D_A	angular distance
D_L	luminosity distance
ECF	Empty Control Field
EW	Equivalent Width
Fermi	Fermi Gamma-ray Space Telescope
FIRST	Faint Images of the Radio Sky at Twenty-centimeters
FR I	Type I Fanaroff-Riley source
FR II	Type II Fanaroff-Riley source

FSRQ	Flat Spectrum Radio Quasar
FWHM	Full Width Half Maximum
G	Gravitational constant
H_0	Hubble constant
HEG	High Excitation Galaxy
HLRG	High Luminosity Radio Galaxy
HST	Hubble Space Telescope
HzRG	High redshift radio galaxy
IGM	Inter-Galactic Medium
IC	Inverse Compton
ICM	Intra-Cluster Medium
IR, NIR, and FIR	Infrared, near-IR, and far-IR, respectively
ISM	Inter Stellar Medium
GALEX	Galaxy Evolution Explorer
GPS	GigaHertz Peaked Spectrum
JWST	James Webb Space Telescope
Jy	Jansky (1 Jy = 10^{-23} erg cm^{-2} s^{-1} Hz^{-1})
LAT	Large Area Telescope
LEG	Low Excitation Galaxy
LLAGN	Low Luminosity AGN
LLRG	Low Luminosity Radio Galaxy
LOFAR	LOw Frequency ARray
LRG	Luminous Red Galaxy
LSST	Large Synoptic Survey Telescope
$M_\odot$	solar mass
$M_\bullet$	black hole mass
M_{200} and M_{500}	mass enclosed within the radius encompassing the matter density 200 and 500 times the critical one, respectively
NAT	Narrow-Angle Tail
NED	NASA/IPAC Extragalactic Database
NLRG	Narrow Line Radio Galaxy
NRAO	National Radio Astronomy Observatory
NRL	Narrow Line Region
NVSS	NRAO VLA Sky Survey
pc	parsec (1 pc = 3.09×10^{18} cm)
PPM	Poisson Probability Method
QSO	Quasi Stellar Object, also denoted as quasar
r_{200} and r_{500}	Radius at which the enclosed mass encompasses the matter density 200 and 500 times the critical one, respectively
$R_\star$	Innermost stable circular orbit
RLF	Radio Luminosity Function
RLAGN	Radio-Loud AGN
RSF	Randomly Selected Field
SDSS	Sloan Digital Sky Survey
SE	Single Epoch
SED	Spectral Energy Distribution
SKA	Square Kilometer Array
SMBH	Super Massive Black Hole
SSC	Synchrotron self-Compton

SZ	Sunyaev-Zel'dovich
UV, NUV, and FUV	Ultra Violet, Near-UV, and Far-UV, respectively
VLA	Very Large Array
VLBI	Very-Long-Baseline Interferometry
$W1$, $W2$, $W3$, and $W4$	WISE Vega magnitudes at 3.4, 4.6, 12, and 22 μm, respectively
WAT	Wide-Angle Tail
WISE	Wide-field Infrared Survey Explorer
WMAP	Wilkinson Microwave Anisotropy Probe
yr	year
z	redshift
ΛCDM	Lambda Cold Dark Matter
ν	frequency
Ω_m	matter energy density

Table 2: Frequently used bibliographic abbreviations

B13	Baldi et al. (2013)
C09	Chiaberge et al. (2009)
C10	Chiaberge et al. (2010)
FGH07	Finoguenov et al. (2007)
I09	Ilbert et al. (2009)
P08	Papovich (2008)

Part I

Overview

Chapter 1

General properties of AGNs

In this Chapter we introduce the Active Galactic Nuclei (AGNs) and describe their properties with specific emphasis for the Radio-Loud AGN subclass, that is key for the present work. We refer to Krolik (1999) for a comprehensive review of the topic.

AGNs are among the most luminous objects in the Universe and are preferentially located at cosmological distances. Nevertheless, there are also local AGNs such as Centaurus A (located at a distance $\sim 3-5$ Mpc, Ferrarese et al., 2007; Harris et al., 2010; Majaess, 2010). AGNs have a broad band non-stellar spectrum from radio to the hard X- or possibly to the γ-rays. The term AGN is used to indicate the central region of a galaxy where the accretion of material is ultimately responsible for most of the observed energy output. A galaxy hosting an AGN is called active galaxy.

In some cases AGNs appear as much as 10^4 more luminous than a typical galaxy. The typical luminosity of an AGN is in the range $\sim 10^{42-48}\,\mathrm{erg\,s^{-1}}$, even if most of the nearby AGNs occupy the faintest end of the AGN luminosity function.[1] These sources are called Low Luminosity AGNs (LLAGNs). LLAGNs have low luminosities $L \simeq 10^{39-41}\,\mathrm{erg\,s^{-1}}$ (Fernández-Ontiveros et al., 2012) and possibly have low accretion rates $\sim 5\times10^{-6\pm1}\ M_\odot\ \mathrm{yr^{-1}}$ (see Ho, 2008, for a review). Because of their faintness LLAGNs are detected up to redshifts $z \simeq 1$ (Young et al., 2012).

Concerning AGNs, in the local Universe Kauffmann et al. (2003) found that $\sim 18\%$ of a complete sample of Sloan Digital Sky Survey (SDSS, York et al., 2000) galaxies at $z < 0.3$ are associated with AGNs. However, the averaged estimated fraction of AGNs in the Universe rapidly decreases down to $\sim 1\%$ of all galaxies at increasing redshifts $z < 0.7$ (Haggard et al., 2010), suggesting that AGNs are rare objects out of the local Universe.

Furthermore, i) the main properties of the nearby AGNs do not re-

[1] The luminosity function is a function of the luminosity and it is usually defined as the comoving number density of sources per magnitude or (logarithmic) luminosity at a specific energy band.

flect those of higher redshift AGNs because most of the nearby AGNs are LLAGNs (Ho, 2008, for a review) and, unfortunately, ii) finding evidence of nuclear, i.e. AGN, activity out of the local Universe is increasingly more difficult at increasing redshift. This is mainly because of several biases related directly to the redshift and observational selection.

Some caveats should be taken into account when considering AGNs and their luminosities. AGNs much weaker than the host galaxy are not detected. Furthermore, the flux of many AGNs can be weakened by dust extinction. An anisotropic radiation field can also be found in association with AGNs, thus favoring the observations of those AGN components which emit radiation that ultimately reaches the observer. An example is represented by the radio-loud AGNs (see below), and especially the blazar subclass, where the radiation emitted by ejecta moving at relativistic speed is preferentially boosted in the direction of the motion. This effect is known as relativistic beaming. In general, it is often necessary to distinguish between the luminosity inferred assuming an isotropic emission from the luminosity inferred assuming a beamed emission, with important consequences on the energetic of the source and on the sample statistics.

Despite all these observational difficulties and constraints, wide area optical-infrared photometric surveys discovered a statistically significant number ($\sim$ 50) of high-redshift AGNs in the range $5.7 < z < 6.4$ (Fan et al., 2006; Jian et al., 2009; Willott et al., 2010), as well as a few AGNs were detected at higher redshifts (up to $z = 7.085$, Mortlock et al., 2011).

The classification of AGNs is complex and not unambiguous. AGNs show a large variety of phenomena which are hardly seen in normal galaxies but are not univocally and precisely observed in every AGN. We can only make a list of observational properties in terms of e.g. photometry, polarization, and spectrum, which are required to classify a specific source as an AGN. This is an empirical way to define AGNs, but it is the best way, until further comprehension of the underlining AGN physics.

A widely used classification separates AGNs into radio-loud and radio-quiet AGNs (e.g., Wilson & Colbert, 1995, see also Section 1.7). From an observational point of view (1) the radio-loud AGNs (RLAGNs) exhibit large scale radio jets and lobes. The bulk kinetic power of the jets often represents a significant fraction of the total bolometric AGN luminosity. Conversely, radio-quiet AGNs are commonly associated with radio ejecta whose bulk kinetic energy is negligible with respect to the radiative power of the AGN. (2) The RLAGNs are preferentially associated with elliptical galaxies, whereas the radio-quiet ones commonly prefer spiral hosts (see Section 1.1). (3) The space density of the RLAGNs at a given optical luminosity is $\sim$ 10 times lower than that of radio-quiet AGNs. The last point, supported by work on the luminosity function of AGNs (Simpson et al., 2012), suggests that RLAGNs roughly constitute $\sim 10 - 20\%$ of all AGNs (Della Ceca et al., 1994; Kellermann et al., 1998).

Radio-quiet quasars[2] and Seyfert galaxies are usually included among the radio-quiet AGN class, whereas RLAGNs comprise blazars, radio-loud quasars, and radio galaxies. Blazars emit over the entire electromagnetic spectrum, from radio to gamma-rays, and reach at these highest frequencies their largest luminosities, up to 10^{48} erg s^{-1}. A large fraction of the radiative power of radio galaxies is instead emitted in radio. Radio galaxies have typical 1.4 GHz rest frame powers in the range $\sim 10^{39-44}$ erg s^{-1}.

Only a few radio-loud quasars have been discovered at $z \gtrsim 5$ (McGreer et al., 2009; Yi et al., 2014, the great majority of AGNs detected at $z \gtrsim 5$ is in fact constituted by radio-quiet quasars). Similarly, both radio galaxies (De Breuck et al., 1999; van Breugel et al., 1999) and blazars (more recently, Sbarrato et al., 2013a; Ghisellini et al., 2014) have been found up to redshifts $z \sim 4 - 5$.

Blazar sources are further distinguished between BL Lacs and Flat Spectrum Radio Quasars (FSRQs). They differ in terms of many observational properties. Among them, at variance with FSRQs, BL Lacs lack emission lines with Equivalent Width $EW \gtrsim 5$Å, show lower isotropic luminosities than FSRQs, and do not exhibit an optical/ultra-violet bump that is commonly found in the spectral energy distributions (SEDs) of FSRQs (see also Section 2.2).

Similarly, on the basis of the radio morphology, radio galaxies are divided into Fanaroff-Riley radio sources of Type I and II, abbreviated as FR Is and FR IIs, respectively (Fanaroff & Riley, 1974). FR I radio galaxies are bright in the proximity of the core and show a slowly decreasing surface brightness at increasing distance from the core. On the other hand, FR II radio galaxies are edge-brightened, i.e. they are very bright at their extremities, whereas they are fainter in the proximity of the core (see also Section 3.1). We refer to Chapters 2 and 3 for a thorough discussion of the blazar and the radio galaxy populations, respectively.

Similarly to the above mentioned radio-quiet AGN versus RLAGN classification, according to the original classification of Kellermann et al. (1989), a QSO is classified as radio-loud if the ratio of radio (5 GHz) to optical (B-band) flux is $\gtrsim 10$. Vice-versa, the QSO is radio-quiet.

From an observational point of view, the nucleus of an AGN usually appears point-like in optical images and produces its luminosity in a tiny, sub-pc scale, volume. However, this simple scenario might be misleading. The ability to detect the bright nucleus depends on many factors, such as the above mentioned luminosity contrast between the nucleus and the host galaxy. Furthermore, the typical luminosity of an AGN can easily increase by two orders of magnitudes from redshift $z = 0$ to $z \sim 2$ and it also depends on the wavelength.

In general, while QSOs and many blazars appear point-like, the other

[2]Quasars are also commonly denoted as Quasi Stellar Objects (QSOs).

AGNs such as radio galaxies and Seyfert galaxies show an extended morphology. This is because of the observational appearance of the host galaxy or (some of) the AGN components surrounding the active nucleus. The latter include jets, lobes, and dusty clouds (see also the following Sections).

Using low-frequency radio *very-long-baseline interferometry* (VLBI) well collimated variable structures with apparent speeds of $\sim 10\ c$ are detectable in the sky plane. This is especially true for blazars, where the apparent velocity of the inhomogeneities is pointing towards the observer, thus originating strong relativistic aberration. In radio galaxies the inhomogeneities observed in radio at low-frequencies, i.e. $\lesssim 5$ GHz, have a jet-like morphology and are extended up to several-kpc or Mpc scales. However, the jets of radio galaxies are almost perpendicular to the line-of-sight. Therefore the relativistic aberration is weak and superluminal motions are more difficult to observe than in blazars.

The present belief is that the power of AGNs comes from accretion onto super massive black holes (SMBHs) situated in the center of the active nuclei. Lines of essential evidence in favor of the presence of a central super massive black hole in the center of an AGN are based on theoretical arguments, an array of circumstantial facts, and a few observations. Even if the presence of a SMBH in AGNs has achieved a widespread acceptance, such a scenario is not completely confirmed yet. This is because direct signatures of accretion onto massive black holes are hardly possible to obtain and only indirect evidence of the existence of SMBHs is available.

Observational evidence in favor of the existence of SMBHs includes rapid time variability observed in different types of AGNs, superluminal jets, that might be explained in association with rotating SMBHs (Blandford & Znajek, 1977), and the fact that AGN engines keep the jet ejection directions unchanged for up to 10^7 yr, as for example inferred by the presence of collimated and straight Mpc-scale jets in powerful radio galaxies, thus suggesting that SMBHs are good gyroscopes. The observed very high AGN luminosity demands minimum central masses in the range $\sim 10^{6-10}\ M_{\odot}$, in order to avoid that the AGN luminosity does exceed the Eddington limit[3]

Concerning the above mentioned variability argument, observations of AGNs such as Seyfert galaxies in the X-rays show flux variability by a factor of ~ 2 on a time scale of a few hours (Mushotzky et al., 1993) . Observations of blazars, especially those at high energies (X-ray and γ-ray bands and the

[3]The Eddington limit, also denoted as Eddington luminosity, is the maximum luminosity a self-gravitating radiating source can reach in hydrostatic equilibrium, i.e. when the radiation pressure balances that originated by the gravitational force. It can be shown that the Eddington limit corresponding to an object of mass M is equal to $L_{\rm Edd} \simeq 1.5 \times 10^{38}\ (M/M_{\odot})$ erg s^{-1}. Such a value is obtained by assuming spherical symmetry and the Thomson cross-section. The latter assumption is reasonable for photon energies $\lesssim 100$ keV. The Eddington ratio is an adimensional quantity defined as the luminosity divided by $L_{\rm Edd}$.

most recent observations at TeV energy band with Cherenkov telescopes) exhibit variability on time scales down to less than an hour (Aharonian et al., 2007; Albert et al., 2007), revealing the compact nature of these sources and consistently with the hypothesis of strong relativistic beaming and spatial emitting-region dimensions of less than $\sim 10^{-3}$ pc, after beaming correction.

Both theoretical models and observations agree with the fact that AGNs undergo different evolution depending on their type. Furthermore, these studies are sensitive to the specific wavelengths considered in estimating the luminosity function, to the sample selection, and to the related possible biases. However, it is generally accepted that the luminosity function of the overall AGN population undergoes positive evolution with increasing redshift and reaches its maximum at redshift $z \sim 2.5$, when AGNs were ~ 2 orders of magnitude more numerous than today (e.g. Aird et al., 2010). The statistics at redshifts $z \gtrsim 2$ is fragmentary and the AGN evolution at these redshifts is debated. In the context of source count analysis both BL Lacs and FR Is play a remarkable role because their number density seems to be fairly unevolved with redshift, even if hints for their evolution have been reported in the literature in both theoretical and observational work (Sadler et al., 2007; Ajello et al., 2014).

1.1 AGNs and their host galaxies

There are lines of evidence that SMBHs and host galaxies follow a common evolutionary path. One of them is the relationship between SMBH mass $M_\bullet$ and both the stellar velocity dispersion, $\sigma_\star$ (Ferrarese & Merritt, 2000; Gebhardt et al., 2000) and the mass of the spheroidal component of the host galaxy. Similar relations have been found between the SMBH mass and the near-IR (NIR) luminosity of the galaxy bulge (e.g. Marconi & Hunt, 2003).

Despite this knowledge, we actually do not fully understand the interplay between AGNs and their host galaxies. For example, an unresolved problem is that radio-quiet AGNs are found in both spiral and early-type (E and S0, according to the Hubble classification) galaxies, instead RLAGNs are found only in early-type galaxies (e.g., Zirbel & Baum, 1998; Scarpa et al., 2000; Donzelli et al., 2007; Nilsson et al., 2007). Furthermore, RLAGNs are generally associated with the most massive SMBHs as there is a clear difference between the radio-quiet and radio-loud black hole mass distribution, where RLAGNs are statistically associated with black-hole masses $\gtrsim 10^8\ M_\odot$ (e.g. Chiaberge & Marconi, 2011). A possible exception may be represented by Radio Loud Narrow Line Seyfert 1s that seem to be associated with lower mass, $\sim 10^{6-8}\ M_\odot$, black holes (e.g., Foschini et al., 2014).

Furthermore, it was found that spheroidal hosts become more prevalent with increasing nuclear luminosity such that, for nuclear magnitudes $M_V < -23.5$, the hosts of both radio-loud and radio-quiet AGNs are virtually all

massive ellipticals (Dunlop, 2001). However, the basic properties of these hosts seem to be indistinguishable from those of quiescent, evolved, low-redshift ellipticals of comparable mass (Dunlop, 2001). This result seems to indicate that radio-loudness is not determined by host-galaxy morphology only and also sets severe constraints on evolutionary schemes.

1.2 Spectra

In the energy range from the MIR to the soft X-rays several emission components that may typically contribute to the AGN spectrum (see e.g. Elvis et al., 2012). Among them there are the non-thermal broadband emission from the jet, the accretion disc optical and ultraviolet (UV) emission, the MIR light from dusty clouds surrounding the nucleus, the host galaxy emission, the lines emitted by regions surrounding the central nucleus, and the soft X-ray emission from highly energetic particles such as those in the corona (see the following Sections for discussion of all these components).

Although the presence of these components that are commonly associated with bumps and excesses observed in the SED, in the MIR to soft X-ray energy range the AGN SED may be described, in first-order approximation, by a power law or a sum of power laws (e.g., Hao et al., 2010). The deviation from the simple power-law description is often well described by a thermal single or multi-temperature black-body spectrum to take the observed bumps and features (e.g. associated with the accretion disc and the MIR emitting dusty clouds) into account.

At lower frequencies, the fraction of the total AGN luminosity radiated in radio is usually an order of magnitude or in some cases several orders of magnitude higher than that of a typical galaxy, as in the case of RLAGNs. Similarly, the X-ray power emitted by an AGN is three to four orders of magnitude greater than in normal galaxies.

Remarkably, for the RLAGNs the above mentioned power-law description extends down to the radio frequencies. Furthermore, some nearby RLAGNs (e.g. the radio galaxy M87, Acciari et al., 2009a) and the blazars emit up to GeV or, in some cases, TeV energy. In Figure 1.1 we show some SEDs for both RLAGNs (Panels a, b) and radio-quiet AGNs (Panels c, d).

On the contrary a normal galaxy can be roughly considered as a set of stars, whose spectra are well approximated by black bodies. The total span of stellar surface temperatures is only about a factor of ten, so that a typical galaxy emits most of the power within a decade of frequency, in the optical-ultraviolet energy range. Figure 1.2 illustrates the spectra of typical spiral (top panel) and elliptical (bottom panel) galaxies. Note that a clear drop off in intensity at rest frame 4000Å is commonly present in the spectrum of a passively evolving early-type galaxy. The presence (or absence) of such a feature, often denoted as 4000Å Ca break, is due to the presence (or

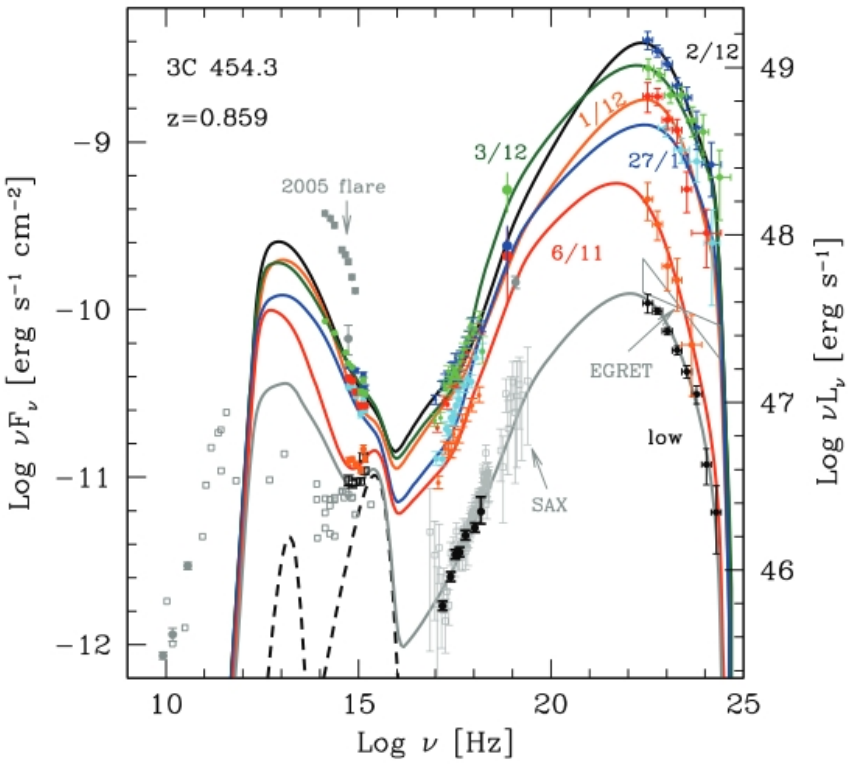

(a)

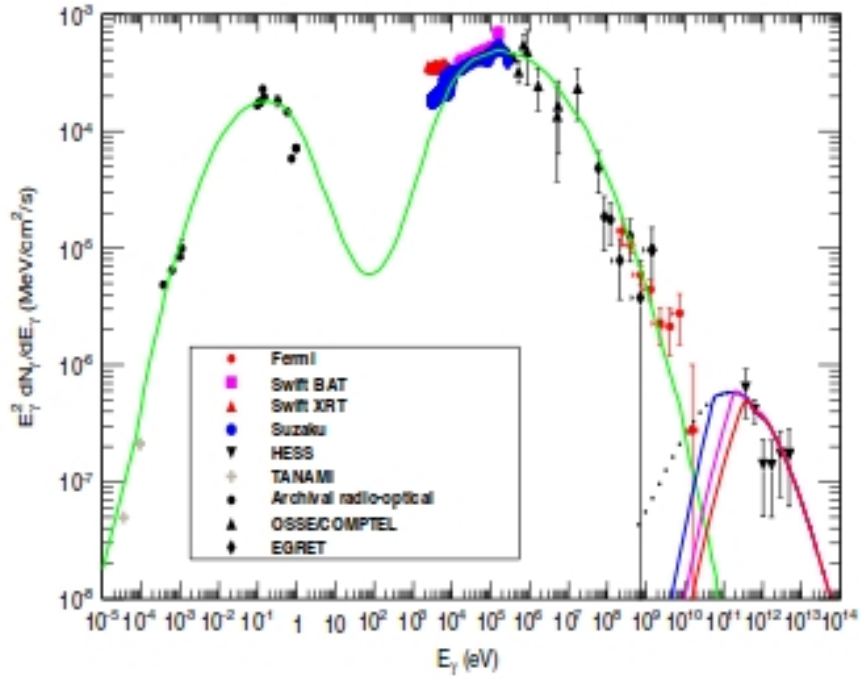

(b)

Figure 1.1: Examples of SEDs of both radio-loud (a, b) and radio-quiet (c, d) AGNs. (a) SED and modeling of the FSRQ 3C454.3 from Bonnoli et al. (2011). (b) SED and modeling of the radio galaxy Centaurus A from Sahu et al. (2012). (c) SEDs of Seyfert 1 galaxies (Prieto et al., 2010). (d) SEDs of Seyfert 2 galaxies (Prieto et al., 2010).

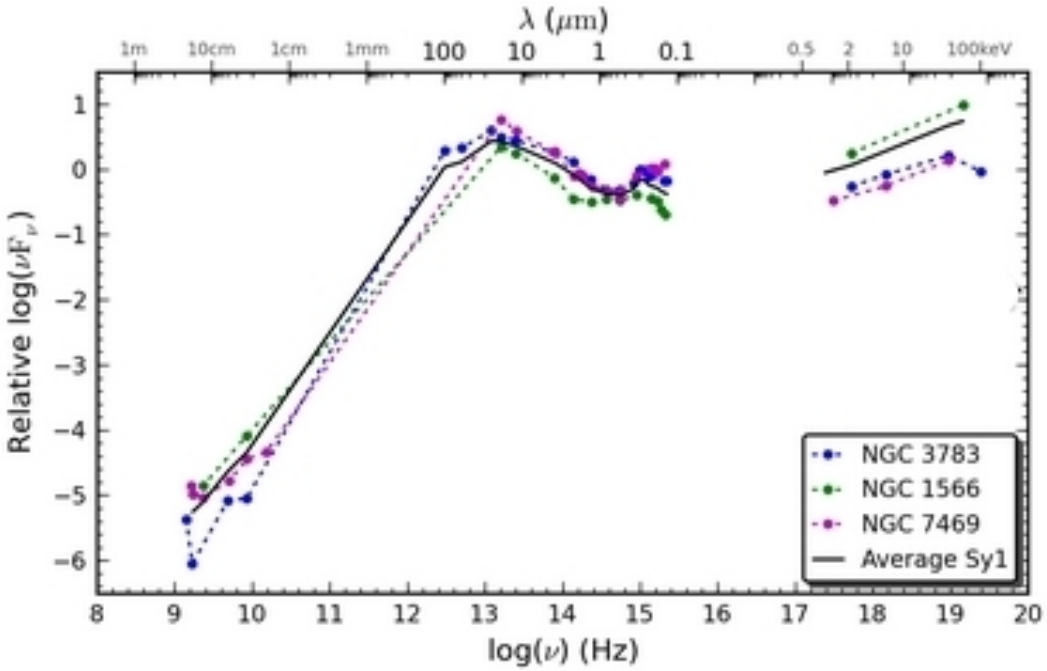

(c)

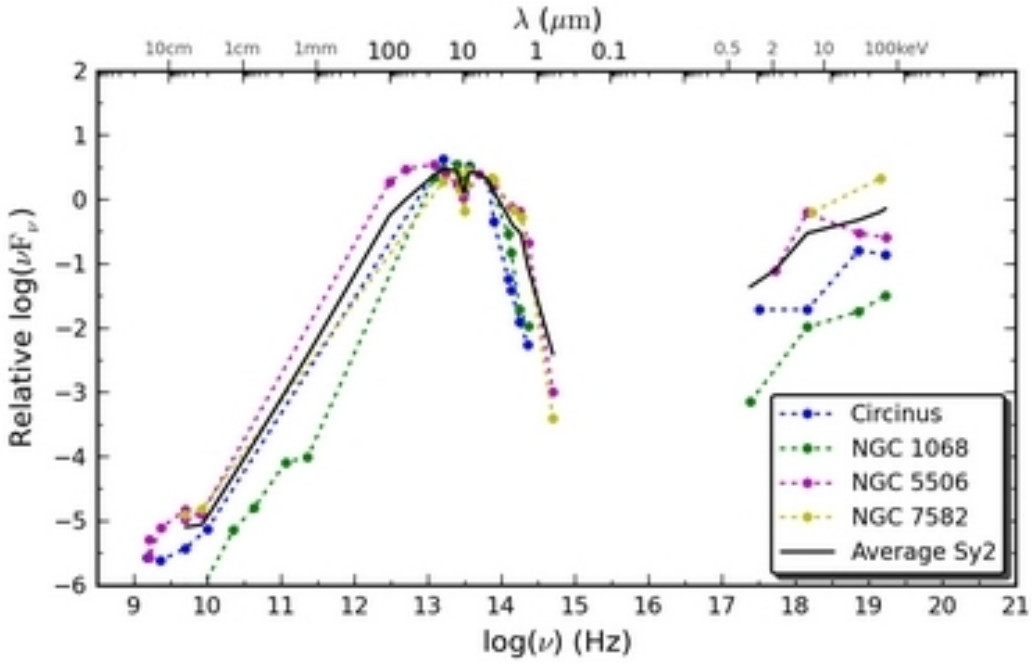

(d)

Figure 1.1: Continued.

absence) of metals in the stellar atmospheres of the low luminosity stellar population. Spiral galaxy spectra are characterized by emission lines, due to hot young stars which heat the surrounding gas, as well as by absorption features due to the older stellar population.

1.3 Lines

AGN emission lines are usually very prominent. The presence of emission lines is a clear signature of an AGN because spectral lines of most stars and galaxies are relatively weak and usually in absorption (see e.g. Figure 1.2). In the optical and UV energies AGNs show emission (only occasionally absorption) lines whose total flux is several percent to tens of percent of the continuum flux in that band. The Balmer lines (e.g., Hα and Hβ), Lyα, C IV 1549 Å doublet, OIII 5007 Å, Mg II 2798 Å, and other ionization lines are very frequently seen in AGN spectra. The Fe Kα X-ray line near 6.4 keV is often observed in X-ray emitting AGNs. In some sources the lines have broad wings whose widths indicate velocities up to several thousand km s^{-1}. These lines often have a narrow core. In other sources the lines are predominantly narrow and correspond to velocities not greater than hundreds of km s^{-1}.

Permitted and semi-forbidden lines are seen in both narrow and broad lines, whereas the forbidden lines are only associated with the narrow lines. Another correlation is that AGNs which exhibit only narrow lines are also usually dim from NIR to X-ray energies and most of their light is emitted in the MIR.

1.4 The broad and the narrow line regions

The presence of both broad and narrow (optical and UV) emission lines in the spectra of AGNs suggests the existence of two different regions where the emission associated with these lines comes from. These regions are denoted as the Broad-Line Region (BLR) and the Narrow Line Region (NLR), respectively. The distribution and the composition of the matter in these regions are quite uncertain (Dopita et al., 2014; Valencia-S. et al., 2014). However, both BLR and NLR are thought as a large number of optically thin clouds that are photoionized by the continuum UV radiation and then emit the observed lines.

The BLR extends from 0.01-0.1 pc for Seyfert galaxies up to $\sim$ 1 pc for the brightest quasars, as deduced from the study of broad-line variability (e.g., from reverberation mapping studies, Kaspi et al., 2007; Peterson, 2007). Because of the absence of forbidden lines, one can infer an electron density $\geq 10^8$ cm^{-3} and a typical gas velocity of $3000 - 10000$ km s^{-1} can be derived from the width of the lines.

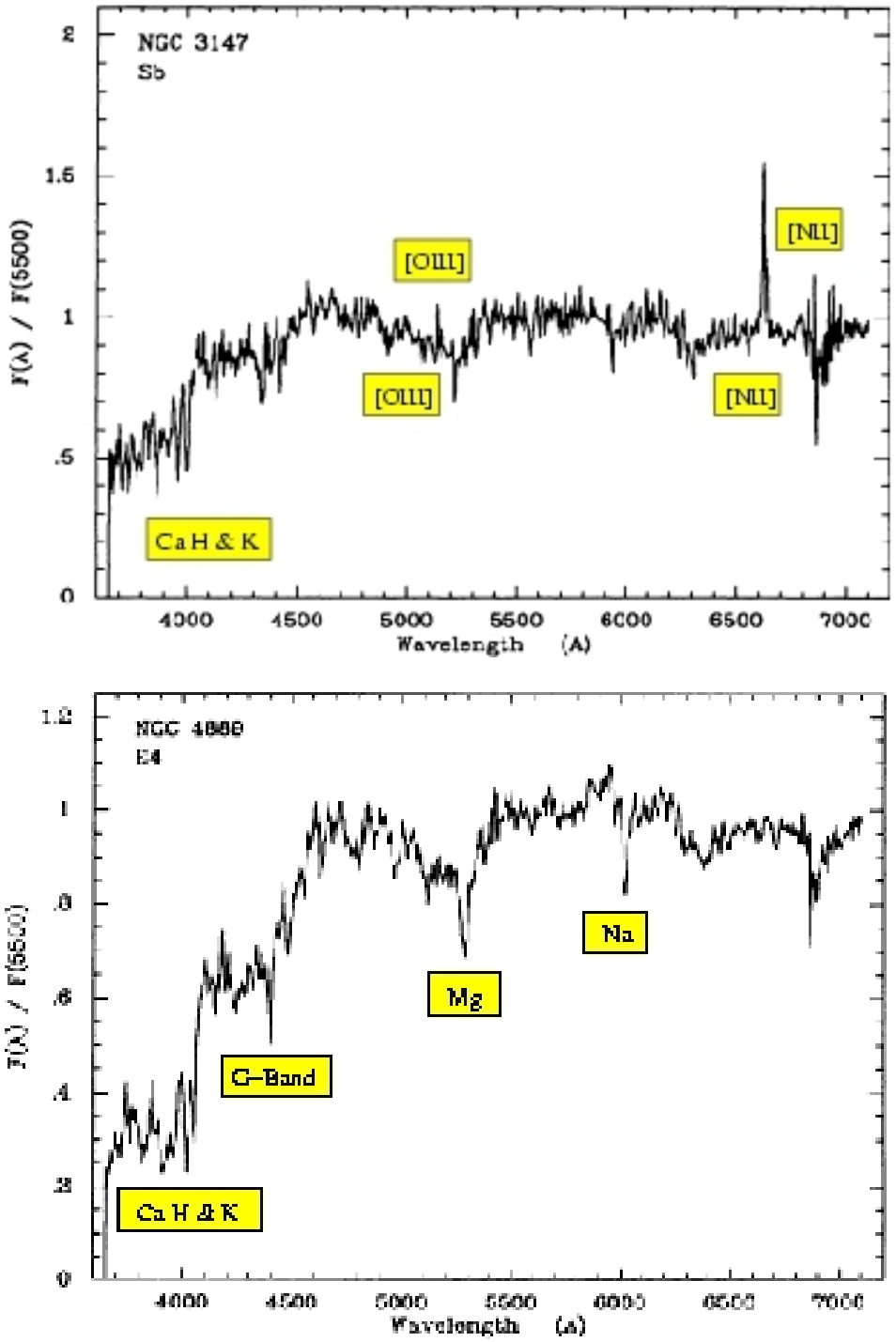

Figure 1.2: Rest-frame spectra of the spiral galaxy NGC 3147 (top panel) and the elliptical galaxy NGC 4888 (bottom panel) from Kennicutt (1992). Some emission and absorption lines are reported in both panels. The Figure is from `http://astronomy.nmsu.edu/nicole/teaching/ASTR505/lectures/lecture26/slide01.html`

.

The narrow line region is instead constituted by gas with lower velocities $300 - 1000\,\mathrm{km\,s^{-1}}$, inferred from the line width. Unlike the broad lines, no correlation is observed between the narrow-line variations and the variability of the continuum emission, suggesting that the NLR is located at much larger distances from the central black hole than the BLR. The location of the NLR (sometimes directly resolved, e.g. Radomski et al., 2003; Bennert et al., 2006) with respect to the central AGN region varies from 100-300 pc in Seyfert galaxies to a few kpc for the brightest quasars.

AGNs are further classified as either of Type 1 (e.g., Seyfert 1s and Type 1 quasars) or of Type 2 (e.g. Seyfert 2s and Type 2 Quasars), depending on the presence or absence of broad lines in their spectra, respectively. Consistently with the AGN unification scheme outlined below (Antonucci, 1993, see Section 1.6), Type 1 QSOs are the high luminosity and high redshift counterparts of Seyfert 1s. This simple picture is nevertheless debated, since most of the QSOs are hosted in ellipticals, while Seyfert 1s are generally hosted in spirals (McLure et al., 1999). On the other hand, the high redshift counterparts of Seyfert 2s are still uncertain.

1.5 The accretion disc

Accretion of matter onto compact objects is the most effective way of extracting energy from baryonic matter. It is widely accepted that this process occurs in the brightest objects in the Universe, including AGNs, binary stars, stellar mass black hole systems, and possibly Gamma Ray Bursts. We refer to e.g. Pringle (1981), Frank et al. (2002), King (2008), and Abramowicz & Fragile (2013) for some reviews of the accretion disc theory.

In AGNs the gas infalls onto a massive $M_\bullet \sim 10^{6-10}\ M_\odot$ compact object (usually a SMBH is assumed) and has to lose almost all of its angular momentum via internal friction. Some form of disc accretion is therefore inevitable (as recent numerical simulations show, e.g. Wurster & Thacker, 2013).

During the accretion process the infalling material loses its angular momentum and converts its gravitational binding energy into radiation via a sort of viscosity in the disc, with an efficiency $\eta = L_d/(\dot{M}c^2)$, where L_d is the accretion disc luminosity, $\dot{M}$ is the mass accretion rate, and c is the speed of light. This accretion process continues until the infalling material reaches the innermost stable circular orbit, $R_\star$, of the order of a few Schwarzschild radii, at which the accretion disc is assumed to be truncated (Shakura & Sunyaev, 1973).

Then the material may fall into the black hole either directly (e.g. following magnetic field lines associated with the black-hole magnetosphere) or through different accretion processes (e.g. adiabatic accretion or non-Keplerian disks). The standard disc truncation might also occur at larger

radii than $R_\star$, as for example in the case of strong interactions between the disc and the magnetic field associated with the black-hole magnetosphere (see e.g Krolik, 1999; Vietri, 2008, for discussion). However, we stress that the exact configuration of the accretion disc and the properties of the accretion around the innermost stable orbit are not settled yet.

An efficiency $\eta = 0.06$ is estimated for the accretion onto a Schwarzschild, i.e. non-rotating, black hole, assuming a geometrically thin and optically thick accretion disc (Shakura & Sunyaev, 1973). The efficiency increases up to $\eta = 0.42$ in the case of a maximally rotating Kerr black hole corotating with the disk (Wald, 1984). However, it is likely that the limit corresponding to the maximally rotating black hole cannot be reached (Thorne, 1974). This result, combined with the fact that η strongly depends on the black-hole spin, implies that the efficiency cannot exceed the value $\eta = 0.3$.

Atomic viscosity associated with ordinary matter leads to negligible and, therefore, unrealistic, accretion rates. This argument shows that the nature of the internal friction might be non-classical. It has been suggested that such a non-classical friction is due to magneto-hydrodynamical turbulence and instability in the disc (Shakura & Sunyaev, 1973; Balbus & Hawley, 1991). Alternative scenarios invoke convection in the disc (Stone & Balbus, 1996), photon viscosity (Loeb & Laor, 1992), and the self-gravity of the disc (Paczynski, 1978a,b).

Following Shakura & Sunyaev (1973), for a standard, i.e. geometrically thin and optically thick, accretion disc the internal viscosity ν can be expressed as follows:

$$\nu = \alpha\, H\, c_s \ , \tag{1.1}$$

where H is the thickness of the disc, c_s is the local speed of sound in the disc, and $\alpha \lesssim 0.1$ is a fudge factor introduced in the parametrization.

Three locally defined time scales play a role in standard discs. The first one is the dynamical time scale $t_{\rm dyn}$ at which the matter orbits around the black hole with Keplerian velocity v_K:

$$t_{\rm dyn} \simeq \frac{R}{v_K} = \sqrt{\frac{R^3}{GM_\bullet}} \ , \tag{1.2}$$

where R is the radius of the orbit and G is the gravitational constant. The hydrostatic equilibrium in the direction perpendicular to the disc plane is restored on a timescale $t_{\rm z} \simeq H/c_s = R/v_K = t_{\rm dyn}$. Note that the second equality, i.e. $H/c_s = R/v_K$, implies that the condition $H \ll R$, required to ensure the thinness of the disc, corresponds to assume $c_s \ll v_K$ or, equivalently, that the orbital motion is supersonic.

Another two time scales are involved. i) The thermal time scale $t_{\rm th}$ is that at which the thermal energy content (enthalpy) of the disc per unit surface area is increased because of the heating rate due to viscous dissipation. ii) The time scale for radial drift towards the black hole through the disk over

a distance of order R is the viscous time scale $t_{\rm v}$. The following ordering can be proved:

$$t_{\rm dyn} \simeq t_z \simeq \alpha t_{\rm th} \simeq \alpha \left(\frac{H}{R}\right)^2 t_{\rm v} \ . \tag{1.3}$$

For a thin disc, i.e. $H \ll R$, the previous relations imply

$$t_{\rm dyn} \simeq t_z \lesssim t_{\rm th} \ll t_{\rm v} \ . \tag{1.4}$$

This represents a strong result. It shows that the infall, driven by the internal disc viscosity, is a very slow process. The timescale $t_{\rm v}$ on which mass moves inwards to power the AGN approaches the Hubble time for disc radii of order 0.3 pc, i.e. $\sim 10^{18}$ cm, for a typical AGN black hole mass $\sim 10^8\ M_\odot$, and an accretion rate $\dot{M} \sim 1 \times\ M_\odot\ {\rm yr}^{-1}$. This shows that the infalling material should have a small angular momentum to form a disc and ultimately reach the central black hole.

On the other hand, the dynamical and thermal timescales are much shorter than $t_{\rm v}$ and in the central regions are $\sim 10^3$ and 10^4 sec, respectively. These are the shortest possible timescales expected for significant variability.

A simple argument can be used to estimate the temperature of the disc. Under the assumptions that i) differential rotation in the disc is ultimately responsible for the local heating in the disc and ii) the heating is dissipated locally into radiation through black body emission, the temperature profile $T(R)$ is given by

$$T(R) = \left\{ \frac{3GM_\bullet \dot{M}}{8\pi R^3 \sigma} \left(1 - \beta\sqrt{\frac{R_\star}{R}}\right) \right\}^{1/4} , \tag{1.5}$$

where σ is the Stefan-Boltzmann constant, and β is the fraction of the angular momentum that is retained by the infalling material when it leaves the inner edge of the disc. The value $\beta = 1$ is often conservatively assumed in the literature. However, accreting magnetospheres, for example, can spin down by interaction with the disk, thus allowing values of $\beta < 1$ (Spruit & Taam, 1993; Rappaport et al., 2004).

It is clear from Equation 1.5 that the gravitational energy release is dominated by the central regions located at $R \sim {\rm few} R_\star$, i.e. at a distance $\sim$ few $\times\ GM_\bullet/c^2 \sim$ few $\times\ 10^{13}$ cm $[M_\bullet/(10^8 M_\odot)]$ from the central SMBH. For typical accretion rates and SMBH masses the disc temperatures are $\sim$ few 10^5 K. Thus most of the luminosity from the AGN disc is in the UV and soft X–rays (in the rest–frame). Note that the AGN disc temperatures are much smaller than those of discs observed in X-ray binaries, where viscous stresses heat the material to millions of degrees.

From an observational point of view, an optical/UV bump, commonly denoted as big-blue bump, is often detected in SEDs of bright AGNs (see

also Section 1.8.4). It has been interpreted as a signature of thermal emission from the accretion disc since early work by Malkan (1983), who tried to compare directly the accretion disc model with the observational data.

Furthermore, the high-energy (X-ray) tail of the AGN disc spectrum is often associated with a region, called corona, made by electrons that reside in the proximity of the disc surface and upscatter the optical/UV emission from the disc in X-rays through Inverse Compton (IC, e.g. Fabian et al., 1987; Sazanov et al., 2012).

Another major feature in the optical/UV spectra of quasars is the small blue bump (Wills et al., 1985; Elvis , 1985) between $\sim 2200 - 4000$ Å in the rest frame. Such a feature is due to the blending of emission lines from both the ion Fe II and the Balmer recombination continuum. Since in this work we will consider the big-blue bump only, we will denote it blue bump or optical/UV bump, with no distinction.

1.6 The AGN torus

A fraction of the radiation produced by accretion into the central SMBH is absorbed and re-emitted mainly at MIR wavelengths by a dusty, massive, possibly clumpy (Markowitz et al., 2014) medium commonly referred to as the torus (see Hoenig , 2013, for a recent review). The clumpiness of the torus is mainly required to reproduce the torus emission in SEDs of AGNs, see Bianchi et al. (2012) for a review. Nevertheless, while there is broad agreement about the essence of the unified scheme concept, the detailed properties of the tori remain unsettled.

Several lines of observational evidence support the presence of a dusty torus in AGNs. Among them there is the direct imaging of disk-shaped dust around some AGNs (see Figure 1.3). Furthermore some sources such as NGC 1068 show a Type 2 AGN spectrum and a Type 1 AGN spectrum is revealed in polarized light (Antonucci & Miller, 1985). This suggests that electrons polarize and scatter a fraction of both nuclear and the BLR's emission into observer's line-of-sight with no substantial reprocessing by dust.

Remarkably, the presence of the dusty torus is key for the so called AGN unification scheme (Antonucci, 1993), where the difference between Type 1 and Type 2 AGNs is explained as due to a different orientation of the line-of-sight with respect to the torus axis of symmetry. According to this scenario, Type 2 and Type 1 AGNs are those where the light observed from the BLR is and is not reprocessed by the torus, respectively. For this reason, Type 2 AGNs are also often associated with obscured AGNs, for which a substantial fraction of the light emitted by the active nucleus is scattered and reprocessed in the MIR by the torus.

Typically, the soft X-ray flux at $\lesssim$ few keV is reduced in Type 2 AGNs

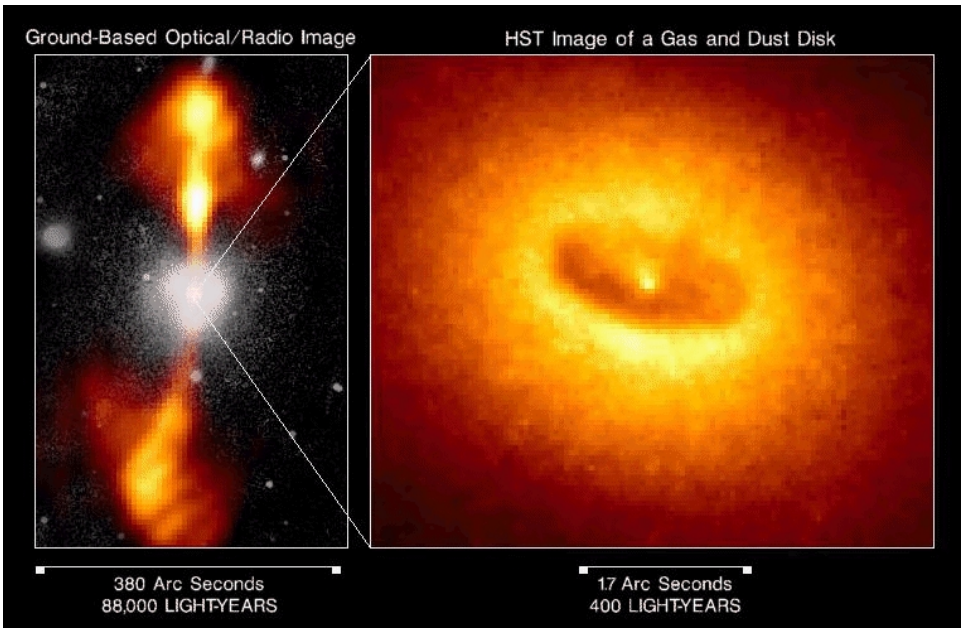

Figure 1.3: Images of the radio galaxy NGC 4261. Left: ground based composite optical (white) and radio (yellow/orange) image showing the optical emission from the galaxy and the radio jets with a few tens of kpc extension. Right: Hubble Space Telescope (HST) image of the galaxy center showing the gas and the AGN dusty torus. Credit: HST/NASA/ESA. Figure from `http://astronomy.swin.edu.au/~gmackie/DarkStar/alpha.html`.

by torus absorption. This evidence, combined with broad band spectral X-ray observations suggest that typical hydrogen column densities associated with the AGN torus are in the range $\sim 10^{20-25}$ cm^{-2}.

Torus absorption affects the X-ray emission by means of photoelectric absorption and Compton scattering. Photoelectric absorption is effective for hydrogen column densities $\gtrsim 10^{21}$ cm^{-2}, is energy-dependent, and is not significant above 10 keV and for column densities $< 10^{24}$ cm^{-2}. Compton scattering becomes significant at column densities $\gtrsim 10^{24}$ cm^{-2} and does not have a significant energy dependence below 150 keV.

Column densities lower than $\sim 10^{22}$ cm^{-2} are commonly associated with unobscured AGNs, whereas obscured AGNs are identified by column densities $\sim 10^{22-24}$ cm^{-2} At higher column densities, when the X-ray obscuring matter has a column density higher than the inverse of the Thomson cross-section $\sigma_{\rm T}^{-1} \sim 1.5 \times 10^{24}$ cm^{-2}, Compton scattering highly affects the X-ray spectrum and the source is called Compton thick .

The soft X-ray flux of Type 2 AGNs is commonly reduced at energies $\lesssim 2$ keV by torus absorption for typical column densities $\sim 10^{22}$ cm^{-2}. In general, for column densities $\lesssim 10^{25}$ cm^{-2} the nuclear radiation is visible above 10 keV and the source is called mildly Compton thick. For higher column densities, i.e. heavily Compton thick, the entire X-ray spectrum is down-scattered and suppressed by Compton scattering. See Comastri (2004) for a review on Compton thick AGNs.

In the case of heavily Compton thick sources the evidence of obscuring material can be inferred with indirect arguments, such as studying the above mentioned iron Kα line complex at ∼6.4 keV (see Section 1.3). In fact the gas surrounding the central regions of the AGN, reprocessing the continuum radiation, may affect the intensity of the iron line (Leahy & Creighton, 1993; Ghisellini et al., 1994; Matt et al., 1996). Similarly, the *EW* of the iron line can be powerfully used to study Compton thick sources. The *EW*, estimated in contrast to the absorbed continuum, is expected to increase with increasing column density. In fact, while in Compton thin sources the *EW* of the iron line is of a few hundred eV (Bianchi & Matt, 2002), in Compton thick sources the iron line can easily reach an $EW \gtrsim 1$ keV (Levenson et al., 2002; Feruglio et al., 2011).

Short period, i.e. from month to several-year, variability studies in the X-rays suggest a torus inner edge < 1 pc and that most of the obscuring gas is located within a radius of a few 10 pc from the active nucleus (e.g., Risaliti et al., 1999, 2002, 2005). However, variability studies are less sensitive to the total torus extension than recent high-resolution studies. In fact, recent work based on molecular emission line observations suggests the presence of high density, $\sim 10^{5-6}$ cm^3, molecular hydrogen gas and circum-nuclear dust, interpreted as torus components, at distances ∼50-150 pc from the active nucleus (Davies et al., 2012; Hailey-Dunsheath et al., 2012; Sani et al., 2012).

The circum-nuclear tori around AGNs have a key role in determining both their physical properties and their observed SEDs. Clues to the morphology of the torus also come from studies of obscuration of the nuclei and of the re-emission by heated dust. Their obscuration properties have been recently investigated using large samples of X-ray (Hao et al., 2013; Lusso et al., 2013; Merloni et al., 2014) or optically (Calderone et al., 2012; Ma & Wang, 2013; Roseboom et al., 2013) selected AGNs. Two approaches have been used. One is demographic. It statistically gauges the covering factor of the obscuring medium from the ratio of obscured to unobscured AGNs (Ogle et al., 2006; Lawrence & Elvis, 2010). Alternatively, the covering factor, i.e. the solid angle subtended at the center of an AGN by the torus, is estimated from the SED and in particular from the infrared (IR) to bolometric flux ratio of each individual source (SED-based approach, Hatziminaoglou et al., 2008, 2009; Alonso-Herrero et al., 2011); this ratio is a measure of the fraction of the nuclear emission that is absorbed by the dusty torus and re-emitted in the IR.

One of the main goals of our work on blazars is to search for evidence of AGN torus in them (see Part III). We point out that little is known about the properties of tori associated with FSRQs although indications of their presence have been occasionally reported (e.g., Sbarrato et al., 2013b). On the contrary, Plotkin et al. (2012) did not detect any observational signature of a dusty torus from a sample of ~ 100 BL Lacs.

1.7 The RLAGN unification scheme

In addition to the above mentioned AGN unification scheme, the unification of the RLAGN subclass has been proposed on the basis of the orientation of the jet axis with respect to the line-of-sight (Blandford & Rees, 1978). See also Urry & Padovani (1995).

Under the assumption that the RLAGN structure has azimuthal symmetry around the jet axis, a large variety of the observed properties and reliable classifications as a function of the observing angle are naturally manifested.

In this scenario, it is believed that RLAGNs in which the jet is observed end-on belong to the blazar class, whereas ordinary radio loud quasars are viewed at larger angles from the jet axis, and radio galaxies have jets seen almost perpendicularly in the plane of sky. The specific jet orientation is responsible for the high luminosities and for the fast variability observed in these objects. Indeed relativistic time dilation and the relativistic beaming enhance i) the observed bolometric flux and ii) the observed degree of variability estimated as the change in the bolometric flux over a period of time by factors of δ^4 and δ^5, respectively (e.g. Urry & Padovani, 1995), with

respect to an observer comoving with the jet. The quantity

$$\delta = \frac{1}{\Gamma(1 - \beta \cos i)} \tag{1.6}$$

is the Doppler factor of the jet which depends on the viewing angle i, on the bulk Lorentz factor Γ of the jet, and on the apparent velocity v of the jet through the relation $\beta = v/c$.

In summary, most of the RLAGN properties can be explained in terms of plasma moving at relativistic speeds with different orientations with respect to the observer's direction. Figure 1.4 schematically illustrates the AGN unification scenario, where the RLAGNs and radio-quiet AGNs are shown in the top and bottom part of the Figure, respectively.

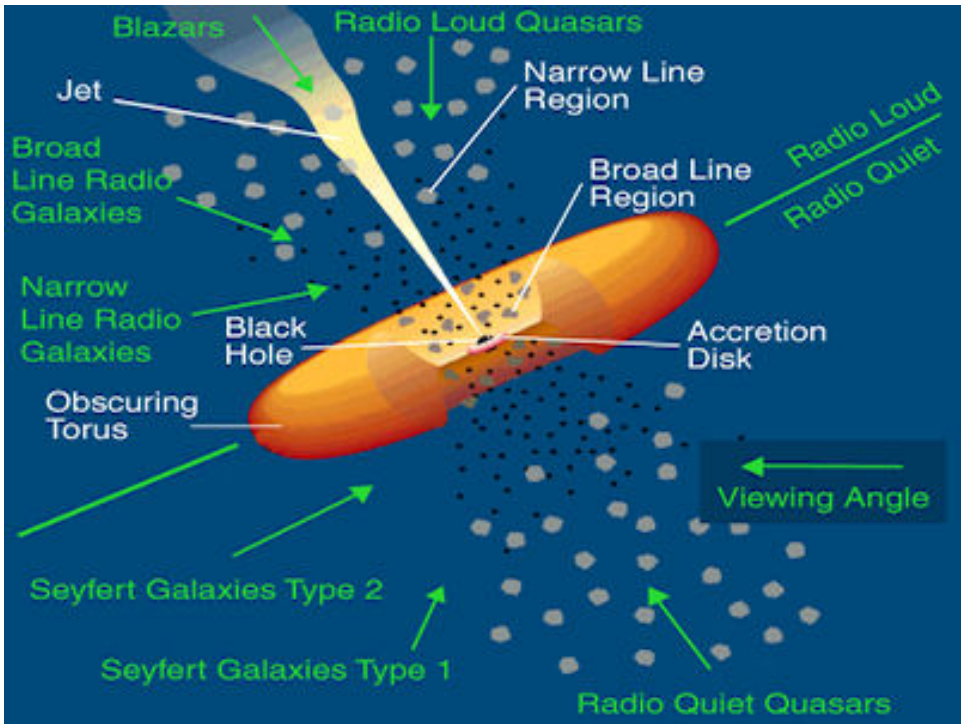

Figure 1.4: Schematic view of an AGN for both RLAGNs (top part) and radio-quiet AGNs (bottom part) from Urry & Padovani (1995). The main AGN components are reported as white labels. Green labels: AGN types corresponding to different orientations of the AGN jet with respect to the observer. The orientations are shown with the green arrows.

1.8 Black hole mass estimates

Reliable mass estimates of black holes (BHs) in active galaxies are essential for investigating the physics of accretion and emission processes in the BH environment and the link between the BH growth and the evolution of galaxy stellar populations. In the following Sections we will describe some of the main methods to estimate BH masses in AGNs. We refer to Kormendy & Ho (2013) and Shen (2013) for recent reviews.

1.8.1 Dynamical mass estimates

Dynamical BH mass estimates are only possible for nearby objects whose parsec-scale BH sphere of influence can be resolved. Such estimates are usually applicable to quiescent galaxies (e.g., the galactic center). So far, there are $\sim$ 90 galaxies for which BH mass estimates have been obtained by means of dynamical modeling of spatially resolved kinematics (see e.g. Kormendy & Ho, 2013, for a review).

There have been several attempts to obtain dynamical black hole mass estimates also for nearby active galaxies such as local radio galaxies, e.g. NGC 4261 (Ferrarese et al., 1996), Centaurus A (Marconi et al., 2001), M87 (Macchetto et al., 1997), M84 (Bower et al., 1998), and Seyfert 1s (Onken et al., 2007, 2014), using spatially resolved stellar kinematics (e.g., Davies et al., 2006; Onken et al., 2007) or gas kinematics (Hicks & Malkan, 2008) down to the BH sphere of influence. However, the number of reliable dynamical AGN black hole mass measurements is still limited. In fact dynamical mass estimates for AGNs, especially the bright ones, are observationally challenging mainly because the AGN continuum overwhelms the stellar absorption features and because non-gravitational forces such as that associated with radiation pressure affect gas dynamics.

Water maser disks are also alternatively used to estimate black hole masses by means of spatially-resolved kinematics. Unfortunately water masers are rare and such dynamical black hole mass estimates are only possible for a few AGNs (typically Seyfert 2s, Miyoshi et al., 1995; Kuo et al., 2011).

Remarkably, dynamical measurements of black hole masses allowed to study the demographics of the black hole population and the connection of the SMBHs with their host galaxies (see e.g. Kormendy & Richstone, 1995, for a review). In particular, the possible correlations involving the black hole masses and some physical properties associated with the galactic bulge (e.g., its stellar velocity dispersion, luminosity, and mass, see Section 1.1) were essential to suggest a coevolution of the SMBH and the bulge during cosmic time and galaxy evolution.

Although all these achievements obtained with dynamical BH mass estimates other methods such as the reverberation mapping and single-epoch

spectroscopy of broad emission lines in AGNs now allow BH mass estimates for large samples of AGNs for which the BH sphere of influence cannot be resolved. These methods will be discussed in the following sections and allow to investigate the BH demographic for AGNs up to higher distances and over a wider range of both AGN luminosities and Hubble types of the host galaxies.

1.8.2 Reverberation mapping

An effective way to estimate BH masses in AGNs is the reverberation mapping technique. Under the commonly used assumption that the BLR is in virial equilibrium, the BH mass is derived as

$$M_\bullet = f\frac{R_{\rm BLR}\Delta V^2}{G}, \tag{1.7}$$

where $R_{\rm BLR}$ is the BLR radius, ΔV is the velocity of the BLR clouds (that can be inferred from the line width), f the virial coefficient that is introduced to account for our ignorance of the structure and kinematics of the BLR, and G the gravitational constant.

The reverberation mapping allows to estimate the BLR size $R_{\rm BLR}$ exploiting the delay, typically of a few weeks, in the response of the BLR to short-term variability of the ionizing continuum in Type 1 AGNs (Blandford & McKee, 1982). While in principle the reverberation mapping technique might be applied to all Type 1 AGNs, it has been successfully used to estimate BH masses in ~ 50 AGNs so far. Nevertheless, such a number might significantly increase in the next future (Shen et al., 2014).

The reverberation mapping technique has limited applicability mainly because it requires long-term monitoring of both the continuum and the broad emission lines. Furthermore, its application is difficult at either redshifts $z \gtrsim 0.3$ or high AGN luminosities in the range $10^{46.4-47.6}$ erg s^{-1} (Kaspi et al., 2007). This is mainly because the cosmological time dilation highly affects the variability study and because the fractional variations in the AGN flux are small at the above mentioned luminosities, respectively.

The $R_{\rm BLR}$ - $L_{\rm opt}$ relation

One remarkable result is a tight correlation, $R_{\rm BLR} \propto L_{\rm opt}^{\alpha}$ (Kaspi et al., 2000, 2005; Bentz et al., 2009), valid over ~ 4 orders of magnitude in luminosity and expected from photo-ionization model predictions (Koratkar & Gaskell, 1991), between the measured BLR radius, estimated with the reverberation mapping technique, and the optical continuum luminosity $L_{\rm opt}$, typically measured at rest-frame 5,100 Å.

Early work reported values of $\alpha \simeq 0.7$ (Kaspi et al., 2000), later work accounting for the starlight contamination in estimating $L_{\rm opt}$ found $\alpha \simeq 0.5$

(Bentz et al., 2009), closer to the value expected from photo-ionization model predictions.

Because of the limited application of the methods outlined so far alternative methods such as the single-epoch method and the blue-bump method have been tested and successfully applied to estimate BH masses in AGNs. We will describe them in the following sections. In particular, as will be clarified in the following, the existence of the luminosity – BLR size relation overcomes some difficulties in estimating the BLR size and allow the exploitation of the single-epoch method as a valuable alternative to the reverberation mapping technique.

1.8.3 Single-epoch method

BH masses of luminous AGNs are most commonly estimated adopting the virial assumption as in Equation 1.7 and using a technique known as 'single-epoch virial method' or, briefly, 'SE method'.

The SE method bypasses some of the above outlined problems affecting BH ass estimates and allows BH mass estimates for large samples of AGNs including those with high luminosities in the range $10^{46.4-47.6}$ erg s^{-1} and at redshifts $z \lesssim 2$ (e.g. Trakhtenbrot & Netzer, 2012). This is achieved by exploiting the correlation between the size of the BLR and the AGN optical/UV continuum luminosity empirically found from reverberation mapping. Therefore, at variance with the reverberation mapping technique, the SE epoch is not demanding in terms of time and is therefore flexibly applicable.

At higher redshifts, i.e. $z \gtrsim 2$, the statistics is less rich. Nevertheless BH mass estimates have been obtained with the SE method for quasars up to $z \sim 7$ (De Rosa et al., 2011, 2014), mainly thanks to the developments of the NIR spectroscopy.

Measurements of the AGN continuum may be affected by various systematics: contributions from broad Fe II emission and/or from the host galaxy and, especially in the case of blazars, contamination by synchrotron emission from the jet (Wu et al., 2004; Greene & Ho, 2005). Fortunately, there are tight, almost linear correlations between the luminosity of the AGN continuum and the luminosity of emission lines such as Hα, Hβ, Mg II, and C IV (Greene & Ho, 2005; Vestergaard & Peterson, 2006; Shen et al., 2011). It is thus an expedient to estimate the BH masses using line luminosities and full widths at half maximum (FWHMs).

Nevertheless, the reliability and accuracy of the method and of the resulting mass estimates, $M_\bullet$, is still debated (Croom, 2011; Assef et al., 2012). Each of its ingredients is endowed with a considerable uncertainty (Vestergaard & Peterson, 2006; Park et al., 2012b). Recent estimates of the virial coefficient, f, differ by a factor $\simeq 2$. The luminosity – BLR size relations have a significant scatter. In addition line widths and luminosities are ob-

served to change on short time scales (while the BH mass clearly remains the same and varies on much longer time scales). This indicates that the BLR structure may change in a way we do not understand yet.

These uncertainties are on top of those on the measurements of line widths and luminosities, which need to be corrected for emissions from outside the BLR. Park et al. (2012b) find that uncertainties in the size–luminosity relation and in the virial coefficient translate into a factor $\simeq 3$ uncertainty in $M_\bullet$. In addition, as pointed out by Shen (2013), other sources of substantial systematic errors due to e.g. selection effects and sample biases may also be present. The outlined uncertainties result in typical statistical uncertainties $\sim 0.4 - 0.5$ dex associated with the BH mass estimates obtained with the SE method (Vestergaard & Peterson, 2006; Shen, 2013).

In the following section we describe an independent method to estimate the BH mass of an AGN. The method is based on the optical/UV bump found in the SED of AGNs (see Section 1.5) and is fundamental for the present work (see Part III).

1.8.4 The blue-bump method

An independent method of estimating $M_\bullet$ rests upon fitting the optical/UV bump (see Section 1.5) of bright AGNs (e.g. Malkan , 1983; Wandel & Petrosian , 1988; Laor , 1990; Ghisellini et al., 2010; Calderone et al., 2013). In the Shakura & Sunyaev (1973) accretion disk model the BH mass is a simple function of the frequency at which the disk emission peaks, which is a measure of the effective disk temperature and of the accretion rate, estimated by the disk luminosity, given the radiation efficiency and the inclination angle, i, which is the angle between the line-of-sight and the normal to the disk plane (Frank et al., 2002)[4]

However, this method had a limited application to estimate $M_\bullet$ (Ferrarese & Ford, 2005), mainly because reliable estimates of the intrinsic disk luminosity are very difficult to obtain. In fact, a) the inclination is generally unknown and the observed flux density is proportional to $\cos i$, b) the observed UV bump is highly sensitive to obscuration by dust either in the circum-nuclear torus or in the host galaxy, and c) we need to subtract the contribution from the host galaxy that may be substantial, in particular for the weaker active nuclei.

Remarkably, these difficulties are greatly eased in the case of FSRQs[5]

[4]Note that, according to the RLAGN unification scheme, for the sake of simplicity, in this work we implicitly assume that the symmetric axis of the accretion disc, that of the torus, and the jet axis all coincide. Therefore, we make no distinction among the different angles between these axes and the line-of-sight direction, respectively. We denote all these angles as i.

[5]At variance with blazars of BL Lac type that usually do not show evidence of optical/UV blue bump in the SED, such a feature is commonly observed in SEDs of FSRQs (see also Chapter 2)

because a) the accretion disk is expected to be almost perpendicular to the jet direction, and indeed there is strong evidence that the jets of FSRQs detected in gamma rays with the Large Area Telescope (LAT) on board of the Fermi Gamma-ray Space Telescope (denoted in this work as *Fermi*) are highly aligned (within 5 degrees) with the line-of-sight (Ajello et al., 2012) so that $\cos i \simeq 1$; b) the obscuration is expected to be negligible because blazar host galaxies are thought to be passive, dust free, ellipticals (e.g. Giommi et al., 2012b, and references therein) and also the torus is likely perpendicular to the line-of-sight; and c) the contamination is also low because elliptical hosts are typically red, i.e. faint in the UV. However, the UV emission may be contaminated by the emission from the relativistic jet.

On the other hand, the BH mass estimates obtained by fitting the blue bump usually rely on the following assumptions whose validity has not been fully proven (see Ghisellini et al., 2010, for a discussion). A first assumption is that the disk is described by a standard Shakura & Sunyaev (1973) model, i.e., the disk is optically thick and geometrically thin (see Section 1.5). For accretion rates close to the Eddington limit the disc geometry may be modified. In fact the formation of funnel-flows may occur in association with slim or thick discs (see e.g. Abramowicz et al., 1988; Madau, 1988; Szuszkiewicz et al., 1996). In the presence of a funnel, a face-on observer, as in the case of blazars, would observe a bluer bump and a higher flux than in the case of a standard disc. The flux enhancement is due to the anisotropic radiation field associated with the funnel and might ultimately lead to an overestimate of both the disc luminosity and the black hole mass (Ghisellini et al., 2009a).

A second assumption is that the black hole is assumed non-rotating, of Schwarzschild type. The efficiency η for a Kerr black hole and a corotating accretion disc is larger, similarly to the temperatures in the proximity of the innermost stable circular orbit, whose radius is in fact smaller than in the case of a Schwarzschild black hole. The exact derivation of the observed spectrum in the presence of a Kerr black hole is complex and not straightforward (see e.g. Li et al., 2005). However, in order to reproduce the observed SED, assuming a Schwarzschild black hole would ultimately lead to an underestimate of the black hole mass with respect to the case of Kerr black hole and a corotating accretion disc. We refer to Section 10.3.1 for a discussion.

A third assumption is that the SED is described as a combination of black body spectra. Concerning the last assumption, since the blackbody is the best radiator it is bound to give a lower limit to the derived mass and accretion rate.

In general, if any of these assumptions does not hold, the mass estimates would be affected. In Figure 1.5 from Ghisellini et al. (2010) we report the SED showing the optical/UV bump of the FSRQ PKS 2149-306.

We refer to Part III for a further discussion of the blue-bump method described in this section. In Part III we apply the method to a sample

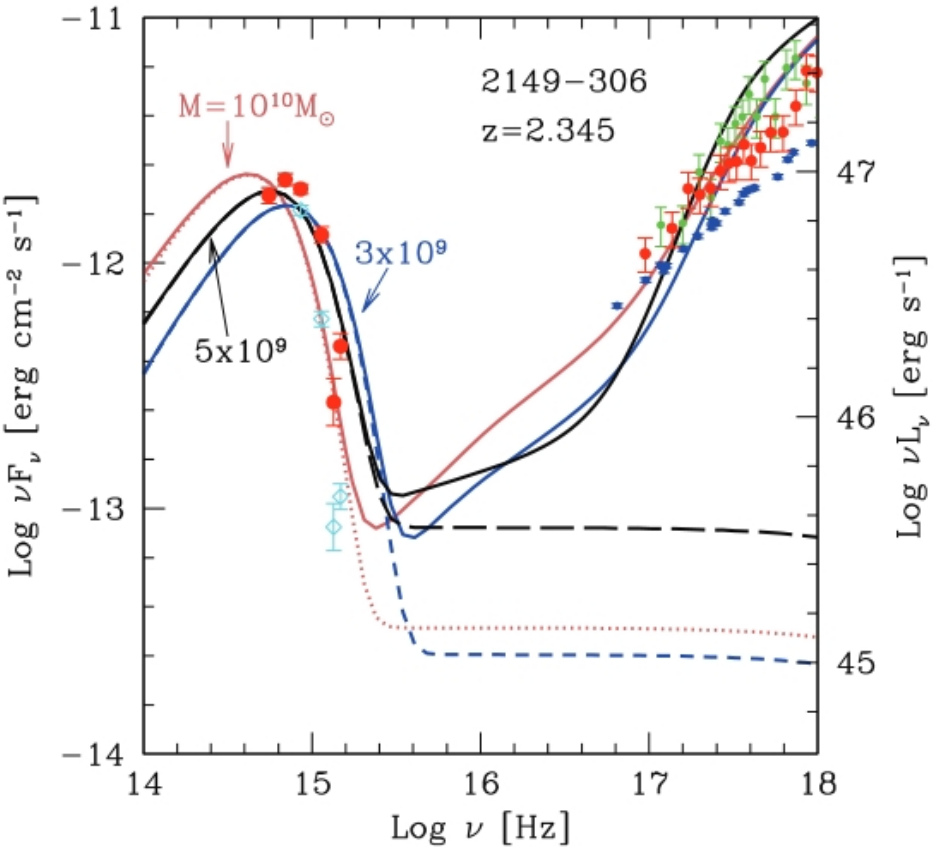

Figure 1.5: SED from Ghisellini et al. (2010) of the FSRQ PKS 2149-306 clearly showing the optical/UV bump. Flux measurements (points) and three theoretical models (lines) are reported. Dotted, short- and long-dashed lines show the contribution of the accretion disc and its X-ray corona, while solid lines show the sum of the thermal and the beamed non-thermal components. The estimated black hole masses corresponding to each model are reported in the Figure.

of blazars and compare the results with those obtained independently with the SE method described above. We point out that a comparison between these two independent methods is important to verify the reliability of both the mass estimates and the underlying assumptions of both methods, to estimate the associated uncertainties.

1.9 Variability

Variability has been detected in AGNs at all frequencies and is a clear signature these sources. We refer to Peterson (2001) for a review. At variance with stars (e.g. eclipsing binaries and Cepheid variables), whose variability is dominated by periodic components easily studied in Fourier analysis, AGNs usually vary with no special timescales. This implies that their Fourier power spectra are broad band. Consequently, the amplitude of variability for AGNs is not trivial to measure.

At first-order approximation, the variability amplitude on most easily measurable timescales is a decreasing function of the wavelength. With only some exceptions (e.g. blazars) lower luminosity objects show higher fractional variability than higher luminosity AGNs.

Early work found optical flux variability in the continuum flux of quasars (Matthews & Sandage, 1963; Smith & Hoffleit, 1963). These early studies suggested significant optical flux variations $\gtrsim 0.1$ mag on a few day timescales. This short time scale variability implies that the size of the continuum emitting region is of the order of light-days (1 light-day $\simeq 10^{-3}$pc), on the basis of source coherence arguments. Such a small, i.e. sub-pc, size of the emitting region is challenging for theoretical models explaining emission mechanisms in AGNs. The variability-size argument can be understood in view of coherence and causality. In fact, for a source whose flux varies coherently, the emitting region must be causally connected. This naturally implies an upper limit to the source size that is set by the light travel time. An alternative might be that flux variations are stochastic and originated by different causally disconnected regions within the variable source. In this case the variability would be smeared on longer time scales and likely ultimately suppressed.

Flux variations with amplitude $\sim 10\% - 20\%$ on longer, i.e. month-to-year, time scales are often observed in the UV light curves of AGNs. Fractional optical variations are often less pronounced because of the starlight contamination from the host galaxies. However, there are some exceptions represented for example by blazars that often exhibit short time scale and high-amplitude variability in the entire optical/UV range and up to Gamma-rays (we refer to Section 2.7 for a separate discussion on blazar variability).

Rapid X-ray variability is an hallmark of AGNs (see e.g. Gaskell & Klimek, 2003, for a review). Variations of a factor of ~ 2 in about 20 minutes

were found for example for the Seyfert galaxy IRAS 13224-3809 (Boller et al., 1997). Other work found variability in soft X-rays up to year time scales e.g. on the basis of power spectrum analysis (see e.g., McHardy, 2010, for a review). Long term, month-to-year time scale, variability has been recently observed in several AGNs of different types in the hard X-rays (Soldi et al., 2014).

1.10 Polarization

Although most stars are typically unpolarized, the light we receive from them is generally linearly polarized by $\sim 0.5\%$ due to interstellar dust transmission polarization. The same is true for many galaxies. Most AGNs are usually weakly linearly polarized by $\simeq 0.5-2\%$ or also up to $\sim 10\%$ in some cases. However, the degree of polarization of AGNs is enough to make their polarization distribution statistically distinguishable from that of stars.

In the following Chapters 2 and 3 we review the properties of blazars and radio galaxies, respectively. As outlined above such sources are key for the present work and constitute two subclasses among the RLAGNs.

Chapter 2

Blazars

2.1 General properties of Blazars

Blazars are the most extreme class of AGNs. The term blazar was coined by Edward Spiegel in 1978 at the Pittsburgh Meeting and was originally introduced to denote objects that exhibit strong and high-frequency radio emission from a compact core as well powerful high energy emission.

Blazars are characterized by strong emission and variability at both X- and gamma-rays extending up to the GeV energy band and in some cases up to TeV energies. Blazars are among the cosmological sources that are detected at energies higher than a few MeV.[1] Blazars generally show smooth spectra (featureless or with low EW emission lines[2]), rapid and large-amplitude variability observed in all accessible spectral regimes (from radio to gamma rays, Fan & Lin, 2000; Ulrich et al., 1997; Webb & Malkan, 2000), strong and variable polarization, especially in optical, and highly relativistic jets with apparent superluminal motion. We refer to Urry & Padovani (1995) for a review of these sources.

The above features defining the blazar class are widely explained in terms of the view originally proposed by Blandford & Rees (1978) and Begelman et al. (1984). This holds the radiation from all these sources to be produced in a collimated, relativistic jet of particles with bulk Lorentz factor $\Gamma \sim 1 - 40$ (e.g. Savolainen et al., 2010). When observed at small angles of the order of Γ^{-1}, the jet produces the *blazing* effects typical of blazar sources. The intrinsic luminosity emitted by the jet over the entire solid angle and the

[1] In addition to blazars other sources are detected at energies higher than a few MeV at cosmological distances. Among them there are Gamma Ray Bursts as well as some nearby starburst galaxies such as NGC 253 (Acero et al., 2009) at a distance of $\sim 2.5 - 3.9$ Mpc (e.g., Rekola et al., 2005), radio galaxies (Aleksić et al., 2014), and Narrow Line Seyfert 1s (Abdo et al., 2009a,b; D'ammando et al., 2013, 2014).

[2] Blazars have emission lines with EW up to a few tens of Å(Véron-Cetty & Véron, 2000). Conversely, Type 1 AGNs typically have emission lines whose EW can easily exceed this value (see Sections 1.3 and 1.4).

total jet kinetic power are reviewed in e.g., Ghisellini (1999).

We stress that, because of both strong variability and the broad-band spectra of blazars, single sources are commonly studied by means of possibly multi-epoch, multiwavelength, and/or simultaneous observations (e.g. Acciari et al., 2009b; Donnarumma et al., 2009; Vercellone et al., 2010). However, requiring both multiwavelength and simultaneous observations for a large sample of sources is demanding in terms of telescope time. Therefore, statistical studies, where simultaneous observations are not always available, are a valuable alternative strategy to study blazars (Abdo et al., 2010a).

2.2 The blazar subclasses

Within the blazar class, two main subclasses are usually identified, namely, BL Lac objects and flat-spectrum radio quasars (FSRQs). The former differs from the latter subclass on several accounts. They lack emission lines with $EW \gtrsim 5$Å and lack the big blue bump in the SED (see also Sections 1.5 and 1.8.4); they have total luminosities $\lesssim 10^{46}$ erg s^{-1}, compared with FSRQs often exceeding this limit and in some cases approaching 10^{48} erg s^{-1}; they have SED peaking at frequencies from optical to X-ray and at energies of $\sim$ 10 GeV, compared with the FSRQs peaking at far-IR to optical frequencies and around 10^{-1} GeV (see Panel a of Figure 1.1 for the SED of a FSRQ); they exhibit no signs of (strong) cosmological evolution, compared with the strong evolution clearly displayed by the FSRQs in common with other quasars (Fichtel et al., 1994; Chiang et al., 1995; Ajello et al., 2014).

2.3 The environments of blazars

Blazars are commonly hosted in bright and large elliptical galaxies (Scarpa et al., 2000; Nilsson et al., 2007; Giommi et al., 2012b). Mpc-scales studies of blazars (especially BL Lacs, e.g., Falomo, 1996) suggested that they are hosted in clusters consistently with what has been found for low power radio galaxies (Hill & Lilly, 1991). However, the properties of the Mpc-scale environment of blazars are far from being well established and are still debated in the literature (e.g., Wurtz et al., 1993, 1997; Willett et al., 2012). Possible discrepancies concerning the cluster environments of blazars with respect to those of radio galaxies might set severe indirect constraints on the RLAGN unification scheme.

2.4 The Internal Shock Scenario

One of the most currently accepted basic models for the emission mechanisms in RLAGNs assumes a relativistic jet that contains electrons, protons,

and a tangled magnetic field. Different substructures (i.e., shells, inhomogeneities) may travel with different velocities. When some of the shells collide may generate relativistic shock waves. The shock, e.g. through first-order Fermi acceleration processes, may significantly increase the energy of the electrons. In other words, a fraction of the bulk kinetic energy of the colliding shells is used to accelerate electrons up to highly relativistic energies. The relativistic electrons escape from the shock front into the downstream region of the shock, where they lose their energy through the synchrotron and the IC processes. These are the main assumptions of the so called internal shock scenario, proposed for the first time by Rees (1978) and successfully applied for the Gamma Ray Bursts (Meszaros, 2006) and blazars (e.g. Begelman et al., 1994; Sikora et al., 1994).

The main uncertainties of this model are the magnetic field strength in the fluid frame, the comoving size scale of the emitting region (the shell) and the jet Doppler factor δ (see Equation 1.6). The success of the internal shock scenario is mainly due to the fact that it can provide the energetic required to produce the observed energy output in powerful RLAGNs and at the same time allows the jet to propagate to large scales.

Let us consider two shells escaping from the AGN and moving with different Lorentz factors $\Gamma_2 \gtrsim \Gamma_1 \gg 1$ along the jet direction towards the observer. We also assume that the shell with Lorentz factor Γ_2 is following the other one, so that they can collide along the jet and constitute a single moving shell whose front is the surface of discontinuity of the shock wave. Momentum conservation (Lazzati et al., 1999; Moderski et al., 2004) allows to estimate the fraction $\eta_{\rm diss}$ of the bulk energy that is released when two identical shells inelastically collide:

$$\eta_{\rm diss} \simeq \frac{\left(\sqrt{\Gamma_2/\Gamma_1} - 1\right)^2}{\Gamma_2/\Gamma_1 + 1} \ . \tag{2.1}$$

Assuming Lorentz factors Γ_1, $\Gamma_2 \sim 1 - 40$ typical of blazars, this simple argument shows that the efficiency $\eta_{\rm diss}$ of the radiation production process results to be a few percent, and always $< 10\%$. The latter roughly corresponds to the highest radiation production efficiency occurring in astrophysical context and due to accretion onto black holes. Therefore, the internal shock scenario predicts one of the highest radiation production efficiency, i.e. greater than nuclear burning efficiency,[3] but smaller than accretion disk one.

[3]The hydrogen burning in the stellar interiors has a typical efficiency ~ 0.007, corresponding the energy radiated per unit mass energy.

2.5 Emission mechanisms and SED modeling

It is commonly accepted that the non-thermal energy output observed in the SEDs of blazars as the low- and high-frequency bumps (see Figure 1.1) is ultimately due to due to synchrotron emission occurring in the jet and IC radiation, respectively. We refer to Rybicki & Lightman (1979) for a review of radiative phenomena. In the following we briefly outline the present theoretical framework concerning emission processes in the jets of blazars.

Blazar SEDs are commonly modeled with synchrotron and IC radiation emitted from a uniform region, associated with the low-frequency and high-frequency bumps in the SED. Both components must be observationally constrained in order to derive the physical parameters of the emitting region.

The synchrotron radiation emitted at low-frequency (from radio to the UV or to the X-rays) is generally thought to be originated by relativistic electrons. The origin of the high energy emission (from X- to gamma-rays) is less clear and two main different approaches have been proposed in the literature, usually referred to as leptonic and hadronic models. So far we have implicitly assumed the first, more frequently adopted, scenario. We refer to Section 2.10 for a discussion of the hadronic models.

In leptonic models (e.g. Maraschi et al., 1992; Dermer & Schlickeiser, 1993; Bloom & Marscher, 1996), the observed radiation is due to relativistic leptons (electrons and possibly positrons), while the protons, that are more massive and likely present in the jets, are not accelerated to sufficiently high energies to be significantly responsible for the energy output.

Further distinctions occur among blazars of different types in the context of leptonic models. In the case of FSRQs the X-ray emission derives from the IC mechanism (with seed photons external to the jet) and, in some cases, an additional contribution from the synchrotron self-Compton (SSC) scattered photons. In the case of BL Lacs, whose SEDs peak at higher frequencies than FSRQs, the X-ray data constrain the position of the synchrotron peak, whereas information on the IC peak, most frequently explained as SSC radiation, is provided by observations in the gamma-ray (GeV range) or TeV domain. In fact the high-energy, i.e. from X- to gamma-rays, component is observed up to ~ 10 GeV for FSRQs, and up to several TeV for some BL Lacs.

According to this theoretical scenario, semi-analytic models are usually adopted to reproduce the entire SED of blazars. Generally it is assumed that the radiation is produced in a homogeneous emitting region (this condition defines the so called one-zone models) and by a single electron population. These assumptions are supported by lines of observational evidence, at least for the spectral range from the gamma-ray band down to the optical-IR band. In particular, the observations of correlated and short time scale variability at different frequencies suggest cospatial production of low- and high-energy photons via the two above mentioned mechanisms, i.e. synchrotron

and IC, within a relatively tiny region in the jet (e.g., Ulrich et al., 1997; Urry, 1999; Giommi et al., 1999b).

2.6 The blazar main sequence

Many blazar properties can be arranged into a blazar main sequence (BMS) in terms of levels of one single parameter given by the accretion rate $\dot{M}$ expressed in units of the Eddington luminosity $L_{\rm Edd}$, i.e. $\dot{m} = \dot{M}c^2/L_{\rm Edd} \propto \eta^{-1}$. Levels $\dot{m} \sim 1 - 10$ mark the FSRQs, whereas values $\dot{m} \lesssim 10^{-2}$ mark the BL Lac objects (Cavaliere & D'Elia, 2002).

Several studies suggested that disks with high values of $\dot{m}$ are required to produce outputs as strong as those observed in FSRQs (Cavaliere & D'Elia, 2002; Ghisellini et al., 2009c; Ghisellini, 2010). In BL Lac objects, on the other hand, low values of $\dot{m}$ sustain intermediate or low disk luminosities comparable to those directly extractable from a Kerr hole. This yields a limiting disc power of about 10^{46} erg s^{-1}. It is a consequence of the present discussion that BL Lac outputs should not considerably exceed such values, as in fact observed. Furthermore, at variance with FSRQs there is observational evidence that SEDs of BL Lac do not show the big blue bump, that is commonly interpreted as a signature of the accretion disc.

According to this framework, Cavaliere & D'Elia (2002) suggested that BL Lac sources have lower particle densities in the acceleration region and less effectively screened electric fields than in FSRQs. These conditions along with lower photon energies imply electron energies up to a few 10^3 GeV in BL Lac source, higher than in FSRQs. This results in the synchrotron emission peaking at higher frequencies $\nu_{\rm peak}$ for BL Lac.

The apparent inverse scaling of $\nu_{\rm peak}$ with the total radiative output in moving from FSRQs to BL Lac objects has been pointed out in Fossati et al. (1998), and interpreted as a cooling sequence due to the radiative energy losses being faster in the more powerful sources that are also associated with lower maximal electron energies.

We mention that the BMS has been widely debated in the literature (e.g., Giommi et al., 1999a; Padovani et al., 2003; Nieppola et al., 2008; Giommi et al., 2012a). It was suggested that the BMS is mainly due to selection effects arising from the comparison between shallow radio and X-ray surveys and to the fact that high-$\nu_{\rm peak}$ and high-radio-power blazars are hard to study because their redshift is difficult to measure (Giommi et al., 2012a).

Nieppola et al. (2008) interpreted the BMS as an observational artifact resulting from different Doppler factors associated with FSRQs and BL Lac sources. The authors argue that the BMS correlation disappears when the luminosity is corrected for Doppler boosting.

In this work we adopt the more recent version of the BMS model used in Donato et al. (2001) to model SEDs of blazars (see Part III). The BMS model

is chosen because it well reproduces phenomenologically the observed SEDs, also at low and intermediate radio frequencies, where the emission is self-absorbed and the above mentioned one-zone models tend to underestimate the luminosity output.

2.7 Variability of blazars

Blazars show extreme variability at all wavelengths, from radio to gamma-rays. With respect to AGNs of different type they display both larger amplitude and shorter time-scale variability (e.g. Cellone et al., 2007). High continuum variability is often found in association with high degrees, i.e. typically $\gtrsim 3\%$, of polarization of the continuum light. At variance with non-blazar sources, the degree of polarization and the amplitude of variability commonly correlate with the luminosity. Furthermore, unlike other types of AGNs such as radio-quiet quasars and Seyfert galaxies, blazars show strong radio and infrared variability.

Studies of variability in different energy bands and correlations of multi-waveband variability patterns gave some constraints on the physical processes in blazars, such as particle acceleration and emission mechanisms, relativistic beaming, origin of flares and size, and structure and location of the emitting regions. The variability amplitude of blazars seems to be higher as the wavelength becomes shorter and the timescales of the fluctuations usually decrease with the wavelength. Nevertheless, there are some exceptions to this simplified picture, as for example the optical band, where significant variability is often observed in blazars (see below).

Care has to be taken in the modeling about variability especially in those studies of blazars where simultaneous multiwavelength observations are not always available (as in this work, see Part III). Since one of the main goal of our work on blazars is to characterize the optical/UV spectrum of FSRQs in the following we will mainly focus on optical variability of blazars.

In radio/optical wavelengths they may show microvariability (i.e. intra-night variability with time-scales from several minutes to a few hours), as well as intra- and inter-day variability (i.e., with time-scales from hours to several days, e.g., Romero et al., 1999). Among blazars with proven intra-night variability, several objects undergo large intra-night fluctuations of several tenths of a magnitude in a few hours.

Microvariability has been observed in several sources such as the BL Lac S5 0716+71, in which both radio and optical variability have been detected (Quirrenbach et al., 1991). It is widely accepted that the intra-day variability observed in blazars at low frequencies $\lesssim 10$ GHz is predominantly a result of scintillation of the turbulent inter-stellar medium (ISM) of our Galaxy. See e.g. Pursimo et al. (2013) for a recent work. Such a scenario is less established in optical, where for example changes of $\sim$0.5 magnitudes within

one night and ∼1.2 magnitudes between consecutive nights were found for the blazar AO 0235+64 (Romero et al., 2000). Some authors claimed the detection of extremely violent optical microvariability in several blazars, with amplitudes sometimes greater than 1 mag in a few tenths of minutes (e.g., Dai et al., 2001; Xie et al., 2001, 2004). In contradiction to these results no such extreme variations for the same objects were found in other work by Romero et al. (2002); Cellone et al. (2007), showing that the discrepancies might have their origin in an unsuitable choice of the comparison and control stars used for differential photometry.

Furthermore, the study of variability is particularly important also in gamma-ray astronomy, where fluctuations of a factor of ~ 100 have been observed over year timescales (e.g., Marscher et al., 2010) and spectacular high-amplitude and short-time scale flux variations by factor of $\gtrsim 2$ may be observed down to hour- and minute-timescales at GeV (e.g., Mattox et al., 1997; Wehrle, 1998; Foschini et al., 2010, 2013) and TeV energies (e.g., Albert et al., 2007), respectively.

Even accounting for relativistic beaming, such short, intra-day, timescales are challenging for standard emitting models and could be mainly due to the particular geometrical configuration of the emitting regions instead of the compact nature of the emission region (e.g. Ghisellini et al., 2009b, see also Section 2.11). In the following section we briefly introduce some other issues concerning the emission mechanisms outlined so far and overview some alternative emission scenarios concerning energy production in the jets of blazars.

2.8 The compactness problem and Compton drag

As outlined in the previous section short time scale variability observed in blazars sets severe constraints on the size of the emitting region, even accounting for relativistic aberration. Furthermore, in one-zone emission models the radiation densities required to explain the observed energy output at both low- and high-energies are sufficiently high that the MeV-GeV gamma-rays should not escape the emission region without producing electron-positron pairs via interaction with lower-energy photons. Therefore, no high-energy emission should be observed in gamma-rays in the SEDs of blazars. This argument is known as compactness problem and shows that alternative emission mechanisms might be required.

A somehow related issue is that intense radiation fields in the proximity of the central regions should exert a significant Compton drag on electrons and positrons, thus setting severe constraints on the formation and acceleration of relativistic jets.

Both the compactness problem and the Compton-drag argument suggest that the jets could not be both relativistic and pair dominated in the

proximity of the central core. A possible alternative to avoid these radiation problems is to assume that the jet energy in the early stages of its formation and acceleration is carried by other media that overcome the limitations coming from the strong interaction between photons and leptons in the jets.

Possible solutions invoke the presence of relativistic protons (see e.g. Sikora, 2001, for a discussion) and Poynting flux dominated outflows.

2.9 Poynting flux dominated jets

Dynamical arguments suggest that magnetic fields $B \gtrsim 10^3$ G corresponding to a magnetic energy density in equipartition with the radiation energy density seem to be required in order to sustain the bulk kinetic power of the jet. Some work suggested that the jet in its early stages of formation might be powered and gradually accelerated by Poynting flux, until the equipartition is reached (Li et al., 1982; Begelman & Li, 1994). Nevertheless, the existence of such Poynting flux dominated jets is matter of debate and the mechanisms occurring in jet production and acceleration are far from being well understood.

2.10 Hadronic models

As mentioned above, hadronic models represent a possible alternative to the widely used leptonic models. In hadronic models both electrons and protons are accelerated to relativistic energies. Furthermore, the proton energies exceed the threshold for photo-pion production on the soft-energy photon field.

Analogously to leptonic models, hadronic models explain the non-thermal blazar low-frequency emission (from radio to UV or possibly to X-rays) mainly as synchrotron emission emitted by the electrons.

Differently from leptonic models, the emission at higher frequencies is dominated by high-energy mechanisms such as proton synchrotron emission, π^0 decay photons, and synchrotron and Compton radiation from secondary decay products of charged pions (Mannheim & Biermann, 1992; Aharonian, 2000; Mücke & Protheroe, 2001; Mücke et al., 2003). We refer to Böttcher (2010) for a review of both leptonic and hadronic blazar models.

2.11 A jet model

As mentioned in Section 2.7 the strong variability observed in blazars may be explained in view of specific geometrical configurations of the jet. In this framework a jet model has been proposed by Marscher et al. (2008) to explain the repeated multiwavelength radio-to-gamma-ray flares and the

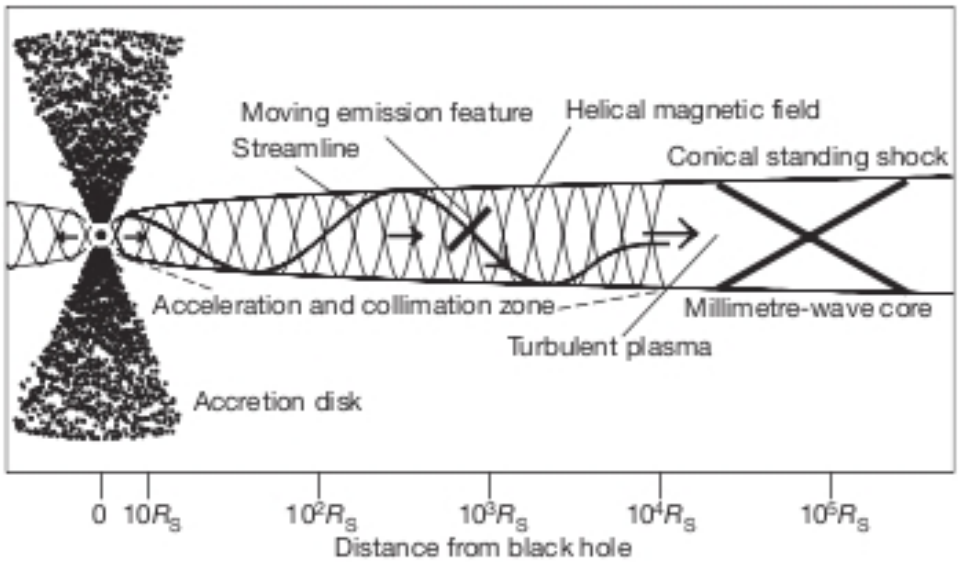

Figure 2.1: Schematic view of the jet model proposed by Marscher et al. (2008). The different components are reported in the labels. The logarithmic distance from the black hole is shown in terms of the Schwarzschild radius [$R_S \simeq 10^{-5}$ pc $\times$ $(M_\bullet/(10^8 M_\odot)$] and is used to illustrate the jet structure at different scales.

rotation of the optical polarization vector with a period of a few days observed in BL Lac (Marscher et al., 2008) and in the FSRQ PKS 1510-089 (Marscher et al., 2010).

The authors proposed that the repeated optical to gamma-ray flares observed in the blazars can have started in a region with a helical magnetic field, which could be identified with the region where the jet is initially accelerated and collimated. The helical structure may be responsible for the rotation of the polarization vector and may partially explain the observed variability.

Furthermore, on the basis of radio interferometric observations the authors suggested the presence of a feature propagating along the jet and that brightened when it crossed a bright core seen in the radio images. By means of multiwavelength cross-correlated variability arguments the authors interpreted such a core as a stationary shock wave responsible for additional radio to gamma-ray flares of the source. In Figure 2.1 we schematically show the jet structure proposed by Marscher et al. (2008).

Chapter 3

Radio Galaxies

In this Chapter we review the properties of the radio galaxies. We refer to Chiaberge (2000), De Young (2001), Miley & De Breuck (2008), and Krawczynski & Treister (2013) for a thorough discussion of the subject.

3.1 General properties of radio galaxies

M87 and NGC 5128 were the first two elliptical galaxies associated with extragalactic radio sources, i.e. Virgo A and Centaurus A, respectively (Bolton et al., 1949). This proved the extragalactic nature of the radio galaxies. At variance with normal galaxies that have radio luminosities $\sim 10^{37}$ erg s^{-1} radio galaxies have luminosities in the range $\sim 10^{41-45}$ erg s^{-1} in the radio band.

Radio galaxies have flat spectrum ($F_\nu \propto \nu_o^{-\alpha}$, $\alpha \sim 0$)[1] radio cores typically unresolved with VLBI observations, thus implying a core size of $\lesssim 0.1$ pc. Radio galaxies have one- or two-sided steep spectrum ($\alpha \sim 0.6-1$) jets that are clearly visible at low-radio frequencies and are extended from the core up to several-kpc or ~ 1 Mpc for the most powerful sources. The jets may have either smooth or knotty morphology. They are either straight and well collimated or less collimated and possibly curved.

3.1.1 The Fanaroff-Riley classification

The original classification of the radio galaxies is based on their radio morphology and it is due to Fanaroff & Riley (1974). The authors defined Type I (Type II) sources those radio galaxies for which the ratio of the distance between the regions with the highest surface brightness on the opposite sides of the central galaxy to the overall source size up to the lowest brightness

[1] F_ν is the observed flux per unit frequency and time at the observed frequency ν_o. Its cgs unit is 1 erg cm^{-2} s^{-1} Hz^{-1}]. In radio astronomy a widely used flux unit is the Jansky (Jy), where 1 Jy = 10^{-23} erg cm^{-2} s^{-1} Hz^{-1}.

contour in the radio map is less (higher) than 0.5. According to this original classification the surface brightness of Fanaroff-Riley Type I radio galaxies (FR Is) tend to peak inward from the outermost regions of the source.

In detail, FR Is are bright in the proximity of the core and commonly show a slowly decreasing surface brightness at increasing distance from the core. Furthermore, FR Is show ejecta that can be called jets and are commonly seen at kpc-scales from the nucleus. At these distances the jets decelerate to sub-relativistic or mildly relativistic velocities $v \sim 0.6 - 0.7c$ (Bicknell et al., 1990; Bicknell, 1994). Furthermore, the jets usually exhibit a symmetric structure, are not well collimated, and inflate radio emitting regions called lobes that are extended up to a few hundreds of kpc.

On the other hand, Fanaroff-Riley Type II radio galaxies (FR IIs) are edge-brightened, i.e. they are very bright at their extremities, whereas they are fainter in the proximity of the core. FR IIs show well collimated, relativistic, usually non-smooth, narrow, and one-sided jets terminating in bright point-like components denoted as hot spots and located at distances up to ~ 1 Mpc. The hot spots are commonly explained as emission coming from shock fronts associated with the jet that interacts with the surrounding inter-galactic medium (IGM) or the intra-cluster medium (ICM).

The one-sidedness of the jets of FR IIs can be explained as a consequence of the relativistic aberration. The emitting particles in the jet are moving with relativistic bulk velocities. Therefore, the radiation is preferentially beamed in the direction of motion.

In Figure 3.1 we show examples of FR I (left) and FR II (right) radio galaxy morphology. We note that in the framework of unified models for RLAGNs, BL Lacs and FSRQs are interpreted as relativistically beamed FR I and FR II sources, respectively.

Despite this unified scenario, we stress that the radio morphology of FR Is is less defined and much more complex than that of FR IIs. Elaborated FR I classification schemes have also been proposed (e.g., Laing, 1993). In general, the simplified picture outlined above is not fully exhaustive. In fact, FR Is may show e.g. twin jets, narrow angle tails, or wide angle tails (see Section 3.8.2 for more discussion about tailed radio galaxies). Sources showing transitional properties in common of both FR Is and FR IIs are also observed (see Section 3.9 for some examples). In Figure 3.2 we show some useful examples of FR I radio galaxies.

One feature that seems to be ubiquitous among FR I radio galaxies is that their extended radio structure and lobes are often convoluted and plume-like. As mentioned above, in many cases the surface brightness slowly decreases going outwards from the nucleus and it has its maximum closer to the nucleus than in the case of FR IIs. The latter criterion is one of the key defining features of FR Is.

The slow declining of the surface brightness and the plume-like structure of FR Is suggest that these sources are dynamically different from FR IIs. An

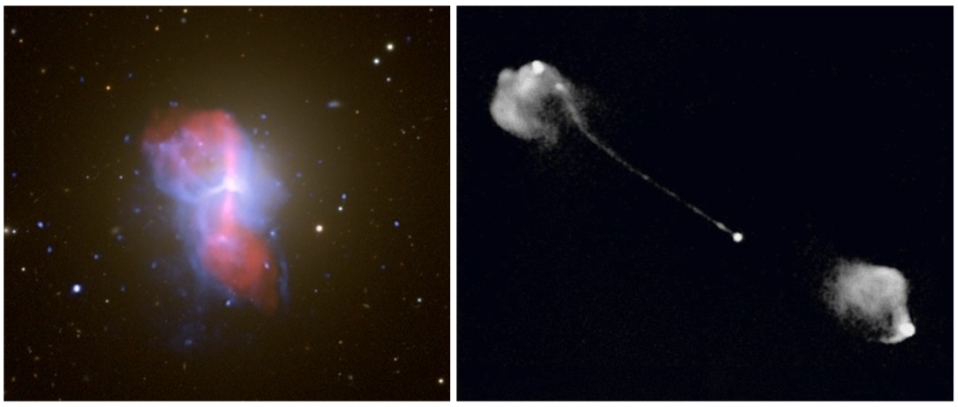

Figure 3.1: Examples of radio galaxies. Left: Multi-frequency image of the FR I radio galaxy M84. The Very Large Array (VLA) 4.9 GHz image of the radio galaxy (red, Laing & Bridle, 1987), the Chandra 0.5-2 keV image of hot galaxy gas (blue, Finoguenov et al., 2008), and an SDSS optical image (yellow and white). The radio galaxy has a projected diameter of 12 kpc. Right: The VLA 4.9 GHz image of the FR II radio galaxy 3C 175 ($z = 0.768$) showing a well-collimated jet and two hot spots separated by a projected distance of 370 kpc. Credits for the left panel: X-ray [NASA/CXC/MPE/Finoguenov et al. (2008)]; Radio [NSF/NRAO/VLA/ESO/Laing & Bridle (1987)]; Optical (SDSS). Credits for the right image: NRAO/AUI.

important problem is whether the observed morphological differences among FR Is and FR IIs are due to intrinsic conditions in the active nucleus or to the interaction of the radio galaxy with its environment. Much work has been done to understand this issue. We refer to Section 3.8 for discussion.

In Figure 3.3 we show radio and optical images of the FR I radio galaxy M87 at different resolutions. The knotty jet transferring energy into the ICM through the radio lobes at kpc-scales as well as the jet structure at few tens Schwarzschild radii from the central unresolved radio-core are shown.

Importantly, along with the purely morphological classification distinguishing FR I and FR II radio galaxies, Fanaroff & Riley (1974) found that they are also associated with 178 MHz rest frame radio powers lower and higher, respectively, than a formal FR I/FR II radio luminosity divide set at $\sim 2 \times 10^{33}$ erg s^{-1} Hz^{-1}. In Figure 3.4 we plot the radio power distributions for FR Is (top panel) and FR IIs (bottom panel) from Zirbel (1996) showing the clear bimodality in the radio power distribution of radio galaxies. Other work suggested that the FR I/FR II radio power divide, at low redshifts, depends on the host galaxy luminosity (Owen & Ledlow, 1994; Ledlow & Owen, 1996, see also Section 3.2). However, it is still unclear whether it is simply a result of selection effects (Scarpa & Urry, 2001).

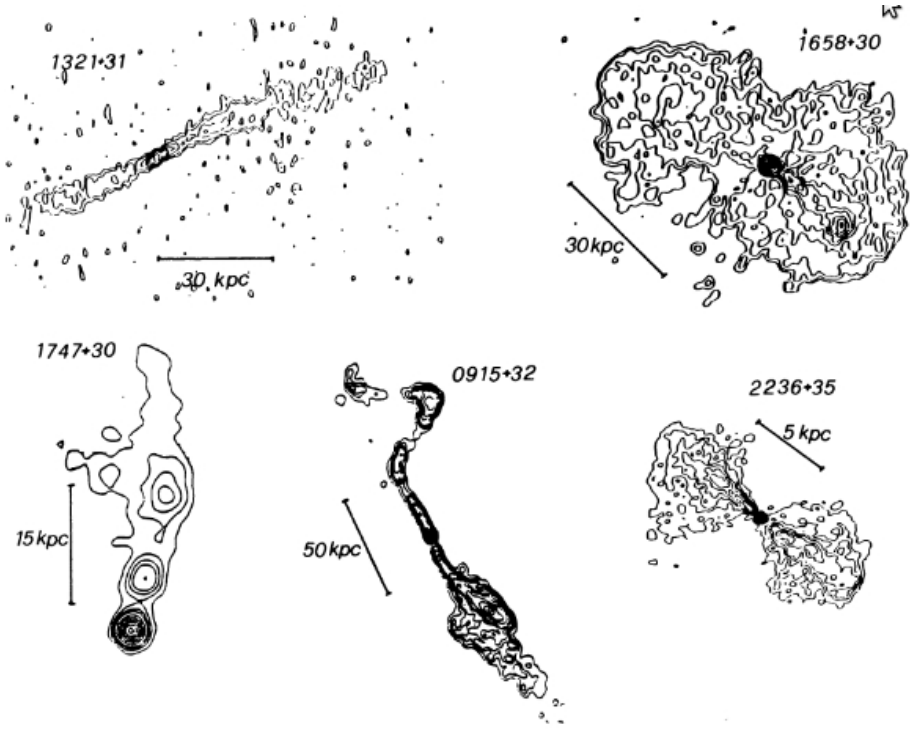

Figure 3.2: VLA radio maps at 1.4 GHz showing examples of FR I radio galaxies. Credits: Parma et al. (1987)

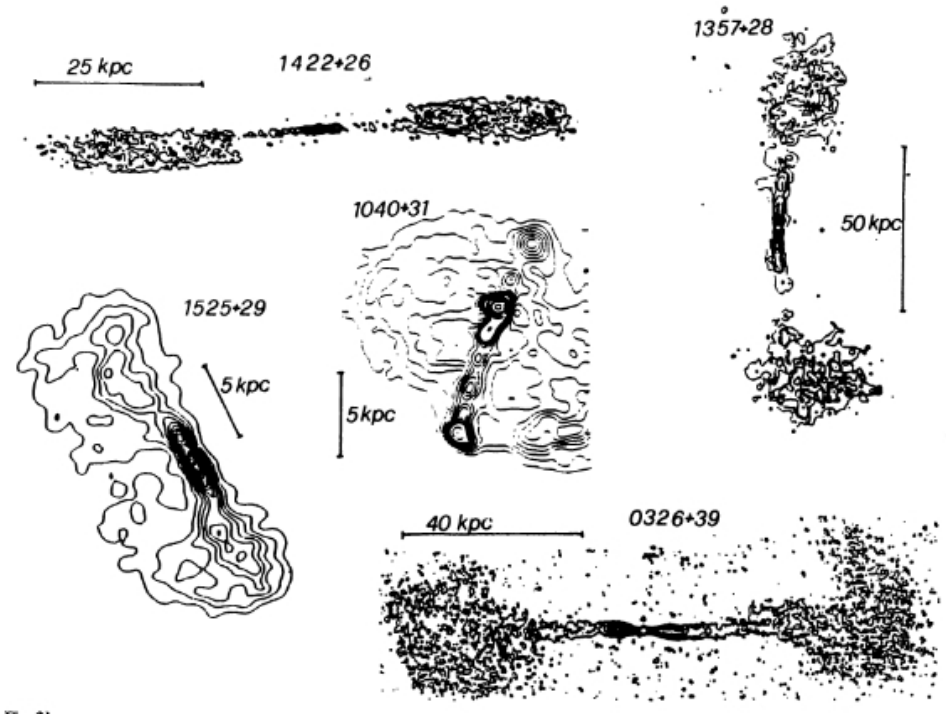

Figure 3.2: Continued.

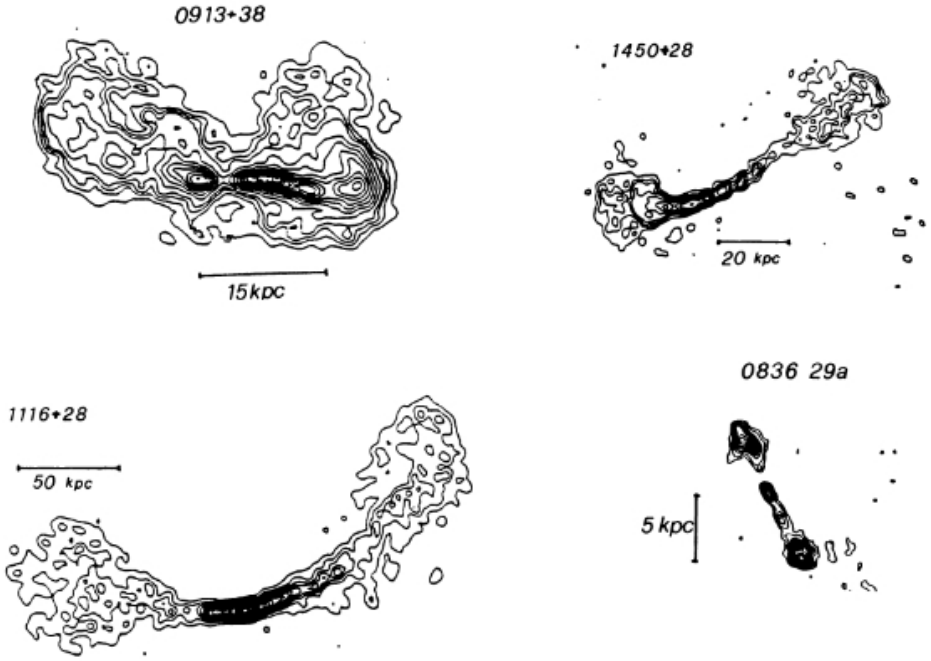

Figure 3.2: Continued.

3.2 Host galaxies

Radio galaxies are almost invariably associated with luminous ellipticals (Zirbel & Baum, 1998; Donzelli et al., 2007). However, Zirbel (1996) found that the host galaxies of FR Is and FR IIs at $z < 0.5$ are different in terms of magnitudes, colors, color gradients, and galaxy structure. In fact, the host galaxies of FR Is are typically giant ellipticals of cD type characterized with diffuse emission. Double nuclei are also often associated with the host galaxies of FR Is. On the other hand, FR IIs are typically hosted in disturbed galaxies that are not of cD type and are dimmer than the hosts of FR Is (Heckman et al., 1994).

Another difference in the host galaxies of FR Is and FR IIs has been suggested in the literature by Owen and collaborators (Owen & Laing, 1989; Owen & White, 1991; Owen, 1993; Owen & Ledlow, 1994; Ledlow & Owen, 1996). They found that FR I and FR II radio galaxies occupy two separate regions in a plot showing the rest frame 1.4 GHz luminosity, $L_{1.4\ \mathrm{GHz}}$, versus the R-band absolute magnitude. The transition between FR Is and FR IIs is set by the line $L_{1.4\ \mathrm{GHz}} \propto L_{\mathrm{opt}}^{1.8}$, where L_{opt} is the R-band optical luminosity.

In Figure 3.5 we report a plot from Ledlow & Owen (1996) showing such a result. The separation between FR Is and FR IIs shown in the plot must be taken with caution. In fact the plot includes both local radio galax-

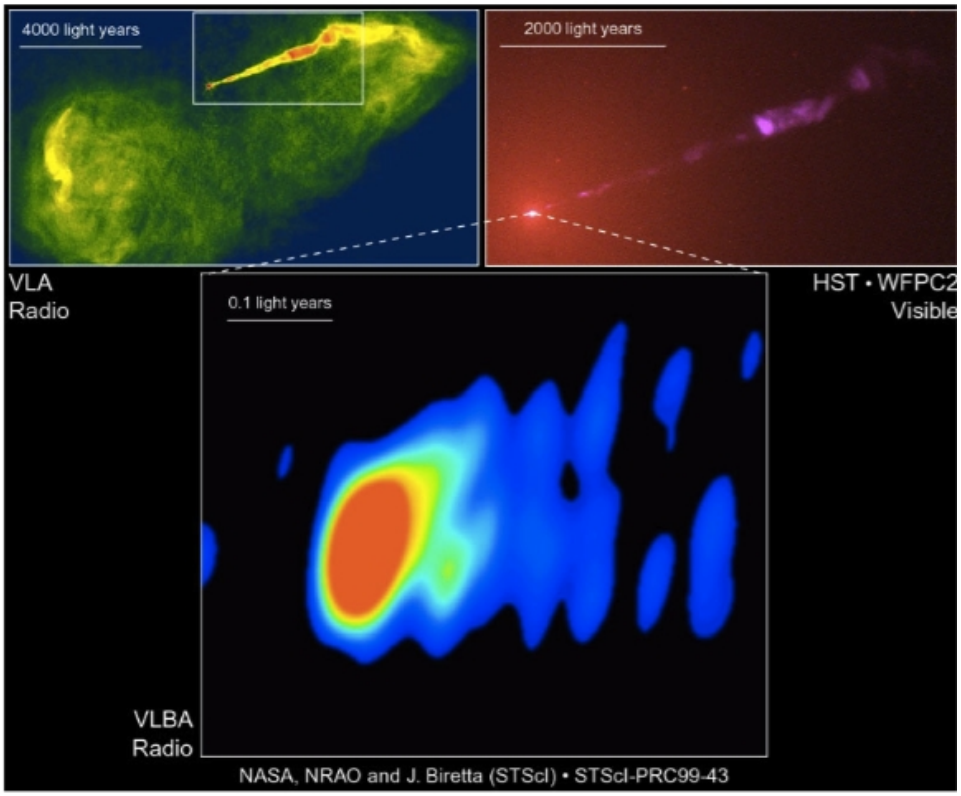

Figure 3.3: Images at different scales of the FR I radio galaxy M87 at the center of the Virgo galaxy cluster. Top left: VLA image shows the broadening kpc-scale jet and the associated lobes. Top right: HST optical image shows the kpc-scale jet structure. Bottom center: VLBI image shows the jet at sub-pc scales in the proximity of the AGN core. Credits: National Radio Astronomy Observatory/National Science Foundation,NASA and John Biretta (STScI/JHU), National Radio Astronomy Observatory/Associated Universities, Inc.

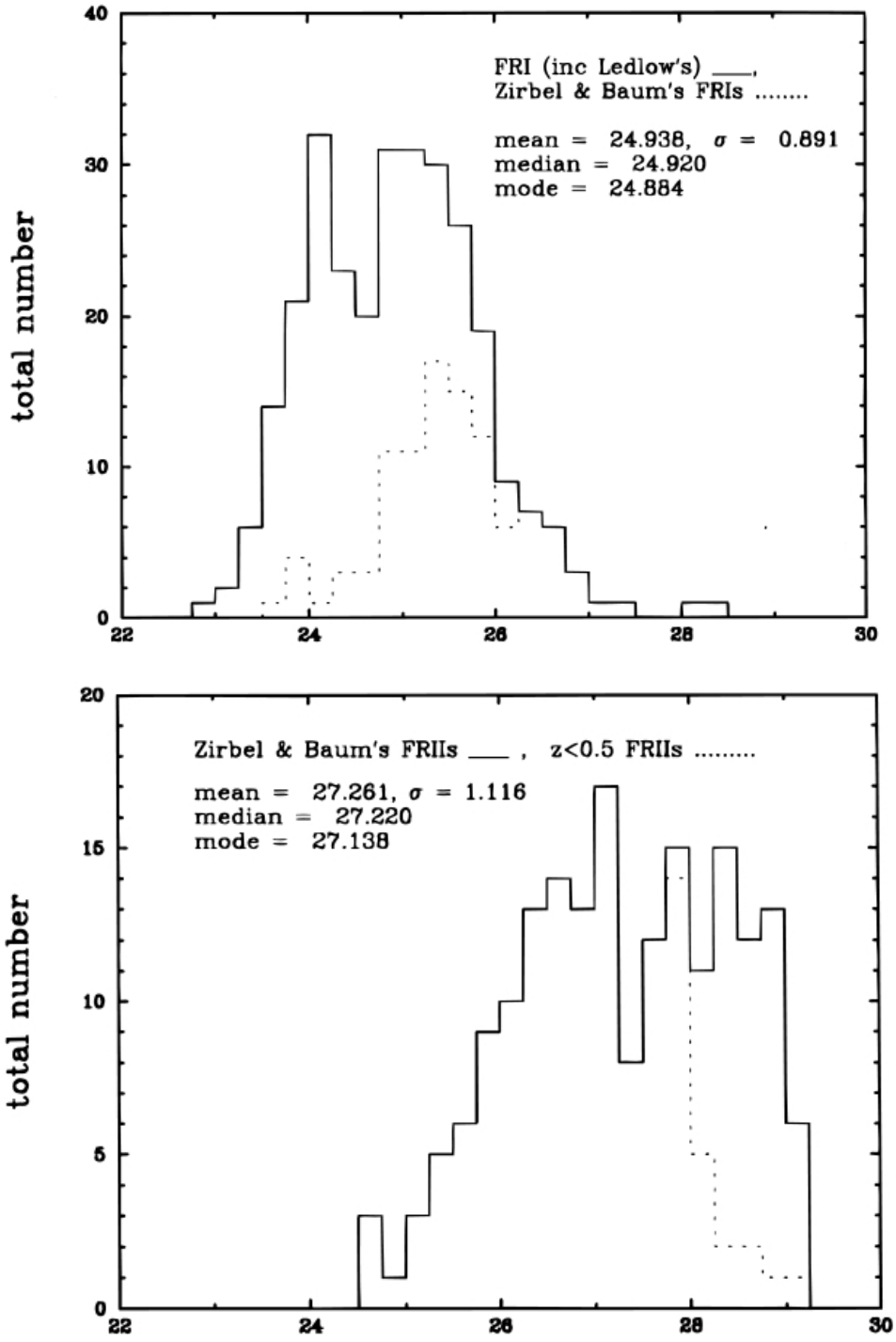

Figure 3.4: Radio power distribution at 408 MHz from Zirbel (1996) for FR Is (top panel) and FR IIs (bottom panel) in the Zirbel & Baum (1998) sample. The x-axis units are W Hz^{-1}.

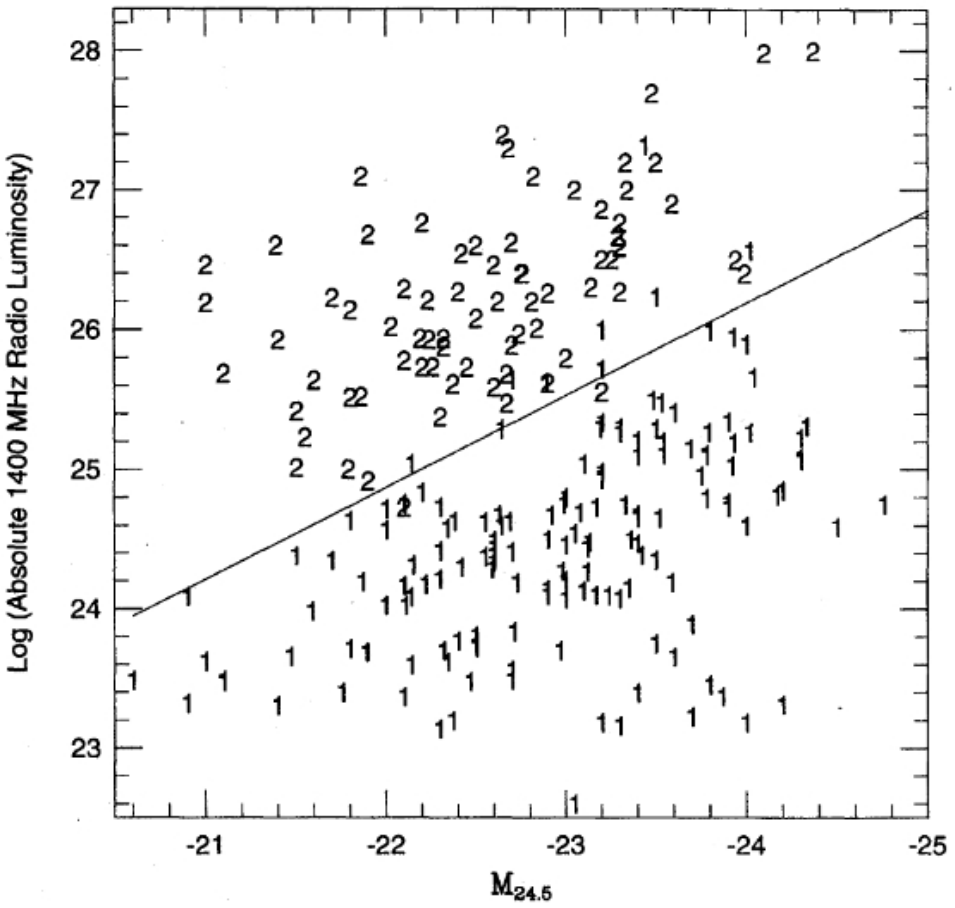

Figure 3.5: FR I/FR II diagram as reported in Ledlow & Owen (1996). Axes are the absolute R-band magnitude (x-axis) evaluated up to the isophote corresponding to 24.5 magnitudes arcsec^{-2} and the logarithmic rest frame 1.4 GHz luminosity density (y-axis) expressed in W Hz^{-1}. The symbols 1 and 2 stand for FR I and FR II, respectively.

ies and sources out to $z = 0.5$ as well as both field and cluster galaxies. In spite of the inhomogeneity of the sample, the result of Ledlow & Owen (1996) is still remarkable. In fact, the plot shows that powerful radio galaxies are not invariably associated with the most luminous host galaxies, as instead intuitively expected. Other work suggested several explanations for the FR I/FR II separation. De Young (1993) suggested that luminous host galaxies might have denser gas cores associated with deeper gravitational well than less luminous host galaxies. According to this scenario, the dense ~ 10 cm^{-3} ISM might explain the different decelerations of FR I and FR II jets. This idea was revised in subsequent studies. Different mechanisms involving the interaction of the radio galaxy with the surrounding ISM have been invoked in the literature to explain the above mentioned FR I/FR II separation represented in Figure 3.5 (e.g., Komissarov, 1994; Bicknell, 1995).

However, as mentioned in Section 3.1, we stress that the $\propto L_{\rm opt}^{1.8}$ separation might be an observational effect and explained in view of the steepness of both the radio and optical luminosity functions (Scarpa & Urry, 2001).

3.3 Emission lines

Most FR IIs exhibit strong emission lines and a hidden quasar-like nucleus (Barthel, 1989). These results suggest the possibility that FR IIs are powered by radiatively efficient accretion. On the contrary, most FR I radio galaxies and a small minority of FR IIs show weak emission lines and starved quasars, indicative of radiatively inefficient accretion (e.g. Ghisellini & Celotti, 2001; Marchesini et al., 2004).

Therefore the two radio galaxy classes are physically different and the distinction is deeper than the mere FR I/FR II morphological classification. Nevertheless, the separation between the two classes might ultimately be related to the AGN gas fueling.

Except for some exceptions, FR Is usually lack broad emission lines, whereas FR IIs can be divided into Narrow Line Radio Galaxies (NLRGs) and Broad Line Radio Galaxies (BLRGs). NLRGs show only both permitted and forbidden $\lesssim 1,000$ km s^{-1} narrow emission lines. On the other hand, BLRGs are associated with a strong ionizing optical/UV continuum ultimately due to accretion of gas into the central regions and show permitted broad $\gtrsim 3000$ km s^{-1} emission lines as well as narrow lines.

The radio galaxy population may also be divided into Low Excitation Galaxies (LEGs) and High Excitation Galaxies (HEGs) on the basis of optical narrow emission line ratios (Hine & Longair, 1979; Laing et al., 1994; Jackson & Rawlings, 1997; Buttiglione et al., 2010). According to Jackson & Rawlings (1997) LEGs are those for which the EW of the OIII 5,007Å line is < 10Å and/or the EW of the OII line is higher than that of the OIII line.

NLRGs and BLRGs are commonly identified as HEGs. Therefore, LEGs represent an additional subclass of FR II radio galaxies, along with the above mentioned NLRGs and BLRGs. However, while BLRGs are clearly HEGs, the case of NLRGs is less established and deserves discussion. Spectropolarimetry (Antonucci, 1984; Ogle et al., 1997; Cohen et al., 1999) and strong nuclear emission from the AGN torus at the MIR (Cleary et al., 2007; Tadhunter et al., 2007) proved the presence of hidden quasars in many NLRGs, as discussed within the unification scheme outlined above (see Section 1.6). In fact, the optical light and spectrum of many NLRGs suggest the presence of an AGN nucleus. Therefore, the presence of high-ionization emission line ratios suggests that NRLGs are HEGs.

In the context of the AGN unified scheme, the lack of evidence for optical/UV ionizing continuum in LEGs suggests that the AGN torus is absent or a radiatively inefficient accretion occurs in LEGs. This is further motivated by the correlations among near-infrared, optical, and radio nuclear luminosities observed in LEGs (Chiaberge et al., 1999; Leipski et al., 2009; Baldi et al., 2010).

3.4 X-ray observations of jets

The Chandra X-ray observatory detected X-ray emission from the kpc-scale jets and hot-spots of many RLAGNs , totaling ~ 120 AGNs and including many radio galaxies[2] (see e.g. Harris & Krawczynski, 2006, for a review). The origin of the X-ray emission observed in radio galaxies is still debated, especially for the higher-power FR IIs. In the cases where the jet can be resolved in the X-rays, bright knots, often spread over the extension of the jet, can be observed.

In FR I radio sources the X-ray emission from the kpc-scale jet can be explained as synchrotron emission from electrons endowed with $\sim$TeV energies and embedded in magnetic fields in the range $\sim 10 - 1000$ μG. For example, as in the case of M87, this hypothesis is mainly motivated i) by rapid X-ray flux variability; ii) by the fact that the radio to X-ray SED can be modeled with a single synchrotron component; iii) by the presence of both radio and X-ray emitting knots along the jet. We refer to Harris & Krawczynski (2006) for a review. In Figure 3.6 we show multiwavelength images of the FR I radio galaxies M87 (a) and Centaurus A (b).

For the FR IIs, the radio to X-ray energy spectrum often requires IC emission, in addition to the synchrotron, to explain radio, optical, and X-ray observations. The most commonly accepted belief is that the X-ray emission is due to IC scattering of the Cosmic Microwave Background (CMB) radiation from mildly relativistic electrons with kinetic energies $\sim$MeV and embedded in a highly relativistic plasma moving with a bulk Lorentz factor

[2] `http://hea-www.cfa.harvard.edu/XJET/`

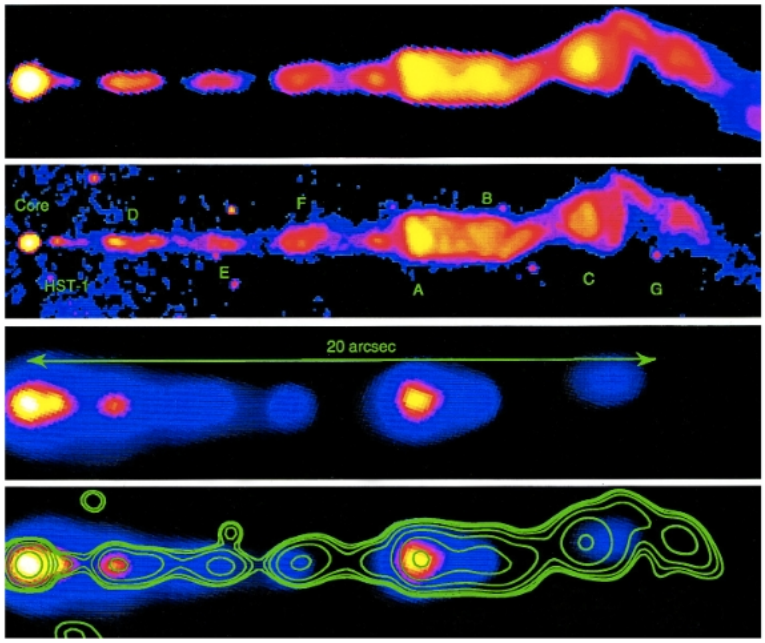

(a)

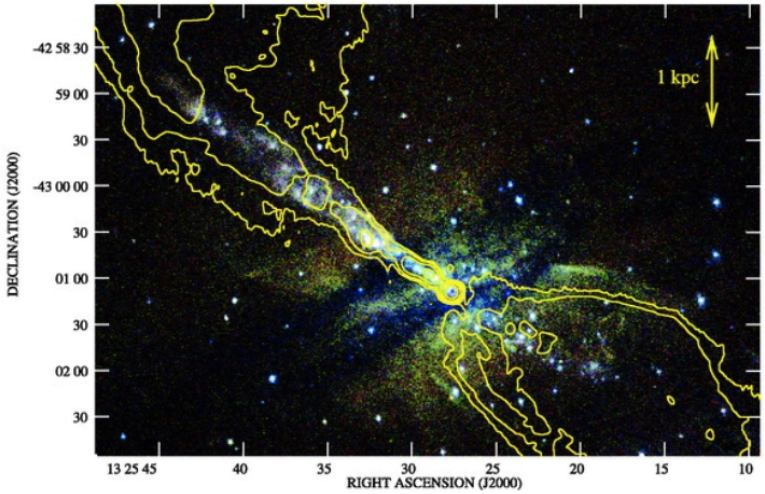

(b)

Figure 3.6: Multiwavelength images of the radio galaxies M87 (a) and Centaurus A (b). Panel (a), from top to bottom: the 14.435 GHz VLA image, optical image in the F814W filter taken with the Planetary Camera on board of HST, the Chandra image in the X-rays, and the Chandra image where the contours of the HST image are overplotted. A logarithmic scale is used for the fluxes in the HST and VLA images, a linear scale is adopted for the fluxes in the X-ray image. Blue, red, and yellow colors are associated with increasing fluxes. The jet shown in the images has a projected length of ~ 1.6 kpc. Panel (b): image of the radio galaxy Centaurus A as seen by Chandra in the 0.4-0.85 keV (red), 0.85-1.3 keV (green), and 1.3-2.5 keV (blue) energy ranges. The 5 GHz VLA contours are overplotted. North is up. The northern part of the X-ray jet has a projected length of 3 kpc. Credits. Panel (a): Marshall et al. (2002) and ©2002 American Astronomical Society. Panel (b): Hardcastle et al. (2007) and ©2007 American Astronomical Society.

$\Gamma \sim 10$ (Tavecchio, 2000; Celotti et al., 2001). An alternative scenario suggests that the observed X-ray emission is due to an additional population of electrons (Harris & Krawczynski, 2002).

3.5 High-redshift radio galaxies

Radio-loud quasars were the first objects discovered at redshifts $z > 1$ (see Stern & Spinrad, 1999, for a review), thus making RLAGNs perfect laboratories to study the Universe at cosmological distances. About 300 high redshift radio galaxies (HzRGs) are known at redshifts $z \gtrsim 1$ and many of them are at $z \gtrsim 2$ (see e.g., Miley & De Breuck, 2008, for a review). In the following we will briefly discuss the properties of FR I and FR II radio galaxies at $z \gtrsim 1$, separately.

3.5.1 FR I radio galaxies at $z \gtrsim 1$

Besides one candidate discussed in Snellen & Best (2001) at $z = 1.0$, no other $z \geq 1$ FR Is were known before the work by Chiaberge et al. (2009). FR I radio galaxies are in fact extremely hard to find at $z \gtrsim 1$. The poor statistics clearly limits our understanding of the properties of FR I at these redshifts.

On the basis of multiwavelength SED analysis Baldi et al. (2013) showed that the hosts of the ~ 30 FR I radio galaxies at $z \sim 1-2$ in the (Chiaberge et al., 2009) sample are old massive galaxies, similar to those associated with local FR Is. However, at variance with lower redshift FR Is, such sources exhibit significant UV and MIR emission thus suggesting a possible contribution from star formation and/or nuclear activity (Baldi et al., 2013).

There are three main reasons for which FR Is are difficult to find at $z \gtrsim 1$. i) FR Is lack strong emission lines and, therefore, they appear as normal galaxies in optical surveys; ii) flux-limited samples of distant radio galaxies selected at low radio frequencies are preferentially biased towards powerful FR IIs (see discussion below); iii) flux limited samples of $z \gtrsim 1$ FR Is selected at low radio frequencies are invariably contaminated by the overwhelming population of star-forming galaxies. In the following we will discuss the last two points in detail.

Flux-limited samples of radio galaxies selected at low radio frequencies such as the 3C sample (the most extensively studied catalog of radio sources) and its deeper successors, i.e. the 6C and 7C catalogs, are constrained by a tight luminosity versus redshift relation fixed by the flux limit of the survey. This, along with the steepness of the radio luminosity function, gives rise to the well-known Malmquist bias which ultimately results in the presence of high- and low-power radio sources at high- and low-redshifts (i.e. $z \lesssim 0.7$ in the case of the 6C and 7C catalogs), respectively.

At low radio frequencies, i.e. $\lesssim 5$ GHz, the extragalactic radio sources that mainly contribute to the number counts are star forming galaxies and steep spectrum sources. At low radio frequencies, star forming galaxy number counts are dominant at flux levels $\lesssim 0.1 - 0.2$ mJy (Windhorst et al., 1985; Benn et al., 1993; Hopkins et al., 1998; Seymour et al., 2004; Muxlow et al., 2005; Moss et al., 2007). At higher fluxes $\sim 1-10$ mJy they still represent a significant fraction of the overall extragalactic radio source population (Chiaberge et al., 2009). This implies that it is extremely difficult to select a sample of $z > 1$ low-power radio galaxies that is not contaminated by the overwhelming population of star-forming galaxies. This problem clearly affects evolutionary studies of FR Is that are based on source number counts, where complete samples are necessary (see also Section 3.6).

3.5.2 FR II radio galaxies at $z \gtrsim 1$

Because of the limited number of known $z \gtrsim 1$ FR Is the great majority of known HzRGs are powerful radio galaxies of FR II type. There is observational evidence that powerful HzRGs of FR II type are associated with the most massive galaxies that have high stellar masses ($M_\star > 10^{11} M_\odot$, Seymour et al., 2007) and actively accreting SMBHs at their centers (Drouart et al., 2014). Large reservoirs of dust (Wylezalek et al., 2013b) and gas (e.g. CO, Papadopoulos et al. , 2000) has been observed in powerful HzRGs. In particular, HI absorption features are often detected in the Lyman-α profiles (van Ojik et al., 1997) associated with luminous and morphologically complex (> 100 kpc scale) Lyman-α halos (Reuland et al., 2004).

Powerful HzRGs differ from low-redshift (FR II) radio galaxies. Some work suggested a trend where higher radio luminosities, smaller typical sizes (Miley, 1968; Nilsson et al., 1993; Neeser et al., 1995; Daly & Guerra, 2002) and steeper radio spectra (Tielens et al., 1979; Blumenthal & Miley, 1979) are found in association with powerful HzRGs. However, such trends are debated and might be due to selection effects and observational biases (see e.g., Miley & De Breuck, 2008, for a review)

Similarly, the host galaxies of powerful HzRGs differ from those of lower-redshift radio galaxies. In fact, at variance with lower-redshift radio galaxies, powerful HzRGs (i) are hosted by the above mentioned emission-line halos (Reuland et al., 2004), (ii) show an increased clumpiness of the continuum emission (Pentericci et al., 1998, 1999), and (iii) are associated with radio sources aligned with both the emission-line halos and the emission from the UV/optical galaxy continuum (Chambers et al., 1987; McCarthy et al., 1987; Pentericci et al., 1999; Bicknell et al., 2000; Pentericci et al., 2001). The alignment is commonly detected in radio galaxies at $z > 0.6$, while it is not observed, at least in the optical, at lower redshifts. In Figure 3.7 we show the radio map superimposed to the optical image of the HzRG 4C 41.17.

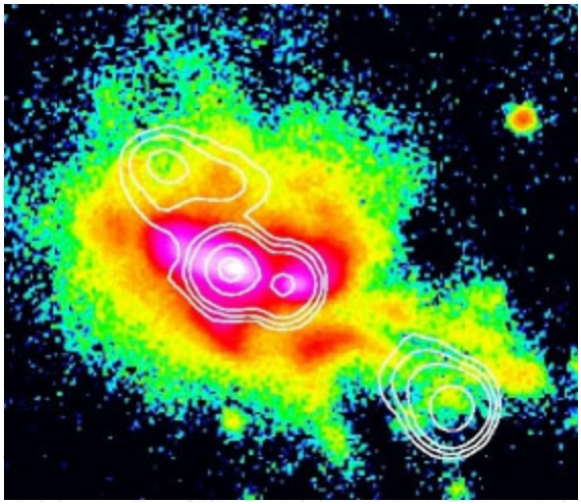

Figure 3.7: Image of the FR II radio galaxy 4C 41.17 at $z = 3.18$. The Keck narrow-band image shows the ionized gas. Radio contours obtained with VLA at 1.4 GHz are superimposed. The angular size is ~ 13 arcsec corresponding to a projected size ~ 100 *kpc*. Credits: van Breugel and Reuland (Reuland et al., 2003).

3.6 Evolution of radio galaxies

It has been accepted since early studies of Longair (1966) that radio source number counts require cosmological evolution. It is known that powerful radio galaxies with rest frame 178 MHz luminosity densities typical of FR II radio galaxies $L_{178\ \mathrm{MHz}} \gtrsim 2 \times 10^{32}$ erg s^{-1} Hz^{-1} sr^{-1} undergo cosmological evolution with number density enhancements ~ 10 and up to 10^{2-3} for the most powerful sources, at least out to $z \sim 2 - 3$ (Wall, 1980; Dunlop & Peacock, 1990).

Conversely, the cosmological evolution of low power radio galaxies, i.e. radio galaxies with radio powers typical of local FR Is, is less clear and is still debated. This is mainly because i) the high complexity of the radio source classification, especially for FR Is, makes difficult both the low power radio galaxy sample selection and an accurate modeling of the observed number counts (see Sections 3.1, 3.3, and 3.5) and ii) low power radio galaxies are more difficult to find at comparable distances than higher power radio sources (see Section 3.5).

Addressing the problem of the cosmological evolution of low power radio galaxies is particularly difficult and important for $z \gtrsim 1$ FR I radio galaxies with luminosities around the FR I/FR II radio power divide. In fact, i) low power radio galaxy number density is expected to reach its maximum around $z \sim 1.2$ (Willott et al., 2001; Massardi et al., 2010); ii) the FR I/FR II

radio power divide approximately corresponds to the radio luminosity break in the radio luminosity function (RLF) of radio galaxies, thus reinforcing an intrinsic physical difference between FR Is and FR IIs that might be translated in different number density cosmological evolutions of the two populations; iii) the FR I and FR II radio power distributions partially overlap (Zirbel, 1996, see Figure 3.4). This implies that complete samples of FR Is (and FR IIs) cannot be drawn on the basis of luminosity and flux criteria only, thus making number count studies of FR Is (and FR IIs) more problematic; iv) the cosmological evolution of the FR I/FR II radio divide is still unknown. Higher redshift FR I sources might have higher radio luminosities than those of local FR Is (Heywood et al., 2007).

Early low redshift studies suggested that low power radio sources are characterized by flat evolution (e.g. Jackson & Wall, 1999). Clewley & Jarvis (2004) confirmed this behavior out to $z \sim 0.8$ for radio sources with rest frame 325 MHz luminosity densities $L_{325\ \mathrm{MHz}} < 10^{32}$ erg s^{-1} Hz^{-1} sr^{-1}.

On the other hand, other studies suggested positive evolution for both the high and low power radio galaxies (Dunlop & Peacock, 1990; Willott et al., 2001; Massardi et al., 2010). Positive evolution for low power radio galaxies was also suggested up to $z \sim 0.4$ (Brown et al., 2001), $z \sim 0.8$ (Sadler et al., 2007; Donoso et al., 2009), and $z \sim 1$ (Rigby et al., 2008; McAlpine et al., 2013).

Although our understanding of the cosmological evolution of low power radio galaxies has significantly improved, there is no general consensus on the details of the evolutionary scenario for this population. A pure luminosity evolution as $\mathrm{L}_\star(z) = \mathrm{L}_\star(0)(1+z)^\kappa$, where $\mathrm{L}_\star(z)$ is the luminosity break in the RLF as a function of the redshift z, is often invoked in the literature to describe the RLF of these sources. Different values of κ are commonly found in the literature, ranging from $\kappa = 2$ (Sadler et al., 2007), $3 < \kappa < 5$ (Brown et al., 2001), and $\kappa = 1.18$, 1.9 (McAlpine et al., 2013). These differences translate into a high uncertainty in the number density enhancement of low power sources.

For example, the number density of RLAGNs with rest frame 1.4 GHz luminosity densities $L_{1.4\ \mathrm{GHz}} < 10^{32}$ erg s^{-1} Hz^{-1} increases from $z \sim 0$ out to $z \sim 0.55$ and $z \sim 1.2$ by a factor of ~ 1.5 (Sadler et al., 2007; Donoso et al., 2009) and ~ 3 (McAlpine et al., 2013), respectively. Because of poor statistics, the enhancement becomes dramatically less certain at $z \sim 1$ and at slightly higher radio power ($L_{1.4\ \mathrm{GHz}} > 10^{32}$ erg s^{-1} Hz^{-1}), where it is estimated to be within $\sim 5 - 9$ (Rigby et al., 2008).

Therefore, constraining the RLF at these luminosities and redshifts is fundamental to understand the entire radio galaxy evolutionary history. In Section 5.3 we estimate the comoving density of FR I radio galaxies at redshift $z \sim 1.1$ and 1.4 GHz rest frame luminosity densities $L_{1.4\ \mathrm{GHz}} \sim 2 \times 10^{32}$ erg s^{-1} Hz^{-1}. We will compare our results with those of previous observational and theoretical work.

3.7 The Mpc-scale environment of radio galaxies

There is observational evidence that the Mpc-scale environments of FR Is and FR IIs are different. Zirbel (1997) found that 70% of low redshift (i.e. $z < 0.25$) FR Is in their sample reside in intermediate/rich groups or clusters. Furthermore, at variance with FR IIs in rich environments at similar redshifts, $z < 0.25$ FR Is in clusters or rich groups are invariably associated with the brightest cluster members (e.g., Best et al., 2007). Furthermore, $z < 0.25$ FR Is are found in groups/clusters that are significantly denser than the typical Mpc-scale environments of FR IIs at similar redshifts (Prestage & Peacock, 1988; Zirbel, 1997).

On the other hand, only 24% of the low redshift (i.e. $z < 0.25$) FR IIs in the Zirbel (1997) sample reside in intermediate or rich groups. Such a percentage increases up to 41% if high redshift (i.e., $0.25 \lesssim z \lesssim 0.5$) FR IIs are considered. Similarly, Hill & Lilly (1991) found that $\sim 50\%$ of the FR IIs at $z \sim 0.5$ are in overdense Mpc-scale environments. These results are also in agreement with what has been independently found for FR IIs at $z < 0.3$ by Smith & Heckman (1990) and with the results of Ramos Almeida et al. (2013) obtained for a $z \leq 0.7$ sample of luminous radio galaxies, mainly dominated by FR IIs. At higher redshifts, i.e. $z \gtrsim 1.2$, powerful FR IIs have been commonly used as beacons to search for high-z (proto)clusters (see e.g., Miley & De Breuck, 2008, for a review). However, the fraction of $z \gtrsim 1.2$ FR IIs in clusters (in the range $23\% - 50\%$, Galametz et al., 2012; Wylezalek et al., 2013a), although in agreement with lower redshift studies, is lower than that of lower-redshift FR Is.

Some of the clusters hosting FR I radio galaxies are well known and studied: M87 (see also Figures 3.6 and 3.3) is the central dominant galaxy of the Virgo cluster. Other spectacular examples are the FR I radio galaxies Perseus A (Fabian et al., 2006, see also Fig. 3.10) and 3C 338 which are located in the cores of the Perseus cluster and Abell 2199, respectively. Remarkably, in the complete sample of Abell clusters, 90% of the clusters include a radio galaxy, 94% of which are FR Is (Ledlow & Owen, 1996).

Nevertheless, because of the difficulties outlined in Section 3.5 in finding higher redshift FR Is a direct comparison of the Mpc-scale environments of high-z FR Is and FR IIs is difficult to perform, especially at redshifts $z \gtrsim 1$, where, furthermore, the properties of galaxy clusters and of the cluster galaxy population dramatically evolve at increasing redshift within $z \sim 1 - 2$, thus making galaxy clusters difficult to find and to study. Such a comparison is fundamental for the present work and we refer to Part II for a discussion.

3.8 Radio galaxies and the intra-cluster medium

3.8.1 Radio source triggering

As outlined in the previous Section, there are lines of evidence that the radio galaxies, especially those of FR I type, are frequently associated with dense Mpc-scale environments typical of rich groups and clusters. The high number density of galaxies in the central regions of the clusters and the specific velocities of cluster galaxies, usually higher in merging clusters, increase the probability of gravitational and dynamical interaction among cluster galaxies. An important problem is to understand whether the environment plays a role in forming a radio galaxy and determining its nature (we refer to Hatch et al., 2014, for a recent work).

Simpson & Rawlings (2002) suggested that powerful radio sources might be triggered by galaxy-galaxy interactions within the cluster. Owen (1996) proposed a scenario where the development of a radio galaxy is due to the interaction of the galaxy with clumps of X-ray emitting gas, similar to those observed in the ICM of clusters (see also Section 3.8.3), that have been commonly detected in the X-rays around elliptical galaxies (Sarazin, 1997; Sarazin et al., 2001). An alternative hypothesis is that the local environment, i.e. the host galaxies, plays a much more important role in triggering the AGN activity and developing the radio galaxy. For example, the latter scenario is motivated by the observed differences in the host galaxies of FR Is and FR IIs (see Section 3.2).

Nevertheless, the interaction between the radio galaxy and the surrounding Mpc-scale environment is not settled and not completely understood yet. In the following Sections we will briefly review some phenomena showing evidence of this interaction. We refer to Fabian (1994), Feretti & Giovannini (2008), Fabian (2012), and Feretti & Venturi (2002) for discussion.

3.8.2 The narrow- and wide-angle tailed radio galaxies

The most striking signature of interaction between the radio galaxy in a cluster and the surrounding ICM is constituted by tailed radio sources. Tailed radio sources are radio galaxies that are characterized by complex structures and significant distortions resulting from the interaction of the jets with the surrounding gas. FR II radio galaxies do not show prominent jet distortions. Therefore, tailed radio galaxies are almost invariably associated with FR I radio galaxies.

Tailed radio galaxies were originally divided into wide-angle tail (WAT) and narrow-angle tail (NAT) sources. NAT sources (Owen & Rudnick, 1976; O'Dea & Owen, 1985) are radio galaxies where the jets are bent towards the same direction and at extreme angles, up to 90 degrees with respect to their original orientation. The tails have a characteristic V shape originated by the bending. These sources have radio luminosities typical of FR Is and

often show a high degree of polarization, up to $40\% - 50\%$. The steep radio spectrum observed in the tails suggests a typical age of 5×10^7 yr associated with the tails Feretti et al. (1998, 1999). In the left panel of Figure 3.8 we show an example of NAT source.

A commonly accepted explanation for the observed distorted morphology is that the jets are curved by ram pressure exerted by the ambient gas when the host galaxy is moving at high velocity through the ICM (Miley et al., 1972; Begelman et al., 1979; Vallèe et al., 1981; Baan & McKee, 1985). The ram pressure model requires velocities $\sim 1,000$ km s^{-1} to explain the jet bending. NAT are commonly identified with cluster galaxies that are located at any distance from the cluster core. This evidence suggests that NATs are possibly traveling in the cluster with significant velocities. Therefore, such a simple model seems to explain successfully the structure of NAT sources.

Similarly to NAT sources WAT sources have radio jets curved towards the same direction from the original orientation. However, WAT radio sources show much larger angles between the tails thus exhibiting a characteristic U shape. WAT sources are preferentially associated with giant ellipticals of D or cD types and located in the optical cores of clusters (Owen & Rudnick, 1976; O'Doghue et al., 1990). WAT sources have transitional properties between FR Is and FR IIs. In fact, i) WAT sources have radio luminosities in the range 10^{42-43} erg s^{-1} and therefore intermediate between those of FR Is and FR IIs; ii) their jets show a sharp transition from being well collimated on small scales and then showing lobes typical of FR Is at larger scales. The polarization properties and tail ages are similar to those of NATs. In the right panel of Figure 3.8 we show an example of WAT source.

At variance with NATs, the ram pressure model is less effective to explain the curved morphology of the jets of WATs. This is because WATs are associated with dominant cluster galaxies with relatively low velocities $\lesssim$ 100 km s^{-1} (Quintana & Lawrie, 1982; Bird, 1994; Pinkney et al., 2000), not sufficient to curve the jets, and are preferentially located in the cluster cores. A possible origin for the curved morphology of the jets of WATs is the ram pressure produced during mergers between clusters (Pinkney et al., 1993; Loken et al., 1995; Roettiger et al., 1996; Gomez et al., 1997)

3.8.3 AGN feedback

Diffuse X-ray emission is commonly observed in clusters of galaxies and rich groups. It is ultimately due to hot intra-cluster gas composed mainly of hydrogen plasma that is thermally emitting bremsstrahlung radiation. A significant fraction of this X-ray emission comes from the dense central regions of clusters and rich groups. For X-ray Bremsstrahlung radiation the cooling time is $t_{\rm cool} \propto T^{\lambda}/n$, where $-1/2 \lesssim \lambda \lesssim 1/2$, T is the gas temperature, and n is the gas density. Relativistic corrections are needed at

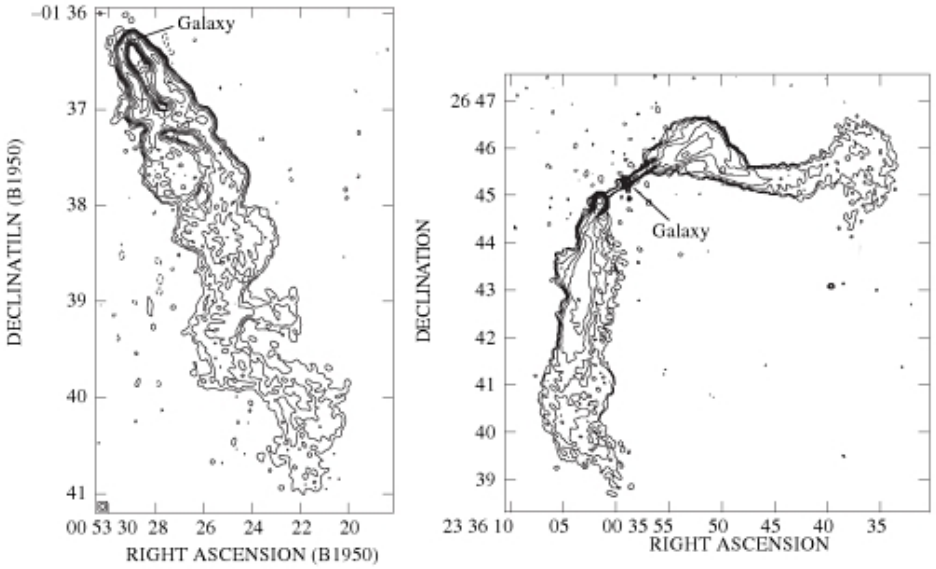

Figure 3.8: Radio maps showing examples of tailed radio galaxies. Left: the NAT 0053-016 in Abell 119. Right: the WAT 3C 465 in Abell 2634. Credits: (Feretti & Giovannini, 2008).

high temperatures $T \gtrsim 10^9$ K (Novikov & Thorne, 1973). This is why the exponent λ varies within the values $\lambda = 1/2$ and $\lambda = -1/2$, corresponding to Bremsstrahlung radiation in the presence of non-relativistic and relativistic electrons, respectively.

The constant loss of energy in the ICM implies the existence of inflows of cooled gas into the cores of clusters. In fact, according to this simplified picture, gas temperatures $\sim 10^{7-8}$ K, gas densities in the range $10^{-4} - -10^{-2}$ cm^{-3}, and X-ray luminosities 10^{43-45} erg s^{-1}, typical of rich groups and clusters, imply cooling times $t_{\rm cool} \lesssim 10^9$ yr, i.e. shorter than the typical age of the clusters, of the order of the Hubble time, and therefore sufficient to produce observable inflows of gas with a rate $\sim 1 - 300$ M$_\odot$ yr^{-1} (see e.g., Fabian, 1994, for a review).

Evidence of cooling flows and cool cores in clusters of galaxies were provided by observations in the X-rays. Nevertheless, there is less evidence in other wavelengths. The lack of evidence in other wavelengths makes the existence of cooling flows less clear and more difficult to understand.

The evidence of cooling flows came from X-ray observations with ROSAT, Chandra, and XMM-Newton. Such observations found evidence of cavities in the hot X-ray emitting gas of elliptical galaxies, galaxy groups, and clusters of galaxies (Fabian et al., 2003b, 2005, 2006; Gitti et al., 2010; Bogdán et al., 2011). Remarkably, such X-ray cavities are often associated with ra-

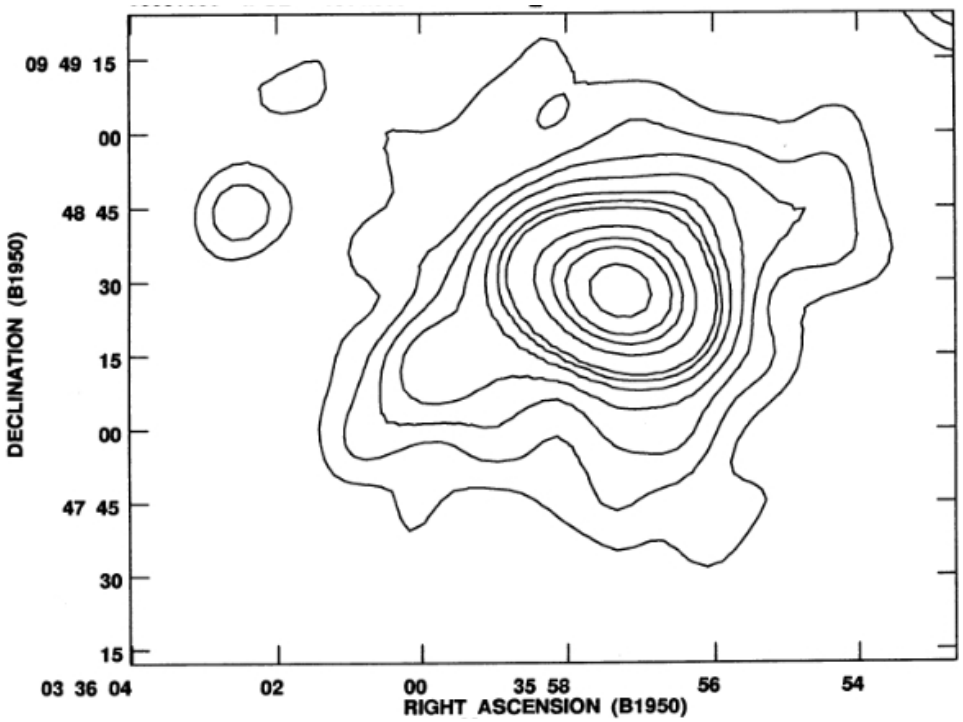

Figure 3.9: Radio map at 1.5 GHz of the center of the 2A 0335+096 cluster showing the structure of the amorphous source hosted in the cool core. Credits: Sarazin et al. (1995).

dio lobes of radio galaxies (Böhringer et al., 1993; Carilli et al., 1994; Fabian et al., 2001, 2003a) and, therefore, represent a clear example of interaction between the radio emitting plasma associated with the radio galaxy and its cluster environment.

The majority of these radio sources are FR Is. There are exceptions such as the FR II radio galaxies Cyg A and 3C 295, and compact (< 10 kpc) sources as for example in Abell 496. FR Is in cool core clusters are distinguished in lobe-dominated sources and amorphous sources. Lobe dominated sources show a typical FR I radio structure with jets going outwards from the nucleus and ending in extended radio lobes. Some examples of clusters hosting these sources are the Abell 1795 and Abell 2029. Amorphous sources (Burns, 1990; Baum & O'Dea, 1991) are less frequently observed than lobe-dominated sources. Nevertheless they are commonly associated only with clusters having cooling flows. Such radio sources have diameters $\sim 100 - 400$ kpc, strong cores, and have almost perfect spherical structures with weak or no evidence of collimated ejecta such as lobes and jets. In Figure 3.9 we show a low-frequency radio map showing an example of amorphous radio source at the center of a cooling flow cluster.

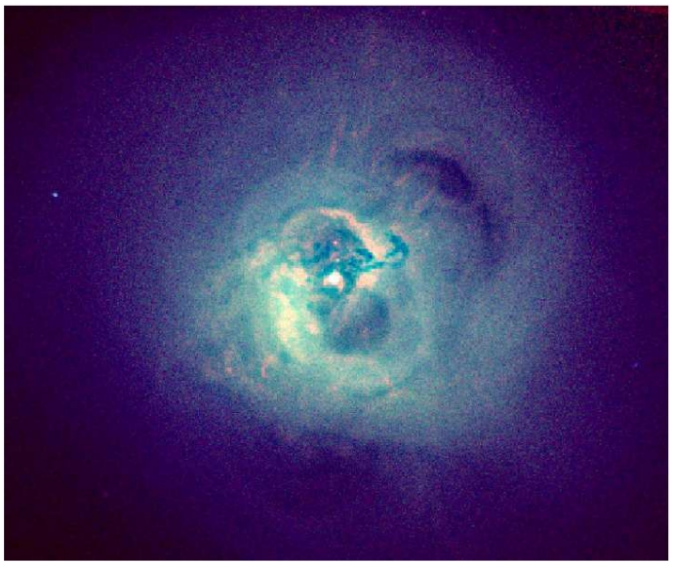

Figure 3.10: Chandra X-ray image of the Perseus galaxy cluster hosting the FR I radio galaxy Perseus A in its core. The emission from the ICM is shown. The ripples in the brightness are likely due to sound waves propagating through the ICM. The radio bubbles located at the opposite sides with respect to the central radio galaxy are at a projected distance of 65 kpc, and the ICM emission has a projected diameter of 360 kpc. Credits: NASA, CXC, IoA, Fabian et al. (2006).

In Figure 3.10 we show the Chandra X-ray image of the Perseus cluster hosting the FR I radio galaxy Perseus A (also known as NGC 1275). The X-ray cavities are clearly shown in the Figure and are another spectacular example of interaction between the radio galaxy and the surrounding ICM.

The overall diffuse X-ray emission clearly seen in the Figure is explained as Bremsstrahlung radiation emitted by the hot plasma residing in the ICM. On the other hand, the X-ray cavities are instead caused by AGNs inflating bubbles within the ISM or the ICM. The original idea that a radio galaxy might inflate cavities or bubbles in the ICM is reported in Gull & Northover (1973). The mechanism is complex and still debated in the literature. It belongs to a general context, known as AGN feedback, including all phenomena occurring in the surrounding medium of an AGN, e.g. in the ICM, the IGM, or the host galaxy, and that are due to some processes and mechanisms for which the active nucleus is responsible. We refer to Fabian (2012) for a review of the AGN feedback.

For galaxy clusters the work required to inflate the X-ray bubbles is estimated by means of the X-ray images and is used, along with an estimate of the age of the cavities, to estimate the power required to inflate the bubbles of radio gas. AGN jets seem to have sufficient power to balance the Bremsstrahlung cooling of the X-ray emitting gas in the ICM and to

explain the lack of cold gas and newly formed stars in the cores of galaxy clusters. However, the role of AGNs in heating the ICM and the interplay between the AGN and its cluster environment are still debated and not well understood (McNamara & Nulsen, 2012). For example, the bulk kinetic jet power may not be efficiently transferred to the ICM and other processes (for example anisotropic heat conduction occurring in the ICM, e.g. Bogdanović et al., 2009) may play an important role in heating the ICM.

3.8.4 AGN feedback: FR Is versus FR IIs

Concerning the AGN feedback in clusters and the interaction between the radio galaxy and its surrounding Mpc-scale environment we stress that FR IIs have powerful active nuclei and relativistic jets that may strongly influence the properties of the host galaxies, those of the surrounding cluster members, and those of the ICM. For example, in the X-rays, the particles in the jets of FR IIs commonly IC upscatter the CMB radiation up to X-ray energies, thus contaminating the X-ray emission from the hot gas in the cluster (see also Section 3.4). This implies that the properties of the gas in ICM cannot be easily studied in the presence of powerful radio galaxies (Fabian et al., 2003a).

Remarkably, because of the lower level of AGN and jet activity typical of FR Is, the properties of clusters and rich groups hosting FR Is, as well as those of the ICM and the cluster galaxy population can be more effectively studied than in the case of clusters hosting powerful FR IIs. This aspect is particularly important for studies of clusters of galaxies at redshifts $z \sim 1-2$, where their properties and those of the cluster galaxy population are rapidly evolving at increasing redshifts and are not completely understood yet. The study of the Mpc-scale environments of $z \sim 1-2$ FR Is is key for the present work. We refer to Part II for discussion.

3.9 Compact sources

Compact radio sources deserve a separate treatment because they are not classical radio galaxies, i.e. they are classified neither as FR I nor as FR II sources. In this section we outline their properties since they are relevant for the present work. We refer to O'Dea (1998) for a review and to Section 5.2.7 for a discussion about $z \sim 1-2$ compact radio sources.

Compact radio sources are preferentially found at redshifts $z \lesssim 1$ (Fanti et al., 1990; O'Dea et al., 1991). They have been originally divided into Compact Steep Spectrum (CSS, e.g. Saikia, 1988; Fanti et al., 1990; Fanti & Fanti, 1994; Dallacasa et al., 1993; Fanti & Spencer, 1995) sources and GigaHertz Peaked Spectrum (GPS, e.g. O'Dea et al., 1991) sources.

GPS and CSS sources were originally classified on the basis of their radio spectra. Almost all compact sources show a steep spectrum characterized

by a low frequency turnover. GPS sources have a turnover at frequencies $\gtrsim$ 1 GHz, whereas for CSS sources it is located near 100 MHz. However, sometimes CSS source spectra do not exhibit such a turnover. The presence of this turnover is likely due to synchrotron self-absorption. Free-free absorption might be another important mechanism. In Figure 3.11 we show some examples of radio spectra of both CSS and GPS sources.

Concerning the radio morphology, compact sources typically show extended and resolved radio emission. These sources may show complex morphology, being often associated with double or triple systems clearly seen in the radio maps. While GPS sources are usually entirely contained within the extent of the narrow-line region ($\lesssim$ 1 kpc), CSS sources are commonly contained within the host galaxy ($\lesssim$ 15 kpc). In Figure 3.12 we show some examples of compact radio sources.

Compact radio sources usually have radio powers typical of powerful FR IIs. Typically the radio power distributions of CSS and GPS sources are essentially indistinguishable. In Figure 3.13 we show the 5 GHz radio power distributions of CSS and GPS sources (O'Dea & Baum, 1997). Compact sources are commonly associated with non-relativistic ejecta (Pearson et al., 1987; Readhead et al., 1996a,b), they usually lack strong variability (De Bruyn, 1990; Stanghellini et al., 1997), and they are often associated with symmetric radio structures Fanti et al. (1990); Saikia et al. (1995). This suggests that compact sources are not affected by relativistic aberration and, therefore, that these objects are intrinsically powerful radio emitters. However, we note that some compact sources with radio powers typical of those of powerful FR Is have been observed (e.g., Drake et al., 2004; Giroletti et al., 2005).

Several theoretical scenarios have been proposed to explain some properties of compact sources such as their morphologies, spectra, and sizes. Some studies suggested that compact sources will evolve into classical radio galaxies increasing their size. However, the exact evolution of compact radio sources into either FR IIs or less powerful FR Is is still debated and not fully understood (Begelman, 1996; Snellen et al., 2000; Tinti & De Zotti, 2006).

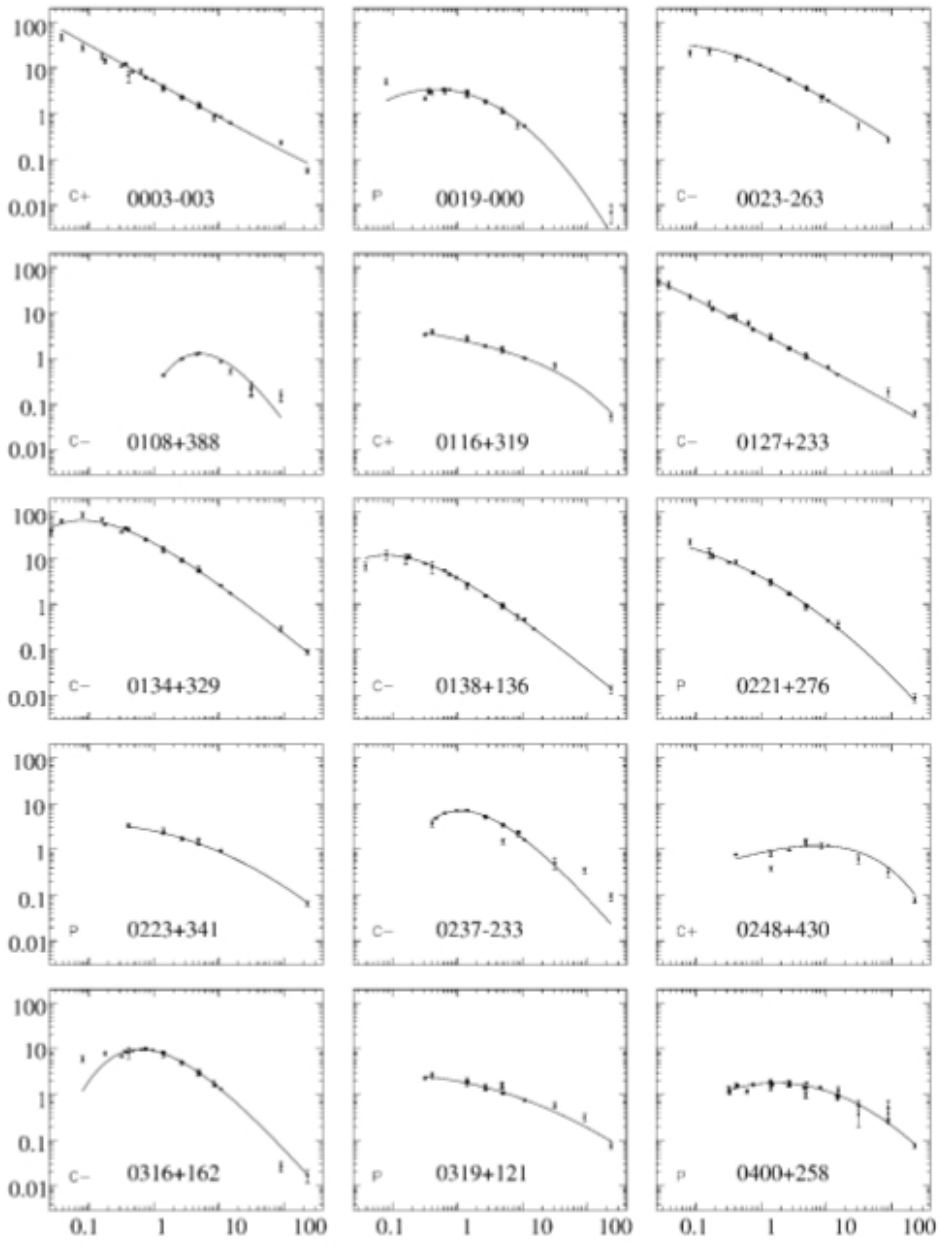

Figure 3.11: Radio spectra showing some examples of CSS and GPS sources. For each plot, the flux in Jy is reported in the y-axis, the frequency in GHz is reported in the x-axis. Credits: O'Dea (1998).

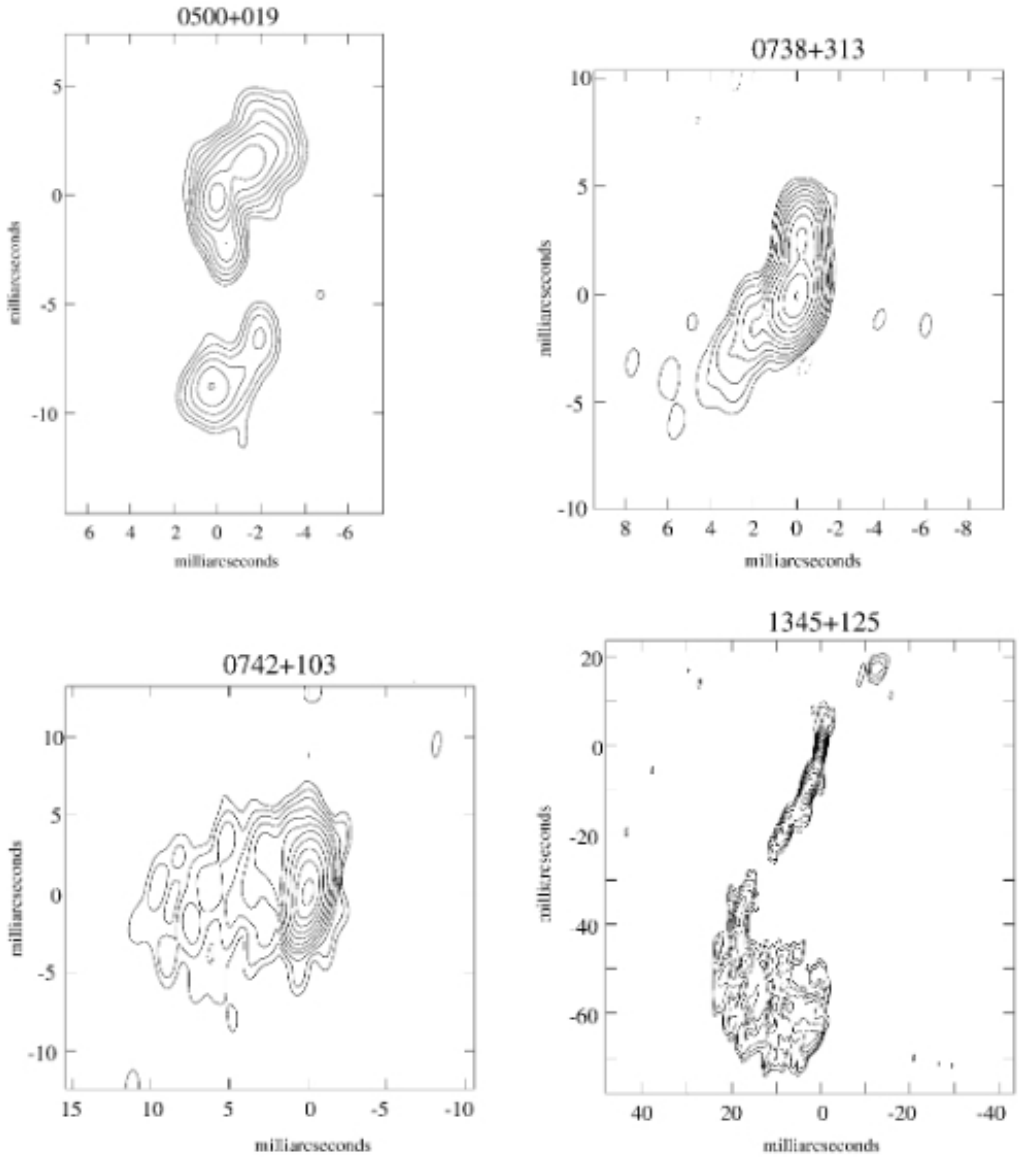

Figure 3.12: Radio maps showing some examples of CSS and GPS sources. Credits: O'Dea (1998).

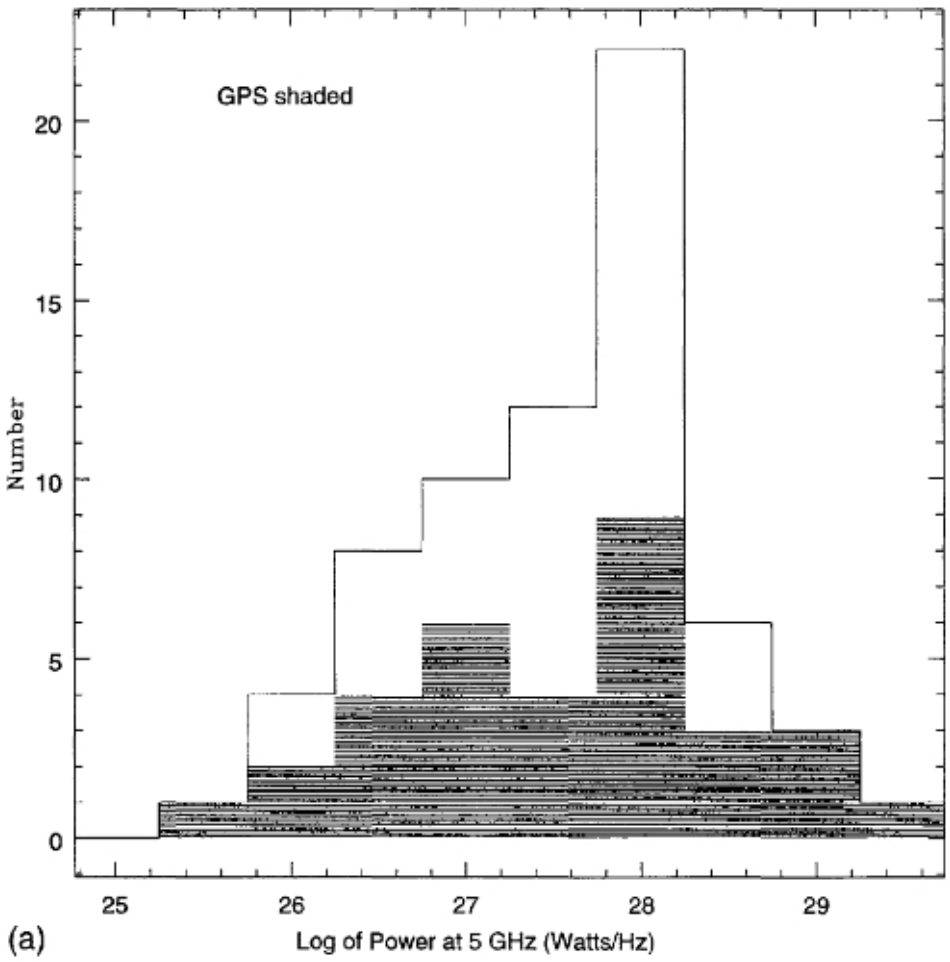

Figure 3.13: Luminosity density distribution for CSS (white histogram) and GPS (shaded histogram) sources. The x-axis shows the logarithmic 5 GHz luminosity density. Credits: O'Dea & Baum (1997).

Part II

Cluster candidates around low luminosity radio galaxies at $z \sim 1-2$

Chapter 4

Introduction

In this Part II we study the Mpc-scale environments of $z \sim 1-2$ FR I radio galaxies. In detail, the main goals of this work are i) to search for high redshift clusters and groups using $z \sim 1-2$ FR I radio galaxies as beacons and ii) to test whether the great majority of FR I radio galaxies at $z \sim 1-2$ reside in dense Mpc-scale environments, as found at lower redshifts.

To achieve such goals we adopt a sample of radio galaxies originally built in Chiaberge et al. (2009, C09) and recently redefined in Castignani et al. (2014b) on the basis of radio power. The sample is introduced and studied in Chapter 5 (see also Castignani et al., 2014b).

In Chapter 6 we introduce the newly developed Poisson Probability Method (PPM, Castignani et al., 2014a) that we primarily introduced to achieve our goals. The PPM searches for dense Mpc-scale environments (i.e. galaxy clusters and groups) around a specific point in the sky (i.e. in our case the coordinates of the radio galaxy) adopting photometric redshifts and number counts of the galaxies in the field.

The PPM naturally arises as an effective mean field theory defined on the ensemble of the photometric redshift realizations of the galaxies in the field. A differential argument embedded in the PPM theory shows that the PPM partially overcomes the limitations deriving from low number-count statistics and shot-noise fluctuations. This is ultimately achieved through the use of a solid positional prior, i.e. in our case the coordinates of the FR I radio galaxies, and an accurate photometric redshift sampling. We stress that the PPM and its theory are key for the work described in this part and they are fundamental for our future work on high-z cluster search.

Therefore, in Chapter 7 we first test the PPM against simulations (Castignani et al., 2014a). Two different approaches are adopted. (1) We use two $z \sim 1$ X-ray detected cluster candidates and we shift them to higher redshift up to $z = 2$. (2) We simulate spherically symmetric clusters of different size and richness and we locate them at different redshifts (i.e., $z = 1.0$, 1.5, and 2.0). In both cases we test if the PPM is able to detect all the considered

(simulated) clusters.

Then, in Chapter 8 we successfully apply the PPM to search for cluster candidates in the fields of our FR I sample (see also Castignani et al., 2014b). For comparison, we also apply the Papovich (2008) method that was previously used in other work to search for high redshift $z \gtrsim 1.2$ cluster candidates (e.g. Galametz et al., 2012; Mayo et al., 2012). We also discuss the properties of the detected overdensities in terms of their significance, estimated redshift, location, richness, and size, as inferred from the PPM. A careful spectroscopic confirmation of the candidates is however required to have a fully reliable picture of the cluster properties.

We refer to Chapter 12 for the conclusions and future work related to the project described in the present Part II.

Before describing our work in detail in the following section we will introduce the specific problem of searching for high-z galaxy clusters. We will put particular emphasis on the role of the radio galaxies to address this specific problem. We refer to Chapter 3 for a general overview on the radio galaxies and their Mpc-scale environments.

4.1 An introduction to the problem

Clusters of galaxies are the most massive gravitationally bound large scale structures in the Universe. They form from gravitational collapse of matter concentrations induced by perturbations of the primordial density field (Peebles, 1993; Peacock, 1999). Galaxy clusters have been extensively studied to understand how large scale structures form and evolve during cosmic time, from galactic to cluster scales (see Kravtsov & Borgani, 2012, for a review).

Despite this, the properties of the cluster galaxy population and their changes with redshift in terms of galaxy morphologies, types, masses, colors (e.g. Bassett et al., 2013; McIntosh et al., 2014), and star formation content (e.g. Zeimann et al., 2012; Santos et al., 2013; Strazzullo et al., 2013; Gobat et al., 2013; Casasola et al., 2013; Brodwin et al., 2013; Zeimann et al., 2013; Alberts et al., 2013) are still debated, especially at redshifts $z \gtrsim 1.5$.

It is also unknown when the ICM virializes and starts emitting in X-rays through Bremsstrahlung radiation (see also Section 3.8.3) and upscattering the CMB through the Sunyaev - Zel'dovich (SZ) effect (Sunyaev & Zel'dovich, 1970, 1972). See Rosati et al. (2002) for a review. More in general, the formation history of large scale structures and the halo assembly history (e.g. Sheth & Tormen, 2004; Dalal et al., 2008; Adami et al., 2013) are not fully understood.

High redshift cluster counts are used to constrain cosmological parameters (e.g. Planck Collaboration XX, 2013), to test the validity of the ΛCDM scenario and quintessence models (Jee et al., 2011; Mortonson et al., 2011;

Benson et al., 2013). Cluster counts are strongly sensitive to the equation of state of the Universe, especially at $z \gtrsim 1$ (Mohr, 2005), when the Universe starts accelerating and the dark energy component starts becoming dominant. The SZ effect, weak lensing measurements (Rozo et al., 2010), X-ray scaling relations and data (Vikhlinin et al., 2009; Mantz et al., 2010) are used to evaluate the mass, the redshift of the clusters, and their mass function. Moreover, high redshift cluster samples might be used to test the (non-)Gaussianity of the primordial density field and to test alternative theories beyond General Relativity (see Allen et al., 2011; Weinberg et al., 2013, and references therein for a review).

Searching for high redshift $z \gtrsim 1$ galaxy clusters is therefore a fundamental issue of modern astrophysics to understand open problems of extragalactic astrophysics and cosmology from both observational and theoretical perspectives.

An increasing number of high redshift $z \gtrsim 1$ spectroscopic confirmations of cluster candidates have been obtained in the last years. To the best of our knowledge, there are in the literature only 12 spectroscopically confirmed $z \gtrsim 1.5$ clusters (Papovich et al., 2010; Fassbender et al., 2011; Nastasi et al., 2011; Santos et al., 2011; Gobat et al., 2011; Brodwin et al., 2011, 2012; Zeimann et al., 2012; Stanford et al., 2012; Muzzin et al., 2013; Newman et al., 2014; Yuan et al., 2014). Only some of them have estimated masses greater than 10^{14} $M_{\odot}$. In addition to them, Tanaka et al. (2013) spectroscopically confirmed a $z = 1.6$ X-ray emitting group, whose estimated mass is 3.2×10^{13} $M_{\odot}$. A $z \sim 1.7$ group associated with a $z \sim 8$ lensed background galaxy was found by Barone-Nugent et al. (2013).

Several methods use photometric and/or spectroscopic redshifts to search for high redshift overdensities (Eisenhardt et al., 2008; Knobel et al., 2009, 2012; Adami et al., 2010, 2011; George et al., 2011; Wen & Han, 2011; Jian et al., 2014). Similarly to the methods outlined above, they are generally less efficient at $z \gtrsim 1.5$. This is due to the difficulty of obtaining spectroscopic redshift information for a sufficient number of sources at $z > 1$, to the significant photometric redshift uncertainties, and to the small number density of objects.

In fact, typical 1-σ statistical photometric redshift uncertainties are $\sim$0.15 at redshifts $z = 1.5$, while the mean number of galaxies within a redshift bin $\Delta z = 0.3$ and a circle of 1 Mpc diameter is $\lesssim 9$ and $\lesssim 3$, at $z = 1.5$ and $z = 2.0$, respectively.

High redshift clusters have been searched for by using several other independent techniques; such as e.g. those that use X-ray emission (e.g. Cruddace et al., 2002; Böhringer et al., 2004; Henry et al., 2006; Šuhada et al., 2012) or the SZ effect (e.g. Planck Collaboration XXIX, 2013; Hasselfield et al., 2013; Reichardt et al., 2013).[1] However, such methods require a mini-

[1] Distortions of the CMB map due to the SZ effect are searched for and used as evidence

mum mass and are rapidly insensitive for detecting $z \gtrsim 1.2$ clusters (see e.g. the discussion in Zeimann et al., 2012).

It is commonly accepted that early-type passively evolving galaxies segregate within the cluster core and represent the majority among the cluster galaxy population, at least at redshifts $z \lesssim 1.4$ (e.g. Menci et al., 2008; Tozzi et al., 2013).

Various methods search for distant clusters taking advantage of the segregation of red objects in the cluster core. Such searches are commonly performed adopting either optical (Gladders & Yee, 2005) or infrared (Papovich, 2008) color selection criteria. They find a great number of cluster (candidates), even at $z \sim 2$ (e.g. Spitler et al., 2012; Yuan et al., 2014). However, all these methods seem to be less effective at redshifts $z \gtrsim 1.6$. Moreover, such methods require a significant presence of red galaxies. There might be a bias in excluding clusters with a significant amount of star forming galaxies or, at least, in selecting only those overdensities whose galaxies exhibit specific colors (Scoville et al., 2007b; George et al., 2011).

FR II radio galaxies have been extensively used for high redshift cluster searches (e.g. Rigby et al., 2014; Koyama et al., 2014). High redshift (i.e. $z \gtrsim 2$) high power radio galaxies are frequently hosted in Lyman-α emitting protoclusters (see also Sections 3.5 and 3.7, as well as Miley & De Breuck, 2008, for a review). Recently Galametz et al. (2012) and Wylezalek et al. (2013a) searched for Mpc-scale (proto)clusters around high redshift (i.e. $z \gtrsim 1.2$) high power radio galaxies using an IR color selection (Papovich, 2008).

FR I radio galaxies are intrinsically dim and are more difficult to find at high redshifts than the higher power FR IIs (see Section 3.5). This has so far limited the environmental study of the high redshift ($z \gtrsim 1$) radio galaxy population to the FR II class only (see Section 3.7).

However, due to the steepness of the luminosity function, FR I radio galaxies represent the great majority among the radio galaxy population. Furthermore, on the basis of the radio luminosity function, hints of strong evolution have been observationally suggested (Sadler et al., 2007; Donoso et al., 2009, see also Section 3.6). Furthermore, their comoving density is expected to reach a maximum around $z \sim 1.0-1.5$ followed by a slow declining at higher redshifts, according to some theoretical model (e.g. Massardi et al., 2010).

At variance with FR II radio galaxies or other types of AGNs, low-redshift FR Is are typically hosted by undisturbed ellipticals or giant ellipticals of cD type (Zirbel, 1996, see also Section 3.2), which are often associated with the Brightest Cluster Galaxies (BCGs, von der Linden et al., 2007). Furthermore, FR Is are preferentially found locally in dense environments (Hill & Lilly, 1991; Zirbel, 1997; Wing & Blanton, 2011). This suggests that

for the presence of galaxy clusters.

FR I radio galaxies could be more effective for high redshift cluster searches than FR IIs (see also Sections 3.7 and 3.8).

C09 derived the first sample of $z \sim 1-2$ FR Is within the Cosmic Evolution Survey (COSMOS) field (Scoville et al., 2007a). Chiaberge et al. (2010) suggested the presence of overdensities around three of their highest redshift sources. Based on galaxy number counts, the authors found that the Mpc-scale environments of these sources are 4σ denser than the mean COSMOS density. Tundo et al. (2012) searched for X-ray emission in the fields of the radio galaxies of the C09 sample. They took advantage of the Chandra COSMOS field (C-COSMOS). They did not find any evidence for clear diffuse X-ray emission from the surroundings of the radio galaxies. Their stacking analysis suggests that, if present, any X-ray emitting hot gas would have temperatures lower than ∼2-3 keV. Furthermore, Baldi et al. (2013) derived accurate photometric redshifts for each of the sources in the C09 sample.

Throughout this Part II we refer to the Mpc-scale overdensities as clusters, cluster candidates, and overdensities, with no distinction. However, we keep in mind that these large scale structures could show different properties and they might be virialized clusters or groups, as well as still forming clusters or protoclusters. We will refer to the sources in the C09 sample using also the ID number only instead of the complete name COSMOS-FR I nnn.

Chapter 5

FR Is at $z \sim 1-2$ in COSMOS

As outlined in Chapter 4 one of the main goals of this work is to search for high redshift clusters and groups using $z \sim 1-2$ FR I radio galaxies as beacons. In this Chapter we will focus on the sample of FR Is drawn from the original C09 sample and adopted in this work to achieve such a goal. In Sections 5.1 and 5.2 we introduce the FR I sample and we redefine it on the basis of the radio power. This is done by estimating the luminosity of each radio galaxy in the sample on the basis of their most accurate photometric redshifts available to date (Baldi et al., 2013), and a careful revision of all the adopted radio fluxes. By taking advantage of the careful sample selection, in Section 5.3 we also estimate the space density of 1.4 GHz sources at $z \sim 1$.

5.1 The FR I sample

The COSMOS survey is a $1^{\circ}.4 \times 1^{\circ}.4$ equatorial survey that includes multiwavelength imaging and spectroscopy from the radio to the X-ray band. COSMOS is also entirely covered by the Very Large Array Faint Images of the Radio Sky at Twenty-centimeters (VLA FIRST) survey at 1.4 GHz (Becker et al., 1995) and it includes HST observations (Koekemoer et al., 2007).

Due to its high sensitivity, angular resolution, and wide spectral coverage, COSMOS is suitable to study large scale structures at high redshifts, with unprecedented accuracy and low cosmic variance.

Hereafter in this work we will refer to Low (High) Luminosity Radio Galaxies, i.e. LLRGs (HLRGs). The LLRGs will denote those radio galaxies with radio power typical of FR Is, while the HLRGs will denote radio galaxies with radio powers generally higher than the FR I/FR II radio power divide

($L_{1.4\ \mathrm{GHz}} \sim 4 \times 10^{32}$ erg s^{-1} Hz^{-1}, Fanaroff & Riley, 1974).[1] This does not imply that the LLRGs are FR Is and the HLRGs are FR IIs, especially at high redshift. This is because the HLRGs of our sample have radio powers only slightly higher than those typical of local FR Is. In fact, all the sources in our sample (including the HLRGs) have radio powers about ~ 2 orders of magnitude lower than those typical of high-z radio galaxies ($z \gtrsim 2$, Miley & De Breuck, 2008). Furthermore, both the LLRGs and HLRGs might include radio galaxies of transitional type. Therefore, despite the radio galaxies in our sample do not clearly exhibit all the properties typical of local FR Is we will refer to both the LLRGs and the HLRGs as FR I radio galaxies, except where otherwise specified.

C09 searched for FR Is candidates at $1 \lesssim z \lesssim 2$ in the COSMOS field, using multiwavelength selection criteria. Here, we briefly summarize the main steps of the procedure, while more details are given in C09.

The two basic assumptions are: (i) the FR I/FR II divide in radio power per unit frequency (set at $L_{1.4\ \mathrm{GHz}} \sim 4 \times 10^{32}$ erg s^{-1} Hz^{-1}) does not change with redshift; (ii) the magnitudes and colors of the FR I hosts at $1 < z < 2$ are similar to those of FR IIs within the same redshift bin, as in the case of local radio galaxies (e.g. Zirbel, 1996; Donzelli et al., 2007). Note that the photometric redshifts are affected by great uncertainties, so they do not constitute a selection criterion. In the following we summarize the source selection procedure adopted by C09:

1. FIRST radio sources in the COSMOS field whose observed 1.4 GHz fluxes are in the range expected for FR Is at $1 < z < 2$ ($1 < F_{1.4\ \mathrm{GHz}} < 13$ mJy) are considered.

2. Sources with FR II radio morphology, i.e. showing clear edge-brightened radio structures, are rejected.

3. Those with bright optical counterparts ($\mathrm{m_{i,Vega}} < 21$) are then excluded since they are likely lower redshift galaxies with radio emission produced by e.g. starbursts. Note also that this constraint assumes that the magnitude of the FR Is hosts are similar to those of FR IIs.

4. u-band dropouts are rejected as they are likely Lyman-break galaxies at $z > 2.5$ (Giavalisco, 2002).

The selection of the radio sources is mainly based on a flux requirement, criterion (1). The following ones (2, 3, 4) are used only to discard spurious sources from the sample.

The source COSMOS-FR I 236, tentatively classified in C09 as a QSO, was later identified with a known QSO at the spectroscopic redshift $z = 2.132$ (Prescott et al., 2006). Similarly to what has been been done for

[1] See Sections 5.2.4 and 5.2.5 for definitions of the two classes, concerning our sample.

all sources in our sample (see Sections 5.2.4 and 5.2.5), we estimate that the total radio power of this source is 1.96×10^{33} erg s^{-1} Hz^{-1}, based on its redshift and FIRST radio flux of 7.10 mJy (see Baldi et al., 2013). See Section 5.2.3 for the assumptions adopted in estimating the radio luminosity. Therefore, since this is typical of high power FR IIs and radio loud QSOs, we do not consider this source in this work. Steepening the radio spectrum, i.e. increasing the value of the spectral index α, would increase the estimated radio power, reinforcing our conclusions. Hence, our sample comprises 36 sources. Note that the sample, as for any flux limited one, is affected by the well-known Malmquist bias and thus includes higher/lower power radio sources at high/low redshifts (see Section 5.2.4, 5.2.5).

As one of the main goals of this work is to search for clusters of galaxies in the fields of the low power radio galaxies of the C09 catalog, in the following section we redefine the sample by selecting only *bona fide* low luminosity objects, based on the latest photometric (or spectroscopic, when available) redshift estimates. While we cannot exclude that the remaining (high power) sources are associated with a dense environment, we will consider them separately.

Hereinafter, we will refer to our sources using the ID number only, as opposed to the complete name COSMOS-FR I nnn.

5.2 Sample redefinition

The aim of this section is to derive a reliable sample of low luminosity radio galaxies (LLRGs) that, based on the information available to date, have $L_{1.4\ \mathrm{GHz}}$ lower than the fiducial separation between FR Is and FR IIs. In order to do so we require robust measurements of the total radio fluxes, accurate photometric redshifts (in absence of firm spectroscopic redshifts) and assumptions on the K-correction.

5.2.1 Radio fluxes

As discussed above, the C09 sample was selected using the radio fluxes from the FIRST survey (Becker et al., 1995) which was performed by using the VLA B-configuration at 1.4 GHz and it covers 10,000 square degrees of the North and South Galactic Caps. The COSMOS field entirely resides within the area mapped by FIRST. Post-pipeline radio maps have a resolution of $\sim$ 5 arcsec. The detection limit of the FIRST catalog is $\sim$ 1 mJy with a typical rms of 0.15 mJy. When we make use of the FIRST survey, we adopt the flux densities from the catalog as of October 10th, 2011. However, the FIRST radio maps may be missing a substantial fraction of any extended low surface brightness radio emission from the lobes of our radio sources, which are close to the detection limit. This is particularly important because of the

relatively high angular resolution provided by the used VLA configuration, which is more suitable for detecting compact or unresolved radio sources.

While being slightly shallower than FIRST, the NRAO VLA Sky Survey (NVSS) survey (Condon et al., 1998) may be more suitable for our purposes, since it was obtained by using the VLA-D configuration at 1.4 GHz. The angular resolution of the NVSS radio maps is 45 arcsec (FWHM). Thus, it is more suitable for detecting extended emission of the sources in our sample. Therefore, in order to derive the total radio luminosity of our sources, we use the NVSS fluxes and upper limits (as of October 10th, 2011), when possible. In the NVSS catalog[2], at the coordinates of the C09 objects, we find 26 of the 36 sources.

While the FIRST survey is complete down to a flux of 1 mJy, the completeness of the NVSS catalog is only 50% at its formal limit of 2.5 mJy, while rises rapidly to 99% at 3.4 mJy (Condon et al., 1998). Thus, the drawbacks of using NVSS sources are as follows: i) sources with total radio flux < 3.4 mJy might not be included. ii) The identification of the NVSS counterpart of each source is not trivial. Due to the lower angular resolution rms uncertainties are about 7 arcsec at the NVSS limit, as affected by confusion. Furthermore, the extended radio morphology of many of the radio sources might be complex. Therefore, since the NVSS is more sensitive to the extended emission than FIRST, the centroid of the FIRST source could not coincide with that in the NVSS map. Also note that, even if the limit of the NVSS catalog is set at 2.5 mJy, some of our fainter sources are detected in the radio maps.

To overcome these inconveniences we use FIRST (Becker et al., 1995) and VLA COSMOS (Schinnerer et al, 2007). FIRST has a flux density threshold of 1 mJy and a positional accuracy of $\lesssim$1 arcsec for radio pointlike sources. VLA COSMOS has a angular resolution of 1.5"$\times$1.4" and a sensitivity limit of 45 μJy/beam. It is therefore deeper and with higher angular resolution than FIRST. For the majority of the objects it is straightforward to identify the radio sources in the above surveys. The few cases in which the identification is problematic are discussed in the following.

For these cases we consider the VLA COSMOS maps to clearly identify the radio sources, as described in the following for source 05. In Figure 5.1 we show the NVSS radio map of the field around the object 05. Visual inspection reveals the presence of a complex radio morphology, which might be (erroneously) identified with either the NAT (e.g. NGC 1265, O'Dea & Owen, 1986) or the WAT (e.g. 3C465, Venturi et al., 1995) radio morphology. The NVSS catalog reports sources at distance of $\sim$ 60 and $\sim$ 67 arcsec to the SW and SE from the VLA-COSMOS coordinates of the source 05, and fluxes of 3.4 and 3.7 mJy, respectively. A third radio source located at the position of 05 is visible in the map, but it is below the threshold of the NVSS

[2] `http://www.cv.nrao.edu/nvss/`

catalog.

In Figure 5.2 (left) we show the same field as seen with VLA-COSMOS, at much higher angular resolution. Such image shows the presence of a number of point-like sources and some extended emission. In the right panel we report the HST image of the same field, taken with the Advanced Camera for Surveys (ACS) and the F814W filter, as part of the COSMOS survey. The radio contours from VLA-COSMOS are over-plotted in yellow. It is clear that the radio sources seen in VLA-COSMOS overlap with foreground galaxies. This generates the complex extended emission seen in the NVSS map. By using higher resolution radio data and the optical image, we are able to overcome the confusion problem in the NVSS map. The NVSS catalog misses our source and detects only the two unrelated brighter radio emitting regions.

Similarly, other sources have extended radio morphology, as clear from visual inspection of the NVSS maps. The angular separation between the coordinates reported in the NVSS catalog and those obtained by using VLA-COSMOS are about $\sim$15 arcsec. This is the case of sources 26, 52, 202, 224, and 228, where such angular separations are 15.37, 16.4, 12.82, 12.43, and 18.52 arcsec, respectively. In Figure 5.3 we report the NVSS fields of 26 and 224, as examples. These sources show a radio morphology similar to that of 05. However, a bright source is clearly present in each of these two fields, very close to the radio galaxy. They are merged in the NVSS map in a single structure due to the low NVSS angular resolution.

We consider the radio NVSS maps of all of the ten sources that are not present in the NVSS catalog. Among them there are the sources 27 and 66 that will be rejected from the sample on the basis of their spectroscopic redshift (see Section 5.2.2). Therefore, they are not considered for the present analysis. We visually inspect the maps of the remaining eight sources and search for the presence of radio contours centered around the position of the radio source. For five out of the eight we find evidence of a radio source located at the coordinates of the radio galaxy. This is the case of sources 11, 20, 22, 27, and 39, where the radio contours are consistent with a radio flux close to the NVSS formal limit of 2.5 mJy. In Figure 5.4 we report the fields of 22 and 39, as examples. Being very close or below the formal completeness limit, we expect that possible systematics might occur in the flux measurements. Therefore we adopt a fiducial 2.5 mJy upper limit for all of the eight sources which are not included in the NVSS catalog.

The fiducial FIRST and NVSS flux uncertainties for the sources in our sample are within $\sim$0.1-0.2 mJy and $\sim$0.4-0.6 mJy, respectively. However, we prefer not to report the flux uncertainty associated with each source. This is because we are considering fluxes down to the completeness limit of both the FIRST and the NVSS surveys and, therefore, the flux uncertainties might be underestimated.

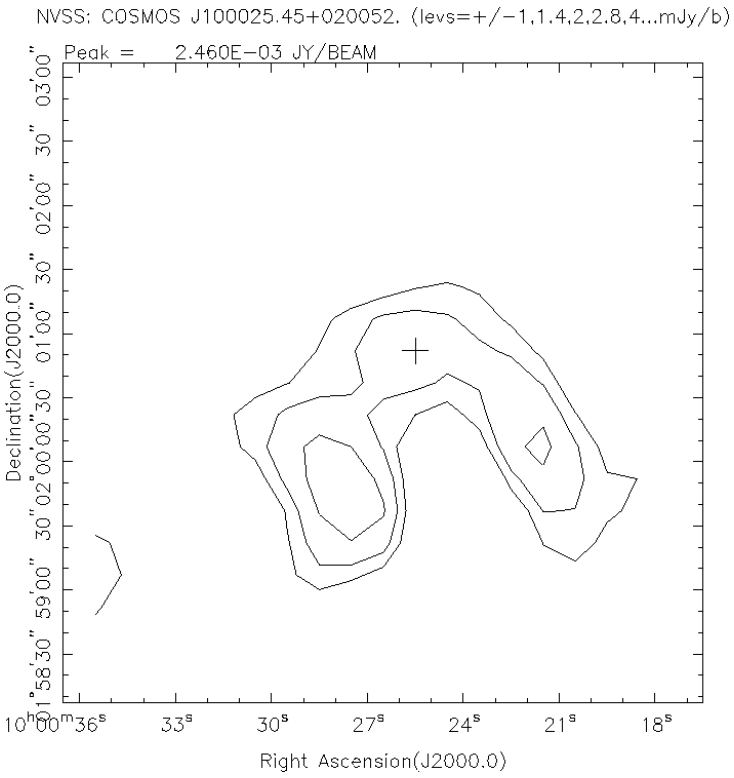

Figure 5.1: NVSS map, field of 05. The cross marks the coordinates of the radio source.

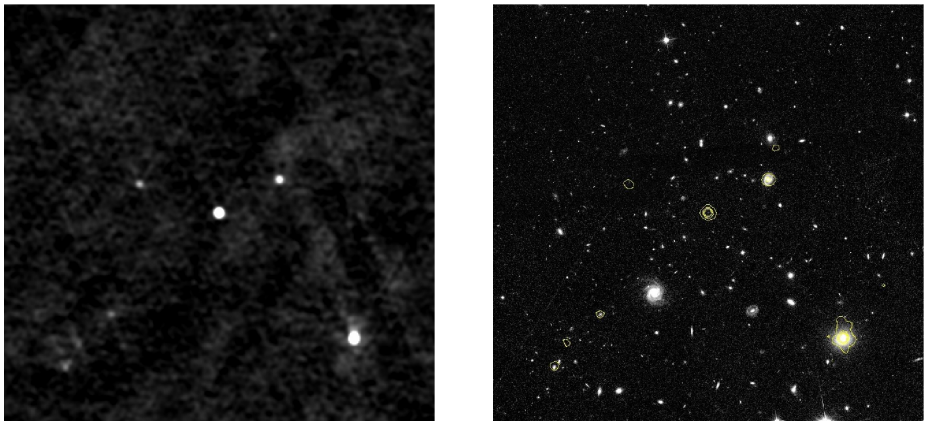

Figure 5.2: Field ($3' \times 3'$ dimensions) of 05. Left: VLA-COSMOS map. Right: HST image taken from ACS and the F814W filter. Yellow contours are from VLA-COSMOS. The angular scale is the same for both of the panels.

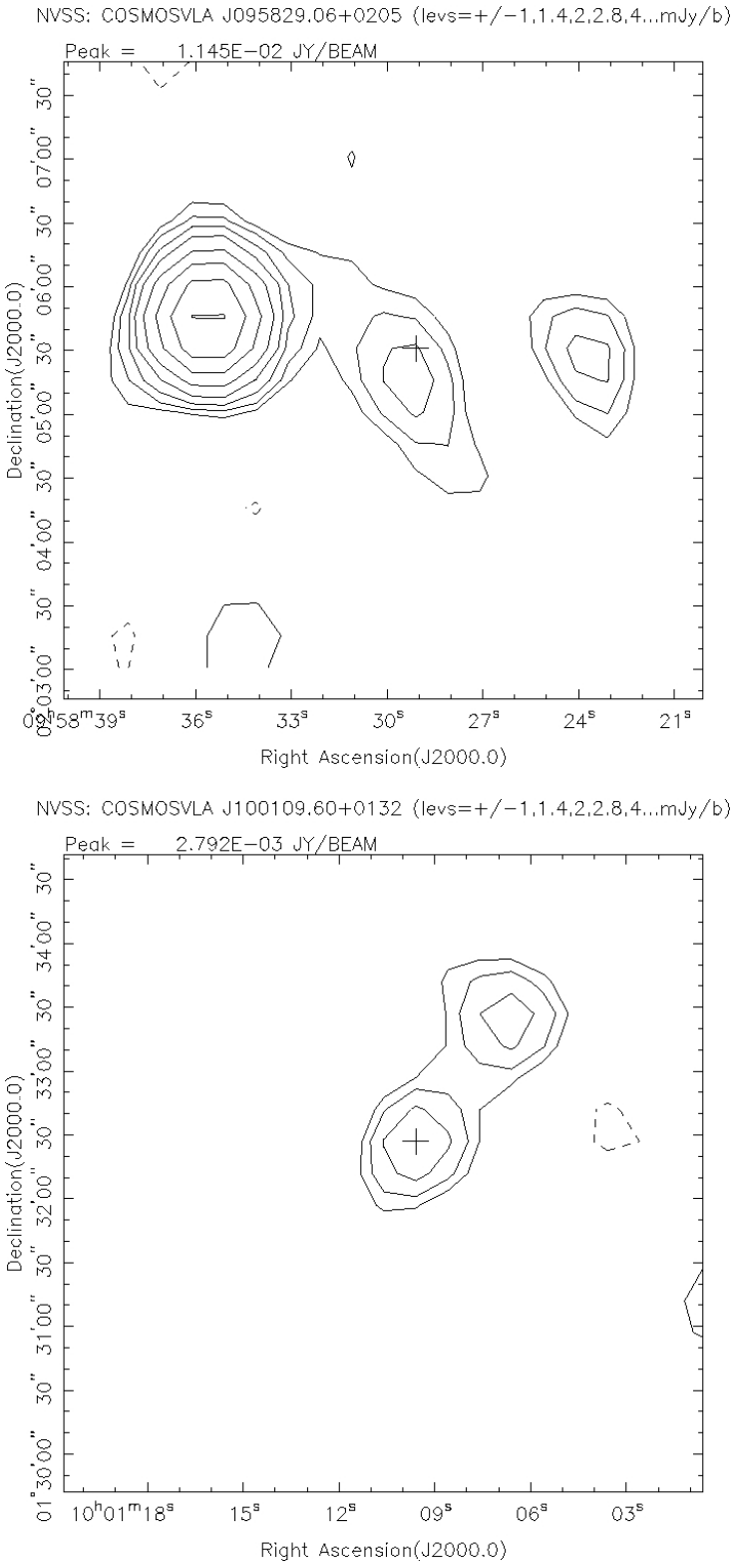

Figure 5.3: NVSS maps, the cross marks the coordinates of the radio source. Top: field of 26. Bottom: field of 224.

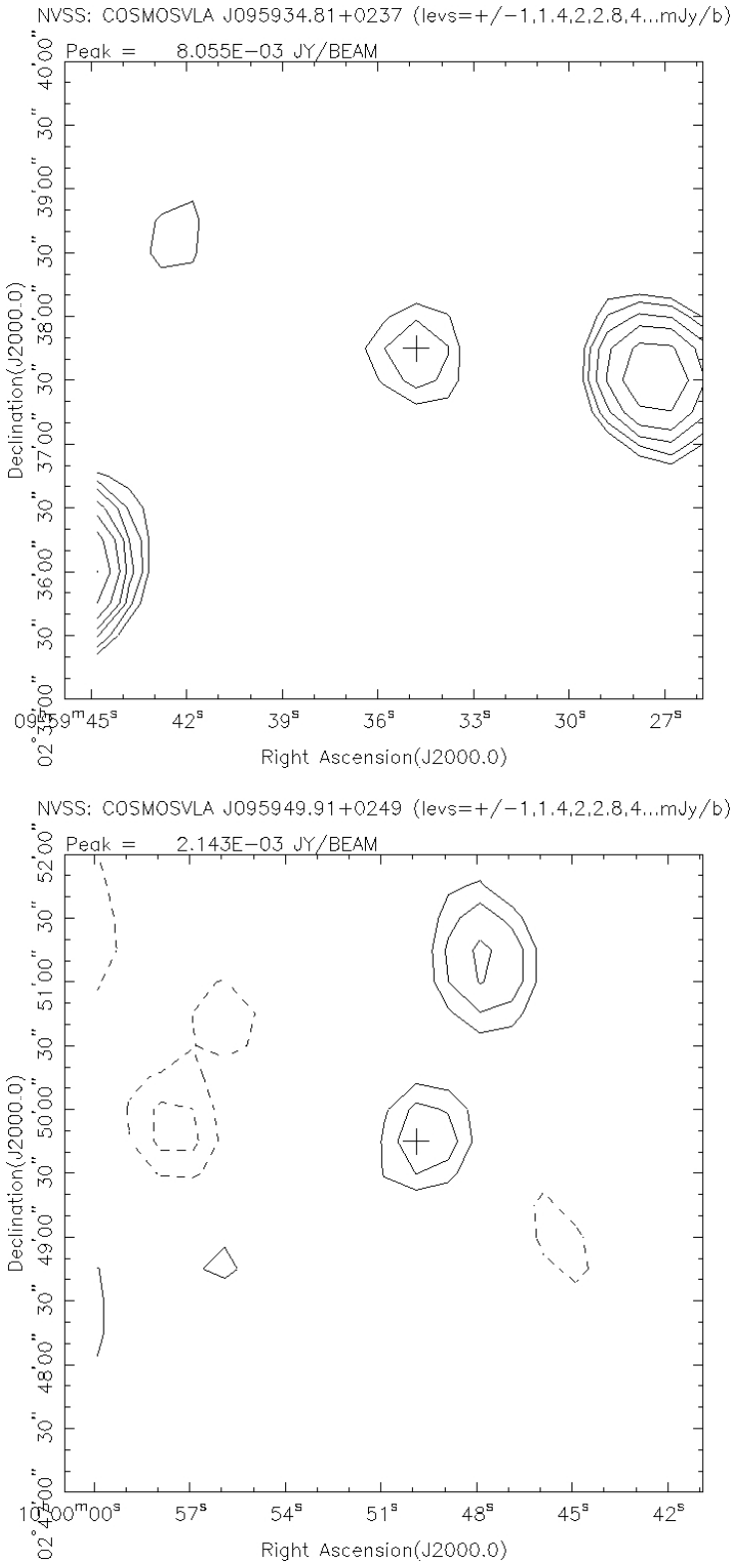

Figure 5.4: NVSS maps, the cross marks the coordinates of the radio source. Top: field of 22. Bottom: field of 39. Examples of sources not included in the NVSS catalog, but clearly present in the NVSS maps. Their 1.4 GHz fluxes are close to the NVSS 2.5 mJy limit.

5.2.2 Redshifts

We adopt accurate photometric redshifts derived by Baldi et al. (2013, B13) through a careful analysis of the spectral energy distribution (SED) of the host galaxies. As mentioned in Section 5.1, we adopt the photometric redshifts derived in B13, that specifically focused on the radio galaxy sample considered here. These photometric redshifts have a great advantage with respect to those in Mobasher et al. (2007) and Ilbert et al. (2009, I09), which were automatically derived by using the COSMOS photometric catalogs.

I09 estimated photometric redshifts by using the photometric data points from 30 bands for those sources with $I < 25$ in the deep Subaru area of the COSMOS field (Taniguchi et al., 2007). B13 carefully identified the optical counterparts of the radio sources in all of the photometric bands. The authors discovered that, in a few cases, sources in different bands were misidentified in the COSMOS source list, therefore leading to erroneous photometric redshift estimates. B13 also performed a more refined SED modeling, with the inclusion of two stellar populations. At variance with the I09 catalog, B13 considered only broad band photometric data and excluded narrow and medium band data, which can be strongly contaminated by emission lines that are not included in the stellar templates.

We also search for the spectroscopic redshift of our sources in the zCOSMOS-bright (Lilly et al., 2007) and MAGELLAN (Trump et al., 2007) catalogs. Only 7 out of the 36 sources in our sample are found.

In agreement with B13 we do not use the spectroscopic redshift for object 25 (not included in the sample of the above mentioned 7 sources). This is because of its clear misidentification in the MAGELLAN catalog (see Section 6.1 in B13). Therefore, for the great majority of the sources we have to rely on photometric redshifts.

The redshifts of three (namely 27, 52, and 66) out of the 7 sources for which spectroscopic redshifts are available are significantly outside the $z \sim 1-2$ range of C09 selection. Therefore we exclude them from the sample. Redshifts $z = 0.2847$ and $z = 0.7417$ are reported in the MAGELLAN catalog for the sources 27 and 52, respectively. The redshifts reported for source 66 in the MAGELLAN and the zCOSMOS-bright catalog are consistent with each other and equal to $z = 0.6838$ and $z = 0.6803$, respectively. Searching for cluster candidates at intermediate or low redshifts (i.e. $z \lesssim 0.8$) is not the aim of this project. Therefore, we naturally reject the sources 27, 52, and 66, that are all located at $z \leq 0.75$. [3] We also exclude the source 07 from the sample because it is a peculiar radio source (as suggested in Baldi et al., 2013). It might be a FR II radio galaxy at significant high redshift. Conversely, we do not exclude those sources (e.g. 28 and 32) that have a

[3]The remaining four sources with spectroscopic redshift information are the sources 01, 16, 31, and 258. For all of them the spectroscopic redshifts agree with the photometric redshifts from B13, within the uncertainties.

photometric redshift formally above $z \sim 2$. This is because, even if they are at redshifts well outside the fiducial range of our interest, they were not rejected during the C09 selection. Therefore, they could comprise similar properties to those of the other galaxies in our sample. Furthermore, since such sources populate the high redshift tail of our sample, their Mpc-scale environments are still worth to investigate (see also Section 8.9 for further discussion about source 28).

Summarizing, with respect to the original list given in C09, we reject sources 07, 27, 52, and 66 (in addition to 236, the QSO we already discussed above). The sample is thus reduced to 32 objects.

5.2.3 Rest frame radio luminosities

In agreement with C09 we assume that the radio spectrum in the region around 1.4 GHz is a power-law of the form $F_\nu \propto \nu_o^{-\alpha}$, where F_ν is the radio flux density at the observed frequency ν_o, and α is the spectral index assumed to be $\alpha = 0.8$, accordingly to C09. Such an assumption requires that the flat ($\alpha \sim 0$) radio emission of the core is negligible with respect to the extended emission (jets and lobes) in the considered spectral range. This is formally correct at the lowest radio frequencies, but it is less certain at higher frequencies. However, since the radio data do not allow us to separate the emission of our sources into different components, we assume that the measured flux at 1.4 GHz is dominated by the extended emission. If $\alpha = 0.3$ instead of 0.8, the luminosity would increase by only a factor of < 1.8, for the worst case of a source at $z = 2$.

Thus the isotropic rest frame 1.4 GHz luminosity density is given by:

$$L_{1.4\ \mathrm{GHz}} = 4\pi F_{1.4\ \mathrm{GHz}} D_L(z)^2\,(1+z)^{\alpha-1}\,, \tag{5.1}$$

where $F_{1.4\ \mathrm{GHz}}$ is the observed flux density at 1.4 GHz, D_L is the luminosity distance.

5.2.4 The Low Luminosity Radio Galaxy subsample

In Figure 5.5 (top panel) we report the luminosity versus redshift scatter-plot. The lower/upper thick black lines in the plot are the FIRST sample selection lower/upper boundaries adopted in C09 (1.0 mJy and 13.0 mJy, respectively). Since NVSS fluxes are in general higher than FIRST fluxes, we expect all the sources to lie above the lower line.

Since we are interested in searching for clusters around FR Is, we consider the 1.4 GHz luminosity intervals spanned for each source, within the redshift uncertainties, for an assigned 1.4 GHz radio flux.

Therefore, we conservatively select only those sources whose 1.4 GHz luminosity intervals lie entirely below the FR I/FR II radio luminosity divide of 4×10^{32} erg s^{-1} Hz^{-1}. According to this criterion we select 21 *bona fide*

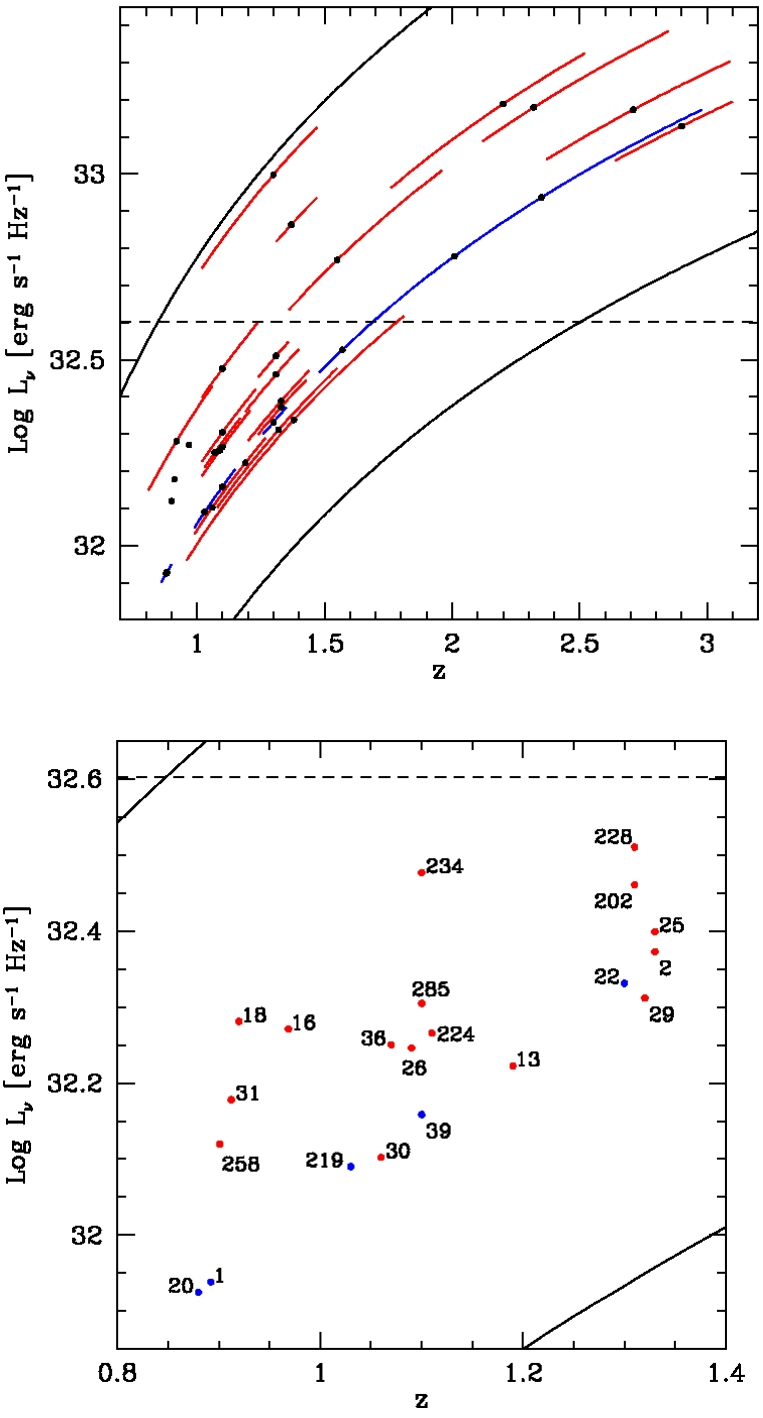

Figure 5.5: Top: Luminosity vs redshift scatterplot. Red lines correspond to sources with NVSS counterpart and fluxes. Blue lines correspond to upper limits at 2.5 mJy flux for the sources with no NVSS flux. Solid black lines: FIRST cut at 1mJy, 13mJy; The blue and the red lines indicate the uncertainties on the photometric redshift. The x- and y-values of the dots are the redshift and the luminosity of each source, respectively. Dots that are not associated with lines show the objects with spectroscopic redshifts. Horizontal dashed line: FR I/FR II luminosity divide, assumed to be constant with redshift. Bottom: LLRGs only. Color legend is the same as for the top panel. Each dot represents a source, identified by the corresponding ID number.

LLRGs, whose redshifts span the range z = 0.88-1.33 and have radio luminosities between $L_{1.4\ \mathrm{GHz}} = (0.84\text{-}3.24)\times10^{32}$ erg s^{-1} Hz^{-1}. In Figure 5.5 (bottom panel) we plot the scatterplot focused on the LLRGs only. The median redshift and 1.4 GHz luminosity of the LLRGs are $z_{\mathrm{median}} = 1.1$ and $L_{1.4\ \mathrm{GHz,\ median}} = 1.84 \times 10^{32}$ erg s^{-1} Hz^{-1}, respectively. For comparison, radio galaxies of similar power, selected within the 3C catalog, span a much smaller redshift range. Chiaberge et al. (1999) report a range $z = 0.0037 - 0.29$ and a median value $z = 0.03$ for their sample of 33 FR Is.

The LLRGs span a limited range of luminosity and slightly broader range of redshift than the FR Is in the Chiaberge et al. (1999) sample. However, because of the steepness of the RLF, most of the LLRGs are at $z \sim$1.

Being at relatively low redshifts, the LLRGs and their Mpc-scale environment can be studied in greater detail than the whole sample of FR I candidates considered in this work. This is mainly because COSMOS field number densities are much higher and statistical photometric redshift uncertainties are smaller than at higher redshifts (Ilbert et al., 2009). Furthermore, spectroscopic redshift information is available for some of the LLRGs only and photometric redshifts from B13 are more accurate for the LLRGs than for the HLRGs, being the latter, on average, at higher redshifts.

Therefore we separate the LLRGs from the remaining sources, that are generally at higher luminosities and redshifts than the HLRGs. In particular, the photometric redshifts of the LLRGs are better constrained, since the typical statistical uncertainty dramatically increases above $z \sim 1.3$ (see e.g. Figure 9 in I09) and because all of the sources in our sample with spectroscopic redshifts belong to the LLRG class.

5.2.5 The High Luminosity Radio Galaxy subsample

We consider in this section the remaining sources of the sample, i.e. the HLRGs, that do not belong to the LLRG subclass. Note that the radio morphology of both the LLRGs and the HLRGs is not of FR II type. In fact, sources with a clear FR II morphology have been rejected as part of the original sample selection in C09. Furthermore, the cosmological evolution of the FR I/FR II radio divide is still unknown, i.e. high-z FR I sources might have higher radio power than those of local FR Is, as suggested by Heywood et al. (2007).

This makes the nature of these HLRGs very unclear and suggestive to investigate. In the following, we consider the HLRGs separately from the rest of the sample (i.e. the LLRGs) in order to avoid any bias due to possible differences in the Mpc-scale environments of low and high luminosity sources.

We find 11 HLRGs. Their redshifts and radio luminosities span the intervals $z = 1.30-2.90$ and $L_{1.4\ \mathrm{GHz}} = (2.18-15.44)\times10^{32}$ erg s^{-1} Hz^{-1}, respectively. The median redshift and luminosity are $z_{\mathrm{median}} = 2.01$, $L_{1.4\ \mathrm{GHz,\ median}} = 8.64 \times 10^{32}$ erg s^{-1} Hz^{-1}, respectively.

The Low Luminosity Radio Galaxy subsample

ID	RA [deg]	DEC [deg]	redshift	FIRST flux [mJy]	NVSS flux [mJy]	$L_{1.4\ \mathrm{GHz}}$ [10^{32} erg s^{-1} Hz^{-1}]	radio morph.
COSMOS FR I 01	150.20744	2.2818749	0.8823^{a}	1.06	—	0.85	c
			0.8827^{b}				
COSMOS FR I 02	150.46751	2.7598829	$1.33\pm^{0.10}_{0.09}$	2.25	2.6	2.36	e
COSMOS FR I 13	149.97784	2.5042069	$1.19\pm^{0.08}_{0.11}$	1.50	2.4	1.67	c
COSMOS FR I 16	150.53772	2.2673550	0.9687^{a}	5.70	4.4	1.87	u
COSMOS FR I 18	149.69325	2.2674670	$0.92\pm^{0.14}_{0.11}$	4.39	5.1	1.91	e
COSMOS FR I 20	149.83209	2.5695460	$0.88\pm^{0.02}_{0.02}$	1.33	—	0.84	e
COSMOS FR I 22	149.89508	2.6292144	$1.30\pm^{0.05}_{0.04}$	2.74	—	2.14	c
COSMOS FR I 25	150.45673	2.5597000	$1.33\pm^{0.11}_{0.13}$	2.18	2.7	2.45	c
COSMOS FR I 26	149.62114	2.0919881	$1.09\pm^{0.12}_{0.07}$	1.88	3.2	1.80	e
COSMOS FR I 29	149.64587	1.9529760	$1.32\pm^{0.23}_{0.24}$	2.13	2.3	2.05	c
COSMOS FR I 30	149.61542	1.9910541	$1.06\pm^{0.11}_{0.07}$	1.26	2.4	1.27	c
COSMOS FR I 31	149.61916	1.9163600	0.9123^{a}	3.71	4.1	1.51	c
			0.9132^{b}				
COSMOS FR I 36	150.55662	1.7913361	$1.07\pm^{0.10}_{0.04}$	3.19	3.3	1.78	u
COSMOS FR I 39	149.95804	2.8288901	$1.10\pm^{0.05}_{0.05}$	1.37	—	1.44	c
COSMOS FR I 202	149.99506	1.6324950	$1.31\pm^{0.09}_{0.12}$	1.08	3.3	2.89	e
COSMOS FR I 219	150.06444	2.8754051	$1.03\pm^{0.02}_{0.04}$	1.85	—	1.23	c
COSMOS FR I 224	150.28999	1.5408180	$1.10\pm^{0.10}_{0.04}$	3.31	3.2	1.84	e
COSMOS FR I 228	149.49455	2.5052481	$1.31\pm^{0.05}_{0.07}$	2.04	3.7	3.24	c
COSMOS FR I 234	150.78925	2.4539680	$1.10\pm^{0.14}_{0.08}$	4.43	5.2	3.00	e
COSMOS FR I 258	149.55934	1.6310670	0.9009^{b}	2.24	3.7	1.32	c
COSMOS FR I 285	150.72131	1.5823840	$1.10\pm^{0.13}_{0.08}$	2.95	3.5	2.02	e

The High Luminosity Radio Galaxy subsample

ID	RA [deg]	DEC [deg]	redshift	FIRST flux [mJy]	NVSS flux [mJy]	$L_{1.4\ \mathrm{GHz}}$ [10^{32} erg s^{-1} Hz^{-1}]	radio morph.
COSMOS FR I 03	150.00253	2.2586310	$2.20\pm^{0.32}_{0.44}$	4.21	5.2	15.44	u
COSMOS FR I 04	149.99153	2.3027799	$1.37\pm^{0.10}_{0.06}$	5.99	7.5	7.30	e
COSMOS FR I 05	150.10612	2.0144780	$2.01\pm^{0.22}_{0.35}$	1.30	—	6.01	c
COSMOS FR I 11	150.07816	1.8985500	$1.57\pm^{0.14}_{0.09}$	1.13	—	3.36	c
COSMOS FR I 28	149.60064	2.0918673	$2.90\pm^{0.20}_{0.26}$	1.77	2.4	13.46	c
COSMOS FR I 32	149.66830	1.8379777	$2.71\pm^{0.38}_{0.34}$	1.39	3.1	14.88	c
COSMOS FR I 34	150.56023	2.5861051	$1.55\pm^{0.41}_{0.19}$	5.25	4.5	5.87	u
COSMOS FR I 37	150.74336	2.1705379	$1.38\pm^{0.43}_{0.42}$	1.87	2.2	2.18	c
COSMOS FR I 38	150.53645	2.6842549	$1.30\pm^{0.17}_{0.28}$	10.01	11.6	9.95	c
COSMOS FR I 70	150.61987	2.2894360	$2.32\pm^{0.53}_{0.20}$	3.90	4.5	15.10	c
COSMOS FR I 226	150.43864	1.5934480	$2.35\pm^{0.63}_{0.31}$	1.25	—	8.64	c

Table 5.1: Sample Properties. Column description: (1) source ID number; (2) RAJ2000 [degree]; (3) DECJ2000 [degree]; (4) Redshifts. Photometric from B13 and spectroscopic from either MAGELLAN (Trump et al., 2007) or zCOSMOS-bright (Lilly et al., 2007) catalogs are denoted with the superscript a or b, respectively. The spectroscopic redshifts are separately reported in two consecutive rows for those sources where multiple spectroscopic redshifts are available; (5) 1.4 GHz FIRST fluxes [mJy]; (6) 1.4 GHz NVSS fluxes [mJy]. We assume 2.5 mJy flux (reported as — in the table) for those sources that are not in the NVSS catalog; (7) 1.4 GHz radio power [10^{32} erg s^{-1} Hz^{-1}]. NVSS flux or 2.5 mJy upper limit adopted. Radio spectrum assumed: $L_\nu \propto \nu^{-\alpha}$, $\alpha = 0.8$; (8) radio morphology as in C09. The following legend is adopted: compact (c), extended (e), unresolved (u).

5.2.6 Statistical properties

In Table 5.1 we summarize the properties of the sources in our sample, separating them between the LLRGs (top) and the HLRGs (bottom). We refer to C09 and their Table 1 for more details about the sample. In Figure 5.6 we report the radio power distribution for our sample obtained by considering NVSS fluxes (top panel) and FIRST fluxes (bottom panel). Limited to this section only, we consider also the FIRST instead of the NVSS radio powers only. This is because FIRST fluxes are available for all the sources in our sample, while this is not the case for NVSS.

The averages of the logarithmic FIRST and NVSS luminosities of the sources in our sample are $\log[L_{1.4\ \mathrm{GHz,\ FIRST}}/(\mathrm{erg\ s^{-1}\ Hz^{-1}})] = 32.32 \pm 0.41$ and $\log[L_{1.4\ \mathrm{GHz,\ NVSS}}/(\mathrm{erg\ s^{-1}\ Hz^{-1}})] = 32.47 \pm 0.37$, respectively, where the reported uncertainties are the rms dispersions around the averages. This shows that the sources in our sample have, on average, 1.4 GHz radio luminosities slightly below the FR I/FR II radio luminosity divide and that this result is independent of the two different sets of radio fluxes adopted (i.e. FIRST or NVSS). However, the logarithmic difference between the FIRST and NVSS luminosities for the sources in our sample is, on average, $\langle \log(L_{1.4\ \mathrm{GHz,\ NVSS}}/L_{1.4\ \mathrm{GHz,\ FIRST}}) \rangle = 0.15$ and the rms dispersion around the average is 0.14 dex. This can be translated into the fact that, on average, the 1.4 GHz luminosities estimated from the NVSS fluxes are 1.5 times than those estimated by adopting FIRST fluxes.

Therefore, NVSS are slightly higher than FIRST luminosities for the FR Is in our sample. This suggests that the NVSS survey is more sensitive to the extended emission and it might be more effective than FIRST in order to estimate the true radio luminosity of our sources.

We test the presence of bimodality in both the FIRST and NVSS radio power distributions by applying the KMM algorithm described in Ashman et al. (1994). The KMM test assumes that the considered distributions are Gaussian functions or a sum of them. We find that the luminosity distribution is strongly inconsistent with being unimodal at 99.75% confidence level (i.e. more than 3σ) if the NVSS fluxes (or upper limits) are adopted. If we adopt the FIRST fluxes for those sources for which we have the NVSS upper limits we find that the unimodality is rejected at 70.10% confidence level (i.e. just above 1-σ). The unimodality is rejected at a level less than 1-σ (i.e. 63.88%) if the FIRST fluxes are instead considered for all sources.

The presence of bimodality in the NVSS radio power distribution of the FR Is in our sample suggests that the HLRGs might be drawn from a different parent population. However, the bimodality disappears when the FIRST fluxes are included. Furthermore, the Gaussian approximation is a strong assumption and it might not correspond to our case. Therefore, even if we find evidence of bimodality in the radio power distribution, we cannot draw firm conclusions.

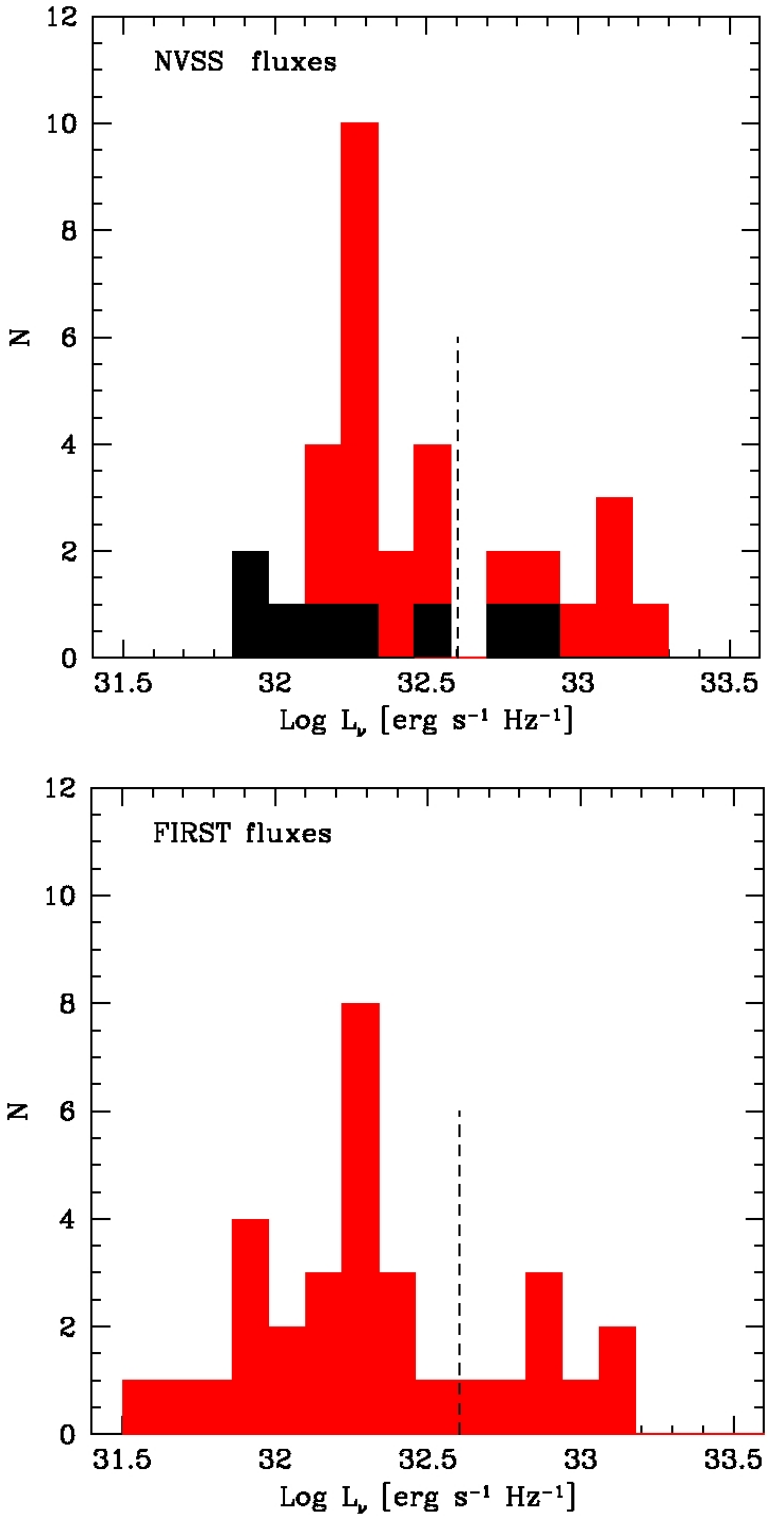

Figure 5.6: 1.4 GHz luminosity histograms for the whole sample. The vertical dashed line is the FR I/FR II radio power divide. Top: NVSS fluxes adopted. The black regions refer to sources with no NVSS flux, for which a fiducial 2.5 mJy upper limit is assumed. Bottom: FIRST fluxes adopted.

5.2.7 The nature of the HLRGs

The HLRGs represent the class of relatively higher power radio galaxies in our sample. As discussed above and clearly shown in Figure 5.5 such sources have radio power slightly above the formal FR I/FR II radio power divide. Furthermore, the possible presence of bimodality in the radio power distribution of the FR Is in our sample suggests that the HLRGs might be drawn from a different parent population (see Section 5.2.6). In this section we will discuss the properties of the HLRGs with respect to their radio properties.

Radio galaxies with clear FR II morphology (i.e. that showed evidence of clearly separated hot spots) were rejected during the C09 sample selection procedure. This immediately excludes the possibility that the HLRGs might be classical FR II radio sources, on the basis of their radio morphology.

Radio galaxies of transitional type

A possible scenario is that the HLRGs are radio galaxies of transitional type, i.e. with radio morphology typical of FR I sources and radio power typical of the local faint FR II radio galaxy population. This is not surprising, because the high power tail of the FR I radio power distribution partially overlaps with the low luminosity tail of the FR IIs, at least at low redshifts.

Furthermore, it has been proposed that the classical FR I/FR II radio luminosity divide undergoes a positive evolution with increasing redshift (e.g. Heywood et al., 2007). In such a scenario, radio galaxies with radio morphology typical of FR I sources and radio power typical of local FR IIs would be more common at the redshifts of our interest than at low-intermediate redshifts.

Compact radio sources

As discussed in C09, the rejection of radio galaxies with clear FR II morphology was performed firstly on the basis of the FIRST survey (Becker et al., 1995), and then by using the VLA-COSMOS survey (Schinnerer et al, 2007). Their radio maps have a typical resolution of $\sim$5 arcsec (FIRST) and $\sim$ 1.5 arcsec (VLA-COSMOS), that correspond to 43 kpc and 13 kpc, at redshift $z = 1.5$, respectively. This selection excludes the presence of classical FR IIs in the sample, since the radio jets of these sources typically extend to distances larger than $\sim$a few tens of kpc, up to Mpc scale.

Almost all of the LLRGs and all of the HLRGs are observed as compact radio sources in both the FIRST and the VLA-COSMOS surveys. As pointed out in C09, there are two possible scenario. i) While the core has a flat radio spectrum, the extended emission of radio sources has a steep spectrum. Because of the light redshifting, the extended emission is therefore increasingly more difficult to detect at increasing redshifts. Therefore it

might be that both the FIRST and the VLA-COSMOS surveys detect the core emission only. ii) Alternatively, the radio galaxies in our sample are intrinsically small. We refer to C09 for a comprehensive discussion of the first scenario. In this work we limit our discussion to the second possibility.

If the sources in our sample are intrinsically compact, they are entirely contained within a few ~ 10 kpc scale. They might show a radio morphology somehow different from that of classical FR Is. If this is the case we suggest that the HLRGs might be CSS (e.g. Saikia, 1988; Fanti et al., 1990; Fanti & Fanti, 1994; Dallacasa et al., 1993; Fanti & Spencer, 1995) or GPS (e.g. O'Dea et al., 1991) sources (see also Section 3.9).

The GPS sources are commonly contained within the Narrow Line Region at $\lesssim 1$ kpc scale, while the CSS sources are usually contained within the host galaxy (i.e. $\lesssim 15$ kpc). They would not be resolved at redshift $z \gtrsim 1$ by using the VLA-COSMOS and the FIRST surveys. Therefore, the possibility that some of the HLRGs are GPS or CSS cannot be excluded.

The GPS and CSS sources show a complex multiple radio morphology (see also O'Dea, 1998, and references therein for a review). They are preferentially found at lower redshifts ($z \lesssim 1$ Fanti et al., 1990; O'Dea et al., 1991), and have higher radio powers (i.e. ~ 2 orders of magnitude brighter, O'Dea & Baum, 1997) than those of HLRGs. This also implies that the presence of GPS or CSS sources within the HLRGs is more likely than for the LLRGs.

However, the radio powers of the FR Is in our sample (including both the LLRGs and the HLRGs) are fully consistent with those of local faint radio sources studied by Drake et al. (2004). Most of the galaxies in their sample are compact and therefore resemble CSS or GPS sources. They have redshifts and low frequency radio luminosities between $z \simeq 0.05 - 0.35$ and $L_{1.4\ \mathrm{GHz}} \simeq 10^{31.0-34.2}$ erg s^{-1} Hz^{-1}, respectively. Interestingly, this suggests that all of the radio galaxies in our sample might be similar to the local radio sources in the Drake et al. (2004) catalog.

If some of our sources were confirmed to be CSSs or GPSs, they would constitute a population of compact radio sources with higher redshifts and lower radio power than those included in previous samples of intermediate redshift objects of these two classes (e.g. Dallacasa et al., 1995, 1998, 2013).

It would be interesting to study the spectral properties of the HLRGs in our sample with multiwavelength radio observations, to see if they are consistent with the steep spectra typical of CSS or if the SEDs are instead consistent with those of GPS sources that show a peak at high radio frequencies. High angular resolution ($\lesssim 0.1$ arcsec) radio observations with the VLBI network may allow us to investigate in detail the radio morphology of these sources.

According to the theoretical evolutionary scenario suggested for CSSs and GPSs by Snellen et al. (2000), if the radio galaxies in our sample are compact $\gtrsim 1$ kpc sources, they will evolve into classical FR Is increasing

their size and decreasing their radio luminosity. Alternatively, if our sources are $\lesssim 1$ kpc GPSs, they will increase their luminosities and sizes, until they reach a ~ 1 kpc size. Then, they will decrease their radio power evolving into CSSs and finally into radio galaxies.

Conversely, Tinti & De Zotti (2006) found observational evidence that GPS sources always evolve decreasing their luminosity and increasing their size. This is in agreement with the theoretical model suggested by Begelman (1996).

Therefore, it might be that, during their evolution, some of our sources will reach a higher radio power. However, it is unlikely that they will increase their radio luminosities enough to evolve into radio galaxies with a radio morphology typical of classical FR IIs, as also suggested by Drake et al. (2004) for their sample of lower redshifts compact sources.

5.3 Source space density

The careful selection of our sample and the accurate photometric redshifts make possible a reliable estimate of the space density of 1.4 GHz sources at $z \simeq 1$, albeit in a narrow luminosity range. For this purpose we consider a flux limited sample with NVSS flux density brighter than 2.5 mJy. Most (13 out of 19) sources are in the redshift and luminosity ranges $0.9 \leq z \leq 1.4$ and $10^{32.11}\,\mathrm{erg\ s^{-1}Hz^{-1}} \leq L_{1.4\ \mathrm{GHz}} \leq 10^{32.51}\,\mathrm{erg\ s^{-1}Hz^{-1}}$. Their median redshift and radio luminosity are $z_{\mathrm{median}} = 1.1$ and $L_{1.4\ \mathrm{GHz\,median}} = 10^{32.30}\,\mathrm{erg\,s^{-1}\,Hz^{-1}}$, respectively. Only for these there is sufficient statistics to get a meaningful estimate of the space density.

The NVSS catalog is 50% complete for unresolved sources with corrected flux density of 2.5 mJy, although its completeness rises rapidly to 99% at 3.4 mJy (Condon et al., 1998). To correct for the incompleteness of our sample we have exploited the FIRST survey, estimated to be 95% complete down to 2 mJy. In our field there are three FIRST sources within the considered luminosity and redshift ranges, not present in the NVSS catalog. Only one of them (i.e. source 22) has a FIRST flux density ≥ 2.5 mJy. We have added it to the sample that, concerning this analysis, comprises 14 sources.

Using the classical $1/V_{\mathrm{max}}$ estimator (Schmidt, 1968) we get a comoving density of $(6.09^{+1.97}_{-1.77})\,10^{-6}\mathrm{Mpc}^{-3}\,(\mathrm{d}\log L)^{-1}$. The positive error takes into account the possibility that also the other two FIRST sources not present in the NVSS catalog are above the 2.5 mJy limit if observed with the larger NVSS beam. Then, the fractional positive error due to incompleteness would be $2/14 \simeq 0.14$; we have added it in quadrature to the Poisson error.

A further uncertainty is due to errors on photometric redshifts that may have moved some sources unduly in or out of the chosen redshift range. To estimate this uncertainty we have generated $N = 1,000$ simulated samples randomly assigning to each of the 20 sources in the flux limited sample (in-

cluding the FIRST source) a redshift randomly drawn from a distribution made of two half-Gaussians with mean equal to the estimated photometric redshift and dispersions equal to the positive and negative 1-σ redshift errors. For each simulated sample we have derived the comoving space density with the $1/V_{\rm max}$ estimator, finding $(5.4 \pm 0.4)\,10^{-6}{\rm Mpc}^{-3}\,({\rm d}\log L)^{-1}$, where the errors correspond to the range encompassing 68% of the distribution. Then, these errors have been added in quadrature to those estimated above. This leads to our final estimate for the comoving space density: $(5.4^{+2.0}_{-1.8})\,10^{-6}{\rm Mpc}^{-3}\,({\rm d}\log L)^{-1}$.

In Figure 5.7 we compare our estimate (open square) of the comoving space density of 1.4 GHz radio sources with $L_{1.4\ {\rm GHz}} \simeq 10^{32.3}\,{\rm erg\,s^{-1}\,Hz^{-1}}$ and $z \simeq 1.1$ with results found in the literature for different redshifts. Our result is somewhat higher than that by Smolčić et al. (2009, see their Table 2) at a similar redshift. It is also higher than expected from the model by Willott et al. (2001), but consistent with predictions by Massardi et al. (2010) and McAlpine et al. (2013).

A comparison with comoving space densities of sources with similar luminosities at lower redshifts confirms that they are strongly evolving. We find an enhancement of the density by a factor $6.1^{+2.4}_{-2.2}$ compared with the Mauch & Sadler (2007) estimate at $z \sim 0$, consistent with Rigby et al. (2008) who reported an increase by a factor of 5–9 from $z \sim 0$ to $z \sim 1$ for FR I radio galaxies with $L_{1.4\ {\rm GHz}} > 10^{32}\,{\rm erg\,s^{-1}\,Hz^{-1}}$.

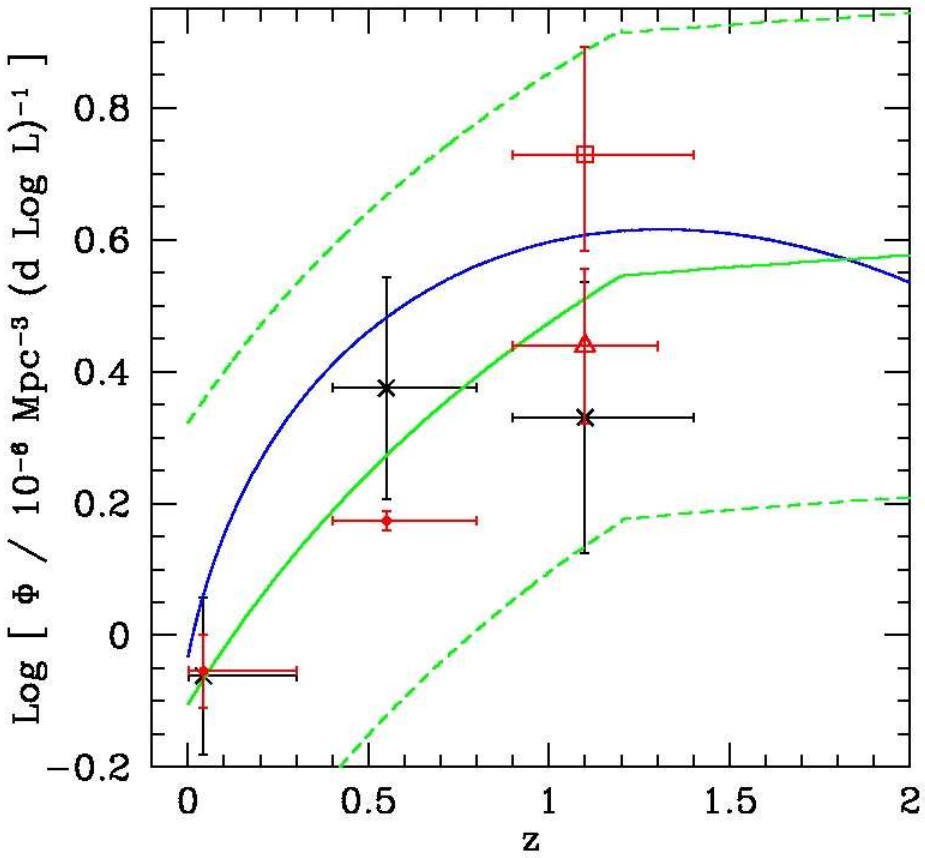

Figure 5.7: Redshift dependence of the comoving space density of 1.4 GHz radio sources with $L_{1.4\ \mathrm{GHz}} \simeq 10^{32.3}\,\mathrm{erg\,s^{-1}\,Hz^{-1}}$. The red points are observational estimates by Mauch & Sadler (2007) at $z \simeq 0.043$, Donoso et al. (2009) at $z \simeq 0.55$, Smolčić et al. (2009) at $z \sim 1$ (open triangle), and this work (open square). The black points are from the Willott et al. (2001) model, corrected to the cosmology used in this work. The solid blue line shows the predictions by Massardi et al. (2010) for steep-spectrum radio sources. The green lines refer to the pure luminosity evolution model by McAlpine et al. (2013, model 3 in their Table 3), with its errors. The uncertainties are at 1-σ level.

Chapter 6

The Poisson Probability Method

In this Chapter we introduce a new method to search for high redshift ($z \gtrsim 1$) Mpc-scale overdensities on the basis of photometric redshifts and galaxy number counts. We primarily introduce the method to search for groups and clusters in the COSMOS field (Scoville et al., 2007a) around FR I radio galaxies. Due to the COSMOS multiwavelength coverage, increasingly accurate photometric redshift determinations have been derived (Mobasher et al., 2007; Ilbert et al., 2009).

Our method is tailored to the specific properties of both the $z \sim 1-2$ FR I sample described in Chapter 5 and the survey adopted, to which we refer throughout the method description. We also use photometric redshifts from the Ilbert et al. (2009) catalog. However, the method may also be applied to other multiwavelength surveys and samples, if accurate photometric redshift information is available.

The method requires the projected coordinates of fiducial beacons (e.g. in this work we adopt the sample of $z \sim 1-2$ radio galaxies). This implies that our method relies on a positional prior, i.e. it is introduced to search for a cluster or group environment around assigned locations in the projected sky. Therefore, it is not properly a method to search blindly for clusters and groups within a given survey, even if it can be possibly applied for such purposes. This strategy is similar to that adopted in George et al. (2011), who associated galaxies with previously selected groups and that adopted in Hao et al. (2010) who searched for clusters around the BCGs.

6.1 Motivations for a new method

In this section we briefly discuss the problems that affect methods that search for high redshift clusters on the basis of number densities, with particular attention to those that use photometric redshifts. Then, we focus on

the peculiarities of our sample and the resulting need for introducing a new method to search for high redshift Mpc-scale overdensities.

1. As pointed out by Scoville et al. (2007b), methods that identify high redshift structures on the basis of the observed surface densities have to discriminate galaxies at different redshifts, to avoid projection effects. As noted in Eisenhardt et al. (2008), galaxy number counts are more susceptible to projection effects than, for example, the detection of X-ray emission from the Intra-Cluster Medium (ICM). This makes problematic the identification of the structures at different distances along the line-of-sight.

2. Number densities are increasingly small for increasing redshifts, at $z \gtrsim 1$. This affects also the deepest sky surveys. For example, the COSMOS field survey has, on averages, number densities per unit redshift of $\sim$25, 10, and 3 counts arcmin^{-2} dz^{-1} at redshift $z \sim$1, 1.5, and 2.0, respectively (Ilbert et al., 2009), where only those galaxies with i^+ AB magnitudes in the range $21.5 < i^+ < 24.5$ are considered. These low number counts imply that shot-noise strongly affects any $z \sim 1-2$ cluster search based on galaxy number counts and photometric redshifts, since Mpc-scale overdensities are extended and detected over scales of $\sim$1 arcmin (e.g. Santos et al., 2009), typical of those of cluster cores. In fact, 1 arcmin corresponds to ~ 480 kpc at $z = 1$.

3. Typical statistical photometric redshift uncertainties are $\sigma_z \sim 0.1-0.2$ at redshifts $z \sim 1-2$. This applies to surveys such as COSMOS (Ilbert et al., 2009) and the Canada-France-Hawaii Telescope Legacy Survey (CFHTLS, Coupon et al., 2009). Note that a distance of $\sigma_z = 0.1$ along the line-of-sight corresponds to more than 100 Mpc, which is significantly higher than the typical size of large scale structures in the Universe. Therefore, these uncertainties highly affect the line-of-sight discrimination of real cluster members from the foreground and any attempts to determine cluster membership on the basis of photometric redshifts only.

   Furthermore, the typical statistical photometric redshift uncertainty increases within the redshift interval of our interest and undergoes a catastrophic failure at $z \gtrsim 1.5$ (Ilbert et al., 2009). In fact, photometric and spectroscopic redshift information cannot be easily obtained between $z \sim 1-2$ because most of the relevant spectral features fall outside of the instrumental wavelength bands in that redshift range, which is therefore called *redshift desert* (Steidel et al., 2004; Banerji et al., 2011).

4. Mpc-scale overdensities might undergo significant evolution between $z \sim 1-2$. Their structure and number density might significantly

change with cosmic time. Diffuse protoclusters with star-forming galaxies have been in fact found at redshifts higher than $z \sim 2.0$ (Steidel et al., 2000; Venemans et al., 2007; Capak et al., 2011).

Methods that search for high redshift groups or galaxy clusters that are based on optical number counts and photometric redshifts have to carefully identify the different Mpc-scale structures that are present along the line-of-sight, in order to avoid projection effects.

Most of the existing methods such as those that are based on wavelets, Friend-of-Friends algorithms, peak finding methods, Delaunay, Voronoi tessellations, adaptive kernel (see e.g. Ebeling & Wiedenmann , 1993; Postman et al., 1996; Scoville et al., 2007b; Eisenhardt et al., 2008; Soares-Santos et al., 2011) that search for high redshift clusters on the basis of number counts and redshifts are very efficient at $z \lesssim 1.5$, but show reduced efficiency at higher redshifts because of the above mentioned problems.

All these methods are based on the 2-d surface density more than on the 3-d number density. As noted in Scoville et al. (2013), considering the 3-d number density would require a more accurate photometric redshift information. All the above mentioned methods characterize the projected space with a high accuracy, in order to identify Mpc-scale structures of different scales. However, such a detailed multi-scale projected space analysis implies that establishing whether multiple overdensity peaks in the 2-d projected density field are part of a single larger structure in practice becomes extremely difficult and subjective (Scoville et al., 2013). For this reason, previous studies are not always able to provide galaxy cluster and group candidate catalogs (Scoville et al., 2013). Therefore, we will introduce a less sophisticated but flexible method to overcome these limitations.

Furthermore, high photometric redshift uncertainties do not allow us to consider the 3-d number density. Therefore, we consider the 2-d surface density and the redshift information separately. In order to overcome the problems listed above, a detailed distance discrimination based on photometric redshifts is therefore required. As we show in the following this can be achieved to the detriment of a less detailed tessellation of the projected space.

6.2 The Poisson Probability Method (PPM)

Our method is based on galaxy number counts and photometric redshifts. It consists in searching for a dense environment around a given location in the sky. Concerning our specific goal to search for cluster environments around the FR Is in the C09 sample, we will adopt the photometric redshift information for the galaxies in the COSMOS field as given in the Ilbert et al. (2009) catalog. Limiting the sample to only FR Is, we consider their recently estimated photometric redshifts from Baldi et al. (2013), when spectroscopic

redshifts from the zCOSMOS-bright (Lilly et al., 2007) and MAGELLAN (Trump et al., 2007) catalogs are not available. Note that this applies to any catalog and dataset with characteristics similar to those we adopted.

The PPM is adapted from that proposed by Gomez et al. (1997) to search for X-ray emitting substructures within clusters. The authors note how their method naturally overcomes the inconvenience of dealing with low number counts per pixel ($\gtrsim 4$), which prevents them from applying the standard techniques based on χ^2-fitting, e.g. Davis & Mushotzky (1993), see Gomez et al. (1997). We are similarly dealing with the problem of small number counts. Therefore standard methods might not be appropriate, as discussed above. We refer to the following sections for a comprehensive description of the PPM. Here we briefly summarize the basic steps of the procedure:

- We tessellate the projected space with a circle centered at the coordinates of the beacon (in our specific case this is the location of the FR I radio galaxy) and a number of consecutive adjacent annuli. The regions are concentric and have the same area (2.18 armin^2). In Figure 6.1 we show the RGB image of the field of 01. The first three regions of the tessellation are shown.

- For each region, we count galaxies with photometric redshifts from the I09 catalog within a given interval Δz centered at the centroid redshift $z_{\rm centroid}$, for different values of Δz and $z_{\rm centroid}$. The values of Δz and $z_{\rm centroid}$ densely span between $0.02 - 0.4$ and $0.4 - 4.0$, respectively.

- For each area and for a given redshift bin we calculate the probability of the null hypothesis (i.e. no clustering) to have the observed or a higher number of galaxies, assuming Poisson statistics and the average number count density estimated from the COSMOS field.[1] Starting from the coordinates of the beacon we select only the first consecutive overdense regions for which the probability of the null hypothesis is $\leq 30\%$. We merge the selected regions and we compute the probability, separately, as done for each of them. Then, we estimate the detection significance of the number count excess as the complementary probability. We set it equal to zero, if the annulus closest to the radio galaxy has an innermost radius $r \gtrsim 132$ arcsec, i.e. we do not consider overdensities that start to be detected at a significant angular separation from the location of the source. This projected distance corresponds to 0.8 h^{-1} Mpc, that is the scale where the amplitude of the correlation function between RLAGNs and Luminous Red Galaxies (LRGs) is reduced to a few percent ($\sim 4\%$) of the value at its maximum, up

[1] We test if cosmic variance affects our analysis selecting four disjoint quadrants in the COSMOS survey to estimate the field density separately from each quadrant. We verify that the results are independent of the particular choice of the field. We also note that the beacon is not excluded in estimating the number count density.

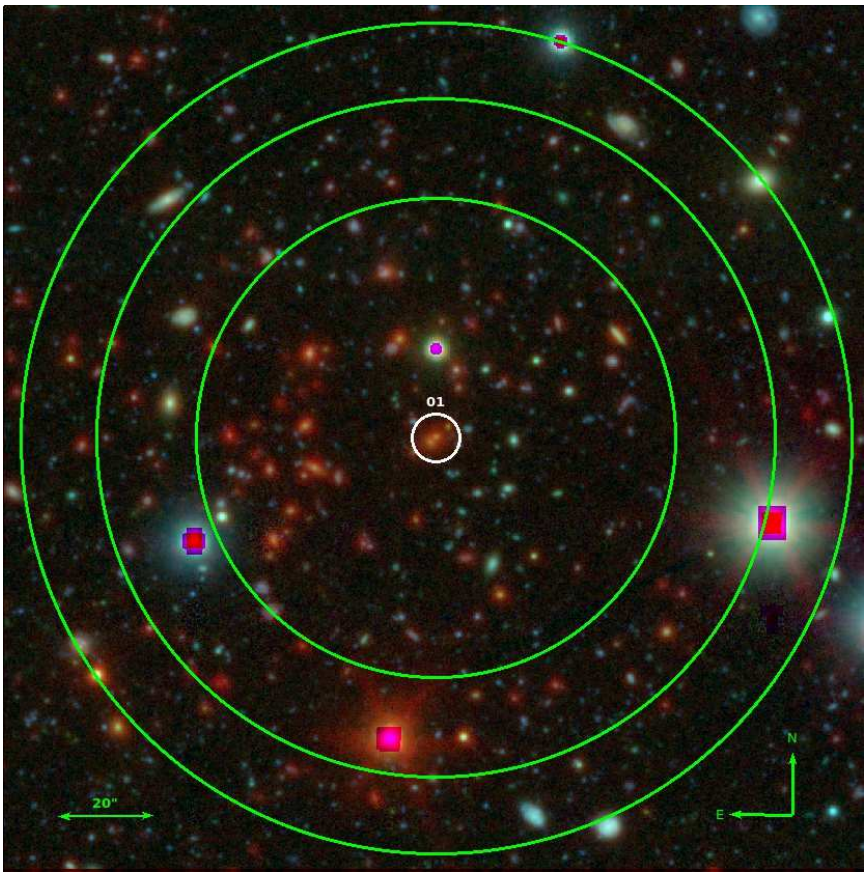

Figure 6.1: RGB image of the field of 01. The image is obtained using Spitzer 3.6μm, Subaru r$^+$- and Subaru B-band images for the R, G, and B channels, respectively. Green circles show the first three regions of the PPM tessellation. The white circle is centered at the position of the coordinates of the radio source 01.

to $z \simeq 0.8$ (e.g., Donoso et al., 2010; Worpel et al., 2013). LRGs are here considered since they are commonly found in the cores of galaxy clusters and represent a substantial fraction of the cluster galaxy population, at least at redshifts $z \lesssim 1.4$ (Menci et al., 2008; Tozzi et al., 2013).

- In Figure 6.2 we report the PPM plots for the fields of some of the sources in our sample. All PPM plots for all 32 radio sources in our sample are reported in Figure A.1 in Appendix A. For each choice of the parameters $z_{\rm centroid}$ and Δz we plot the detection significance defined in the previous step. We adopt the following color code: $\geq 2\sigma$, $\geq 3\sigma$, and $\geq 4\sigma$ points are plotted in cyan, blue, and red, respectively. We do not plot $< 2\sigma$ points. The abscissa of the vertical solid line is at the redshift of corresponding source. The vertical dashed lines show the redshift uncertainties as given in B13. We apply a Gaussian filter to eliminate high frequency noisy patterns, an issue that will be discussed in detail in Section 6.7. Figure 6.2 shows the plot where the filter is applied.

- We define as overdensities only those regions for which consecutive $\geq 2\sigma$ points are present in a region of the PPM plot at least $\delta z_{\rm centroid} = 0.1$ long on the redshift axis $z_{\rm centroid}$ and defined within a tiny $\delta(\Delta z) = 0.01$ wide interval centered at $\Delta z = 0.28$. These values are chosen because of the properties of the errors of the photometric redshifts of our sample and of the size of the Gaussian filter we apply. In particular the redshift bin ($\Delta z = 0.28$) corresponds to the estimated statistical 2-σ photometric redshift uncertainty at $z \sim 1.5$ for dim galaxies (i.e. with AB magnitude $i^+ \sim 24$, Ilbert et al., 2009). These magnitudes are typical of the galaxies we expect to find in clusters in the redshift range of our interest. We verified that the results are stable with respect to a slightly different choice of the redshift bin Δz. The 2σ threshold is not high, nevertheless it is equal to that adopted by previous work that searched for high redshift galaxy clusters (e.g. Durret et al., 2011; Galametz et al., 2012).

- In order to estimate the actual significance of each Mpc-scale overdensity we apply the same procedure outlined in the previous step, but progressively increasing the significance threshold until no overdensity is found. We assign to each overdensity a significance equal to the maximum significance threshold at which the overdensity is still detected. Note that in case the overdensity displays multiple local peaks we do not exclude the lower significance ones.

- We estimate the redshift of each overdensity as the centroid redshift $z_{\rm centroid}$ at which the overdensity is selected in the PPM plot.

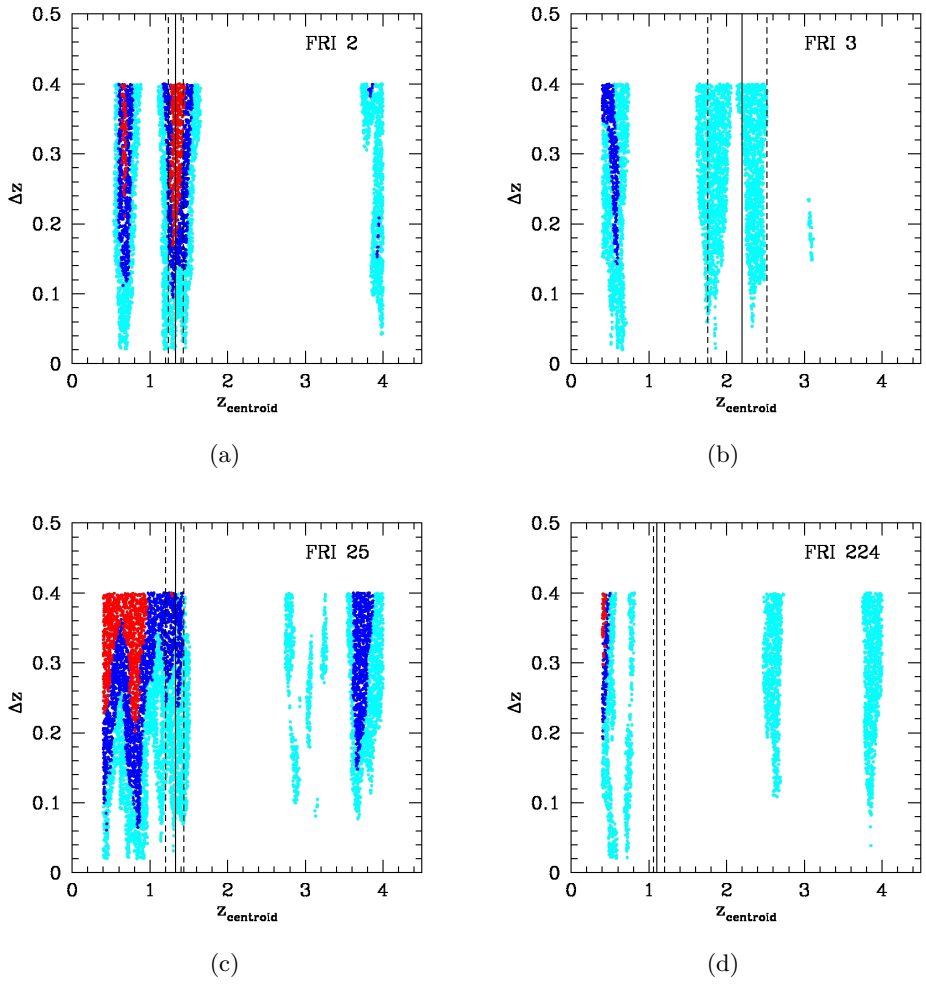

Figure 6.2: PPM plots for the fields of sources 02 (a), 03 (b), 25 (c), and 224 (d) of the C09 sample. The abscissa of the vertical solid line is at the redshift of the source. The vertical dashed lines show its uncertainties as given in Baldi et al. (2013). Each point represents the detection significance of the number count excess for a specific choice of the values of the redshift bin Δz (within which we perform the number count) and its centroid $z_{\rm centroid}$. The detection significance is estimated as the complementary probability of the null hypothesis (i.e. no clustering) to have more than the observed number of galaxies in the field of the beacon (i.e. the FRI radio galaxy in our case), assuming Poisson statistics and the average number density estimated from the COSMOS field. We plot only the points corresponding to overdensities with a $\geq 2\sigma$ detection significance. Color code: $\geq 2\sigma$ (cyan points), $\geq 3\sigma$ (blue points), $\geq 4\sigma$ (red points). A Gaussian filter which eliminates high frequency noisy patterns is applied. A discussion of the PPM plots reported in the panels is reported at the beginning of the Chapter 8.

- We also estimate the size of each overdensity in terms of the minimum and maximum distances from the FR I beacon at which the overdensity is detected. In order to do so we consider all points in the PPM plot within the region centered around $\Delta z = 0.28$ and at least $\delta z_{\rm centroid} = 0.1$ long on the redshift axis $z_{\rm centroid}$ which defines the overdensity. For each of these points the overdensity is detected within certain minimum and maximum distances. We estimate the minimum and maximum distances of the overdensity as the average (and the median) of the minimum and maximum distances associated with all of these points, respectively. We also compute the rms dispersion of the distances as an estimate for the uncertainty.

- In order to estimate the fiducial uncertainty for the redshift of the overdensity we consider all sources located between the median value of the minimum distance and the median value of the maximum distance from the coordinates of the source within which the overdensity is detected in the projected space. We also limit our analysis to the sources that have photometric redshifts within a redshift bin $\Delta z = 0.28$ centered at the estimated redshift of the overdensity. This value is chosen to ensure consistency with the value used for our detection procedure (see above). We estimate the overdensity redshift uncertainty as the rms dispersion around the average of the photometric redshifts of the sources that are selected in the field of the radio galaxy.

- We associate with each radio galaxy any overdensity in its field that is located at a redshift compatible with that of the radio source itself (i.e. when the interval centered at the redshift estimated for the overdensity and with a half-width equal to 2 times the fiducial redshift error intersects the redshift range defined within the radio galaxy redshift uncertainties). Note that multiple overdensity associations are not excluded.

Our approach implicitly assumes azimuthal symmetry around the axis oriented at the coordinates of the beacon. Since we extend the tessellation up to ∼6 arcmin (i.e. ∼3 Mpc at $z = 1.5$) from the coordinates of the beacon, we do not exclude the possibility of detecting non circularly symmetric systems. (see Postman et al., 1996, for a similar methodology). Furthermore, our method is also flexible enough to find clusters even if the coordinates of the cluster center are known with $\sim$ 100 arcsec accuracy (as tested with simulations, see Sections 7.1.1 and 7.2.2).

We note that the great majority of low-power radio sources in clusters or groups are found within $\sim$ 200 kpc from the core center up to $z \simeq 1.3$ (Ledlow & Owen, 1995; Smolčić et al., 2011). Furthermore, FR Is are typically hosted by undisturbed ellipticals or cD galaxies (Zirbel, 1996), which

are often associated with the BCGs (von der Linden et al., 2007). Similarly to the FR Is, BCGs are preferentially found within ~ 41 kpc from the cluster centers (Zitrin et al., 2012; Semler et al., 2012). Therefore, this suggests that FR Is in cluster environments are preferentially hosted within the central regions of the core, at least at low redshifts. The results presented in Section 8.10.8 for the $z \sim 1-2$ cluster candidates associated with the C09 sample suggest that this is generally true also at higher redshifts. This motivates the peculiar projected space tessellation described in this section and adopted for our cluster search.

6.2.1 The PPM theory

In this section we report a sequential list of logical statements that clarify the theory the PPM procedure is based on. We refer to the following sections for the proofs.

- Since high photometric redshift uncertainties affect any high-z cluster search, the redshifts and projected coordinates of the galaxies are considered separately. The field is tessellated with concentric regions of equal area centered at the projected coordinates of the beacon, i.e. the radio galaxy in our case (see Section 6.3).
- Sources with photometric redshifts within the redshift bin Δz centered at the redshift centroid $z_{\rm centroid}$ are selected. The values of Δz and $z_{\rm centroid}$ densely span the ranges of our interest (see Section 6.4).
- The probability of the null hypothesis (i.e. no clustering) is calculated for each region, given the values of Δz and $z_{\rm centroid}$ (see Section 6.6).
- Starting from the projected coordinates of the beacon, the first consecutive regions for which the null hypothesis is rejected at a level $\geq 70\%$ are selected. Then, the regions are merged to form a new one (see Section 6.6). This procedure aims at selecting the region in the projected space where the overdensity is present.
- The probability $1-\mathcal{P}$ of null hypothesis is calculated for the new region, for each value of Δz and $z_{\rm centroid}$. The null hypothesis is rejected with a probability $\mathcal{P}$. Photometric redshift uncertainties are implicitly neglected (see Sections 6.5 and 6.6).
- Fluctuations of $\mathcal{P}$ on scales $\delta\Delta z$ and $\delta z_{\rm centroid}$ smaller than the typical statistical photometric redshift uncertainties are not physical and ultimately due to noise. They are locally removed by convolving $\mathcal{P}$ with a Gaussian filter, i.e. $\overline{\mathcal{P}} = \mathcal{W} \star \mathcal{P}$.[2] $\overline{\mathcal{P}}$ is an effective mean field defined on the space of $(z_{\rm centroid}; \Delta z)$, see Section 6.7.

[2]The function $h = f \star g$ is the convolution of the function f with the function g.

- We apply a differential approach and show that the filter $\mathcal{W}$ simultaneously suppresses (in linear approximation) the fluctuations of $\mathcal{P}$ both in the space of $(z_{\rm centroid}; \Delta z)$ and in the ensemble of all the possible redshift realizations of the galaxies in the field (see Section 6.7). The fluctuations of $\mathcal{P}$ in the ensemble are originated by the fact that photometric redshift uncertainties are neglected when calculating $\mathcal{P}$ (see Section 6.5).

- $\overline{\mathcal{P}}$ is a good estimate for (i) the probability that the null hypothesis is rejected, where photometric redshift uncertainties are not neglected, and (ii) the significance of the number count excess in the field. In fact, the significance of the number count excess is decreased by the filtering procedure to take the additional variance due to the photometric redshift uncertainties into account (see Sections 6.5 and 6.7).

- We conservatively fix a 2-σ wide redshift bin $\Delta z = 0.28$ and we apply the peak finding algorithm we developed for our discrete case. Such a procedure belongs to a more general context known as Morse theory (see Section 6.8). The algorithm allows to select the cluster candidates in the field within the redshift range of our interest and, for each overdensity, it provides (i) an estimate for its redshift, (ii) an estimate for the cluster core size, and (iii) a rough estimate for the cluster richness (see Section 6.9).

- The association of the cluster candidates detected in the field with the beacon (i.e. in our case the radio galaxy) is performed by using the cluster redshift estimate and the redshift of the radio galaxy, as well as the corresponding uncertainties (see Section 6.10).

- A generalization of the method to other datasets and surveys is provided in Section 6.12.

We stress that the PPM considers the redshift information and the coordinates in the projected space separately, similarly to other methods that use photometric redshift information (e.g. Eisenhardt et al., 2008). This is because the photometric redshift uncertainties are much larger than the typical scale of clusters. Therefore, such uncertainties are significantly dominant with respect to any other observable uncertainty (e.g., flux uncertainties, projected space coordinate uncertainties). In the following we will fully developed the above mentioned statements, first focusing on the projected space and then on the redshifts.

6.3 The projected space

We tessellate the projected space with a circle centered at the coordinates of the beacon (in our specific case this is the location of the FR I radio

galaxy) and 49 consecutive adjacent annuli. These regions are concentric and have the same area, i.e. 2.18 arcmin^2. This is done in order to have the same average field density for each of the regions. The inner radius of the i-th annulus is equal to $\arccos[1 + i(-1 + \cos 50 \text{ arcsec})] \simeq 50 \times \sqrt{i}$ arcsec. This means that the radius of the circle centered at the coordinates of the beacon is equal to 50 arcsec. Such an angular separation is consistent with that adopted by previous work focused on high-z clusters (e.g. Santos et al., 2009; Adami et al., 2010, 2011; Durret et al., 2011; Galametz et al., 2012; Spitler et al., 2012). In fact, it corresponds to 427 kpc at redshift $z = 1.5$, that is typical of the cluster core size at redshift $z \sim 1$. If we chose a smaller scale we would be highly affected by shot noise. In fact, on average, for a fixed area of 2.18 arcmin^2, the differential number counts ($\mathrm{d}N/\mathrm{d}z$) per unit redshift in the COSMOS field are quite small and equal to ~ 55, 22, and 7, at redshifts $z \simeq 1$, 1.5, and 2.0, respectively (Ilbert et al., 2009). Conversely, if we chose a greater scale we would characterize the cluster environment of the FR Is in our sample with a rough (Mpc-scale) accuracy only.

In general, due the specific tessellation of the PPM, the method is effective to detect Mpc-scale rich groups and clusters (as also discussed in Chapter 8). Conversely, it might be less efficient in finding poor groups and larger, i.e. a few Mpc-scale, diffuse structures. Therefore, a more detailed treatment of the projected space typical of sophisticated tessellations such as Voronoi (see e.g. Soares-Santos et al., 2011), Delaunay, correlation estimators (e.g. Adami et al., 2011), wavelet analysis (e.g. Eisenhardt et al., 2008), filter techniques, and adaptive kernels (e.g. Scoville et al., 2007b) might be ineffective and difficult to apply for cluster searches with the use of photometric redshifts only (see also Scoville et al., 2013, for further discussion). On the other hand, such methods might be more useful to study spectroscopically confirmed clusters or groups (e.g. Jelić et al., 2012).

The typical size inspected by our tessellation changes at most $\sim 6\%$ within the entire redshift range of our interest. In fact, 1 arcmin corresponds to a physical size of 482, 512, and 509 kpc, at redshift $z = 1.0$, 1.5, and 2.0, respectively. Depending on the adopted cosmology, the angular distance assumes a maximum between $z \sim 1 - 2$. These considerations imply that our tessellation is effective to characterize Mpc-scale overdensities with the required accuracy, independently of redshift, under the assumption that cluster core size does not dramatically change for increasing redshifts.

Furthermore, our approach implicitly assumes azimuthal symmetry around the axis oriented at the coordinates of the beacon. We do not exclude the possibility to detect non circularly symmetric systems, since we extend the tessellation up to $\sim$6 arcmin (i.e. $\sim$3 Mpc at $z = 1.5$) from the coordinates of the beacon (Postman et al., 1996). Moreover, our method is also flexible enough to find clusters even if the coordinates of the cluster center are known within ~ 100 arcsec only (as tested with simulations in Section 7.2.2).

However, we note that the great majority of low-power radio sources in

clusters or groups are found within ~ 200 kpc from the core center up to $z \simeq 1.3$ (Ledlow & Owen, 1995; Smolčić et al., 2011). Therefore, this suggests that low-power radio galaxies in cluster environments are preferentially hosted within the central regions of the core, at least at low or intermediate redshifts. This seems to be true also at higher redshifts ($z \sim 1-2$, see discussion in Section 8.10.8).

Therefore, all these results support the specific projected space tessellation method described in this section and adopted for our cluster search.

6.4 Redshift information

As discussed in Scoville et al. (2007b), identifying large scale structures on the basis of 2-d number densities requires a careful selection of those galaxies that are at the redshift of the structure. This is because, especially in the case of high-z clusters, foreground galaxies contaminate the field. Despite this, the contamination from foreground sources is limited by the smaller angular size of high-z clusters with respect to that of those at lower redshifts.

As pointed out in Scoville et al. (2007b), three different criteria are commonly adopted to discriminate among the galaxies at different distances by using (i) color selections (e.g. Papovich, 2008; Gladders & Yee, 2005), (ii) spectroscopic redshifts (e.g. Knobel et al., 2009, 2012; Diener et al., 2013), or (iii) photometric redshifts (e.g. Adami et al., 2010; Durret et al., 2011).

(i) Color selection is not used here, since it might be biased towards large scale structures with specific properties in terms of galaxy colors. This is particularly important especially at redshift $z \gtrsim 1.5$, where the properties of the cluster galaxy population and their changes with redshift in terms of galaxy morphologies, types, masses, colors (e.g. Bassett et al., 2013; McIntosh et al., 2014), and star formation content (e.g. Zeimann et al., 2012; Santos et al., 2013; Strazzullo et al., 2013; Gobat et al., 2013) are still debated; (ii) spectroscopic redshifts are preferred to the photometric redshifts. However, spectroscopic redshift catalogs (e.g. Lilly et al., 2007) are limited to a small fraction of the galaxies in the COSMOS field; (iii) we adopt the photometric redshift catalog of Ilbert et al. (2009), that was obtained considering sources with AB magnitude $I < 25$.

We consider $M \gg 1$ redshift bins, i.e. the closed intervals $[z_l^i, z_r^i]$, with $z_r^i > z_l^i$, $i = 1, 2, ..., M$, and $M = 22,500$. We define the length and the centroid of each interval as $\Delta z^i = z_r^i - z_l^i$ and $z^i_{\rm centroid} = (z_r^i + z_l^i)/2$, respectively. The subscripts l and r stand for left and right, respectively. Both the redshift lengths $\Delta z^i \in [0.02; 0.4]$ and the redshift centroids $z^i_{\rm centroid} \in [0.4; 4.0]$ are randomly and independently chosen assuming a uniform distribution. Since $M \gg 1$, the considered ranges are densely spanned concerning both the redshift bin and the redshift centroid. The redshift range of our interest

is $z \sim 1-2$, while the typical statistical photometric redshift uncertainties at those redshifts are $\sigma_z \sim 0.1-0.2$ (Ilbert et al., 2009). Therefore, both Δz^i and $z^i_{\rm centroid}$ are conservatively selected over wider intervals than those of our interest. This is done in order to avoid spurious boundary effects that might derive from our selection. Before describing in detail our method in the following section we will discuss its theoretical framework.

6.5 Theoretical framework

We denote as n the galaxy number density within a given projected area of the sky subtended by a solid angle Ω. The total variance in the number counts n is given by Peebles (1980)

$$\left\langle \left(\frac{n - \langle n \rangle}{\langle n \rangle} \right)^2 \right\rangle = \frac{1}{\langle n \rangle} + \sigma_v^2 \ , \tag{6.1}$$

where

$$\sigma_v^2 = \frac{1}{\Omega^2} \int \int \omega(\theta) \ d\Omega_1 d\Omega_2 \ , \tag{6.2}$$

is the sampling variance due to source clustering. As pointed out e.g. in Massardi et al. (2010), σ_v^2 adds a significant contribution to the uncertainties in the case of small-area fields. As pointed out in Peebles (1980), assuming ergodicity, the average denoted by the brackets $\langle \ \rangle$ is either the ensemble average (i.e. the average among all the field realizations) or the volume average (i.e. the average among different areas in the survey, each of them is subtended by a solid angle Ω). The clustering term in Equation 6.2 is expressed as the integral over the field of the projected two-point correlation function $\omega(\theta)$, where θ is the angular separation between the solid angle elements $d\Omega_1$, $d\Omega_2$.

We note that n would be Poisson distributed if the clustering term, σ_v^2, were not present. Then, we ask what is the probability that the null hypothesis (i.e. no clustering) occurs for the given field. This is equivalent to set $\sigma_v^2 = 0$ and to assume that n is Poisson distributed. According to our formalism, we estimate the probability of not clustering as the probability to have a number density n' equal or higher than the observed value n:

$$\mathcal{P}_{Poisson}(n' \geq n) = \sum_{k=n \times \Omega}^{\infty} \frac{(\langle n \rangle \times \Omega)^k}{k!} e^{-\langle n \rangle \times \Omega} \ . \tag{6.3}$$

As for Equation 6.1, $\langle n \rangle$ and Ω are the average number density for the survey considered and the solid angle subtended by the selected field for which we estimate the null hypothesis probability, respectively. Therefore, the null hypothesis is rejected with a probability

$$\mathcal{P} = 1 - \mathcal{P}_{Poisson}(n' \geq n) = \sum_{k=0}^{(n-1)\times\Omega} \frac{(\langle n \rangle \times \Omega)^k}{k!} e^{-\langle n \rangle \times \Omega} \ . \qquad (6.4)$$

The probability $\mathcal{P}$ is higher in those fields where the sources are more clustered, i.e. where σ_v^2 is non negligible with respect to the shot noise term $1/\langle n \rangle$. Therefore, $\mathcal{P}$ can be independently considered as the probability that an overdensity is present in the field.

So far, our formalism implicitly assumes that the sample selection is a negligible source of uncertainty (i.e. it does not contribute to the total variance of Equation 6.1). However, the cluster membership selection (based on e.g. fluxes, colors, or redshifts) always contributes to the total number count variance because of the observable uncertainties. Equivalently, observable uncertainties imply that the total variance in Equation 6.1 is underestimated. Consequently, Equation 6.4 overestimates the probability $\mathcal{P}$ that null hypothesis (i.e. no overdensity) is rejected.

Limiting the analysis to the PPM, our method is based on number counts and photometric redshifts. According to the PPM procedure, for each redshift bin Δz^i, only those sources within the redshift interval $[z_l^i, z_r^i]$ are considered (see below, Section 6.6). Photometric redshift uncertainties are significantly higher than those of any other observable (e.g. flux, projected coordinates) associated with our sample.

This implies that we can estimate the additional term to the number count variance in Equation 6.1 due to observable uncertainties by considering photometric redshift uncertainties only. We denote such a term as σ_{ph}^2, where the notation ph stands for photometric redshifts. This term can be independently estimated as the number count variance obtained by averaging over all the possible realizations of the photometric redshifts of the galaxies in the selected field. These realizations are ideally drawn from the redshift probability distributions of the galaxies in the field. Hence, we have:

$$\sigma_{ph}^2 = \left\langle \left(\frac{n - \langle n \rangle_{ph}}{\langle n \rangle_{ph}} \right)^2 \right\rangle_{ph} , \qquad (6.5)$$

where $\langle \ \rangle_{ph}$ denotes the average over the ensemble constituted by all the possible redshift realizations. The net effect to increase the number count variance in Equation 6.1 by the amount σ_{ph}^2 is similar to that described in e.g. Sheth (2007) in the context of luminosity functions estimated by adopting photometric redshifts. Sheth (2007) showed that photometric redshift uncertainties (i.e. distance errors) have the effect of scattering objects to the low luminosity and high-luminosity ends of the luminosity function (i.e. towards higher and lower luminosities). Similarly, in our case photometric redshift uncertainties have the effect of scattering the number counts over a wider range.

Given the additional term σ^2_{ph} in the right hand side of Equation 6.1, a rigorous calculation of the probability of the null hypothesis (i.e. no clustering, $\sigma^2_v = 0$) would require to consider the redshift probability distribution associated with each galaxy in the field. Estimating the correct expression of the null hypothesis probability might be done with simulations, i.e. adopting different realizations of the redshifts, that are drawn from the redshift probability distribution associated with each galaxy in the field. However, this procedure would be enormously demanding in terms of central processing unit (CPU) time and would not add a significant contribution to the PPM. We prefer to adopt a different approach. We neglect any additional terms in the number count variance due to observational uncertainties. We prefer to take such an approximation into account by correcting our final estimate (see Section 6.7). Our correction will decrease the probability $\mathcal{P}$. In the next sections we will describe how our method works.

6.6 Number count excess estimate

Firstly, we consider each pair defined by the redshifts z^i_l and z^i_r, as in Section 6.4, and the sources in the Ilbert et al. (2009) catalog that have redshifts within the interval $z^i_l \leq z < z^i_r$ and that fall within the largest circle that can be inscribed in the COSMOS survey. Such a circle subtends a ~ 1.25 deg^2 solid angle. Then, we estimate the average mean density $\langle n \rangle_i$ as the ratio of the number of these sources to the solid angle subtended by the circle. We test if cosmic variance affects our analysis by adopting different choices in estimating such an average number density (i.e. we also selected four disjoint quadrants in the COSMOS survey and we estimated the average number density for each quadrant, separately). We verified that the results are independent of the choice adopted.

For a given beacon, i.e. in our case the projected coordinates of the radio galaxy, we consider each of the 50 projected regions defined in Section 6.3. We denote them with the index $t = 1, ..., 50$, where $t = 1$ corresponds to the central circle, while the adjacent annuli are denoted with progressively higher indexes. We denote as N^i_t the observed number of galaxies within the chosen redshift interval $z^i_l \leq z < z^i_r$ that fall within the t-th area. By construction, each region subtends a solid angle $\Delta\Omega_t = 2.18$ arcmin^2. We also define the observed number density for the selected region and redshift bin as $n^i_t = N^i_t / \Delta\Omega_t$. The probability of the null hypothesis (i.e. no clustering) for the t-th region, consistently with Equation 6.3, is

$$\mathcal{P}^{i,t}_{Poisson}(n'^i_t \geq n^i_t) = \sum_{k=N^i_t}^{\infty} \frac{(\langle n \rangle_i \times \Delta\Omega_t)^k}{k!} e^{-\langle n \rangle_i \times \Delta\Omega_t} \ , \tag{6.6}$$

that corresponds to the probability of having a number density n'^i_t higher or equal than the observed one, according to the Poisson statistics. Note

that, because of the low number counts, the Gaussian statistics is not a good approximation of the Poisson statistics, therefore the latter is required.

Starting from the central region corresponding to $t = 1$ we select the first adjacent regions, denoted with the indexes $\{\bar{t}_i, \bar{t}_i + 1, ..., \bar{t}_i + h_i\}$, for which the probability of the null hypothesis in Equation 6.6 is $\leq 30\%$. Here $\bar{t}_i \geq 1$ and $h_i \geq 0$ are both integer numbers. Note that we do not exclude the possibility to select one single region, i.e. $h_i = 0$. The central circle may be selected or not, depending on whether the threshold criterion is satisfied or not by that region.

According to our prescription, we have selected only those regions for which the null hypothesis is rejected at a level of $\geq 70\%$, i.e. down to about 1σ. Note that the adopted $\sim 1\sigma$ threshold this is not a tight constraint. A 70% threshold is also adopted by Gomez et al. (1997) and is similar to the values adopted for other selection criteria applied by previous work that were focused on high-z clusters and that used photometric redshift information (e.g. Papovich et al., 2010; Finkelstein et al., 2010).

According to the procedure, the probabilities are always estimated according to Poisson statistics. Even if the Gaussian statistics is not adopted we often refer to the probability in terms of σ (e.g. we refer to 68.27%, 95.45%, and 99.73% probabilities as 1-σ, 2-σ, and 3-σ significances, respectively). We adopt this notation for practical reasons, for sake of convenience.

Similarly to what was done in Gomez et al. (1997), in order to determine the true significance of the number count excess in the field, we merge together all the $h_i + 1$ adjacent regions to form a (larger) circle or a annulus, depending whether the central circle is included or not, respectively. Then, we define the total observed number count N_i for the new region as

$$N_i = \sum_{t=\bar{t}_i}^{\bar{t}_i+h_i} N_t^i \,, \tag{6.7}$$

and the corresponding number density n_i as:

$$n_i = \frac{N_i}{(h_i + 1)\Delta\Omega_t} \,. \tag{6.8}$$

We stress that the goal of the procedure described so far is not to quantify the number count excess associated with the field. Merging the $h_i + 1$ regions aims at selecting an area in the projected space for which there is indication of a number count excess and that is most likely associated with the projected coordinates of the beacon.

Note that if we chose a more constraining (i.e. $> 1\sigma$) threshold criterion we would select only those regions that show a significant number count excess. Therefore, we might be biased towards selecting those regions (i) that are associated with highly overdense substructures in the cluster or (ii)

show high shot noise fluctuations. These scenarios might occur because of the small area subtended by each region (i.e. ~ 2 arcmin^2) and the small number densities that occur at the redshifts of our interest. This discussion suggests that a more constraining (i.e. $> 1\sigma$) criterion might not be effective in selecting properly the cluster field in the projected space.

Then, analogously to what has been done for each of the 50 regions (see Equation 6.6) we estimate the probability of the null hypothesis (i.e. no clustering) for the new area as

$$\mathcal{P}^i_{Poisson}(n'_i \geq n_i) = \sum_{k=N_i}^{\infty} \frac{(\langle n \rangle_i \times (1+h_i)\Delta\Omega_t)^k}{k!} e^{-\langle n \rangle_i \times (1+h_i)\Delta\Omega_t} , \quad (6.9)$$

that is the probability to have a number density n'_i higher or equal than that observed, n_i, according to the Poisson statistics. For the sake of clarity, hereafter we omit the argument of $\mathcal{P}^i_{Poisson}$. We also define as $r^i_{\rm min}$ and $r^i_{\rm max}$ the minimum and maximum projected distances from the coordinates of the beacon (in our case it is the radio galaxy) within which the number count excess is detected, respectively. These radii are equal to $r^i_{\rm min} = \arccos[1 + (\bar{t}_i - 1) \times (-1 + \cos 50 \text{ arcsec})] \simeq \sqrt{\bar{t}_i - 1} \times 50$ arcsec and $r^i_{\rm max} = \arccos[1 + (\bar{t}_i + h_i) \times (-1 + \cos 50 \text{ arcsec})] \simeq \sqrt{\bar{t}_i + h_i} \times 50$ arcsec, because of the specific tessellation, consistently with the adopted procedure.

Accordingly to what discussed in Section 6.5, the null hypothesis is rejected with a probability $\mathcal{P}^i = 1 - \mathcal{P}^i_{Poisson}$. We set $\mathcal{P}^i \equiv 0$ if the overdensity starts to be detected from $r_{\rm min} \gtrsim 132$ arcsec, i.e. if $\bar{t}_i \geq 8$. This is done to reject those overdensities that are detected only at large angular separation from the location of the source. In fact, since 132 arcsec correspond to $\sim$1.1 Mpc at $z = 1.5$, these overdensities might not be associated with our beacon. However, note that such a constraint does not exclude the possibility to detect structures that are extended up 132 arcsec or even higher. These extended structures are detected if they start at a distance lower than 132 arcsec.

The specific projected distance of 132 arcsec corresponds to 0.8 h^{-1} Mpc, that is the scale where the amplitude of the correlation function between RLAGNs and LRGs is reduced to a few percent ($\sim 4\%$) of the value at its maximum, up to $z \simeq 0.8$ (e.g., Donoso et al., 2010; Worpel et al., 2013).

Limiting the number counts to the $h_i + 1$ overdense regions between the radii $r^i_{\rm min}$ and $r^i_{\rm max}$ does not bias our results towards overestimating the number count excess because we are allowed to select slightly overdense regions, down to $\sim 1\sigma$ number count excess.

Similarly, the probability to detect those fields that show low number count excess or shot-noise fluctuations is negligible. This is because the number of selected galaxies does not decrease when the $h_i + 1$ regions are merged and then the number count excess probability is re-estimated for the new (larger) region delimited by the radii $r^i_{\rm min}$ and $r^i_{\rm max}$. We will describe in

the following sections the noise mitigation procedure and the peak finding algorithm adopted to detect overdensities. As will be clarified below, both of these procedures further suppress the probability to detect as overdensity any number count excess that is simply due to shot noise fluctuations.

6.7 Noise mitigation

In Figure 6.3, left panel, we plot $\mathcal{P}$ as a function of the redshift bin Δz and its centroid $z_{\rm centroid}$. We omit the index i corresponding to the specific redshift interval. We will introduce such an index only where necessary. Red, blue, and cyan colors refer to points with significances $\geq 4\sigma$, $\geq 3\sigma$, and $\geq 2\sigma$, respectively. We plot as a vertical solid line the spectroscopic redshift of the source.

Isolated high significance spiky patterns are clearly visible in the plot. They occur because of the presence of a significant source number excess at specific redshifts and redshift bins. However, the fact that such patterns are spiky and extended over scales that are smaller than the typical statistical photometric redshift uncertainties ($\sigma_z \sim 0.1 - 0.2$) suggests that they are not physical and are ultimately due to noise fluctuations.

In order to eliminate such high frequency noisy patterns we apply a Gaussian filter to the function $\mathcal{P}^i$ as follows:

$$\overline{\mathcal{P}}^i = \frac{\sum_j \mathcal{W}^{ij}\mathcal{P}^i}{\sum_j \mathcal{W}^{ij}} \,, \tag{6.10}$$

where the kernel

$$\mathcal{W}^{ij} = \begin{cases} e^{-\frac{{\zeta_{ij}}^2}{2\sigma_w^2}} & \text{if } \zeta_{\rm ij} \leq 7.5\ \sigma_w \\ \\ 0 & \text{otherwise} \end{cases} \,, \tag{6.11}$$

and

$${\zeta_{ij}}^2 = (z^i_{\rm centroid} - z^j_{\rm centroid})^2 + (\Delta z^i - \Delta z^j)^2 \,. \tag{6.12}$$

For practical reasons, the sum over j is extended only to those points that are at most 7.5-σ_w from $(z^i_{\rm centroid};\ \Delta z^i)$, so that the kernel has a compact domain and acts as a weighted local average. The newly defined function, $\overline{\mathcal{P}}$, is simply the convolution between the Gaussian filter and the previously defined probability $\mathcal{P}$.

In practice, patterns that are extended over scales of the order of $\lesssim \sigma_w$ with respect to $z_{\rm centroid}$ or Δz are removed from the plots. We choose $\sigma_w = 0.02$, that is much lower than the typical statistical photometric redshift

uncertainty $\sigma_z \sim 0.1 - 0.2$ of the Ilbert et al. (2009) catalog. Therefore, our choice conservatively removes those patterns that are clearly due to noise.

Isolated local maxima are removed from the plots since they are suppressed by the surrounding low significance points. Conversely, local maxima that belong to extended high significance patterns still remain associated with high significance patterns, even if their significance is decreased because of the average procedure.

A heuristic physical interpretation may be provided. Averaging $\mathcal{P}$ among those points that belong to a neighborhood of $z_{\rm centroid}$ and Δz mimics the presence of the redshift uncertainties at fixed $z_{\rm centroid}$ and Δz. This is because changing $z_{\rm centroid}$ and Δz by small amounts has the net effect of including some sources and excluding others when the redshift interval is changed. To understand better such a heuristic equivalence, in the following we will adopt a differential approach.

We note that $\overline{\mathcal{P}}$ can be naturally interpreted as an effective mean field defined on the space of $(z^i_{\rm centroid};\ \Delta z^i)$. This is because the incoherent fluctuations of $\mathcal{P}$ due to noise and small scales are locally suppressed by the filter $\mathcal{W}$.

There is no theoretical and observational reason to prefer one specific form for the kernel $\mathcal{W}$. In the effective field theory context, since the width of the filter is related to the statistical photometric redshift uncertainties, it is more relevant than the specific shape of the filter $\mathcal{W}$. In fact, the Gaussian filter is chosen because its exponential declining assures that noisy features associated with scales (that are smaller than the typical statistical photometric redshift uncertainty) are conservatively removed.

A more physical interpretation of the filtering procedure described in this section may be provided by using a differential approach. Several methods of analysis of Poisson processes, including variational calculus, have been developed in the context of stochastic analysis (e.g., Privault, 1994; Albeverio et al., 1996; Molchanov & Zuyev, 2000). We stress that the following discussion does not intend to be a formal proof, but simply an argument that shows how we can assign a physical meaning to the $\overline{\mathcal{P}}$ values and, thus, better explaining the above mentioned heuristic equivalence that arises when the filtering procedure is reconsidered.

We adopt a compact notation and we define the vector $\overrightarrow{x} = (z_{\rm centroid};\ \Delta z)$ whose i-th component is given by $(z^i_{\rm centroid};\ \Delta z^i)$. We consider the galaxies that are in the field of our beacon (i.e. the radio galaxy in our case) and whose redshifts belong to a neighborhood of the redshift $z_{\rm centroid}$ corresponding to the specific $\overrightarrow{x}$. The values of Δz and $z_{\rm centroid}$ can be expressed as the redshift range spanned by the selected galaxies and the redshift centroid of that redshift range, respectively. This implies that the value of $\mathcal{P}$ at $\overrightarrow{x}$ ultimately depends on the set $\{z_j\}$ of the redshifts of the galaxies in the field of the beacon, where each set $\{z_j\}$ is selected in such a way that the corresponding $(z_{\rm centroid}; \Delta z)$ belongs to a neighborhood of

$\overrightarrow{x}$. This argument shows that $\overrightarrow{x}$ is a function of $\{z_j\}$ and, therefore, $\mathcal{P}$ is a function of $\{z_j\}$, i.e. $\mathcal{P}(\overrightarrow{x}) = \mathcal{P}(\overrightarrow{x}(\{z_j\})) = \mathcal{P}(\{z_j\})$.

Each set $\{z_j\}$ is a specific realization of the photometric redshifts. Each set belongs to the ensemble constituted by all the possible redshift realizations. These realizations are ideally drawn from the redshift probability distributions of the galaxies in the field of the beacon.

Since $\mathcal{P}$ is not an analytic function, first we assume that $\mathcal{P}$ is defined on a discrete domain, given by the points in Figure 6.3 (left panel), then we consider a local analytic first-order approximation of $\mathcal{P}$ at $\overrightarrow{x}$. By construction, the analytic approximation has a local continuous domain. For the sake of simplicity, in the following we do not distinguish $\mathcal{P}$ from its analytic approximation. Adopting the analytic approximation allows us to use a differential approach in the context of standard, i.e. non-stochastic, mathematical analysis[3] and expand $\mathcal{P}$ in Taylor series as follows:

$$\delta\mathcal{P} = \overrightarrow{\nabla}\mathcal{P}\cdot\delta\overrightarrow{x} + o\left(\frac{|\delta\overrightarrow{x}|}{\Delta z}\right) , \tag{6.13}$$

where $\delta\mathcal{P}$ is the fluctuation of $\mathcal{P}$ induced by the displacement $\delta\overrightarrow{x}$.

The first term in the right hand side (rhs) of the equation is the scalar product of the displacement $\delta\overrightarrow{x}$ and the gradient $\overrightarrow{\nabla}$ of $\mathcal{P}$ with respect to $\overrightarrow{x}$.

We stress that it is not straightforward to provide an explicit expression for all the terms in the Taylor series.[4] In fact, the explicit expression depends on the specific number counts in the field, the specific redshift $z_{\rm centroid}$ and redshift bin Δz. We checked that finite differences $\Delta\mathcal{P}$ of $\mathcal{P}$ corresponding to small displacements $|\Delta\overrightarrow{x}|$ in the PPM plots (e.g. in Figure 6.3, left panel) satisfy the relation $|\Delta\mathcal{P}|/|\Delta\overrightarrow{x}| \lesssim 1/\Delta z$ for almost all of the $\geq 2\sigma$ points in the plot (except for a negligible set). This argument leads to the term $o\left(|\delta\overrightarrow{x}|/\Delta z\right)$ in Equation 6.13 and implicitly implies that only those points associated with high significance (i.e. $\gtrsim 2\sigma$) patterns are considered. This constraint does not affect our analysis. In fact, as outlined below, only these patterns may be ultimately associated with cluster detections.

The perturbation $\delta\mathcal{P}$ at $\overrightarrow{x}$ can be alternatively estimated as follows. Limiting our analysis to a neighborhood of $\overrightarrow{x}$ and to the field of the beacon, analogously to what has been done in Equation 6.13, we estimate the perturbation $\delta_{ph}\mathcal{P}$ of $\mathcal{P}$ induced by the different realizations of $\{z_j\}$ within the ensemble or, equivalently, by displacements δz_j around each redshift z_j,

[3] We note that a variational approach may also be applied considering the fact that $\mathcal{P}$ may be expressed as a functional of the galaxy number count function at $z_{\rm centroid}$ and Δz.

[4] Let f and g be two functions defined on some subset of the real numbers. $f(x) = o(g(x))$ as $x \to x_0$ if and only if for all $K > 0$ there exists $\delta > 0$ such that $|f(x)| \leq K|g(x)|$, for each x: $|x - x_0| < \delta$.

as follows:

$$\delta_{ph}\mathcal{P} = \sum_j \frac{\partial \mathcal{P}}{\partial z_j}\delta z_j + o\left(\frac{\sqrt{\sum_j \delta z_j^2 / \sum_j 1}}{\Delta z}\right) , \tag{6.14}$$

where the sum over j is restricted to a neighborhood of $\overrightarrow{x}$ as specified above and to the galaxies in the field of the beacon. The subscript ph stands for photometric redshifts and it is introduced to distinguish the perturbation $\delta_{ph}\mathcal{P}$ from $\delta\mathcal{P}$. The first and second terms in the rhs of the equation are the first term and the higher order terms of the Taylor expansion, respectively. The second term reported in Equation 6.14 is estimated similarly to what has been done done in Equation 6.13. The chain rule is also applied to express the derivatives with respect to z_j into derivatives with respect to Δz and $z_{\rm centroid}$.

We stress that the perturbations $\delta\mathcal{P}$ and $\delta_{ph}\mathcal{P}$ are different; $\delta\mathcal{P}$ is the perturbation of $\mathcal{P}$ due small displacements $\delta(\Delta z)$ and $\delta z_{\rm centroid}$ of the redshift bin and the redshift centroid, respectively. Conversely $\delta_{ph}\mathcal{P}$ is the perturbation of $\mathcal{P}$ due to the photometric redshift uncertainties of the redshifts of the galaxies in the field of the beacon. Equivalently, $\delta_{ph}\mathcal{P}$ is the perturbation of $\mathcal{P}$ in the ensemble of all the possible redshift realizations of the galaxies in the field of the beacon. Combining Equation 6.13 and Equation 6.14 we estimate the difference between the two perturbations of $\mathcal{P}$ as follows:

$$\delta\mathcal{P} - \delta_{ph}\mathcal{P} = o\left(\frac{|\delta\overrightarrow{x}| + \sqrt{\sum_j \delta z_j^2 / \sum_j 1}}{\Delta z}\right) , \tag{6.15}$$

where the same notation and the chain rule adopted above is used. The equation, combined with the Equation 6.13 and Equation 6.14, shows that the two perturbations $\delta\mathcal{P}$ and $\delta_{ph}\mathcal{P}$ are equal up to the first order in the Taylor expansion.

By construction, the filter $\mathcal{W}$ removes the fluctuations of $\mathcal{P}$ on small scales. Because of the exponential declining of the Gaussian filter, it is effective on scales $|\delta\overrightarrow{x}| \lesssim 3\sigma_w = 0.06$. As will be explained below, cluster candidates are selected at the fixed redshift bin $\Delta z = 0.28$. This redshift bin corresponds to the estimated statistical 2-σ photometric redshift uncertainty at $z \sim 1.5$ for dim galaxies (i.e. with AB magnitude $i^+ \sim 24$, Ilbert et al., 2009).

Therefore, $|\delta\overrightarrow{x}|/\Delta z \simeq 2\% \ll 1$. This inequality implies that the scales are sufficiently small to assure that the filter $\mathcal{W}$ suppresses the perturbation $\delta\mathcal{P}$ up the first order, as in Equation 6.13, i.e. $\delta\mathcal{P} = 0$ at the first order.

Similarly, the condition $\sqrt{\sum_j \delta z_j^2 / \sum_j 1} \lesssim \Delta z$ is reasonably satisfied, because $\sqrt{\sum_j \delta z_j^2 / \sum_j 1}$ approximately corresponds to the quadratic average of the photometric redshift uncertainties of the galaxies in the field. Such

an average is reasonably smaller than the selected redshift bin $\Delta z = 0.28$. Therefore, the perturbation $\delta_{ph}\mathcal{P}$ in Equation 6.14 is well approximated, for our purposes, by the linear expansion.

Resuming, Equation 6.13 and Equation 6.14, combined with the two reported inequalities, suggest that in our case both $\delta\mathcal{P}$ and $\delta_{ph}\mathcal{P}$ can be expressed in linear theory. Similarly, Equation 6.15, combined with the two inequalities, tells that the two perturbations are equal in first-order approximation. Therefore this argument suggests that the filter $\mathcal{W}$ simultaneously suppresses (in linear approximation) both the perturbation $\delta\mathcal{P}$ and the perturbation $\delta_{ph}\mathcal{P}$ due to the photometric redshift uncertainties.

This discussion suggests that $\overline{\mathcal{P}}$ is a good estimate of the number count excess probability. In fact, as discussed in Section 6.5, since the photometric redshift uncertainties add a significant contribution to the total number count variance, $\mathcal{P}$ represents an overestimate of the true detection significance. Our procedure takes into account - *a posteriori* - the initial overestimation: the significance of the local maxima is decreased when the filter is applied. Equivalently, the procedure reasonably removes, as required, the excess of $\mathcal{P}$ that is ultimately due to the photometric redshift uncertainties and the corresponding number count variance expressed in Equation 6.1.

Note that the parameters adopted here for the Gaussian kernel and those used in the following for the cluster detection procedure are chosen because of the properties of the photometric redshifts of our sample and of the Ilbert et al. (2009) catalog. In particular, the parameters Δz (= 0.28) and σ_w (=0.02) are fine tuned in such a way that the linear perturbation theory (see Equation 6.13 and Equation 6.14) is reasonably correct in both the two spaces (that of $\overrightarrow{x}$ and the ensemble of all the redshift realizations). In general, all the parameters are adapted to the specific dataset used. We verified that our results are independent of a slightly (a few percent) different choice of all these parameters. This is ultimately due to the fact that the procedure is not performed on physical observables (e.g. on the density field), but acts directly on the PPM plots as those reported in Figure 6.3.

In Figure 6.3, right panel, we plot the values of $\overline{\mathcal{P}}$ as a function of $z_{\rm centroid}$ and Δz. The same color code for the left panel is adopted. When the Gaussian filter is applied, isolated noisy patterns are substantially removed from the plot, as clear from visual comparison of the left panel with the right panel. Furthermore, we observe that triangular shape high significance (i.e. $\gtrsim$ 2-σ) patterns are still clearly present in the plot. They are stable with respect to different values of Δz, i.e. the patterns are extended along the Δz axis. In particular, they tend to increase their width in the $z_{\rm centroid}$ direction for increasing Δz. This is due to the fact that for increasing Δz we are including more and more objects that are far from $z_{\rm centroid}$. Therefore, we still detect a number count excess at values of $z_{\rm centroid}$ that are increasingly far from the true redshift of the overdensity, even if with lower significance. In fact, lower significance is associated with the boundaries of the triangular

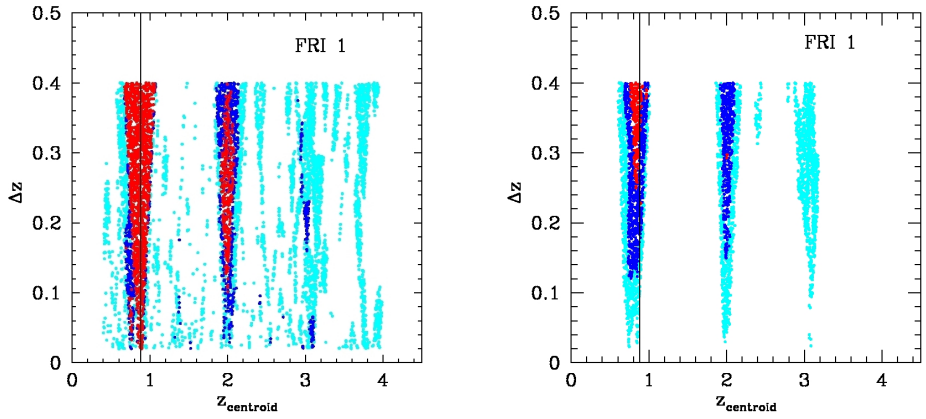

(a) (b)

Figure 6.3: PPM plots for source 01. Left: no filter is applied. Right: the Gaussian filter which eliminates high frequency noisy patterns is applied. The abscissa of the vertical solid line is at the spectroscopic redshift of the source. We plot only the points corresponding to detected overdensities for different values of Δz and $z_{\rm centroid}$. Color code: $\geq 2\sigma$ (cyan points), $\geq 3\sigma$ (blue points), $\geq 4\sigma$ (red points).

shape patterns than that related to the central regions of these patterns.

6.8 Peak finding algorithm

In this section we will describe our procedure to detect and characterize the overdensities we find in the considered field by using the PPM plots. These goals will be achieved by finding the local maxima of the function $\overline{\mathcal{P}}$. The peak finding algorithm we will describe is a specific procedure we developed for our discrete case and it belongs to a more general context known as Morse theory. Such a theory can be used to find and characterize the critical points of differentiable functions defined on a manifold (see e.g. Guest, 2001, for a review). Notably, there are many applications of Morse theory in the context of differential topology (Bott, 1960; Milnor, 1963), and in quantum field theory (Witten, 1982, and following work).

Firstly, since the high significance patterns in the PPM plots are stable with respect to the Δz axis we simplify the problem to a 1-d case as follows. We consider only those points $p_k = (z^k_{\rm centroid}; \Delta z^k)$ such that the redshift bins Δz^k fall within a tiny $\delta(\Delta z) = 0.01$ wide interval centered at $\Delta z = 0.28$. This redshift bin corresponds to the estimated statistical 2-σ photometric redshift uncertainty at $z \sim 1.5$ for dim galaxies (i.e. with AB magnitude $i^+ \sim 24$, Ilbert et al., 2009). These magnitudes are typical of the galaxies we expect to find in clusters in the redshift range of our interest. We verified

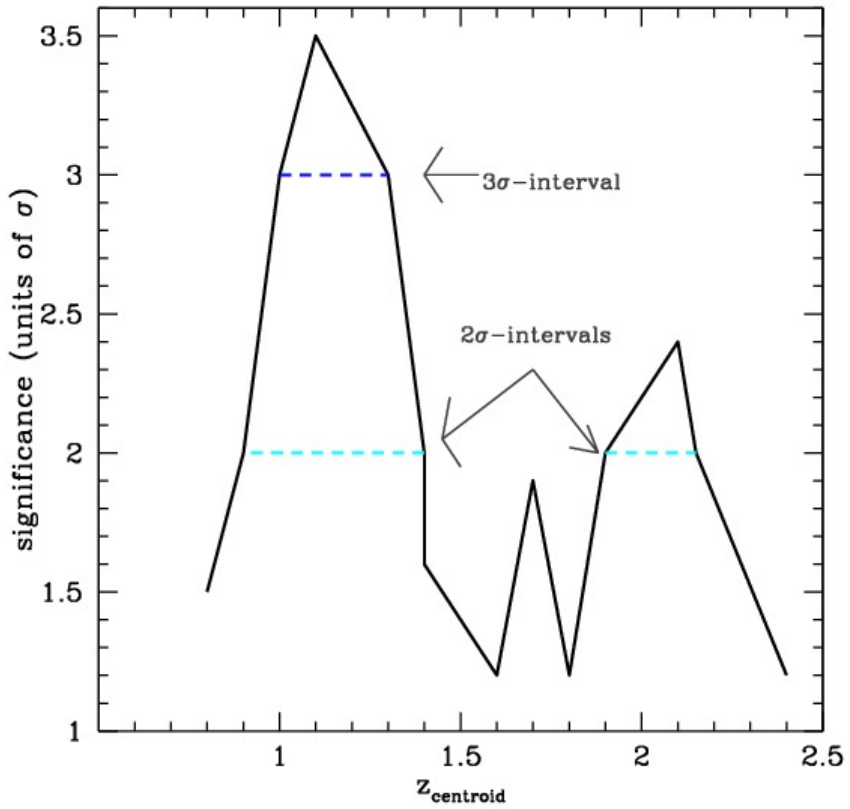

Figure 6.4: Visual representation of the peak finding algorithm. The centroid of the redshift bin $\Delta z \simeq 0.28$ is plotted in the x-axis. The values of $\overline{\mathcal{P}}$ in units of σ are reported in the y-axis. Solid black line: significance as a function of the centroid redshift $z_{\rm centroid}$. Horizontal dashed lines: 2σ- and 3σ-intervals. According to the peak finding procedure, the 2σ-interval in the plot associated with the peak at $z_{\rm centroid} \sim 1.1$ is rejected, since it entirely contains the higher significance 3σ-interval shown in the Figure. No s-interval is associated with the peak at $z_{\rm centroid} \sim 1.7$. This is because its significance is less than the 2σ threshold.

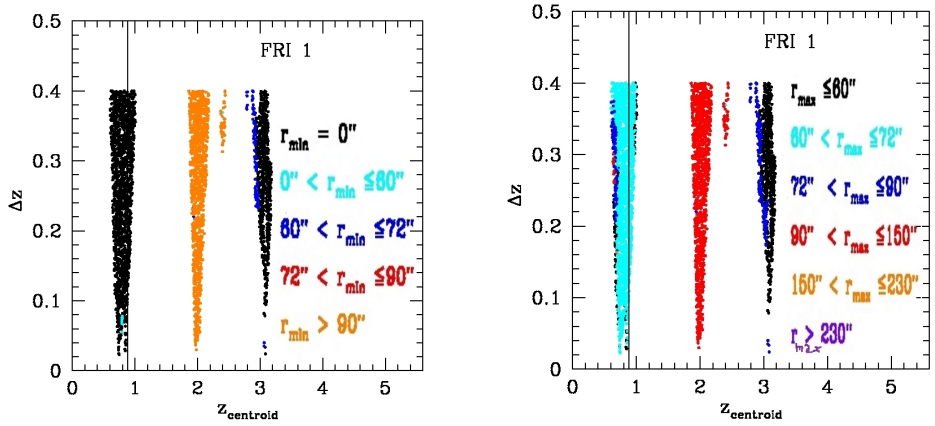

(a) (b)

Figure 6.5: PPM plots for source 01, $\geq$ 2-σ points are plotted. Radial cluster information concerning $r_{\rm min}$ (left panel) and $r_{\rm max}$ (right panel). See legend in the panels for information about the color code adopted. In each panel the abscissa of the vertical solid line is at the spectroscopic redshift of the source.

that our results are stable with respect to a slightly (a few percent) different choice of the redshift bin.

Then, we sort the points $\{p_k\}$ in increasing order of $z^k_{\rm centroid}$, and we redefine the ordering of the points in such a way that $z^{k+1}_{\rm centroid} \geq z^k_{\rm centroid}$. Hence, our problem is reduced into finding the maxima of $\overline{\mathcal{P}}$ defined on the 1-d discrete domain $\{z^k_{centroid}\}$. Having reduced the dimensionality of the domain is a great simplification, since saddle points are not present in the 1-d case, where critical points are of only two types: maxima and minima.

Starting from the significance $s = 2\sigma$, we select those intervals of consecutive points that have significances $\geq s$. We merge consecutive intervals that are separated by $\delta z_{\rm centroid} = 0.02$ or less along the $z_{\rm centroid}$ axis. We also reject those intervals that are smaller than $\delta z_{\rm centroid} = 0.1$ along the $z_{\rm centroid}$ axis. The first condition merges those intervals that are separated by a tiny separation along the $z_{\rm centroid}$ axis. The minimum allowed separation between two consecutive intervals is set equal to the dispersion σ_w adopted for the filtering procedure. In fact, fluctuations that occur on these scales may not be physical since they occur for redshift separations that are well below those of the typical statical redshift uncertainties. Similarly, the second condition is applied in order to detect only high significance features whose length along the $z_{\rm centroid}$ axis is at least comparable with the typical statistical photometric redshift uncertainty of the Ilbert et al. (2009) sample. Given the significance s, this procedure gives a set of intervals that we define as s-intervals.

Then, we increase the significance threshold by a tiny amount $ds = 0.1\sigma$ and we repeat the above outlined procedure. We note that each $(s + ds)$-interval is entirely included within a s-interval. We retain those s-intervals that do not contain any $(s + ds)$-interval, whereas we reject all the other s-intervals.

The significance s is increased and the procedure is repeated until no s-interval is found. The final set of s-intervals represents the local maxima of $\overline{\mathcal{P}}$. These intervals have different significances s and they are centered at different redshifts $z_{\rm centroid}$. Each s-interval corresponds to a cluster candidate detection and is associated with a number count excess found in the given field and around a specific redshift. In Figure 6.4 we show a visual representation of the peak finding algorithm adopted. In the following section we will describe how the method estimates cluster properties such as the redshift and size.

6.9 Cluster candidates selection

The significance s of a given s-interval is interpreted as the detection significance of the corresponding cluster candidate. In this section we describe our procedure that provides (i) an estimate for the redshift of the overdensity, (ii) an estimate for the cluster core size, and (iii) a rough estimate for the cluster richness.

We estimate the size of each cluster candidate in terms of the minimum and maximum distances from the beacon (in our case the FR I) at which the overdensity is detected. According to our procedure, the points of the s-interval are associated with different values of $r^i_{\rm min}$ and $r^i_{\rm max}$. We estimate a minimum and a maximum projected radius of the overdensity as the average (and the median) of the minimum ($r^i_{\rm min}$) and maximum distances ($r^i_{\rm max}$) associated with all of the points of the s-interval, respectively. The uncertainty is estimated with the rms dispersion around the average. The maximum projected radius provides also an estimate for the cluster core size (see also Chapters7 and 8).

In Figure 6.5 we show the PPM plots for source 01, (after having applied the Gaussian filter) where the radial information concerning $r_{\rm min}$ (left panel) and $r_{\rm max}$ (right panel) is considered. Analogously to what has been done for Figure 6.3, we only plot points that are associated with $\geq$ 2-σ overdensities (see the legend in the panels for the color code adopted). The vertical solid line in each panel is located at the redshift of source 01. The values of $r^i_{\rm max}$ and $r^i_{\rm min}$ associated with the high significance patterns of our plots are very stable with respect to the Δz (see Figure 6.5). Therefore, the particular choice $\Delta z = 0.28$ does not affect the results concerning the projected space analysis. All PPM plots concerning $r_{\rm min}$ and $r_{\rm max}$ for all 32 radio sources in our sample are reported in Appendix A, in Figures A.2 and A.3, respectively.

We also estimate the redshift of the cluster as the middle point of the s-interval. To estimate the fiducial uncertainty of the cluster redshift we consider all the sources located within the median value of minimum distance and the median value of the maximum distance from the coordinates of the FR I within which the overdensity is detected in the projected space. We also limit to the sources that have photometric redshifts within a redshift bin $\Delta z = 0.28$ centered at the estimated cluster redshift. This is done consistently with our detection procedure. The cluster richness is roughly estimated by the number of the selected sources. Then, the cluster redshift is estimated at 1-σ level by the rms dispersion around the average of the redshifts of the selected sources.

In particular, if $N \gg 1$ sources were uniformly distributed within the redshift bin $\Delta z = 0.28$ we would obtain an rms dispersion of 0.08. We expect the estimated redshift uncertainty to be around this value.

6.10 Cluster candidate - FR I association

The method described here detects Mpc-scale overdensities within the entire redshift range spanned by the $z_{\rm centroid}$ values. Then, we associate with the radio galaxy only those overdensities that are detected in the field, at a redshift compatible with that of the source, i.e. when the interval centered at the redshift estimated for the overdensity and with a half-width equal to 2 times the fiducial redshift error intersects the redshift range defined by the radio galaxy redshift uncertainties. Multiple overdensity associations are not excluded.

6.11 Considerations about the redshift information

We point out that the redshift of the FR I beacon is considered only during the last step of the method procedure, when we perform the association between the detected overdensities and the radio galaxy. This is primarily motivated by the fact that we do not have spectroscopic information for most of our FR Is. Therefore, our approach is necessarily different from previous studies which select cluster members using photometric redshifts for the majority of the galaxies in the field, but also knowing the spectroscopic redshifts of some of the cluster members (e.g. Papovich et al., 2010).

Furthermore, our choice implies that the high significance patterns in our plots (see e.g. Figure 6.3) have a typical width along the $z_{\rm centroid}$ axis comparable to the statistical photometric redshift uncertainty $\sigma_z \sim 0.054(1+z_{\rm centroid})$. Such an uncertainty corresponds to sources with $i^+ \sim 24$ and $1.5 < z < 3$ sources (see Table 3 of Ilbert et al., 2009), which we expect to find in our clusters. Therefore, our method estimates the cluster redshifts

with similar accuracy. On the other hand, including the (photometric) redshift information of the FR I beacon from the beginning of our procedure would imply an increase of the intrinsic scatter due to the FR I redshift uncertainty. If we sum in quadrature the redshift uncertainty associated with each FR I to the statistical photometric redshift uncertainty $\sigma_z \sim 0.1 - 0.2$, the uncertainty increases up to $\sim 0.2 - 0.5$, depending on the redshift of the radio galaxy and its uncertainty. This effect would make our method ineffective to search for high-z cluster candidates around radio galaxies.

6.12 Generalization to other datasets

In this section we describe how the PPM can be generalized for its application to other datasets and photometric redshift catalogs, whose statistically redshift accuracy is possibly comparable or better than that of the Ilbert et al. (2009) catalog. Surveys with a similar or higher depth than that of COSMOS are preferred. In particular, the PPM might be applied to both present and future wide field surveys such as SDSS Stripe 82, Large Synoptic Survey Telescope (LSST), and *Euclid* (see Section 12.2.1 for a discussion).

The parameters should be adapted to take into account the different mean field number density of galaxies in the survey and the statistical photometric redshift uncertainties of the redshift catalog. Therefore, it is not straightforward to provide precise rules.

In general, the redshift bin Δz at which the overdensities are evaluated in the PPM plots should be set equal to the 2-σ statistical photometric redshift uncertainty of the galaxies at the redshifts of our interest and magnitudes typical of the sources we expect to find in clusters at high redshifts.

Consequently the length of the s-intervals should be at least about one-third of the specific redshift bin Δz adopted to select the overdensities in the PPM plots. We remind that the s-intervals are the high significance intervals in the PPM plots (at the specific Δz) that are associated with overdense regions. Similarly, the Gaussian dispersion σ_w used to remove the noise from the PPM plots should be equal to one-fifth of the above mentioned minimum length for the s-interval. As described and motivated in the procedure description (see Section 6.8) when defining the s-intervals, consecutive intervals that are separated by an amount σ_w ($= 0.02$ in this work) or less along the $z_{\rm centroid}$ axis should be always merged. Such scaling relations are motivated by the fact that the adopted parameters should ultimately rescale linearly with the typical statistical photometric redshift accuracy.

Furthermore, according to the procedure description we do not change the PPM tessellation with increasing cluster redshift. This is mainly because we are looking for overdense regions with sizes typical of cluster cores and the angular distance $D_A(z)$ at the redshift z is fairly constant between $z \sim 1-2$.

However, it might be appropriate to rescale linearly the size of the PPM tessellation by a factor of $\sim D_A(z = 1.5)/D_A(z)$ in the case where the PPM is used to search for diffuse protoclusters at redshifts significantly higher than $z \sim 1 - 2$ (e.g., at $z \gtrsim 6$, Trenti et al., 2012; Toshikawa et al., 2014). This leads to a correction $\sim 21\%$, 46%, and 51% at redshifts $z \sim 4$, $z \sim 6$, and $z \sim 8$, respectively.

Chapter 7

PPM tested against simulations

In this Chapter we test the PPM against simulations. We use the COSMOS survey and the photometric redshift catalog of Ilbert et al. (2009). We follow two different approaches: i) we use two clusters discovered in the COSMOS field at $z \sim 1$ and then we shift them to higher redshifts in order to assess the PPM efficiency to detect Mpc-scale structures at progressively high redshifts; ii) we simulate spherically symmetric clusters of different size and richness, and we locate them at different redshifts (i.e., $z = 1.0$, 1.5, and 2.0) in the COSMOS field. Then, we apply the PPM and we test if we can detect the simulated clusters.

Note that we do not test our method adopting mock catalogs derived from N-body numerical simulations to simulate the COSMOS density field shown in previous work for groups in COSMOS up to to $z \simeq 1$ (e.g. George et al., 2011; Jian et al., 2014). This test omission is motivated by the fact that we lack sufficient spectroscopic redshift information. We also have both smaller number count statistics and larger photometric redshift uncertainties both of which strongly affect these studies at higher redshifts (i.e. $z \gtrsim 1$).

7.1 Clusters at $z \simeq 1$ shifted to higher redshifts

In this section we test the effectiveness of the PPM in detecting overdensities as a function of redshift. We consider the $z \sim 1$ cluster candidates with id numbers 62 and 126 (F062 and F126, respectively) in the Finoguenov et al. (2007, FGH07) group COSMOS catalog, selected by using XMM-*Newton* observations (Hasinger et al., 2007).

F062 is in the field of the source COSMOS-FRI 01. This source is part of the C09 sample and it is found in rich Mpc-scale environment by the PPM (see Chapter 8). The offset between the X-ray centroid of F062 (estimated in FGH07) and the projected coordinates of COSMOS-FRI 01 is

about ∼10 arcsec. This corresponds to 78 kpc at the spectroscopic redshift of the radio galaxy, i.e. $z_{spec} = 0.88$ (Lilly et al., 2007; Trump et al., 2007). The redshift of F126 as estimated in FGH07 is $z = 1.0$. FGH07 also estimated masses $M_{500} = (5.65 \pm 0.37) \times 10^{13}\ M_{\odot}$ and $(6.87 \pm 0.69) \times 10^{13}\ M_{\odot}$ for F062 and F126, respectively.[1]

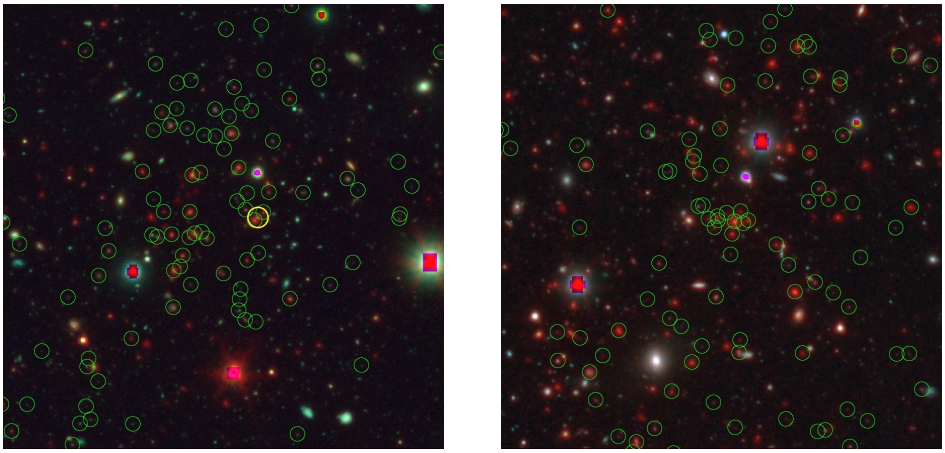

Figure 7.1: RGB images of F062 (left) and F126 (right) centered at the X-ray coordinates of the clusters, as in FGH07. The images are obtained using Spitzer 3.6μm, Subaru r$^+$- and V-band images for the R, G, and B channels, respectively. Green circles indicate objects with $0.78 < z_{\rm phot} < 0.98$ (left) and $0.9 < z_{\rm phot} < 1.1$ (right). The yellow circle in the left panel shows the location of COSMOS-FR I 01. The projected sizes of the fields are 180"×180". North is up.

In Figure 7.1 we plot the RGB images of F062 (left panel) and F126 (right panel) centered at the X-ray coordinates of the clusters, as in FGH07. We plot as green circles the locations of the galaxies in the Ilbert et al. (2009) catalog with photometric redshifts within a $\Delta z = 0.2$ long redshift bin centered at the redshift of the cluster. Concerning F062, we show as a yellow circle the location of COSMOS-FR I 01. The images are obtained using Spitzer 3.6μm, Subaru r- and V-band images for the R, G, and B channels, respectively. As clear from visual inspection, both F062 and F126 exhibit a clear segregation of red objects within their Mpc-scale core. Note that the brightest cluster member of F126 is associated with a radio source that is below the flux threshold of the C09 catalog. F062 and F126 also have comparable core sizes, X-ray fluxes, luminosities and temperatures (see Table 1 in FGH07 for further details). They have similar X-ray properties, but F126 seems significantly richer than F062 (see Figure 7.1). Hence, we prefer to consider both of them, instead of one only. This is in order to

[1]Here M_{500} (M_{200}) is the mass enclosed within the radius encompassing the matter density 500 (200) times the critical one.

make our conclusions more robust. In fact, if we adopted one single cluster candidate, our simulations might be biased by the specific properties of that overdensity and our results might not be valid in a more general sense. In the following we outline the different tests we perform. In Section 7.1.1 we will describe the results in detail.

1. Firstly, we apply the PPM and we test if it detects F062 and F126 (at their actual redshift).

2. We apply the PPM using increasing offsets between coordinates of the center of the PPM tessellation and the X-ray coordinates of the cluster center. This is done to estimate the required accuracy in the projected coordinates of the cluster center in order to detect cluster candidates with the PPM.

3. We shift both F062 and F126 to higher redshifts and we test whether the PPM is able to detect them. The procedure is quite complex and we describe it in the following. We select the fiducial cluster members adopting a color $(I-K)_{AB}$ selection criterion to identify the redder sources. A cluster membership is required since we want to shift the cluster members to increasing redshifts. The cluster members are selected within a redshift bin centered at the redshift of the cluster candidate and within a projected area centered at the X-ray cluster coordinates. Both the redshift bin and the projected area are selected accordingly to the PPM, as we will discuss in detail. A color selection is preferred to a cluster membership assigned on the basis of the photometric redshift information. Our choice is motivated by the fact that we select galaxies that are in the field and at the redshift of F062 and F126, until the mean COSMOS density is reached. A selection based on the photometric redshift information (e.g. Papovich et al., 2010) might be biased towards selecting cluster galaxies as well as field galaxies. This would imply an overestimate of the number of the cluster members as well as of the number count excess associated with F062 and F126. Conversely, our color criterion avoids it, since we select galaxies starting from the reddest ones, that are most likely the elliptical galaxies of the cluster.

   We subtract the cluster members from the fields of F062 and F126. We apply the PPM to see if any residual structure is detected and if the cluster membership has been correctly assigned. Some of the cluster members may have not been identified. If this is the case, the PPM might still detect an overdensity in the field, once the cluster members are subtracted. However, the opposite case in which too many sources are selected as cluster members is not tested with this approach. This is because the PPM is not used to detect the presence of underdense regions.

We add the fiducial cluster members to the fields of two sources of the C09 sample, namely COSMOS-FRI 70 and COSMOS-FRI 66, where no overdensity is detected by the PPM in the redshift range $z \sim 1-2$ of our interest (see Chapter 8). This is done by applying a rigid rotation to the projected coordinates of the selected cluster members. Two fields are used because weak overdensities not detected by the PPM procedure might be present in the redshift range of our interest. Therefore, the clusters would be more easily detected if their members are shifted to the redshifts of these non-detected overdensities. This might imply that the cluster detection significance is overestimated. The choice of two fields reduces the possibility that this bias occurs. Then we apply the PPM in the new field to test if Mpc-scale overdensities is still detected.

We shift the fiducial cluster members to $z_{\rm c,sim} = 1.5$, 2.0. We firstly estimate the AB I-band magnitude $I_{\rm sim}$ that each of the cluster member would have if located at higher redshift $z_{\rm c,sim}$. Then we reject all of the cluster members with $I_{\rm sim} \geq 25$. This is the same selection criterion applied in Ilbert et al. (2009) in estimating the photometric redshifts. This is done to simulate the COSMOS sensitivity and to properly reject the faintest galaxies that would not be detected when shifted to a redshift higher than their own.

We assign a photometric redshift to each of the cluster members selected with the previous procedure, according to a Gaussian probability distribution. The average is set equal to the redshift of the simulated cluster $z_{\rm c,sim}$. We adopt a variance equal to the square of the typical statistical 1-σ accuracy $\sigma_z(z_{\rm c,sim}) = 0.054(1+z_{\rm c,sim})$ of the photometric redshifts around $z_{\rm c,sim}$ for sources with $i^+ \sim 24$ and redshifts within $1.5 < z < 3$ (see Table 3 of Ilbert et al., 2009), typical of the cluster galaxies we consider. This is done in order to assign properly a photometric redshift to each of the cluster members once they are shifted to a redshift higher than the true redshift of the cluster.

We finally apply the PPM to see if the clusters are still detected by the PPM at $z = 1.5$ and 2.0.

7.1.1 Results

1. In Figure 7.2 we show the PPM plots (as in Figure 6.2, see Section 6.2) for F062 (left) and F126 (right). We adopt the following color code: $\geq 2\sigma$, $\geq 3\sigma$, and $\geq 4\sigma$ points are plotted in cyan, blue, and red, respectively. The abscissa of the vertical solid line indicates the redshift of the cluster candidate.

In Table 7.1 we report the PPM results for F062 and F126 (top table). We also report the PPM results of our simulations, when these two clusters

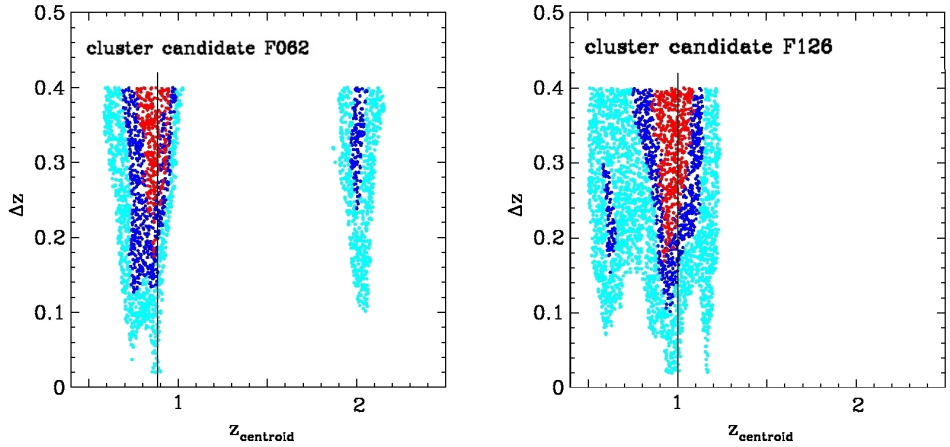

(a) (b)

Figure 7.2: PPM plots for the cluster candidates F062 (left), F126 (right), as given in FGH07. Overdensities: $\geq 2\sigma$ (cyan points), $\geq 3\sigma$ (blue points), $\geq 4\sigma$ (red points). The vertical solid lines indicate the redshift of the cluster candidate.

are added to the fields of COSMOS-FR I 66 and COSMOS-FR I 70 of the C09 sample (middle table). In the bottom table we report the PPM results where the clusters are shifted to $z = 1.5$. In the first four columns we list the cluster ID number (i.e. F062, F126), the cluster redshift, the cluster redshift as estimated by the PPM, and the cluster detection significance. In the fifth column we report the distance $r_{\rm max}$ from the location of the radio galaxy in the projected space at which the overdensity formally ends. For this quantity, the average, the rms dispersion around the average and the median value (between parenthesis) in units of arcsec are reported, as estimated by the PPM procedure. The rms dispersion and the median value are not reported where the former is null, i.e. where the estimated $r_{\rm max}$ is maximally stable with respect to $z_{\rm centroid}$, i.e. where the rms dispersion is null. In the sixth column we report the field to which the cluster is added; 66 and 70 denote that the cluster members are added to the fields of COSMOS FR I 66 and COSMOS FR I 70, respectively. The symbol "—" denotes that the PPM is applied to the fields of F062 and F126, where the cluster members are not subtracted.

Concerning the PPM results for F062 and F126 (top table), they are detected with significance levels of 3.8σ and 4.3σ, respectively. The estimated redshifts are $z = 0.86$ and $z = 0.96$, respectively. In addition to the cluster candidate at $z \sim 1$, the PPM detects another 2.7σ overdensity in the field of F126 at $z = 0.64$. This is a clear example of a projection effect.

Note that our redshift estimates fully agree with the actual redshifts of the two cluster candidates (i.e. $z = 0.88$ and $z = 1.0$ for F062 and F126,

respectively) and that the PPM effectively finds systems whose masses are compatible with those of rich groups and, therefore, they are even below the typical cluster mass cutoff $\sim 1\times10^{14}\ M_{\odot}$, as it is the case for F062 and F126. Hereinafter we do not estimate the redshift uncertainties following the PPM procedure prescription. This is mainly because we know the redshift of the cluster in our simulations. Therefore, we can directly compare our estimates with the original cluster redshifts to derive the statistical uncertainties. Conversely, in Chapter 8 we estimate redshift uncertainties (following the procedure described above) for the overdensities we find within the C09 sample.

2. We then apply the PPM using increasing offsets θ_{off} between the cluster center of the PPM tessellation and the actual center as measured from the X-ray emission. This is done to find the required accuracy in the coordinates of the cluster center in order to detect Mpc-scale overdensities with the PPM. We keep the right ascension of the center of the PPM tessellation fixed and we change its declination from θ_{off} =10 up to 500 arcsec.

We find that F062 and F126 are detected up to $\theta_{off} = 150$ and 500 arcsec, respectively. The clusters are detected with a fairly constant significance (between $\sim 3.2 - 3.8\sigma$ and $\sim 3.7 - 4.8\sigma$ for F062 and F126, respectively). However a mild trend of decreasing significance for increasing offsets is observed. F062 is detected with significances of 3.8, 3.2, and 3.2σ at $\theta_{off} = 0$, 75, and 150 arcsec, respectively. In fact, F126 is detected with significances of 4.3, 3.9, 3.7, and 3.7σ at $\theta_{off} = 0$, 100, 300, and 500 arcsec, respectively.

A clear trend between $r_{\rm max}$ and θ_{off} is observed for F062. The estimated size increases up to $r_{\rm max} \simeq 150$ arcsec for $\theta_{off} = 125$ arcsec. While the estimated size for $\theta_{off} = 0$ arcsec is $r_{\rm max} = 72.6 \pm 5.1$ arcsec. Conversely, no trend is observed for F126.

These results suggest that the PPM is effective to detect Mpc-scale overdensities even if the projected coordinates of the cluster center are known with an accuracy of only ~ 100 arcsec. This implies that the PPM can be efficiently applied even if the cluster center coordinates are not accurately known.

3. We want to shift these two groups to redshifts higher than $z \sim 1$, thus we select the fiducial cluster members of both F062 and F126. We select those sources that fall within circular regions of radius 70.7 and 165.8 arcsec centered at the coordinates of the cluster center, for F062 and F126, respectively. These are the regions in the projected space within which the clusters are detected by the PPM.

We conservatively select sources with photometric redshifts within a redshift slice $\Delta z = 4\sigma_z(z_c)$ centered around the redshift z_c of the cluster, where $\sigma_z(z_c) = 0.054(1 + z_c)$ is the 1-σ statistical photometric redshift uncertainty of faint galaxies with $i^+ \sim 24$ and $1.5 < z < 3$ sources (see Table 3 of Ilbert et al., 2009), typical of the cluster galaxies we consider. The redshift slice

PPM results for F062 and F126

ID	$z_{\rm cluster}$	$z_{\rm PPM}$	significance	$r_{\rm max}$ (arcsec)	field
F062	0.88	0.86	3.8σ	72.6±5.1 (70.7)	—
F126	1.00	0.96	4.3σ	181.3±33.4 (165.8)	—

F062 and F126 added to the ECFs

ID	$z_{\rm cluster}$	$z_{\rm PPM}$	significance	$r_{\rm max}$ (arcsec)	field
F062	0.88	0.86	3.5σ	71.6±3.6 (70.7)	66
F062	0.88	0.86	4.0σ	74.3±6.7 (70.7)	70
F126	1.00	0.94	4.9σ	109.9±6.1 (111.8)	66
F126	1.00	1.00	4.1σ	92.0±10.0 (86.6)	70

F062 and F126 added to the ECFs and shifted to higher redshift.

ID	$z_{\rm cluster}$	$z_{\rm PPM}$	significance	$r_{\rm max}$ (arcsec)	field
F062	1.50	1.61	2.6σ	50.0 ——	66
F062	1.50	1.56	2.9σ	50.0 ——	70
F126	1.50	1.51	3.1σ	111.3±2.4 (111.8)	66
F126	1.50	1.59	2.5σ	85.4±4.2 (86.6)	70

Table 7.1: PPM results for F062 and F126 where the cluster members are not removed (top table). PPM results where the cluster members are added to the Empty Control Fields (ECFs, middle table) and where they are also shifted to $z = 1.5$ (bottom table). Column description: (1) cluster ID number; (2) cluster redshift; (3) cluster redshift estimated with the PPM; (4) significance of the overdensity estimated by the PPM in terms of σ; (5) average maximum radius [arcsec] of the overdensity along with the rms dispersion around the average (both estimated with the PPM). The median value [arcsec] is written between the parenthesis. The rms dispersion and the median value are not reported in those cases where the rms dispersion is null; (6) field to which the cluster is added; 66 and 70 denote that the cluster members are added to the fields of COSMOS-FR I 66 and COSMOS-FR I 70, respectively. The symbol "—" denotes that the PPM is applied to the fields of F062 and F126, where the cluster members are not subtracted.

considered here is higher than that adopted throughout the PPM procedure (i.e. $\Delta z = 0.28$) to make sure that the large majority of the sources at the redshift of the cluster are included in the bin, even if the accuracy of their photometric redshifts is poor. This is not a cluster membership assignment. In fact, the cluster members will be selected among these sources by using an $(I-K)_{AB}$ color criterion, as we will describe in the following.[2]

Since red and passively evolving galaxies constitute the majority among the cluster core galaxies at $z \sim 1$ we also adopt a color selection criterion to define the fiducial cluster members. We sort the selected galaxies according to their $(I-K)_{AB}$ color, from the redder to the bluer. This specific color criterion has been chosen because the rest frame ∼4000 Å absorption feature typical of the spectra of early type galaxies falls just between the K- and I-bands at redshift $z \sim 1$.

The cluster members are then removed from the field starting from the reddest source until the average COSMOS number density within the selected $4\sigma_z$ bin is reached.

According to the outlined procedure we select as cluster members 57 and 249 galaxies down to $(I-K)_{AB} = 1.12$ and 1.30 magnitudes for F062 and F126, respectively. As expected, these cluster members are faint, since their I-band magnitudes are between $I \sim 21.9 - 25.3$ and $I \sim 21.1 - 25.7$, for F062 and F126, respectively.

We want to make sure that the cluster membership is not biased towards preferentially selecting sources that are located in certain regions in the projected space around the cluster center. In order to do this we verify whether the differential radial number counts are consistent with a constant – no clustering – once the cluster members are removed from the field.

In Figure 7.3 we plot the differential number counts of the sources in the fields of F062 (top panel) and F126 (bottom panel), as a function of the distance from the projected cluster center coordinates. Sources are counted within the $4\sigma_z$ redshift slice adopted throughout the cluster membership procedure and within regions of equal areas (i.e. 2.18 arcmin^2), analogously to what has been done for the PPM. The areas are chosen equal among each other in order to have a constant mean field density per region.

The galaxy number counts along with the corresponding 1-σ Poisson uncertainties for the error are plotted as blue symbols. Number counts, once the cluster members are subtracted from the fields of both F062 and F126, are plotted as black points, along with the 1-σ uncertainties estimated according to the Skellam distribution.[3] The uncertainty in the radial

[2] We denote as I the *Subaru* i^+ magnitude and, if absent, the CFHT i' magnitude. We denote as K the CFHT K-band magnitude. All these magnitudes are from the I09 catalog, they are in AB system, and they are measured within an aperture of 3 arcsec diameter.

[3] The Skellam distribution is the discrete probability distribution of the difference of two statistically independent random variables each having Poisson distributions. The Skellam probability is chosen because we subtract the cluster members from the field.

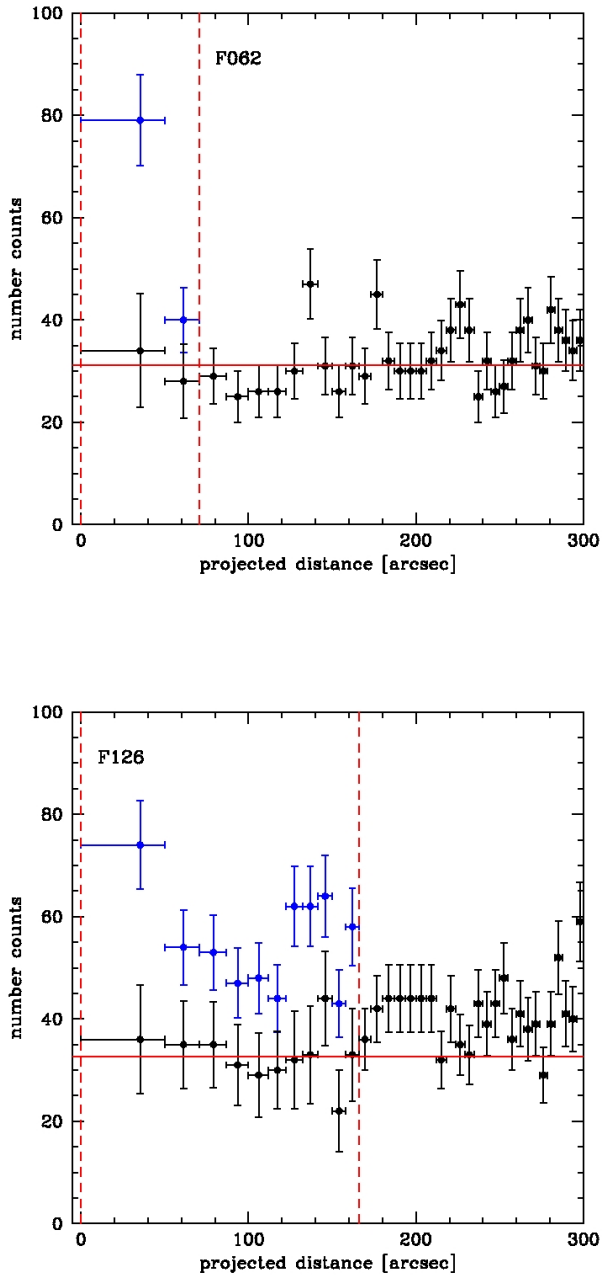

Figure 7.3: Blue points: differential number counts of the sources in the fields of F062 (top panel) and F126 (bottom panel), as a function of the distance from the cluster center coordinates. Sources are counted within a $\Delta z = 4\sigma_z$ redshift bin centered at the redshift of the cluster (i.e. $\Delta z = 0.406$ and 0.432 for F062 and F126, respectively). Black points: differential number counts. Differently from the blue points the cluster members are now subtracted from the field of the cluster. Number count 1-σ uncertainties are plotted along the y-axis. The uncertainty in the radial coordinate is the half-width of each region within which the number counts are performed. Vertical dashed lines show the region where the cluster members are selected. The horizontal solid red line show the mean COSMOS number count per area.

coordinate corresponds to the half-width of each region.

The vertical red dashed lines show the radial interval within which the cluster members are selected. By construction, according to the cluster membership procedure, black and blue points coincide outside of this interval. The horizontal line shows the mean COSMOS number counts of ~ 30 galaxies associated with a 2.18 arcmin^2 area around which the black points are scattered.

The radial profiles of both F062 and F126 clearly show that the number count excess (blue points) is limited within the projected area defined within the vertical dashed lines. Furthermore, once the cluster members are subtracted, such a number count excess disappears. In fact, the values associated with the black points are consistent with the mean COSMOS number density within the reported 1-σ uncertainties, at least within the radial interval defined by the vertical dashed lines where the cluster members are subtracted. Furthermore, considering also the number counts outside such interval the discrepancy is always less than 2-σ.

In Figure 7.4 we report the PPM plots of the fields of F062 and F126, where the cluster members are subtracted. The adopted color code is analogous to that of Figure 7.2. We apply the PPM and we verify that neither F062 nor F126 are now detected. In fact, as clear from visual inspection, the high significance pattern at the redshift of the cluster completely disappears in the case of F062, while a residual $\gtrsim 2\sigma$ feature is still present in the case of F126 at its redshift. According to the PPM procedure, such a feature is interpreted as noise because it is not enough extended to be detected as overdensity, i.e. it is less than $\delta z_{\rm centroid} = 0.1$ long on the redshift axis $z_{\rm centroid}$ at fixed $\Delta z = 0.28$.

The other Mpc scale overdensity that was previously detected by the PPM in the field of F126 at $z = 0.64$ with a significance of 2.7σ is still detected with similar significance (2.6σ) and redshift ($z = 0.61$). This confirms that the specific cluster membership assigned here combined with the PPM is efficient at removing the degeneracy resulting from the projection effect.

As explained above, for our simulations we perform the cluster membership by selecting fiducial cluster members within a circular region centered at the X-ray coordinates of F062 and F126. The radius of the region corresponds to the projected size of the cluster, as estimated by the PPM. In the following we reconsider our estimates by using the PPM plots and we compare the fiducial sizes estimated with the PPM with those obtained by previous work.

In Figure 7.5 we report the PPM plots for F062 (left panel) and F126 (right panel), where only the points corresponding to $\geq$3-σ overdensities are plotted. This is because the two clusters are detected with significance higher than 3-σ. Since we are interested in the cluster size, we plot the cluster size ($r_{\rm max}$) associated with each point in the plot, as estimated by the PPM for specific $z_{centroid}$ and Δz. We refer to the legend in Figure 7.5

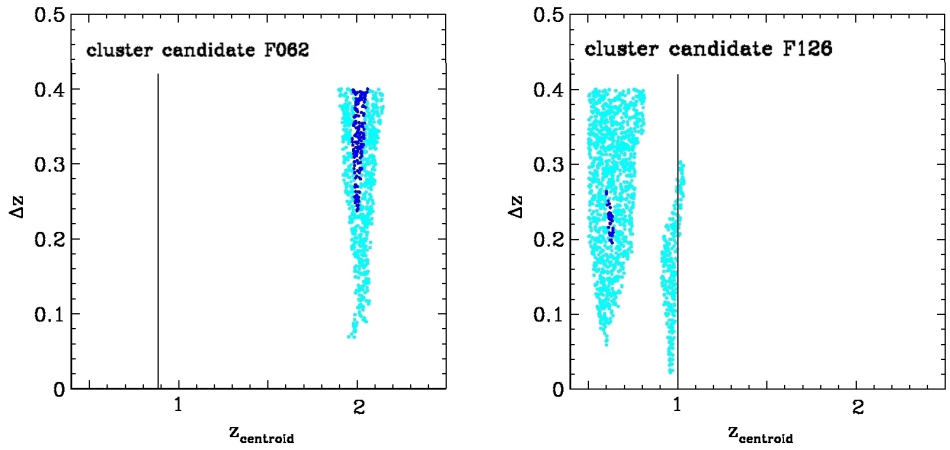

Figure 7.4: PPM plots where the clusters F062 (left) and F126 (right), in the FGH07 catalog, are subtracted. Overdensities: $\geq 2\sigma$ (cyan points), $\geq 3\sigma$ (blue points), $\geq 4\sigma$ (red points). Note that no $\geq 4\sigma$ overdensity is present. The vertical solid line indicates the redshift of the cluster candidate.

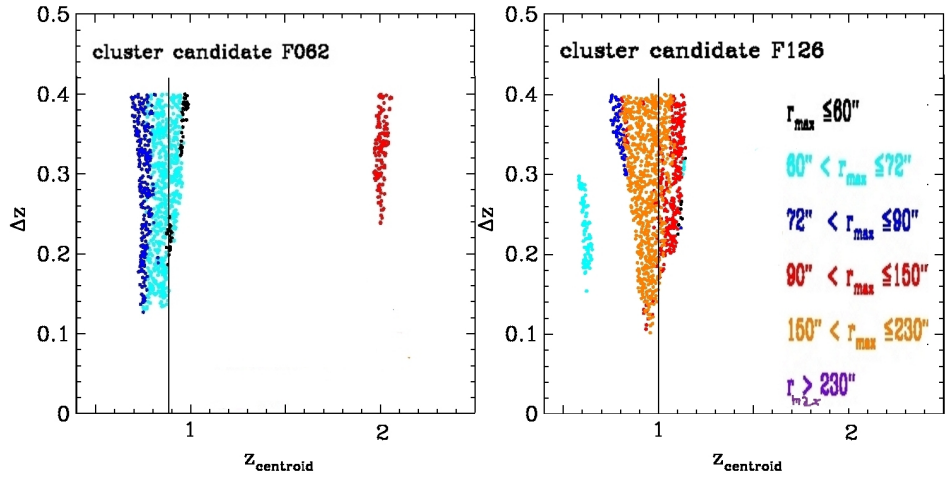

Figure 7.5: PPM plots for F062 (left) and F126 (right). We plot only those points that correspond to $\geq 3\sigma$ overdensities for a specific choice of the redshift bin Δz and its centroid $z_{\rm centroid}$. Different colors correspond to different values of the cluster size $r_{\rm max}$ associated with each point and estimated with the PPM. The color code is the same for both of the panels. See legend in the right plot.

for the specific color code adopted. As clear from visual inspection of the plots, the values of $r_{\rm max}$ are stable with respect to the Δz parameter.

By averaging among the values associated with the points at $\Delta z \simeq 0.28$ that define the overdensities we estimate the sizes $r_{\rm max} = 72.6 \pm 5.1$ arcsec and $r_{\rm max} = 181.3 \pm 33.4$ arcsec for F062 and F126, respectively, according to the PPM procedure. Here we report the average value and the rms dispersion around the average. The cluster sizes 70.7 arcsec and 165.8 arcsec that are assumed when performing the cluster membership correspond to the median values of $r_{\rm max}$ for F062 and F126, respectively.

On the basis of the X-ray surface brightness FGH07 estimated a core size $r_{500} = 48$ arcsec for both F062 and F126. By assuming spherical symmetry and a β-model density profile for the cluster matter distribution (Cavaliere & Fusco-Fermiano, 1978) we estimate $r_{200} = 76$ arcsec for both F062 and F126[4].

George et al. (2011) estimated core sizes $r_{200} = 73$ arcsec and 81 arcsec and core masses $M_{200} = 5.25 \times 10^{13} M_{\odot}$ and $8.32 \times 10^{13} M_{\odot}$, for F062 and F126, respectively, on the basis of the mass versus X-ray luminosity relation given in Leauthaud et al. (2010). By using virial assumption and spectroscopic redshift information Knobel et al. (2012) estimated a size of 659 kpc (i.e. $\sim$84 arcsec at the redshift of the cluster) for F062.

Concerning F062 we find that our size estimates are in good agreement with those reported by previous work. However, for F126 our estimate is higher than previous work. This is likely due to the fact that, as mentioned above, F126 seems to have a galaxy distribution that has a higher radial extent than the X-ray core (see Figure 7.1).

Since we want to shift the cluster members of both F062 and F126 to higher redshifts we select two fields where no overdensity is detected with the PPM in the redshift range $z \sim 1-2$. We prefer to shift the cluster members of both F062 and F126 into other fields because we want to make sure than no overdensity is detected by the PPM in the redshift range $z \sim 1-2$ for the considered field. We note in fact that this is not the case of F062, i.e. a 2.4σ overdensity is detected at $z = 2.00$. Furthermore, the choice of the same field for both F062 and F126 allows us to directly compare the results we obtain with the PPM for the two clusters, once the cluster members are added to such a field.

In Figure 7.6 we report the PPM plots for the fields of COSMOS-FR I 66 (left panel) and COSMOS-FR I 70 (right panel). As clear for visual inspection of the plots, no high significance pattern is detected in these plots within the redshift range $z \sim 1-2$. A weak 2σ overdensity is detected by the PPM at redshift $z = 1.60$ in the field of COSMOS-FR I 66. However such a feature

[4]Here r_{500} (r_{200}) is the radius at which the enclosed mass encompasses the matter density 500 (200) times the critical one. In estimating r_{200} for both F062 and F126 we also assume hydrostatic equilibrium. We use Equation 3 of Reiprich & Böhringer (1999) and the core radius estimates as in Equation 4 of FGH07.

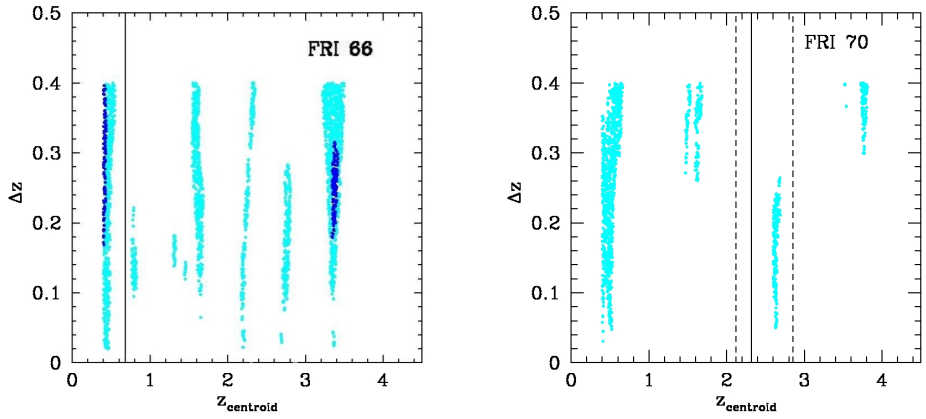

Figure 7.6: PPM plots for the fields of COSMOS-FR I 66 (left) and COSMOS-FR I 70 (right) in the C09 sample. Overdensities: $\geq 2\sigma$ (cyan points), $\geq 3\sigma$ (blue points), $\geq 4\sigma$ (red points). Note that no $\geq 4\sigma$ overdensity is present.

is not detected if a slightly different redshift bin (i.e. $\Delta z = 0.24$) is adopted throughout the PPM procedure. All of the other isolated $\gtrsim 2\sigma$ patterns clearly visible in the plots are interpreted as noise. This is because either they are not located around the y-axis value $\Delta z = 0.28$ that is relevant for the overdensity detection or they are not enough extended to be detected as overdensity (i.e. they are less than $\delta z_{\rm centroid} = 0.1$ long on the redshift axis $z_{\rm centroid}$ at fixed $\Delta z = 0.28$), according to the PPM procedure.

Since no clear overdensity is detected in the fields of COSMOS-FR I 66 and COSMOS-FR I 70 we use them as empty control fields (ECFs). Note that we cannot exclude the presence of underdense or dense regions that are not detected by the PPM, but still present in these two ECFs at the redshifts of our interest.

If a cluster is superimposed on an underdense region the PPM might underestimate the detection significance or it might detect no overdensity. Conversely, if the cluster is added to an overdense region, the PPM tends to overestimate the overdensity significance. The reason to choose two ECFs instead of one is to check whether these two scenarios occur. In particular, we will compare our results obtained from each ECF separately to look for a possible mismatch.

We add to each ECF the fiducial cluster members of F062 and F126, separately, and we apply the PPM at the coordinates of COSMOS-FR I 66 and COSMOS-FR I 70.[5] In Figure 7.7 we report the resulting PPM plots, where the clusters F062 (left panel) and F126 (right panel) are in the field

[5]We add the cluster members into each ECF by applying a rigid rotation to all the projected coordinates of the cluster members.

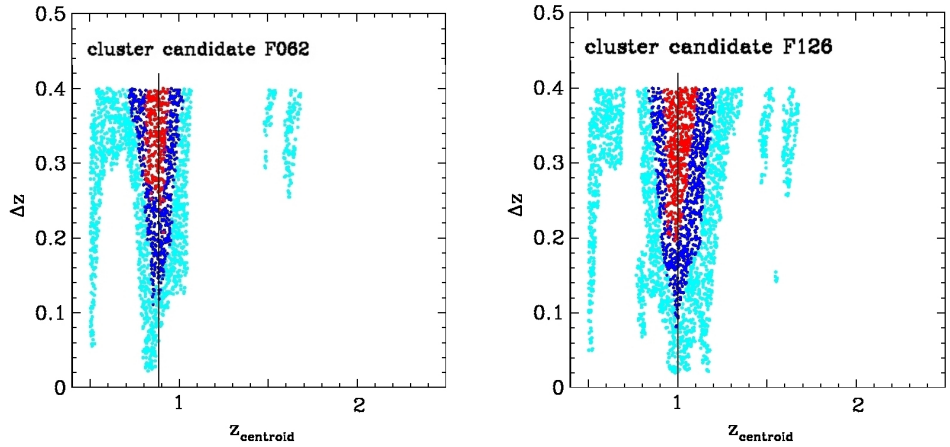

Figure 7.7: PPM plots of F062 (left) and F126 (right), where their cluster members are added to the field of COSMOS-FR I 70. The vertical solid line in each panel is located at the redshift of the cluster. Overdensities: $\geq 2\sigma$ (cyan points), $\geq 3\sigma$ (blue points), $\geq 4\sigma$ (red points).

of COSMOS-FR I 70. As clear from visual inspection of the plots, both F062 and F126 are still detected at their true redshift with significances between $\sim$3-4σ. In Table 7.1 (middle table) we report the PPM results of our simulations. The estimated redshifts for F062 and F126 are $z = 0.86$ and $z = 1.0$, respectively, where the cluster members are added to the fields of COSMOS-FR I 70. Therefore, the estimated redshifts fully agree with those of the clusters. The estimated sizes of F062 and F126 are $r_{\rm max} = 74.3 \pm 6.7$ arcsec and $r_{\rm max} = 92.0 \pm 10.0$ arcsec, respectively, where the cluster members are added to the field of COSMOS-FR I 70. These size estimates agree, independently of the ECF adopted (within the errors), with those previously obtained where the cluster members are not subtracted from their own fields (see Table 7.1, top table). These results suggest that the cluster properties estimated by the PPM are not affected by the applied cluster membership and by the fact that the cluster members are added to a field different from that original of the cluster.

In order to shift the cluster members of both F062 and F126 to higher redshifts (i.e. $z_c = 1.5$ and 2.0) we need to address the problem of the detection limit. The COSMOS number density drops off rapidly with increasing redshift. In fact, the number density per unit redshift is, on average, $\mathrm{d}n/\mathrm{d}z/\mathrm{d}\Omega \simeq 25$, 10, and 3 arcmin^{-2} at redshift $z \sim$1, 1.5, and 2.0, respectively (see Ilbert et al., 2009). Therefore we expect some of the selected cluster members would not be detected if they were located at higher redshifts, since their flux would be lower than the survey threshold.

In order to address this problem we estimate the I band magnitude each

cluster member would have if located at higher redshift. Then we reject all the sources with $I \geq 25$, that is the magnitude cut applied to the Ilbert et al. (2009) catalog.

We assume that each cluster member is located at the redshift of the clusters F062 and F126, i.e. $z_c = 0.88$ and 1.0, respectively. Then, we estimate the simulated I-band magnitude each cluster member would have if shifted to $z_{c,sim} = 1.5$ and 2.0. Practically, we perform the K-correction by using the SED of each object, i.e. we linearly interpolate the flux measurements reported in the I09 catalog, and we correct the apparent magnitude for the luminosity distance.

Then, as outlined above, we reject all the members for which $I_{\rm AB} \geq 25$. This procedure reduces the number of the cluster members from 57 to 9 sources ($z_{c,sim} = 1.5$) and one source ($z_{c,sim} = 2.0$) in the case of F062 and from 249 to 58 ($z_{c,sim} = 1.5$) and 9 galaxies ($z_{c,sim} = 2.0$) for F126. We note that the magnitude cut ($I < 25$) is applied in the Ilbert et al. (2009) to the I(auto) magnitude, that corresponds to the Subaru i^+ band magnitude obtained with SExtractor (Bertin & Arnouts, 1996). Therefore, the I(auto) magnitudes should be considered instead of the I (Subaru or CFHT) magnitudes. However, we prefer to adopt the I magnitude instead of the I(auto) magnitude because the latter is automatically estimated by SExtractor and, therefore, the former is more reliable for our simulations. However, we verify that the I(auto) magnitudes of the selected cluster members are, on average only 0.3 ± 0.4 and 0.3 ± 0.2 lower than the corresponding I magnitudes, for F062 and F126, respectively. The reported uncertainty is the rms dispersion around the average. Therefore, the I magnitudes are consistent within $\sim$1-σ with the I(auto) magnitudes for the selected cluster members. This suggests that the results of our simulations would not change if we chose the I(auto) instead of the I magnitudes.

In the following we will address the problem of assigning coordinates to the cluster members of both F062 and F126, when they are located at $z_{c,sim} \geq 1.5$. The K-correction applied here neglects any contribution from possible evolution.

4. Having addressed the problem of cluster membership, we assign fiducial coordinates to each of the cluster members, when the overdensity is shifted to a higher redshift. We assume that the coordinates in the projected space of each galaxy remain unchanged when the overdensity is shifted to higher redshift. Therefore, projection effects and the peculiar motions of the galaxies are neglected. This approximation is good enough because a high accuracy of the projected coordinates of the cluster members is not required in order to apply the PPM. In fact, each area of the PPM tessellation has a projected size of a few $\sim$ 100 kpc. Such a size is much larger than the projected positional uncertainty resulting from our approximation.

Concerning the galaxy redshifts we assume that all the selected members

are at the same distance to the observer, corresponding to redshift $z_{c,sim} = 1.5$, 2.0, equal to that of the simulated cluster. Then, we assign to each cluster member a photometric redshift accordingly to a Gaussian probability distribution centered at the redshift of the cluster $z_{c,sim}$ and a standard deviation $\sigma_{c,sim} = 0.054(1 + z_{c,sim})$.

This value corresponds to the 1-σ statistical photometric redshift uncertainty of $i^+ \sim 24$ and $1.5 < z < 3$ sources (see Table 3 of Ilbert et al., 2009), typical of the cluster galaxies we consider.

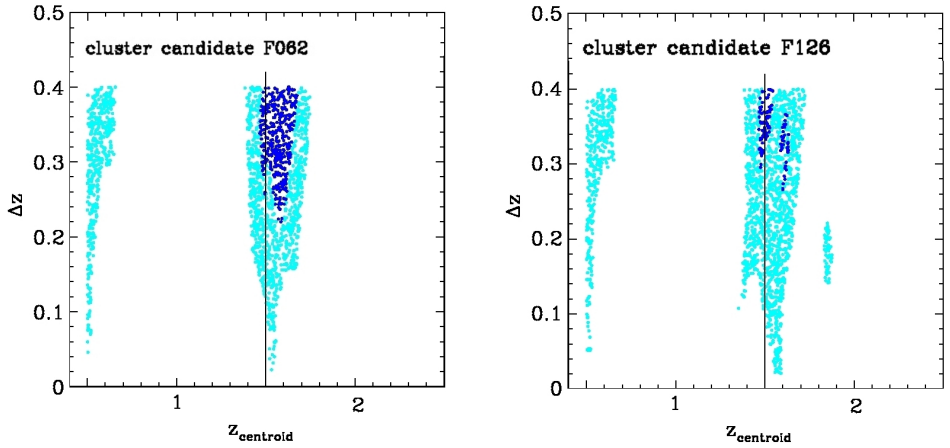

(a) (b)

Figure 7.8: PPM plots for the F062 (left panel) and F126 (right panel), shifted at $z_{c,sim} = 1.5$ and located in the field of COSMOS-FR I 70. The abscissa of the vertical solid line is at the redshift of the overdensity ($z_{c,sim} = 1.5$). We plot only the points corresponding to detected overdensities for different values of Δz and $z_{\rm centroid}$. Color code: $\geq 2\sigma$ (cyan points), $\geq 3\sigma$ (blue points), $\geq 4\sigma$ (red points). Note that no $\geq 4\sigma$ overdensity is present. The Gaussian filter which eliminates high frequency noisy patterns is applied.

5. We shift both F062 and F126 to higher redshift, i.e. $z_{c,sim} = 1.5$, where the cluster members are added to the fields of COSMOS-FR I 66 and COSMOS-FR I 70, separately. In Figure 7.8 we report the corresponding PPM plots for both F062 (left panel) and F126 (right panel). The vertical solid line is located at the redshift of the overdensity. As clear from visual inspection of the PPM plots, both F062 and F126 are still detected, if they are located at $z_{c,sim} = 1.5$. In Table 7.1 (bottom table) we report the PPM results for these simulations. F062 and F126 are detected with significances of 2.9σ and 2.5σ; the estimated redshifts are $z = 1.56$ and $z = 1.59$, respectively, if the cluster members are added to the field of COSMOS-FR I 70. This suggests that the PPM is effective in finding high redshift groups at

$z \simeq 1.5$, albeit with lower significance than at $z \sim 1$ (i.e. $\sim$2.5-3σ). The estimated sizes for both F062 and F126 are consistent, within the reported errors, with those previously obtained for these two clusters at their true redshift (see Table 7.1, top table) The results are quite independent of the ECF considered. Neither F062 nor F126 is detected at $z_{c,sim} = 2.0$.

7.2 Simulated clusters

We perform another set of simulations, by creating simulated clusters with different richness and size. Then, we apply the PPM to test if they are detected at different redshifts. Therefore, we now adopt a different approach with respect to that adopted in the previous Section, that, as will be clarified below, will allow to obtain further information about the ability of the PPM to detect clusters.

We consider as cluster members N_c sources uniformly distributed within a sphere of comoving radius R_c centered at the redshift z_c.

As we will simulate a larger number of clusters than that considered in Section 7.1, for sake of cautiousness we also increase the number of ECFs in order to draw more solid conclusions. The ECFs might host some overdensities that are just slightly below the 2σ PPM detection threshold, but they might be detected once other galaxies are added to the same field. The effect of overdensities and underdensities in the location of our simulated clusters should be marginalized with the increased number of random fields.

Therefore, we here consider both the two ECFs used in Section 7.1 and four additional ECFs (denoted as ECF 3, 4, 5, and 6) where no overdensity is detected by the PPM within the redshift range $z \sim 1 - 2$. In Figure 7.9 we report the PPM plots for the four additional ECFs. Concerning the cluster sizes, in this section we only refer to comoving sizes, unless otherwise specified.

We choose the following parameters: N_c = 10, 30, 60, 100, 150, and 200; z_c = 1.0, 1.5, and 2.0; R_c = 1.0, 2.0, and 3.0 Mpc. This results in 54 simulated clusters obtained by considering all the possible combinations of the values of N_c, z_c, and R_c. In particular, the redshifts are chosen in the range of our interest, while the adopted comoving sizes and the considered values for the richness are typical of clusters and groups we expect to find in the COSMOS survey adopting our method.

In fact, in Chapter 8 we estimate cluster core sizes for the $z \sim 1 - 2$ cluster candidates found in the fields of the C09 sample. Average physical and comoving core sizes $r_{\max} = (772 \pm 213)$ kpc and $r_{\max} = (1762 \pm 602)$ kpc are obtained, respectively. The average is performed using all the cluster candidates and the reported uncertainty is the 1-σ rms dispersion around the average.

The estimated number of the fiducial cluster members varies with the

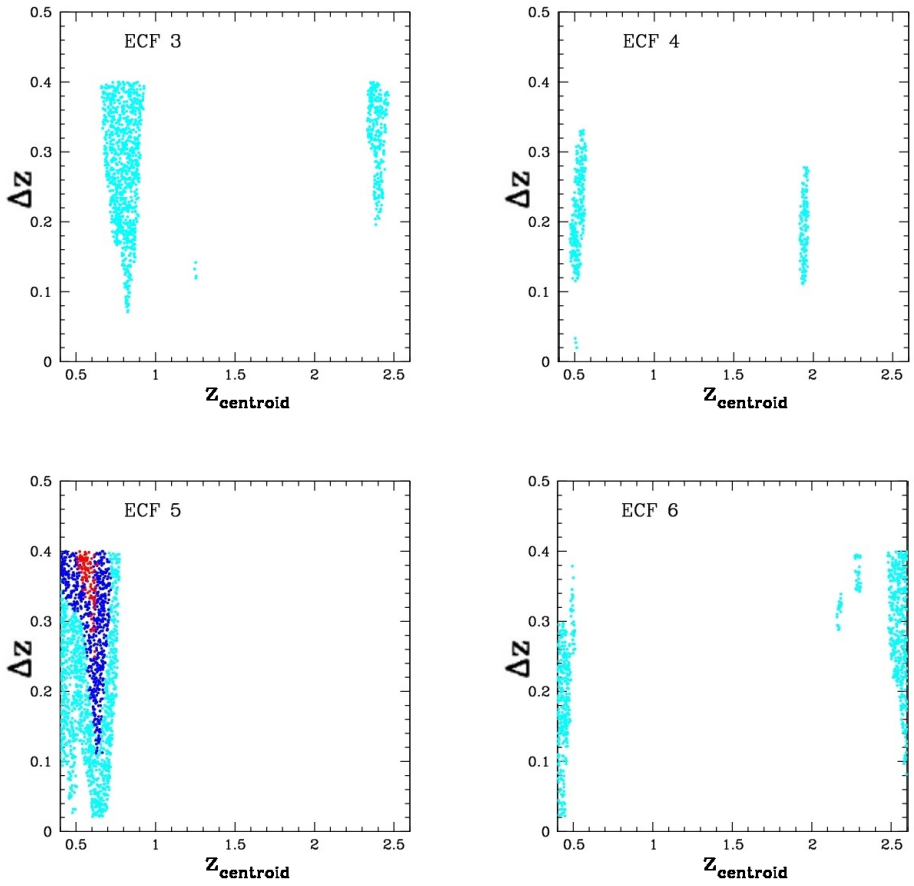

Figure 7.9: PPM plots for the four additional Empty Control Fields. Overdensities: $\geq 2\sigma$ (cyan points), $\geq 3\sigma$ (blue points), $\geq 4\sigma$ (red points).

cluster detection significance from ∼10 for our cluster candidates at the highest redshifts ($z \sim 2$) to more than ∼200 for our $z \sim 1$ clusters candidates.

Note that clusters of galaxies usually include up to thousands of galaxies. Here we adopt smaller values for N_c because the Ilbert et al. (2009) catalog lacks of faint $I > 25$ galaxies that still constitute a significant fraction of the cluster galaxies at redshifts $z \gtrsim 1$ (Rudnick et al., 2012).

Mass estimates are found in the literature for some of our cluster candidates at redshift $z \sim 1$. In particular, FGH07 estimated a cluster mass $M_{500} = 5.65 \times 10^{13}\ M_{\odot}$ for the rich group associated with the source 01, for which the PPM selects ∼ 100 cluster members within a circle of $r_{\rm max} = 70.7$ arcsec radius and a redshift bin $\Delta z = 0.28$ centered at the spectroscopic redshift $z = 0.88$ of the cluster. Knobel et al. (2009, 2012) reported masses within $M \sim 1.4 - 2.2 \times 10^{13} M_{\odot}$ for the cluster candidates in the fields of sources 16, 18, and 20, for which ∼ 100, ∼ 200, and ∼ 100 fiducial cluster members are selected by the PPM, respectively. Source 16 has a spectroscopic redshift $z = 0.97$, while the photometric redshifts of sources 18 and 20 are $z = 0.92$ and $z = 0.88$, respectively. As pointed out in Section 7.1.1, such mass estimates and cluster detections further suggest that PPM effectively finds systems whose masses are compatible with those of rich groups. Therefore, the PPM is able to detect structures whose mass is even below the typical cluster mass cutoff $\sim 1 \times 10^{14}\ M_{\odot}$ (see Chapter 8 for a detailed discussion about the properties of the clusters found with the PPM).

For a given simulated cluster we change the exact redshift of each of the N_c members to account for the observational uncertainties. Conversely, we do not change the projected coordinates of the cluster members because the angular positional uncertainties are negligible with respect to the photometric redshift uncertainties (Ilbert et al., 2009). For the same reason we also neglect the galaxy peculiar velocities and, therefore, all of the cluster members are assumed to be at the same redshift z_c. We assign to each of the N_c sources a *photometric* redshift drawn from a Gaussian probability distribution centered at the mean z_c and whose standard deviation is $\sigma_c = 0.054(1 + z_c)$. This is the 1-$\sigma$ statistical photometric redshift uncertainty of $i^+ \sim 24$ and $1.5 < z < 3$ sources (see Table 3 of Ilbert et al., 2009), typical of the cluster galaxies we consider, consistently with what has been done throughout this work (see e.g. Section 7.1).

We consider the case where (i) the equatorial coordinates at which we choose to center the tessellation of the PPM, (ii) the equatorial coordinates of the adopted ECF and (iii) the equatorial coordinates of the center of the spherically symmetric simulated cluster all coincide. In particular, for our simulations we keep (i) the equatorial coordinates at which we choose to center the tessellation of the PPM and (ii) the equatorial coordinates of the adopted ECF unchanged, i.e. (i) and (ii) will always coincide. The

ECFs are in fact chosen because the PPM does not detect any overdensity in these fields at the redshift range ($z \sim 1-2$) of our interest. Conversely, some overdensities might be present at a certain offset from the equatorial coordinates of the adopted ECF. In this case the PPM might detect these overdensities if the the equatorial coordinates at which we choose to center the PPM tessellation do not coincide with those of the center of the adopted ECF.

However, in order to test the efficiency of the PPM to detect clusters if the cluster center coordinates is not accurately known, in Section 7.2.2 we will offset (by an angle θ) the input PPM coordinates with respect to the center of the spherically symmetric simulated cluster.

7.2.1 General results and trends

In Table 7.2 we summarize the results for all the 54 simulated clusters. Each entry of the table shows the fraction of ECFs in which the cluster with specific values of N_c, R_c, and z_c is detected. For example, the fraction 4/6 means that the cluster is detected in four out of the six ECFs.

Our simulations suggest that the majority, i.e. 47, 44, and 41 out of the 54 simulated clusters are detected at least in three, four, and five ECFs. For the 41 clusters that are detected in at least five out of the six ECFs the redshift $z_{\rm PPM}$ estimated by the PPM is fully consistent with the input simulated cluster redshift z_c. In fact, the average difference for the 41 clusters is $\langle z_{\rm PPM} - z_c \rangle = 0.02 \pm 0.05$, where all the detections for the 41 clusters are considered and the reported uncertainty is the rms dispersion around the average. Therefore, the statistical 1σ uncertainty for our redshift estimates is ~ 0.05. It is estimated by Gaussian propagation of the mean offset with the rms dispersion. Interestingly, this is fully consistent with the independently estimated redshift uncertainties ($\sim 0.06-0.09$) described throughout the PPM procedure

The 41 overdensities that are found in at least five ECFs are detected with significances spanning from $\gtrsim 2.7\sigma$ up to $\sim 12\sigma$, depending on the adopted parameters, and a median value of 5.2σ. At a fixed richness (N_c) and size (R_c), the clusters are more easily detected for increasing redshifts. This is because the mean COSMOS number density rapidly drops down for increasing redshifts. At fixed richness (N_c) and redshift (z_c), more compact clusters are more easily detected with higher significance than more extended overdensities. This is because compact clusters have higher number densities than more extended overdensities.

Furthermore, clusters with low values for N_c are more easily detected at redshifts higher than at $z_c = 1$. This is due to the decreasing mean number density for increasing redshifts. In fact, at redshifts $z \geq 1.5$, only 10 cluster members seem to be sufficient (see also the results outlined in Chapter 8). In fact, among the six clusters with $N_c = 10$ and $z \geq 1.5$, five are detected

in at least three ECFs. However, only one of them is detected in at least five ECFs.

The reported trends are clearly due the fact that we consider the cluster parameters N_c, R_c, and z_c as independent. In fact, we do not change the cluster parameters N_c and R_c when we shift the cluster to higher redshift. This is motivated by the fact that the statistics at $z \gtrsim 1$ is poor and we prefer to investigate whether the PPM is able to detect overdensities over a wide range of adopted parameters. However, the results of these simulations are clearly dependent on all the simplifications we made (e.g. spherical symmetry, N_c, R_c, and z_c are considered independent). We note that this is a different approach to that adopted for the simulations in Section 7.1, where we simulate how the cluster would be observed if it were located at higher redshift. Given all the assumptions we make, the accuracy of our simulations is reasonably good for our purpose to detect high-redshift overdensities on the basis of number counts and photometric redshifts, given the specific properties of both real clusters and the adopted survey.

The general relationship between the richness parameter N_c, the size R_c of the cluster, the cluster mass, and the significance of the cluster detection is complex (i.e. it depends on the depth of the photometric catalog, the redshifts, the evolution of luminosity function), especially at the redshift of our interest ($z \sim 1-2$), where the properties of cluster galaxy population in terms of luminosity and segregation within the cluster are expected to evolve and are not fully understood.

Projected cluster sizes

We find that the comoving sizes, estimated by our method, are consistent with the comoving cluster sizes (R_c) of our simulations within $\sim 30\%$.

The case of a 2 Mpc comoving size cluster

As outlined in Table 7.2, at $z_c = 1$, 11 out of 18 simulated clusters are detected in at least five ECFs. Among the 18 simulated clusters, apart for the clusters with $R_c \geq 2$ Mpc and $N_c = 10$, the remaining 16 simulated clusters are all detected at $z_c \geq 1.5$ in at least four ECFs.

The simulated cluster with $N_c = 30$ cluster members and $R_c = 2.0$ Mpc is one of the four clusters that are detected in at least four ECFs only if located at $z_c \geq 1.5$

In Figure 7.10 we report the PPM plots for this specific cluster in the case where it is located in the field of COSMOS-FR I 70 and where the offset $\theta = 0$ arcsec. The abscissa of the vertical dashed line is equal to the input redshift of the simulated cluster: $z_c = 1.0$ (Panel a), $z_c = 1.5$ (Panel b), and $z_c = 2.0$ (Panel c). We adopt the same color code as in Figure 6.2.

In particular, the cluster at $z_c = 1.5$ and $z_c = 2.0$ is detected with

significances of 3.7σ and 4.7σ, respectively. The estimated redshifts are $z = 1.56$ and $z = 2.00$, respectively. The estimated sizes are $r_{\rm max} = 86.6$ arcsec and $r_{\rm max} = 70.7$ arcsec, that correspond to 1.9 Mpc and 1.8 Mpc (comoving), at the estimated cluster redshifts, respectively.

Interestingly, both the redshift and size of these overdensities fully agree with the input parameters of our simulations. All these results further confirm that the PPM is very effective in finding clusters and rich groups and in estimating their properties such as redshift and size, if the projected cluster coordinates are known. In the following we will test the PPM against simulations in the case where the projected cluster coordinates are known with an accuracy of 100 and 200 arcsec.

7.2.2 Increasing the offset θ

We repeat all the 54 simulations for increasing offsets θ between the input coordinates of the PPM and the center of the simulated cluster. In order to do so, we shift the coordinates of cluster members by $\theta = 100$ arcsec. We keep unchanged both the PPM input cluster equatorial coordinates and the equatorial coordinates of the adopted ECF. As explained above, this is because the surroundings of the ECFs might host dense regions in the redshift range of our interest. In Table 7.3 we summarize our results, where $\theta = 100$ arcsec, analogously to what is reported in Table 7.2 for the case of null offset θ.

For $\theta > 100$ arcsec the PPM becomes highly inefficient mainly because of the constraint applied to an angular separation of $\sim$2 arcmin from the coordinates at which the PPM tessellation is centered. In fact, for $\theta = 200$ arcsec, the simulated clusters are all detected in less than five ECFs. Only four high redshift ($z_c = 1.5$), rich ($N_c \geq 60$) and extended ($R_c \geq 2$ Mpc) clusters are detected in at least three ECFs. Among the four, only the cluster with with $z_c = 1.5$, $N_c = 200$, and $R_c = 3$ Mpc is detected in four ECFs. This is not surprising. In fact, for such a high value of θ very extended and rich structures have more chances to be detected.

Note that by considering all the possible combinations of the parameters (i.e. the different empty control fields, the offsets, and the different values for N_c, R_c, and z_c) 972 clusters are simulated as part of this work.

General results and trends

Our simulations suggest that the great majority, i.e. 30 out of the 41 clusters that are detected in at least five ECFs in the case where $\theta = 0$ arcsec are also found in at least five ECFs if $\theta = 100$ arcsec. Note that 23 out of the 30 clusters have $N_c \geq 60$ and $z_c > 1$ (see Table 7.3).

For the 30 simulated clusters the redshift $z_{\rm PPM}$ estimated by the PPM is fully consistent with the input simulated cluster redshift z_c. In fact, the

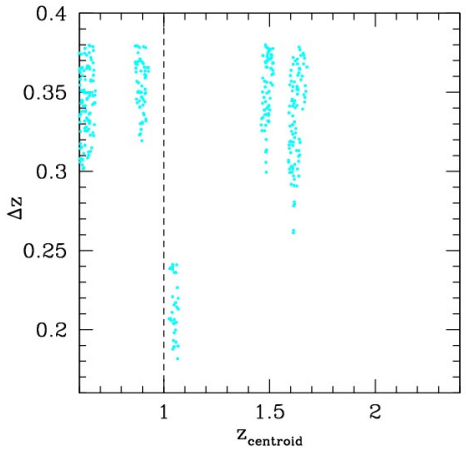

(a)

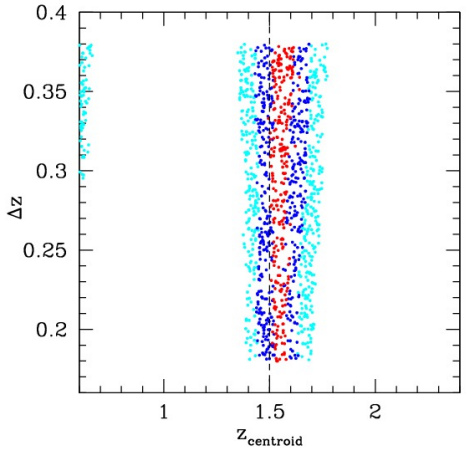

(b)

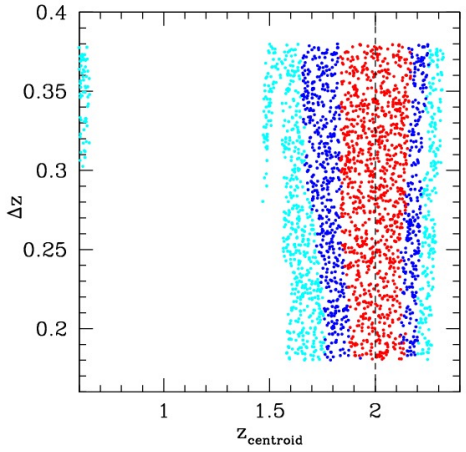

(c)

Figure 7.10: PPM plots for the simulated cluster located in the field of COSMOS-FR I 70, with $\theta = 0$ arcsec, and at different redshifts: $z = 1.0$ (a), $z = 1.5$ (b), and $z = 2$ (c). Dashed vertical line corresponds to the input redshift of the simulated cluster. Overdensities: $\geq 2\sigma$ (cyan points), $\geq 3\sigma$ (blue points), $\geq 4\sigma$ (red points). A Gaussian filter to eliminate high frequency noisy patterns is applied.

average mismatch for the 30 clusters, in the case where $\theta = 100$ arcsec, is $\langle z_{\rm PPM} - z_c \rangle = 0.02 \pm 0.07$, where all the detections for the 30 clusters are considered and the reported uncertainty is the rms dispersion around the average. Therefore, the statistical 1σ uncertainty for our redshift estimates is ~ 0.07, estimated with Gaussian propagation of the mean offset with the rms dispersion. Interestingly, this is again fully consistent with the independent redshift estimate uncertainties ($\sim 0.06 - 0.09$) described throughout the PPM procedure.

Furthermore, note that poorer overdensities or clusters of intermediate richness (i.e. $N_c \leq 60$) are more difficult to detect than richer clusters. This is especially true at redshift $z_c = 1.0$ and in the case of $\theta = 100$ arcsec, where $N_c = 100$ cluster members or more are required, unsurprisingly. At variance with the case of null offset (i.e. $\theta = 0$ arcsec), poor and intermediate richness clusters are more difficult to detect by the PPM at such a high offset $\theta = 100$ arcsec. This in fact corresponds to a comoving distance of 1.6 Mpc, at redshift $z_c = 1.0$, that is comparable to the input $\sim$Mpc size of the simulated clusters.

Among the 18 clusters with intermediate richness, i.e. $N_c = 30$ and 60, seven are detected in at least five ECFs. Six among the seven have $z_c \geq 1.5$ and $R_c \leq 2$ Mpc.

Rich simulated clusters with $N_c \geq 100$ are always detected at $z_c \geq 1.5$ in at least five ECFs. At $z_c = 1.0$, these rich clusters are detected with more difficulty, especially in the case $N_c = 100$, while they are detected in at least four ECFs if they have $N_c \geq 150$.

Detection significances

The overdensities found in the case of $\theta = 100$ arcsec are detected, by construction, with significances $\geq 2\sigma$, and a median value of 3.9σ. Therefore, the overdensities tend to be detected with lower significances than in the case of $\theta = 0$ arcsec.

In particular, for $\theta = 100$ arcsec and similarly to what is found in the case of null offset, at fixed size and richness, the clusters are detected with increasing significances for increasing redshifts. However, at variance with the case $\theta = 0$ arcsec, at each fixed richness and redshift, no specific trend is observed for the detection significances, for increasing sizes R_c. This is because of two competing effects: a larger sized cluster is more easily detected than more compact overdensities, at a larger offset θ. On the contrary, similarly to what discusses in the case of null offset $\theta = 0$ arcsec, a larger size implies a lower projected number density that makes the cluster detection more difficult.

Projected cluster sizes

The comoving cluster size estimated by the PPM as $r_{\max}$ in the case where $\theta = 100$ arcsec is $\sim$1.6 times the input comoving cluster size R_c (and up to a factor of $\sim$2.6 at 1-σ). The reason of this mismatch is due to the fact that, by construction, the simulated cluster formally ends at a larger distance from the input PPM coordinates than in the case of $\theta = 0$ arcsec.

These aspects suggest that, if the coordinates of the cluster center are not accurately known, the cluster sizes might be overestimated up to a factor of ~ 2.6, that corresponds to the extremal case where we are looking for a cluster environment around a radio source that resides in the outskirts of the cluster core.

Simulated cluster detections (null offset)

R_c	$N_c = 10$			$N_c = 30$			$N_c = 60$			$N_c = 100$			$N_c \geq 150$		
(Mpc)	$z_c = 1$	1.5	2	1	1.5	2	1	1.5	2	1	1.5	2	1	1.5	2
1.0	0/6	4/6	5/6	6/6	6/6	6/6	6/6	6/6	6/6	6/6	6/6	6/6	6/6	6/6	6/6
2.0	0/6	3/6	3/6	1/6	5/6	6/6	5/6	6/6	6/6	6/6	6/6	6/6	6/6	6/6	6/6
3.0	0/6	2/6	3/6	0/6	4/6	6/6	0/6	6/6	6/6	4/6	6/6	6/6	6/6	6/6	6/6

Table 7.2: Detection results for the simulated clusters with different input richness (N_c), redshift (z_c), and size (R_c), in the case where (i) the equatorial coordinates at which we choose to center the tessellation of the PPM, (ii) the equatorial coordinates of the adopted ECF and (iii) the equatorial coordinates of the center of the spherically symmetric simulated cluster all coincide. Column description: (1) comoving size (Mpc) of the simulated cluster; (2-13) detection rates for simulated clusters of different richness N_c and redshift z_c. Each fraction $n/6$ denotes that the cluster is detected in n out of the six adopted ECFs.

Simulated cluster detections ($\theta = 100''$ offset)

R_c	$N_c = 10$			$N_c = 30$			$N_c = 60$			$N_c = 100$			$N_c = 150$			$N_c = 200$		
(Mpc)	$z_c = 1$	1.5	2	1	1.5	2	1	1.5	2	1	1.5	2	1	1.5	2	1	1.5	2
1.0	0/6	1/6	1/6	0/6	3/6	6/6	2/6	5/6	5/6	4/6	5/6	6/6	6/6	6/6	5/6	6/6	6/6	6/6
2.0	1/6	1/6	0/6	0/6	3/6	5/6	2/6	5/6	6/6	2/6	5/6	5/6	6/6	6/6	6/6	6/6	6/6	6/6
3.0	0/6	0/6	0/6	0/6	2/6	4/6	1/6	3/6	5/6	3/6	6/6	6/6	4/6	6/6	6/6	6/6	6/6	6/6

Table 7.3: Detection results for the simulated clusters with different input richness (N_c), redshift (z_c), and size (R_c), in the case where (i) the equatorial coordinates at which we choose to center the tessellation of the PPM, (ii) the equatorial coordinates of the adopted ECF and (iii) the equatorial coordinates of the center of the spherically symmetric simulated cluster do not coincide. We fix the offset $\theta = 100$ arcsec between (i) and (iii), changing the equatorial coordinates of the center of the spherically symmetric simulated cluster, while (i) and (ii) still coincide. Column description: (1) comoving size (Mpc) of the simulated cluster; (2-13) detection rates for simulated clusters of different richness N_c and redshift z_c. Each fraction $n/6$ denotes that the cluster is detected in n out of the six adopted ECFs.

Chapter 8

Cluster candidates at $z \sim 1 - 2$

In this Chapter we apply the PPM described and tested against simulations in Chapter 6 and Chapter 7, respectively, to the fields of the FR I sample described in Chapter 5. In the following we first discuss four examples of typical PPM results for fields of the FR Is in our sample, previously shown in Figure 6.2, in Chapter 6. The results of our analysis for the entire FR I sample will be described in the following sections.

In Panel (a) of Figure 6.2 we report the PPM plot for the LLRG 02. The photometric redshift of source 02 and that estimated for the overdensity perfectly match. Other two overdensities are detected in the field of 02 at redshifts $z = 0.66$ and 3.94, respectively. They are clearly identified at their estimated redshift by visual inspection of the PPM plot.

Interestingly, the lower redshift cluster is present ($\sim$20 arcsec far from the location of our FR I) in both the $z \lesssim 1$ group catalogs of Knobel et al. (2009, 2012), who estimated a redshift of $z = 0.69$ for the overdensity.

In Panel (b) we report a similar example for the $z \sim 2$ HLRG 03. Despite the high photometric uncertainties for this source two distinct overdensities are clearly detected within the redshift uncertainties of the source 03 at $z = 1.82$ and 2.39, respectively. Another overdensity is detected at $z = 0.56$, as also clearly identified by visual inspection of the plot. Interestingly, it is present (with an angular offset of $\sim$20 arcsec from the coordinates of our FR I) in the $z \lesssim 1$ group catalogs of Knobel et al. (2009, 2012), who estimated a redshift of $z = 0.66$ for the overdensity.

In Panel (c) we report the PPM plot for the LLRG 25. A clear overdense (i.e. $\geq 2\sigma$) region extends in the PPM plot from $z_{\rm centroid} = 0.40$ to $z_{\rm centroid} = 1.51$. Due to such a large redshift range we interpret the overdense region in the plot as due to a projection effect, where multiple overdensities are present in the field of 25 at different redshifts. Our peak finding procedure detects in fact four overdensities within such a redshift interval, at $z = 0.46$,

0.80, 1.23 and 1.37, respectively. Only the last two redshifts agree with the redshift of the radio galaxy, consistently with our association criterion. The significances of the two overdensities are similar and equal to 2.7σ and 2.8σ, respectively. Therefore, we are confident that these two peaks are associated with the same overdensity. On the contrary, the first two lower redshift overdensities are detected with higher significances of 3.8σ and 4.2σ, respectively. Moreover, since they are detected at redshifts significantly below that of the radio galaxy, we suggest that they are overdensities which are in the field of 25 but they are not associated with the source. In fact, two overdensities are found in the Knobel et al. (2012) group catalog at redshifts of z =0.35 and 0.82 and at angular separations of 8 arcsec and 46 arcsec from the coordinates of the source 25, respectively. The fact that the redshifts of the $z \sim 0.4$ overdensity estimated by Knobel et al. (2012) and in this work marginally agree with each other might be due to the fact that, according to our procedure, we consider sources down to $z_{\rm centroid} = 0.4$. Therefore, the inconsistency might be due to a boundary effect that would disappear if we considered lower redshift sources. Note also that we find another clear overdensity in the field of 25 at an estimated redshift of $z = 3.72$. High significance (i.e. $\gtrsim 2\sigma$) patterns are also clearly visible in the PPM plot around $z_{\rm centroid} \sim 3$. According to our selection criteria, they are not detected as overdensities but interpreted as noisy features. This is because they are spiky features that are not stable with respect to different values for the Δz and $z_{\rm centroid}$ parameters.

In Panel (d) we show a clear example where no overdensity is found to be associated with the radio galaxy 224, although other three overdensities are detected at redshifts $z = 0.46$, 2.58, and 3.88, well outside the redshift range of our interest. No group associated with this field is found within the Knobel et al. (2009); George et al. (2011); Knobel et al. (2012) catalogs.

In the following sections we will show our results. In Section 8.1 we will describe our cluster candidate catalog, in Section 8.2 we will discuss the presence of other cluster candidates in the fields of our sample of FR Is that are not associated with our sources. In Sections 8.3 and 8.4 we will discuss the Mpc-scale environments of the remaining fields and the multiple Mpc-scale overdensity detections that occur for some of the sources in our sample, respectively. In Section 8.5 we reconsider our work by rejecting those sources that were masked, classified as stars, or identified as X-ray AGNs in the I09 catalog. In Section 8.6 and 8.7 we will discuss the projected space information obtained with the PPM, focusing on our cluster size estimates. In Section 8.8 we will apply the Kolmogorov-Smirnov test to our sample. In Sections 8.9 and 8.9.1 we will apply the Papovich (2008) method to our sample and compare the results with those obtained independently by using the PPM, respectively.

8.1 Cluster candidates

In Table 8.1 we report the overdensities found in the fields of our sample that are associated with the corresponding sources, according to the PPM procedure. We distinguish between the LLRGs (top table) and the HLRGs (bottom table). We discuss the estimated sizes in Section 8.6. All of the overdensities are robustly detected with respect to slightly different choices of the involved parameters (e.g. a different choice of the redshift bin Δz, a different selection threshold, a different choice in the parameters of the tessellation of the projected space).

According to the overdensity PPM selection procedure described in Chapter 6 we find that 22 out of the 32 sources in our sample are hosted in a dense Mpc-scale environment. The cluster candidates associated with the sources in the sample have an average redshift of $z_{\rm avg} = 1.41$ with an rms dispersion around the average of 0.55. The median redshift is $z_{\rm median} = 1.31$. When calculating these quantities for the fields in which multiple associations between distinct overdensities and the beacon radio galaxy are identified we only consider the overdensity whose estimated redshift is the closest to that of the radio galaxy.

In particular, we find that 14 radio galaxies out of the 21 LLRGs and 8 out of the 11 HLRGs are associated with overdensities. This corresponds to a percentage of 67%±10% and 73%±13%, for the two subsamples, respectively, where the 1-σ uncertainties are estimated according to binomial statistics. These percentages fully agree within the reported errors. Therefore the environments of the two subsamples are statistically indistinguishable. Thus, if we do not distinguish between the two different classes (i.e. the LLRGs and the HLRGs) we find that 22 out of the 32 radio galaxies in our sample (i.e. 69%±8%) are found in dense Mpc-scale environments.

The overdensity in the field of 16 is formally not associated with the radio galaxy, according to the outlined procedure. However, we do not reject it from Table 8.1. It would be included if the photometric redshift of the radio source ($z = 0.97^{+0.12}_{-0.07}$, see Table 6 in B13) would be considered instead of the spectroscopic redshift. Furthermore, the spectroscopic redshift of 16 and the redshift estimated with the PPM for the overdensity in its field are consistent with each other within $\sim 2 - \sigma$ (see Table 8.1).

In general, *a posteriori*, the redshift estimated for each overdensity in the sample is remarkably consistent with that of the source estimated in B13. The overdensity redshift uncertainties are generally small and comparable to typical statistical photometric redshift uncertainties in I09.

As expected, the overdensities associated with the LLRGs are generally at lower redshifts than those of the HLRGs. These lower redshift overdensities are also detected, on average, with higher significances ($\sigma_{\rm avg} = 3.36$) than those associated with the HLRGs ($\sigma_{\rm avg} = 2.64$). This effect is in agreement with what pointed out in Chapter 7 and it is mainly due to both

The Low Luminosity Radio Galaxy subsample

ID	$z_{\rm source}$	$z_{\rm overdensity}$	significance	$r_{\rm min}$ (arcsec)	$r_{\rm max}$ (arcsec)	$r_{\rm max,phys.}$ (kpc)	$r_{\rm max,comov.}$ (kpc)
01	0.8823[a]-0.8827[b]	0.84±0.07	3.5	0.0 ——	70.7 ——	536 ——	987 ——
02	$1.33\pm^{0.10}_{0.09}$	1.33±0.09	4.3	$19.2^{+24.3}_{-19.2}$ (0.0)	119.3±16.2 (122.5)	1008±136	2349±319
16	0.9687[a]	1.12±0.06	3.5	0.0 ——	100.5±3.3 (100.0)	830±27	1760±57
18	$0.92\pm^{0.14}_{0.11}$	0.80±0.08	5.6	0.0 ——	110.4±25.4 (132.3)	834±191	1501±345
20	$0.88\pm^{0.02}_{0.02}$	0.96±0.06	3.9	0.0 ——	80.4±8.3 (86.6)	637±65	1249±129
22	$1.30\pm^{0.05}_{0.04}$	1.41±0.09	3.3	$20.8^{+24.6}_{-20.8}$ (0.0)	94.2±11.6 (86.6)	800±98	1929±237
25[c]	$1.33\pm^{0.11}_{0.13}$	1.23±0.07	2.8	57.2±9.9 (50.0)	120.9±19.5 (132.3)	1009±162	2250±363
		1.37±0.08	2.7	51.1±4.6 (50.0)	86.6 ——	736 ——	1745 ——
26	$1.09\pm^{0.12}_{0.07}$	1.15±0.07	3.9	42.6±27.4 (50.0)	149.0 ±12.3 (158.1)	1237±102	2659±219
29	$1.32\pm^{0.23}_{0.24}$	1.34±0.09	2.1	77.5±7.9 (70.7)	120.5±11.2 (122.5)	1020±94	2387±221
36	$1.07\pm^{0.10}_{0.04}$	1.18±0.07	3.0	0.0 ——	82.6±6.9 (86.6)	685±57	1494±124
39	$1.10\pm^{0.05}_{0.05}$	1.27±0.06	3.5	0.0 ——	70.7 ——	597 ——	1356 ——
228	$1.31\pm^{0.05}_{0.07}$	1.17±0.06	3.2	0.0 ——	70.7 ——	588 ——	1276 ——
234[d]	$1.10\pm^{0.14}_{0.08}$	0.93±0.08	2.5	0.0 ——	108.7±8.3 (111.8)	854±65	1649 ±125
285	$1.10\pm^{0.13}_{0.08}$	1.01±0.07	2.1	50.0 ——	70.7 ——	568 ——	1143 ——

The High Luminosity Radio Galaxy subsample

ID	$z_{\rm source}$	$z_{\rm overdensity}$	significance	$r_{\rm min}$ (arcsec)	$r_{\rm max}$ (arcsec)	$r_{\rm max,phys.}$ (kpc)	$r_{\rm max,comov.}$ (kpc)
03[c]	$2.20\pm^{0.32}_{0.44}$	1.82±0.08	2.6	0.0 ——	58.7±11.4 (50.0)	502±97	1416±275
		2.39±0.09	2.5	$15.8^{+23.2}_{-15.8}$ (0.0)	74.9±7.0 (70.7)	617±57	2093±195
04	$1.37\pm^{0.10}_{0.09}$	1.57±0.09	2.0	0.0 ——	62.4±10.1 (70.7)	532±86	1368±221
05	$2.01\pm^{0.22}_{0.35}$	1.97±0.07	2.2	0.0 ——	50.0 ——	424 ——	1261 —
28[c]	$2.90\pm^{0.20}_{0.26}$	2.71±0.07	2.0	86.3±11.0 (86.6)	129.9±4.2 (132.3)	1044±33	3876±125
		2.98±0.09	2.5	0.0 ——	101.0±11.7 (100.0)	793±91	3159±366
34	$1.55\pm^{0.41}_{0.19}$	1.31±0.07	2.7	45.7±27.9 (50.0)	103.6±8.3 (100.0)	871±69	2012±161
37	$1.38\pm^{0.43}_{0.42}$	1.95±0.07	3.0	86.6 ——	121.6±2.9 (122.5)	1035±24	3054±72
38	$1.30\pm^{0.17}_{0.28}$	0.88±0.07	3.7	0.0 ——	90.0±9.4 (86.6)	698±72	1312±137
226	$2.35\pm^{0.63}_{0.31}$	1.99±0.06	2.5	70.5±4.9 (70.7)	107.2±5.8 (111.8)	910±49	2723±147

Table 8.1: Cluster candidates and their properties as inferred with the PPM. Cluster candidates in the fields of the LLRGs (top) and HLRGs (bottom) associated with the corresponding source. Column description: (1) source ID number; (2) photometric redshift of the source along with uncertainties from B13. Spectroscopic redshifts from either MAGELLAN (Trump et al., 2007) or zCOSMOS-bright (Lilly et al., 2007) catalogs are denoted with the superscript *a* or *b*, respectively; (3) redshift of the overdensity and corresponding rms dispersion, both estimated with the PPM; (4) significance of the overdensity estimated by the PPM in terms of σ; (5) average minimum radius [arcsec] of the overdensity along with the rms dispersion around the average (both estimated with the PPM). The median value [arcsec] is written between the parenthesis; (6) average maximum radius [arcsec] of the overdensity along with its rms dispersion around the average (both estimated with the PPM). The median value [arcsec] is written between the parenthesis; (7) average physical size [kpc] of the overdensity along with the rms dispersion; (8) average comoving size [kpc] of the overdensity along with the rms dispersion; The rms dispersions and the median values in columns 5, 6, 7, and 8 are not reported in those cases where the rms dispersion is null.

[c] Sources number 03, 25, 28 are counted twice because multiple peaks are found to be associated with the corresponding radiogalaxies within the photometric redshift uncertainties.
[d] Photometric redshifts from Ilbert et al. (2009) denoted as *zpbest* are adopted. They do not include masked sources, stars, and X-ray AGN.

increasing photometric redshift errors and to the smaller number counts that occur for increasing redshifts. If we focus on the overdensities found among the two different subsamples, separately (i.e. the LLRGs and the HLRGs) we find that the average, the rms dispersion around the average and the median values of the redshifts of the overdensities associated with the LLRGs are $z_{\rm avg} = 1.13$, rms $= 0.20$, and $z_{\rm median} = 1.17$, respectively. The average, the rms dispersion around the average and the median values of the redshifts of the overdensities associated with the HLRGs are $z_{\rm avg} = 1.88$, rms $= 0.65$, and $z_{\rm median} = 1.97$, respectively.

Chiaberge et al. (2010, C10) suggested the presence of overdensities around three of our highest redshift sources, namely sources 03, 05, 226. Based on galaxy number counts, the authors found that the Mpc-scale environments of these source are 1.7 times denser with respect to the mean COSMOS density. They translated this into a 4-σ overdensity significance. Interestingly, we find this is in full agreement with our results, since we find that all of the three sources reside in high significance ($\sim 2.5\sigma$) and high redshift ($z \simeq 2$) Mpc-scale overdensities. The cluster candidate associated with our source 03 is also present in the protocluster and group catalog of Diener et al. (2013). They estimated a redshift of 2.44, that is in good agreement with our estimate ($z = 2.39$) for one of the two Mpc-scale overdensities associated with the source 03. Spitler et al. (2012) found a cluster candidate that is about ∼3.8-5.4 arcmin from the source 03. Yuan et al. (2014) recently spectroscopically confirmed the cluster, located at $z = 2.095$. Even if both the redshift and the projected coordinates are only marginally consistent with those of our cluster candidate, it might be possible that the source 03 belongs to the same large scale cluster structure presented in Spitler et al. (2012). We also report the PPM plot for the field of this source in Figure 6.2, panel (b). Interestingly, whereas the independent Papovich (2008, see Section 8.9) method suggests that the source 03 is in a $\sim 3.3\sigma$ overdensity, it does not detect any overdensity in the fields of sources 05 and 226. We will discuss this in detail in Sections 8.9.1 and 8.9.2.

We searched for cluster candidates in catalogs of $z \lesssim 1$ groups in the COSMOS field that were obtained by using spectroscopic redshift information (Knobel et al., 2009, 2012) or photometric redshifts combined with previous X-ray selected cluster samples (George et al., 2011). Interestingly, five groups in the fields and redshifts of our FR Is are present in these catalogs. These five source are 01, 16, 18, 20, and 31. However, we note that the coordinates reported in Knobel et al. (2012) for the groups and in the fields of 16, 18 and 20 and those of the FR Is are separated by ∼63, 40, and 42 arcsec, respectively. Therefore, these three associations are only marginally consistent. Conversely, the offsets for the other two FR Is (i.e. 01 and 31) are $\lesssim 14$ arcsec; hence the associations are more robust. The source 258 is the only FR I in our sample with a photometric or spectroscopic redshift less than $z = 1$ for which no group was found in these catalogs.

Similarly, the PPM does not find any Mpc-scale overdensity associated with that source. We also note that the cluster candidate in the field of 01 was previously suggested in FGH07.

Redshifts $z = 0.88$, 0.92, 0.79, and 0.96 are reported for the groups associated with the sources 01, 16, 18, and 20, respectively (FGH07, Knobel et al., 2009; George et al., 2011; Knobel et al., 2012). The redshifts fully agree with our estimates obtained with the PPM method (see Table 8.1) for all these overdensities. A group is also present in the field of our source 31 at an estimated redshift $z = 0.91$ in Knobel et al. (2009). This is exactly the spectroscopic redshift of the FR I. Based on spectroscopic redshifts, Knobel et al. (2009) associated only two members with this group. They also estimated a relatively low mass of $M = 8.9 \times 10^{12}\ M_{\odot}$. The PPM does not find this group. It might be explained by the fact that the PPM is more effective to find more massive structures, as discussed in Section 8.10 and tested against simulations in Chapter 7.

8.2 Other cluster candidates

We now consider those fields in which no overdensity associated with the radio source is found. In Table 8.2 we report for such fields the overdensities that would be associated with the radio galaxies if their photometric redshifts, as estimated in B13, had significantly higher photometric redshift errors. We adopt the same column description as in Table 8.1. We do not consider source number 31, for which a spectroscopic redshift is available. We also report only those overdensities which are still detected if a smaller redshift bin Δz is chosen throughout the PPM procedure. Interestingly, among these other overdensities, there is a high significance 3.5σ overdensity which is detected in the field of 13 at a redshift $z = 1.42 \pm 0.06$. Zatloukal et al. (2007) also found the presence of a cluster candidate (i.e. their cluster candidate number 13) in the same field at the redshift $z = 1.45$. We suggest that the two overdensities correspond in fact to the same cluster.

8.3 The remaining fields

We discuss in this section the remaining cases for which the difference between the redshift of the source and the redshift of any overdensity detected in the field is too large to make the association plausible. This is the case for the sources 11, 30, 31, 70, 224, and 258.

Source 11 is a HLRG with a photometric redshift $z = 1.57^{+0.14}_{-0.09}$. No overdensity is found in its field within the redshift range $z_{\rm centroid} = 0.4 - 4.0$ considered by the PPM.

Source 30 is a LLRG with a photometric redshift $z = 1.06^{+0.11}_{-0.07}$. Three overdensities are found in its fields. Their estimated redshifts are $z = 1.36$,

The Low Luminosity Radio Galaxy subsample

ID	$z_{\rm source}$	$z_{\rm overdensity}$	significance	$r_{\rm min}$ (arcsec)	$r_{\rm max}$ (arcsec)	$r_{\rm max,phys.}$ (kpc)	$r_{\rm max,comov.}$ (kpc)
13	$1.19\pm^{0.08}_{0.11}$	1.42±0.06	3.50	0.0 ——	84.4±8.0 (86.6)	719±68	1741±165
202	$1.31\pm^{0.09}_{0.12}$	0.91±0.08	2.30	$7.6\pm^{17.9}_{7.6}$ (0.0)	114.3±16.6 (122.5)	899±130	1718±249
219	$1.03\pm^{0.02}_{0.04}$	1.20±0.06	2.60	0.0 ——	70.7 ——	589 ——	1297 ——

The High Luminosity Radio Galaxy subsample

ID	$z_{\rm source}$	$z_{\rm overdensity}$	significance	$r_{\rm min}$ (arcsec)	$r_{\rm max}$ (arcsec)	$r_{\rm max,phys.}$ (kpc)	$r_{\rm max,comov.}$ (kpc)
32	$2.71\pm^{0.38}_{0.34}$	2.22±0.07	2.20	0.0 ——	67.1±7.8 (70.7)	561±65	1808±210

Table 8.2: Cluster candidates not associated with the radio galaxies as inferred with the PPM. Cluster candidates in the fields of the LLRGs (top table) and HLRGs (bottom table) not associated with the radio galaxies. Column description: (1) source ID number; (2) photometric redshift of the source along with uncertainties from B13. (3) redshift of the overdensity and corresponding rms dispersion, both estimated with the PPM; (4) significance of the overdensity estimated by the PPM in terms of σ; (5) average minimum radius [arcsec] of the overdensity along with the rms dispersion around the average (both estimated with the PPM). The median value [arcsec] is written between the parenthesis; (6) average maximum radius [arcsec] of the overdensity along with its rms dispersion around the average (both estimated with the PPM). The median value [arcsec] is written between the parenthesis; (7) average physical size [kpc] of the overdensity along with the rms dispersion; (8) average comoving size [kpc] of the overdensity along with the rms dispersion; The rms dispersions and the median values in columns 5, 6, 7, 8 are not reported in those cases where the rms dispersion is null.

1.82, and 2.30, respectively. Their detection significances are 2.0σ, 2.0σ, 2.7σ.

Source 31 is a LLRG at $z_{\rm spec} = 0.91$. Four overdensities are detected in its field at redshifts $z = 0.70$, 1.91, 2.27, and 3.62, respectively. They are detected at a significance level of 3.6σ, 2.1σ, 3.1σ, and 2.7σ. Note that none of these overdensities would be associated with the radio galaxy if the photometric redshift $z = 0.88^{+0.03}_{-0.05}$ were adopted from B13, instead of the spectroscopic redshift. As outlined in Section 8.1, a group was found by previous work in the field of 31. The estimated redshift and mass are $z = 0.91$ and $M = 8.9 \times 10^{12}\ M_{\odot}$, respectively (Knobel et al., 2009). As discussed in Section 8.10 and tested in Chapter 7 the PPM is more effective to find richer groups and clusters. Therefore, it is not surprisingly that our method does not detect this relatively low mass group.

Source 70 is a HLRG with a photometric redshift $z = 2.32^{+0.53}_{-0.20}$. One single overdensity at $z = 0.49$ is detected in its field, with a significance of 2.0σ.

Source 224 is a LLRG with a photometric redshift $z = 1.10^{+0.10}_{-0.04}$. In Figure 6.2 (panel d), we report the corresponding PPM plot. Three overdensities are detected in its field at redshifts $z = 0.46$, 2.58, and 3.88, respectively. There high significance patterns are in fact clearly visible in the PPM plot. Their significance levels are 2.3σ, 2.5σ, and 2.6σ.

Source 258 is a LLRG with at $z_{\rm spec} = 0.9009$. Four overdensities are detected in this field at redshifts $z = 2.07$, 2.40, 3.03, and 3.24, respectively. They are detected with significances of 3.4σ, 2.4σ, 2.5σ, and 2.3σ.

8.4 Multiple associations

As clear from Table 8.1, multiple associations are found in the case of sources 03, 25, and 28, only. Multiple overdensities might be detected (i) in presence of projection effects; (ii) because of incorrect photometric redshift estimates that might be affected by systematics, especially in the case of the dimmer cluster members (e.g. those with AB magnitude $i^+ \sim 24$ in the I09 catalog); (iii) as a result of multiple local maxima that characterize the patterns of the PPM plot around a given redshift $z_{\rm centroid}$.

We here reconsider in detail all cases where we find multiple overdensities associated with a single galaxy. As mentioned above, two overdensities are associated with the source 25 (see also Figure 6.2, panel c). They have similar significances ($\sim 2.5\sigma$) and they are also both detected starting from 50 arcsec from the location of the FR I. Such an angular separation corresponds to $\sim$ 400 kpc at the redshift of the LLRG. Similar sizes of $\sim$0.7-1.0 Mpc are estimated for the two overdensities (see Table 8.1).

We visually inspected the field of this source and we did not find any evidence that the non-null offset and the multiple association are present

because of an artificiality or a technical bias of the I09 catalog occur at the redshift of the radio galaxy (e.g. that some sources at the redshift of the cluster candidate and in the field of the FR I are not included in the I09 catalog or that their redshifts are erroneously estimated). Since we do not find any clear discrepancy between the two overdensities and, furthermore, we estimate similar properties for these two Mpc-scale structures, we suggest that both the detections are real and they could also correspond to a single cluster candidate associated with source 25.

As mentioned above, two $\sim 2.5\sigma$ overdensities are associated with the HLRG 03 (see also Figure 6.2, panel b). They are both detected starting from the coordinates of the radio galaxy (i.e. $r_{\rm min} \sim 0$ arcsec) and their estimated sizes are similar (i.e. ∼500-600 kpc, see Table 8.1). However, they are detected at significantly different redshifts $z = 1.82$ and 2.39, respectively. Analogously to the case of source 25, we visually inspected the field of 03 and we did not find any evidence that the multiple association is present because of a technical bias. Therefore, both the overdensities are equally considered as good, but distinct, cluster candidates, since they are found at different redshifts.

Two overdensities are associated with the source 28. They are detected at similar (but different) redshifts $z = 2.71$ and 2.98, and with similar significances (∼2.0-2.5σ). We also estimate similar sizes for both of them (i.e. $\sim 0.8 - 1.0$ Mpc, see Table 8.1) However, we find that the overdensity at the lower redshift starts to be detected from 87 arcsec from the radio galaxy. This corresponds to $\sim$ 700 kpc at the redshift of the overdensity. Analogously to the case of sources 03 and 25, we visually inspected the field of 28 and we did not find any evidence that the non-null offset and the multiple association are present because of a technical bias. Since we do not find any clear discrepancy between the two overdensities, but nevertheless we estimate different redshifts, we are not able to conclude if the associations correspond either to two separate Mpc-scale overdensities at different redshifts or to a single Mpc-scale structure that is identified as a double pattern in the PPM plot.

8.5 The clean catalog

We repeat all the analysis not considering sources that are classified as stars, X-ray AGNs, or that are in masked areas in the I09 list. Hereinafter we refer to this as the clean catalog.

Stars and X-ray AGNs are about $\sim 4\%$ of the sources in the catalog, while masked sources are about $\sim 13\% - 18\%$ (in the redshift range of our interest). The fields of 36 and 285 were almost completely masked-out most likely because the seeing in the *Subaru* optical images (Taniguchi et al., 2007) was poor. We visually inspect the HST image of these fields and we

find that all the masked-out objects are in fact galaxies. Therefore, in these cases we include these masked out objects in our analysis. If the full I09 catalog is adopted we find evidence of overdensities in both of these fields.

Interestingly, we find evidence for a 2.5σ overdense region associated with the radio galaxy 234 only if the clean catalog is adopted, while no overdensity is found if the complete I09 catalog is adopted. We visually inspect the HST image of that field and verify that some sources have been masked southern of the location of source 234 because they are most likely foreground bright sources. We also find evidence for a segregation of $z \sim 0.93$ sources in the proximity of the radio galaxy 234. We believe that the discrepancy in adopting the two I09 catalogs is due to the fact that the estimated mean number density of the COSMOS field is lower if the clean catalog is adopted rather than if the full catalog is considered, while the number of masked sources in the field of 234 is low enough to detect the overdensity only if the clean catalog is used. For the sake of completeness, we report the overdensity associated with source 234 in Table 8.1. The fields of 36, 234, and 285 are the only cases for which we find a significant difference adopting the two I09 catalogs.

Since we do not find any substantial mismatch adopting the clean catalog instead of the full catalog we preferred to adopt the full catalog and then, for comparison, repeat the PPM analysis adopting the clean catalog.

8.6 Inferred cluster size

In this section we limit our discussion to the cluster core sizes estimated by the PPM. The PPM detects all of the overdensities within given areas in the projected sky around the location of each radio galaxy. The procedure is fully described in 6. The PPM infers the minimum and maximum distances from the coordinates of the radio galaxy at which the overdensity is detected.

The distances are estimated by averaging over all the points of the PPM plot having the significance of the overdensity and located around the redshift of the overdensity at the fixed bin ($\Delta z = 0.28$). Such estimates are shown in Table 8.1 for our cluster candidates. Both the average and median values are reported. The median values are less affected by the outliers and are always nevertheless consistent with the corresponding averages within the rms uncertainties. These aspects suggest that the overdensities are detected in the projected space with good accuracy and that these detections are stable with respect to a different choice of the parameters (i.e. a different centroid of the redshift bin adopted).

In Figure 8.1 we plot the comoving (bottom panel) and physical (top panel) average maximum radii for each overdensity, in addition to the corresponding rms dispersions as a function of the estimated redshift of the overdensity in addition to its formal uncertainty. We conservatively reject

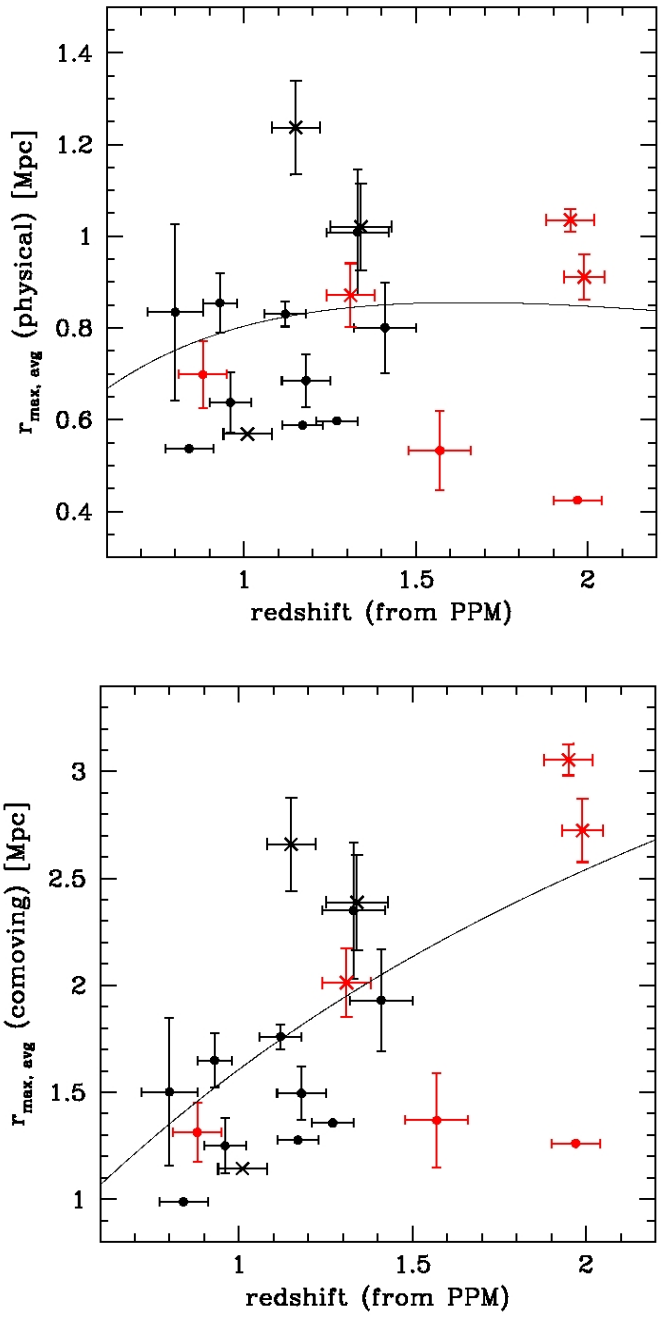

Figure 8.1: Cluster sizes estimated by the PPM as a function of their estimated redshifts. Red and black points refer to the cluster candidates around the HLRGs and the LLRGs, respectively. The reported uncertainties are the 1-σ rms dispersions around the average. No error is reported in those cases where the rms is null. Overdensities detected starting from a non null angular separation from the locations of the radio galaxies are plotted as crosses. The remaining overdensities are plotted as full points. Sizes are plotted in physical units (top) and in comoving units (bottom). Sources with multiple overdensity detections have been conservatively rejected. The solid black line shows the physical (top panel) and comoving (bottom panel) sizes that correspond to 100 arcsec, at each redshift.

all the sources with multiple overdensity detections.

The cluster candidates around the LLRGs have, on average, comoving (physical) estimated sizes of $r_{\rm avg} = 1672$ (784) kpc, with an rms dispersion around the average of 522 (211) kpc and a median value $r_{\rm median} = 1501$ (800) kpc. The overdensities around the HLRGs have an estimated average comoving (physical) size of $r_{avg} = 1955$ (745) kpc, an rms dispersion around the average of 780 (236) kpc and a median value $r_{\rm median} = 2012$ (871) kpc. If we do not distinguish between the two different classes we have an average comoving (physical) value of $r_{\rm avg} = 1762$ (772) kpc, an rms dispersion around the average of 607 (213) kpc and a median value $r_{\rm median} = 1501$ (800) kpc.

Note that these are only rough estimates of the core size of our cluster candidates. However, concerning our project, we can use them to infer interesting considerations (see also Section 8.10.7 and 8.10.8). In general, these results suggest that the overdensities in our sample have similar core sizes, independently of the class considered (i.e. the LLRGs or the LHRGs).

More in general, there seems to be a trend where high redshift sources are also found in overdensities with higher comoving sizes. We do not find any statistical significance by performing the Spearman test. Nevertheless, we cannot exclude that less dense overdensities occur at high redshifts. Diffuse protoclusters with star-forming galaxies have been in fact found at redshifts higher than $z \sim 2.0$ (Steidel et al., 2000; Venemans et al., 2007; Capak et al., 2011; Noble et al., 2013). However, we suspect that this trend is artificial and due to the dependence of the estimated size with redshift or by the low number count statistics. Another possibility is that the cluster size could be overestimated at most by a factor of ~ 2 if (i) the radio galaxy were not located in the central regions of the cluster core (as tested against simulations in Chapter 7); (ii) in the cases when $r_{\rm min}$ is not null (the crosses in Figure 8.1), where $r_{\rm max}$ might not be a good cluster size estimator (see also the discussion in Section 8.10.8).

8.7 The minimum distances

The cases where the minimum distances are estimated to be small or null likely correspond to those where the coordinates of the radio galaxy fairly coincide with the center of the associated overdensity.

However, some of the overdensities are detected starting from a positive angular separation of $\gtrsim$50 arcsec from the coordinates of the radio galaxy. Such an offset corresponds to a physical scale of 422 kpc at the median redshift estimated for our cluster candidates (i.e. $z = 1.3$).

These cases are controversial and are further discussed in Section 8.10.8. They might be Mpc-scale overdensities where the radio galaxy is in the outskirts of the overdensity. This has been investigated in Chapter 7 through

the help of simulations. We have found that the method is able to detect cluster candidates even if the coordinates of the cluster are known with an accuracy of ∼100 arcsec and that the inferred minimum radii are only in some cases greater than zero. Alternatively, in these cases the radio galaxies might be hosted in underdense regions within their cluster environment.

As outlined above we also visually inspected the fields of some sources (namely 25 and 28) for which the overdensity starts to be detected from a non null separation from the location of radio galaxy. Even if we find a depletion in the number of photometric redshifts that are around the assumed redshift of the radio galaxy and are associated with galaxies in its field, we are confident that no technical bias occurred, concerning the estimation of photometric redshifts in the I09 catalog.

8.8 The Kolmogorov-Smirnov test

In this section we apply the Kolmogorov-Smirnov (KS) test to the cumulative number distributions of galaxies in the fields of our FR I sample. We perform such a test in order to prove - *a posteriori* - that standard statistical methods such as the KS test are ineffective. Limited to this analysis we also include in the sample the fields of both F062 and F126 from FGH07 These two clusters were also considered in our simulations (see Chapter 7). This approach based on the KS test is similar to that applied by previous work to search for clustering of sources in the COSMOS field (e.g. Harris, 2012).

For each field of our sample, we consider only those galaxies that fall within a 2-σ long redshift bin centered at the redshift associated with the FR I, with F062, or with F126. The length of the bin is set by summing in quadrature the uncertainty associated with the redshift of the FR I (as given in Baldi et al., 2013) with the statistical 1-σ photometric redshift uncertainty, that is estimated as $\sigma_z = 0.054(1 + z)$ (Ilbert et al., 2009, and consistently with what adopted for our simulations). A null uncertainty is associated with the redshifts of both F062 and F126. This is because F062 is associated with the source COSMOS-FR I 01 (C09) for which the spectroscopic redshift $z = 0.88$ is known. The redshift of F126 is $z = 1.0$ and it is estimated by means of photometric redshift information in FGH07. This estimate fully agrees with that obtained with the PPM (see Section 7.1).

We consider 70 non overlapping Randomly Selected Fields (RSFs) in the COSMOS survey. The centers of each pair of these fields are separated by at least ∼6 arcmin. This assures that the RSFs are pairwise independent.

For each field in our sample we consider each of the RSFs and we apply the KS test to compare the cumulative radial distributions of the galaxies in the two fields. Only those sources that fall within the 2-σ long redshift bin are considered, as explained above. We repeat the KS test for all the 70 RSFs and we average among the p-values obtained with the test. Small p-

values imply the null hypothesis that the compared distributions are drawn from the same distribution is rejected. We find that the average p-values for the fields in our sample are high, within $\sim 0.1 - 0.6$. Similarly, the rms dispersion is large and comparable to the corresponding average. Therefore, our results are not conclusive. This suggests that the KS test is not effective in searching for Mpc-scale overdensities by using photometric redshifts.

Furthermore, we pairwise compare the cumulative distributions of the 70 RSFs. The average KS p-value is equal to 0.24. The rms dispersion around the average is 0.26. Therefore, both the fact that the estimated KS probability is high and that it is associated with a large rms dispersion suggest that shot noise fluctuations affect the results of the KS test.

8.9 The Papovich method

In this section we adopt a method (Papovich, 2008, P08) based on an IR color selection to search for cluster candidates in the field of the galaxies of our sample. The P08 method has been widely used in the literature (Mayo et al., 2012; Galametz et al., 2012; Wylezalek et al., 2013a) to search for clusters at $z \gtrsim 1.3$; it utilizes the 1.6 μm bump in the SED of red galaxies, due to a minimum in the opacity of the H^- ion, present in the atmospheres of cool stars (John, 1988; Galametz et al., 2012, and references therein). We apply such a method to our sample to see how many objects we can positively detect. In Section 8.9.1 we compare these results with those obtained by adopting our newly developed PPM.

The P08 method requires wide field observations at both 3.6 and 4.5 μm. We use the Spitzer-COSMOS (S-COSMOS) archive catalog[1]. S-COSMOS covers the entire COSMOS field. It is a deep infrared imaging survey carried out with the *Spitzer* Telescope. Mpc-scale overdensities are identified as regions of higher concentration of red sources with respect to the average density, which is derived as follows, similarly to what was done in previous work (Mayo et al., 2012; Galametz et al., 2012).

We choose ∼300 randomly selected non overlapping circular fields of 1 arcmin radius each. The number of the fields is limited and cannot be increased indefinitely because we require the fields to be non overlapping and to lie within the COSMOS area.

We conservatively consider the objects in the S-COSMOS catalog that are detected at both 3.6 and 4.5 μm with a signal to noise ratio $S/N > 10$. This criterion is equivalent to that applied by P08 and similar to what was done in previous work (Galametz et al., 2012; Wylezalek et al., 2013a). The S/N limit ensures that only well-detected objects enter the sample (Papovich, 2008). We also limit our analysis to those sources that are brighter

[1] `http://irsa.ipac.caltech.edu/data/SPITZER/S-COSMOS/`

than 1 μJy, which is the confusion limit of the S-COSMOS survey at both 3.6 and 4.5 μm (Sanders et al., 2007).

Then, we select all the sources satisfying $([3.6]-[4.5])_{AB}$ >-0.1 mag. Hereafter we denote as [3.6] and [4.5] the apparent AB magnitudes at the (observer frame) wavelength equal to 3.6 and 4.5 μm, respectively.

In Figure 8.2 we plot the number count distribution for the $\sim$ 300 fields as a function of the number of sources in each field that satisfy the P08 criterion.

Similarly to what was done in Mayo et al. (2012) and Galametz et al. (2012), we fit such a distribution with a Gaussian function, iteratively clipping at 2-σ above the best fit average. This is done in order to exclude from the fit the high number count tail of the distribution. In fact, it might be contaminated by those fields that are populated by a significant high number of red objects. They might be associated with Mpc-scale overdensities and therefore, not representative of the overall number count distribution in the COSMOS survey.

We estimate the average number of sources per field which satisfy the P08 criterion. It is equal to $N = 30.0 \pm 6.4$ where the average and the reported uncertainty are the mean value and square root of the variance of the best fit Gaussian function, respectively.

For each 1 arcmin radius field centered around the galaxies in our sample we count the sources in the S-COSMOS catalog that satisfy the P08 criterion, analogously to what has been done for each of the $\sim$ 300 randomly selected fields. Then, we estimate the overdensity significance level as the ratio of the number excess with respect the average $N = 30.0$ and the 1-σ dispersion ($= 6.4$) associated with N.

The P08 method is expected to be effective at redshifts $z \gtrsim 1.3$ (see e.g. Galametz et al., 2012; Mayo et al., 2012). As further discussed in Galametz et al. (2012), this is due to the fact that the specific color selection criterion detects the rest-frame 1.6μm bump in the SED of the galaxies, that is originated by a minimum in the opacity of the H^- ion in the atmospheres of cool stars (John, 1988). Such a feature is redshifted out of the Spitzer filters at 3.6μm and 4.5μm, in the case of lower redshift ($z \lesssim 1.3$) sources.

Note that, even if the radio galaxy is at a redshift $z < 1.3$, the P08 method might detect those overdensities in the field that are not associated with the radio galaxy, but are at $z \geq 1.3$. As discussed in Section 8.2 and as it is clear from visual inspection of the PPM plots in Figure 6.2, overdensities not associated with the radio galaxy are also found by the PPM in the fields of the radio sources, at different redshifts.

The results of the P08 method are shown in Table 8.3, where we report the number counts and the associated significance levels of the overdensities in the fields of the sources in our sample. In the Table we only report two objects at $z < 1.3$, namely 13 and 39. This is because these are the only two fields at $z < 1.3$ in which overdensities are detected by such a method. For

all other objects that are not reported in the Table the P08 method does not find any overdensity.

Negative significances correspond to underdense fields. Similarly to what was done in Galametz et al. (2012) and Mayo et al. (2012), we consider as dense Mpc-scale environments only the regions with an overdensity detected at a level $> 2\sigma$, i.e. sources with more than 42 counts within 1 arcmin radius.

According to the P08 method, six sources are found to be in a $\geq$ 2-σ dense Mpc-scale environment. The source for which the highest significance is observed is object 03 with a photometric redshift of 2.2. Note also that the field of 28, that has a photometric redshift $z = 2.9$, is detected with a $\sim 2.6\sigma$ significance. While this object is formally beyond the redshift range for which this sample has been built it is still an interesting case worth mentioning. This is because such an overdensity might be a $z \sim 3$ (proto)cluster around a ~ 2 orders of magnitude lower power radio galaxy than those commonly found in clusters or protoclusters at similar redshifts (Miley & De Breuck, 2008; Galametz et al., 2013).

ID	n. of sources	σ	ID	n. of sources	σ
02	36	0.93	32	33	0.47
03	51	3.26	34	31	0.16
04	47	2.64	37	38	1.24
05	28	-0.31	38	37	1.09
11	24	-0.93	39*	47	2.64
13*	49	2.95	70	33	0.47
22	40	1.56	202	34	0.62
25	30	0.00	226	34	0.62
28	47	2.64	228	33	0.47
29	49	2.95			

Table 8.3: Papovich (2008) method results. Column description: (1) ID number of the radio galaxy, radio galaxies 13 and 39 have photometric redshift $z < 1.3$ and are marked with an asterisk; (2) number of sources within 1 arcmin radius with flux >1 μJy and S/N>10 at both 3.6 and 4.5 μm, as well $([3.6]-[4.5])_{AB} > -0.1$ mag; (3) overdensity significance (in units of σ). Negative values refer to underdense regions.

In the following sections we discuss the results obtained by the P08 method and we compare them with those of the PPM.

8.9.1 Comparison with the results of the Papovich (2008) method

We compare our results with those obtained independently by using the P08 method, as described in Section 8.9. All the six cluster candidates found with the P08 method are also detected by the PPM. Five of them are associated with radio galaxies in the sample, according to the PPM procedure. The

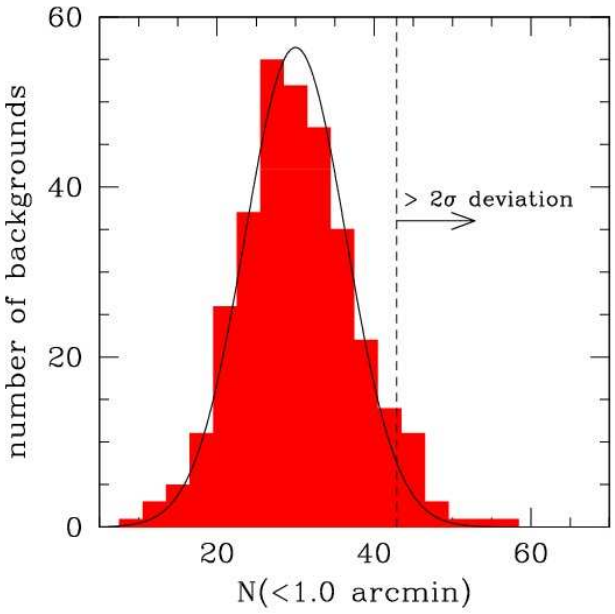

Figure 8.2: Results of the Papovich (2008) method. Red histogram: distribution of sources within ∼300 randomly selected non-overlapping circular fields of 1 arcmin radius selected from the COSMOS area. The solid line represents the Gaussian best fit curve obtained iteratively clipping at 2σ above the best fit average. The vertical dashed line is located at the 2σ deviation from the best fit average.

sixth overdensity is the cluster candidate found in the field of 13 by both the PPM and the P08 method. However, according to the method procedure, such an overdensity is not associated with the radio galaxy by the PPM (see Section 8.2). Note that all of the six overdensities detected by both the P08 method and the PPM are at redshift $z \gtrsim 1.3$ (within the corresponding uncertainties), as estimated by the PPM procedure. This is also true for the overdensities in the fields of 13 and 39. Even if the radio sources are at redshift $z = 1.19\pm^{0.08}_{0.11}$ and $z = 1.10\pm^{0.05}_{0.05}$, the PPM detects overdensities in their fields at $z = 1.42 \pm 0.06$ and $z = 1.27 \pm 0.06$, respectively. These results are not surprising since the P08 method is effective to find clusters at $z > 1.3$.

Excluding the overdensity in the field of 13 that is not associated with source 13, only five out of the 12 cluster candidates at $z \gtrsim 1.3$ in our catalog are also found with the P08 method. Among the 12 clusters we conservatively do not consider the overdensities in the fields of the sources 38 and 228. Even if these sources have photometric redshifts $z = 1.30\pm^{0.17}_{0.28}$ and $z = 1.31\pm^{0.05}_{0.07}$, respectively, the PPM detects clusters in their fields at redshifts below $z = 1.3$.

Two out of the five clusters, namely 29 and 39, that are associated with the radio galaxies and detected by both the P08 method and the PPM, are around LLRGs, the other three (namely source 03, 04, and 28) are around HLRGs. As discussed above, source 39 is the only source out of those five that has a photometric redshift below $z = 1.3$.

If we consider our seven cluster candidates at $z \gtrsim 1.3$ in our catalog that are not detected by the P08 method we find that three of them are associated with LLRGs (i.e. sources 2, 22, and 25). The remaining four out of the seven are associated with $z \gtrsim 1.3$ HLRGs (i.e. 05, 34, 37, and 226). Since the P08 method was primarily designed to search Mpc-scale overdensities at these redshifts, it is interesting that many of our $z \gtrsim 1.3$ cluster candidates are not detected by such a method. It is therefore worth reconsidering in more detail our cluster candidates found around our $z \gtrsim 1.3$ sources.

Three of our cluster candidates are at $z \simeq 2$. These are the overdensities associated with sources 03, 05, and 226. As mentioned before, the presence of Mpc-scale overdensities around those sources were previously suggested in C10. Interestingly, the P08 method finds the overdensity in the field of 03 only.

If we focus on the nine $1.3 \lesssim z \lesssim 2$ sources that the PPM finds to be in dense Mpc-scale environments, (i.e. sources 02, 04, 22, 25, 29, 34, 37, 38 and 228) we find that only two out of the nine are found in dense environments by the P08 method (i.e. sources 04 and 29). However, among them, the estimated redshifts of the cluster candidates associated with the sources 37 and 38 are only marginally consistent within the redshift uncertainties of the two sources. These two cases could correspond to false positive overdensity

PPM detections. Furthermore, the P08 method should not be able to detect the $z = 0.88$ overdensity associated with the source 38, since such a redshift is well below the redshift range where the method is effective. The case of 37 is different, this is because the overdensity associated with this source has an estimated redshift $z = 1.95$. Therefore it falls within the redshift range allowed by the method.

Excluding source 38, the results reported above imply that $75\% \pm 15\%$ of our $1.3 \lesssim z \lesssim 2$ cluster candidates are not detected by the P08 method (we have conservatively excluded the above mentioned source 39 that is at redshift formally below $z = 1.3$). Such a percentage decreases down to $71\% \pm 17\%$ if also the source 37 is not considered.

We consider apart the high redshift $z \sim 3$ source 28 that is detected to be in a dense environment at $\sim 2.6\sigma$ and $\sim 2.5\sigma$ significance levels by the P08 method and by the PPM method, respectively. Even if such a redshift is formally beyond the redshift interval ($z \sim 1 - 2$) of our interest, we do not reject the source.

These results suggest that the great majority ($\gtrsim 70\%$) of our $z \gtrsim 1.3$ cluster candidates are not detected by the P08 method, while all the seven cluster candidates found with such a method are also detected by the PPM. This suggests that our method might be more effective to find cluster candidates, at least limited to our sample and dataset used. We will further discuss these results in the following section.

8.9.2 Do we find blue or still forming clusters?

In the previous section we found that the great majority (i.e. $\sim 70\%$) of our $z \gtrsim 1.3$ cluster candidates are not detected with the P08 method, while all of the cluster candidates detected by such a method are also found with the PPM. This is interesting, since such redshifts correspond to the range within which the P08 method is effective (Galametz et al., 2012). Although we cannot fully understand the details for such a discrepancy we believe that the method might miss those overdensities that do not fulfill the specific P08 color selection.

This result could also have physical implications. The P08 method searches for segregations of red $([3.6] - [4.5])_{AB}$ galaxies. In principle, it is sensitive to both passively evolving and star-forming galaxies. However, the method might miss overdensities that are populated by a significant amount of bluer galaxies than those required in order to detect the overdensity.

As argued by Muzzin et al. (2013), foreground galaxies at redshift $0.2 < z < 0.4$ have colors similar to those at redshift $z > 1.0$ and might add noise, thus affecting the detections.

Furthermore, we also found that the majority of the objects that are used for the PPM and are selected within the I09 catalog are not included in the

S-COSMOS survey and, therefore, they are not used by the P08 method. Hence, a mismatch between the P08 method and the PPM is not surprising.

Note that we applied the P08 method performing a counts-in-cell analysis, i.e. we counted objects within a fixed circle centered at a given position in the sky, as done in previous work (e.g. Galametz et al., 2012; Mayo et al., 2012; Wylezalek et al., 2013a).

On the contrary, the search for cluster candidates performed in this work by adopting the PPM is based on number counts and does not rely on peculiar and specific properties (e.g. colors of the sources) and a specific segregation of the galaxies within the cluster core (see also Section 8.10.8).

Since the P08 method is applied performing a counts-in-cell analysis, some of the clusters that are not detected by such a method might be populated by galaxies that are not completely segregated in the cluster core.

Interestingly, C10 suggested the presence of a high fraction of star forming galaxies in the $z \sim 2$ cluster candidates associated with sources 03, 05, and 226, on the basis of the visual inspection of the RGB images of their fields.

The evidence for star formation activity in some of our clusters is not surprising, especially at $z \gtrsim 1.5$, where cluster galaxies are expected to have ongoing or increasing star formation (Zeimann et al., 2012). In fact, in some of these high redshift clusters, a significant fraction of the cluster galaxy population is constituted by highly dust reddened sources (Strazzullo et al., 2013) or by blue and irregular galaxies (Tozzi et al., 2013).

From a theoretical point of view, previous studies made predictions for the mass function of galaxy clusters (e.g. Bode et al., 2001; Tinker et al., 2008). However, since the cluster/group population at redshift $z \gtrsim 1.5$ is limited to a few known spectroscopically confirmed clusters, observational studies are limited to single high redshift clusters. This implies that the mass function is only poorly determined by observations.

The spectroscopic confirmation of our $z \gtrsim 1.5$ cluster candidates would increase the number count statistics. This will help constraining the cluster mass function and will support previous cluster studies from both a theoretical and observational point of view.

8.10 Discussion

One of the main goals of this project is to search for high redshift $z \gtrsim 1$ clusters and groups using FR I radio galaxies as beacons. For this reason we selected a subsample of *bona fide* Low Luminosity Radio Galaxies (LLRGs) from the original C09 sample. This was done to derive a sample of sources with radio powers compatible with those of FR Is at low redshifts.

We also examine the properties of the subsample of relatively high radio power objects (HLRGs) with respect to the LLRGs. In the following we

discuss the implications of our results for these two groups of objects.

8.10.1 Mpc–scale environments of the C09 sample

As reported in Section 8.1 both the LLRGs and HLRGs are found in dense environments. The fraction of galaxies in groups or clusters is about $\sim 70\%$ for both subsamples, consistently within the 1-σ uncertainties. We also found that the detected overdensities have comparable (within a factor of $\sim$2-3) estimated sizes, independently of both the subsample and the redshift considered (we will discuss this in detail in Section 8.10.7). Therefore, *a posteriori*, this result strongly suggests that, on a statistical basis, the two subsamples constitute a single population of radio galaxies with similar Mpc–scale environments and similar properties.

8.10.2 Comparison with low-redshift radio galaxy environments

We found that the majority (69%$\pm$8%) of the radio galaxies in our sample reside in dense environments. Here we quantitatively compare our results with the results obtained for samples of low redshift FR Is.

Note that it is difficult to compare the estimated cluster richness of our candidates with that of other samples of low redshift clusters associated with radio galaxies. This is mainly because of the different datasets used and of the different techniques employed in measuring the cluster richness.

Zirbel (1997) found that 70% (with an estimated uncertainty of 11%)[2] of low redshift (i.e. $z < 0.25$) FR Is in their sample reside in intermediate/rich groups or clusters (i.e. structures with 10 or more members). In terms of richness, these groups could roughly correspond to the overdensities detected by the PPM around the radio galaxies in our sample.

Instead, only $(24 \pm 8)\%$ of the low redshift (i.e. $z < 0.25$) FR IIs in the Zirbel (1997) sample reside in intermediate or rich groups. Such a percentage increases up to $(41 \pm 8)\%$ if high redshift (i.e. $0.25 \lesssim z \lesssim 0.5$) FR IIs are considered. The results obtained by Zirbel (1997) are also in agreement with what independently found for FR IIs at $z < 0.3$ by Smith & Heckman (1990) and what found by Ramos Almeida et al. (2013) for a $z \leq 0.7$ sample of luminous radio galaxies, mainly comprising FR IIs.

Interestingly, the fraction we found for the $z \gtrsim 1$ sources in our sample is fully consistent with the percentage (i.e. 70%) found by Zirbel (1997) for their sample of low redshift (i.e. $z < 0.25$) FR Is. Note that this holds not only for the LLRGs but also for the HLRGs. This implies that the environments of FR Is and FR IIs are different and that they also evolve differently with redshift. While the majority of FR Is seem to be found in rich groups

[2]We estimated the error on the percentage by adopting 1σ uncertainties according to the binomial statistics, for consistency with our results.

or clusters at all redshifts, the FR IIs seem to inhabit rich environments only at $z > 0.25$. However, as discussed in the following section, the fraction of FR IIs that reside in rich groups or clusters is significantly lower than that of FR Is even at higher redshifts.

8.10.3 Comparison with high-z FR IIs

In this section we compare our results with the environment properties found for high redshift FR IIs. Note that, thanks to the analysis of the C09 sample, this is the first time that the environments of FR Is and FR IIs can be directly compared at such high redshifts.

High redshift ($z \sim 1-2$) low power radio galaxies (i.e. FR Is) are found in rich environments more frequently than high power FR IIs at similar redshifts. In fact, if we consider the sample of high redshift ($z \gtrsim 1.3$) powerful FR IIs studied by Galametz et al. (2012), 11 out of 48 objects (i.e. $23\% \pm 7\%$) reside in Mpc scale environments that are at least 2σ denser than the field.

However, Wylezalek et al. (2013a) extended this analysis to a larger sample of 387 radio galaxies at $1.3 < z < 3.2$. They found evidence for dense environments for 55% of these sources. Interestingly, this percentage is consistent with what found for FR II radio galaxies at redshifts $z \sim 0.5$ ($\sim$ 50%, Hill & Lilly, 1991). It is worth reminding that the results of Galametz et al. (2012) and Wylezalek et al. (2013a) were obtained with the P08 method and not with the PPM.

Note that the radio powers that characterize the objects in all of the samples cited above ($L_{1.4\ \mathrm{GHz}} \gtrsim 10^{34}$ erg s^{-1} Hz^{-1}) are about 2 order of magnitudes higher than those of all of the radio galaxies in our sample, including the HLRGs. Hence, they undoubtedly represent a different class of radio galaxies.

The comparison between our results and those cited above for powerful high-z FR IIs confirms that the environment of high redshift FR Is and FR IIs is different.

This implies that the Mpc–scale environments of FR Is and FR IIs undergo a different evolution. If we adopt a $\sim 50\%$ level of FR IIs in clusters at high redshifts as a fiducial value, we could conclude that at $z > 0.5$ the environments of FR Is and FRII s are similar (but not identical!). However, as we already discussed above, this is clearly not true at lower redshifts. Furthermore, the values reported in Galametz et al. (2012) and Wylezalek et al. (2013a) are not consistent with each other within the number count uncertainties. Wylezalek et al. (2013a) suggested that this may be due to the small size of the Galametz et al. (2012) sample. It might be interesting to study in more detail the selection criteria of these two samples in order to test whether the differences are due to significant discrepancies in the two sample selections.

Therefore, in light of the results presented here, we confirm that the connection between the active nucleus and its large scale environment could play a fundamental role in determining the specific properties of each radio galaxy. Clearly, it would be interesting to study X-ray or optically selected samples of clusters of galaxies at redshifts $z \gtrsim 1$ to investigate how the cluster properties (e.g. richness, halo mass, gas content, and X-ray luminosities) are related to those of the hosted radio galaxies (e.g. their radio power, their number within the cluster sample, and the mass and size of the host galaxy) and more in general, to those of the entire cluster galaxy population. However, these studies require complete and well studied samples of clusters. Therefore, previous work has been so far limited to low or intermediate redshifts (e.g. Ledlow & Owen, 1996).

8.10.4 Intermediate redshift cluster samples

We here focus on previous studies on intermediate ($0.3 \lesssim z \lesssim 1$) redshift cluster samples. Radio sources with radio power $L_{1.4\ \mathrm{GHz}} \simeq 10^{32-33}$ erg s^{-1} Hz^{-1} which is typical of objects in our sample, are found in $10\% - 20\%$ of the X-ray and optically selected clusters (Branchesi et al., 2006; Gralla et al., 2011).

However, such a percentage rapidly increases up to $\gtrsim 90\%$ if lower power radio sources are included ($L_{1.4\ \mathrm{GHz}} \simeq 10^{30}$ erg s^{-1} Hz^{-1}, Branchesi et al., 2006). This is in agreement with previous studies on local Abell clusters (Ledlow & Owen, 1995, 1996).

The fact that such a fraction increases for low power sources might be explained as a straightforward consequence of the steepness of the RLF of the radio galaxies in clusters (Branchesi et al., 2006). This strongly confirms that low power radio galaxies can be more successfully used to search for clusters of galaxies than radio galaxies with higher power.

8.10.5 Detection efficiency

The number density per unit redshift ($\mathrm{d}n/\mathrm{d}z/\mathrm{d}\Omega$) in the COSMOS survey is low and it is equal to $\simeq 25$, 10, and 3 arcmin^{-2} at redshifts $z \simeq 1$, 1.5, and 2.0, respectively (Ilbert et al., 2009). The steep decrease of the number counts for increasing redshifts is a strong constraint for all of the methods (including the PPM) that search for Mpc-scale overdensities on the basis of number counts (Scoville et al., 2013).

In addition, photometric and spectroscopic redshifts cannot be easily obtained within $z \sim 1 - 2$, where most of the relevant spectral features fall outside of the instrumental wavelength bands (Steidel et al., 2004; Banerji et al., 2011).

Therefore, methods that are based on number counts and redshift information and that are used to search for clusters and groups in the COSMOS

survey are usually applied up to redshifts $z \lesssim 1$ (e.g. Knobel et al., 2009; George et al., 2011; Knobel et al., 2012), or at redshifts higher than $z \simeq 2$ (e.g. Diener et al., 2013). Note also that such methods commonly use spectroscopic redshifts so that a small number (i.e. $\lesssim 5$) of cluster galaxies is sufficient to establish the presence of a cluster or group candidate.

The clusters in our sample are detected within the entire $z \sim 1-2$ redshift range. For each overdensity we estimate detection significance, redshift and size. The overdensities are detected up to 5.6σ significance. All these results are ultimately due to the flexibility of the PPM to obtain robust results in presence of low number counts. The overdensities are detected with median significances of 3.3σ and 2.5σ for the LLRGs and the HLRGs, respectively. Since the cluster candidates around the LLRGs and the HLRGs have a median redshift $z = 1.17$ and $z = 1.97$, respectively, we suggest that the discrepancy between the detection significances of the clusters associated with the two different subsamples is due to the decreasing number counts in the COSMOS survey for increasing redshifts. However, such discrepancy is relatively small considering that the number density in the COSMOS field dramatically drops down by a factor of $\sim$8 from $z = 1$ to $z = 2$ (Ilbert et al., 2009).

In Chapter 7 we tested the ability of the PPM to detect overdensities at different redshifts, with richness and size spanned within the ranges found for the cluster candidates in our sample. Interestingly, we found that our method is able to efficiently detect clusters within our redshift interval, despite the wide range allowed for the cluster richness and size.

Therefore, we are confident that the detection efficiency (i.e. the number of clusters with homogeneous properties that are potentially detectable per unit redshift by the PPM) is fairly constant with redshift. The fact that the detection rate is about 70% for both our subsamples confirms it, *a posteriori*. Conversely, if the detection efficiency dramatically decreased for increasing redshifts, we would significantly underestimate the fraction of HLRGs in clusters.

8.10.6 The $z \gtrsim 1.5$ cluster candidates

Six overdensities in our sample are found at redshift $z > 1.5$. These correspond to the sources 03, 04, 05, 28, 37, and 226. All of them are HLRGs. The fact that we find 6 overdensities at such a high redshift, despite the small area of the COSMOS survey, further suggests that these might be clusters with a low or intermediate mass (i.e. $M \simeq 10^{13-14} M_{\odot}$).

Furthermore, the number density of clusters of higher mass (i.e. $M \gtrsim 10^{14}\ M_{\odot}$) is expected to drop down by more than an order of magnitude between $z = 1$ and $z = 2$, according to the current ΛCDM scenario (e.g. Bode et al., 2001; Tinker et al., 2008). In fact, clusters with masses $M \gtrsim 10^{14}\ M_{\odot}$, at redshift $z \sim 2$, are most likely the progenitors of massive

$M \gtrsim 10^{15} M_{\odot}$ clusters at $z = 0$ (Chiang et al., 2013). Conversely, assuming hierarchical clustering (Cooray & Sheth, 2002), at $z \sim 2$, groups of lower mass could represent a larger fraction of the group/cluster population than at lower redshifts.

Furthermore, by definition, groups have a lower richness than clusters, they exhibit fainter X-ray emission, and they have lower mass content in terms both of dark matter and gas than clusters of galaxies. They are therefore more difficult to find with the conventional techniques adopted for clusters. High redshift groups are in fact usually identified up to $z \lesssim 1$ with methods such as those based on number counts (Knobel et al., 2012; More et al., 2012), or searching for strong lensing signatures originated from Mpc-scale dark matter halos (Cabanac et al., 2007; Limousin et al., 2009; More et al., 2012, see also Section 8.10.9). Interestingly, if our cluster candidates were confirmed to be rich groups (see Section 8.10.7), they would constitute a high redshift sample.

Diener et al. (2013) obtained a number of 42 candidate groups at $z \gtrsim 2$ in the COSMOS field. They used spectroscopic redshifts, so that a small number (i.e. $\lesssim 5$) of members is effective to establish the detection of a cluster candidate. Impressively, for the only object in common with our list (i.e. their cluster candidate 22 corresponds to our cluster candidate 03) the redshift and the size of the cluster estimated by the PPM fully agree with the spectroscopic measurement and the cluster size estimated in Diener et al. (2013).[3] Note that this cluster candidate was suggested by previous work (Chiaberge et al., 2010). With its five spectroscopically selected cluster members, this is the richest among the groups in the Diener et al. (2013) catalog.

On the basis of the redshift information, the authors also estimated the velocity dispersion of the cluster members (526 km s^{-1}) which is significantly higher than the average ~ 300 km s^{-1} among the group candidates in their sample. This might suggest that the cluster members are still encompassing a spatial segregation and that the cluster is still forming, as also discussed for other cluster candidates in our sample (see also Section 8.9.2).

8.10.7 Cluster properties

The general relationship among richness, size of the cluster, and the cluster mass is quite complex (i.e. it depends on the depth of the photometric catalog, the redshifts, the evolution of luminosity function), especially at the redshifts of our interest ($z \sim 1 - 2$), where the properties of the cluster galaxy population in terms of luminosity and segregation within the cluster

[3]The redshift and the size estimated by the PPM for one of the two overdensities associated with the source 03 are $z = 2.39 \pm 0.09$ and 617 ± 57 kpc, respectively. Diener et al. (2013) found a spectroscopic redshift $z = 2.440$ and estimated a size of 412 kpc for their group candidate 22.

are expected to evolve and are not fully understood. In the following sections we discuss size, mass, and richness estimates for the clusters we find in COSMOS.

Size and mass estimates for the $z \sim 1$ clusters

In this section we compare our size estimates with those obtained by previous work for our $z \sim 1$ cluster candidates that are also found in the FGH07, Knobel et al. (2009); George et al. (2011); Knobel et al. (2012) catalogs, namely the clusters in the fields of 01, 16, 18, and 20. Interestingly, all of the cluster mass estimates in these catalogs are consistent with each other and the reported cluster sizes are in good agreement with ours.

In particular, for the cluster candidate associated with our source 01 we roughly estimate a core size of ∼71 arcsec (i.e. $\sim$ 500 kpc). On the basis of Newton-XMM data, FGH07 estimated the virial core mass and the size for the same cluster candidate. They reported $r_{500} = 48$ arcsec and $M_{500} = 5.65 \times 10^{13} M_{\odot}$ (see Table 1 in FGH07 for further properties).

By assuming spherical symmetry and a β-model density profile for the cluster matter distribution (Cavaliere & Fusco-Fermiano, 1978) we estimate r_{200} =76 arcsec[4]. George et al. (2011) estimated for the same cluster candidate a core size $r_{200} = 73$ arcsec, and a core mass $M_{200} = 5.25 \times 10^{13} M_{\odot}$, on the basis of the mass versus X-ray luminosity relation given in Leauthaud et al. (2010). Note that the George et al. (2011) group catalog was obtained by using photometric redshifts and previous X-ray selected group catalogs. Both the Knobel et al. (2009, 2012) group catalogs were instead obtained by using spectroscopic redshifts. They reported fiducial mass estimates ($M \sim 6 - 9 \times 10^{13} M_{\odot}$) for the Mpc-scale overdensity associated with the source 01. They were obtained by using spectroscopic redshift information. Knobel et al. (2012) also estimated a size of 659 kpc for this cluster candidate.

Concerning the cluster candidates in the fields of 16, 18, and 20, Knobel et al. (2009, 2012) reported masses ($M \simeq 1.4 - 2.2 \times 10^{13} M_{\odot}$) and sizes ($\sim 327 - 378$ kpc, Knobel et al., 2012). These sizes are roughly consistent even if lower than those estimated by the PPM for these three groups ($\sim 600 - 800$ kpc).

These results suggest that the $z \sim 1$ cluster candidates associated with sources 01, 16, 18, and 20 are all groups of intermediate/small size, even if that in the field of 01 is likely more massive than the others (see also Section 8.10.9 for further discussion). Interestingly, this result seems to be independent of the cluster selection (i.e. optical or based on X-ray data). This is also consistent with previous work by Bahcall et al. (2003, see their Table 1), who found that the clustering lengths for optical selected clusters

[4]In estimating r_{200} we also assume hydrostatic equilibrium. We use Equation (3) of Reiprich & Böhringer (1999) and the core radius estimates as in Equation (4) of FGH07.

are comparable with (even if preferentially smaller than) those obtained for X-ray selected clusters.

We nevertheless note that our cluster sizes are only rough estimates or upper limits of the cluster core in the optical bands (see also Section 8.6) and, therefore, a robust comparison with previous X-ray cluster sizes is beyond the purposes of our work. In particular, the core size might be overestimated by at most a factor of ~ 2 if the radio galaxy is located in the outskirts of the cluster. Despite this, our estimates are reasonable and typical of rich groups and clusters for all of the clusters candidates in our sample. Furthermore, the sizes estimated in this work for each of the two subsamples (i.e. the LLRGs and the HLRGs) are consistent with each other within the uncertainties. On average, comoving and physical sizes for the cluster candidates in our sample are about 1.8 and 0.8 Mpc, respectively. Therefore, all these results allow us to draw general considerations on our cluster candidates, as shown in the following sections.

Cluster richness and mass

According to the PPM procedure, we count the galaxies within a redshift bin $\Delta z = 0.28$ centered at the estimated redshift of the cluster and within the projected area enclosed between the median values of angular separations $r_{\rm min}$ and $r_{\rm max}$ from the coordinates of the radio galaxy (see Table 8.1). This is not the number of cluster members, but simply the number of sources in the I09 catalog that are found in the field of each overdensity, around the estimated redshift of the cluster. Such a number can be considered as a rough estimate of the richness of the cluster, because of both the instrumental and the PPM limitations.

In detail, the overdensities in the fields of 18 and 26 are those that have the highest number of fiducial cluster members (i.e. ~ 200). They are also detected at high significances (5.6σ and 3.9σ, respectively). About $\sim$100 galaxies are instead associated with the overdensities in the fields of 01, 02, 16, and 20, which are detected at significances of 3.5σ, 4.3σ, 3.5σ, and 3.9σ, respectively. About $\sim$ 50 sources are selected as cluster members of the overdensities associated with the sources 39 and 228, which are detected at lower significance levels of 3.5σ and 3.2σ, respectively. At the high redshift end of our sample (i.e. $z \simeq 2$) the overdensities are instead defined by only $\sim$ 10 galaxies, as it is e.g. for the sources 03 and 05, that are detected at 2.6σ and 2.2σ, respectively.

Therefore, the estimated number of the fiducial cluster members varies with the cluster detection significance from ~ 10 for our cluster candidates at the highest redshifts ($z \sim 2$) to more than ~ 200 for our $z \sim 1$ clusters candidates. This is most likely because of the overall decrease in the number count density of the COSMOS survey for increasing redshifts.

High-z faint cluster galaxies (i.e. I $\geq$ 25) are not included in the I09

catalog and therefore we might miss a significant part of the cluster galaxy population. However, as discussed in Section 8.10.5, this does not affect much the detection efficiency of the PPM.

Also note that our method is not highly biased towards large scale structures with specific characteristics. Previous work found that there is no clear correlation between cluster richness and mass and the radio power of the source up to intermediate redshifts ($z \lesssim 0.95$) for radio galaxies with radio power $L_{1.4\ \mathrm{GHz}} \simeq 10^{32}$ erg s^{-1} Hz^{-1} or even lower (Ledlow & Owen, 1995; Gralla et al., 2011). However, Magliocchetti & Brüggen (2007) found contrasting results based on a small sample of 12 X-ray selected clusters at low-intermediate redshift ($z < 0.3$). In particular, they suggested that low power radio sources (down to $L_{1.4\ \mathrm{GHz}} \simeq 10^{28}$ erg s^{-1} Hz^{-1}) are preferentially hosted by low-mass clusters.

However, irrespective of the number of the fiducial cluster members estimated by the PPM, we expect that, on average, our group/cluster candidates have a low or intermediate mass (i.e. $M \simeq 10^{13-14}\ M_{\odot}$). The fact that our size estimates are consistent with those found in previous work and are typical of those of rich groups and clusters strengthens such a scenario. Furthermore, we stress again that the PPM effectively finds systems whose masses are typical of rich groups, i.e. are below the typical cluster mass cutoff $\sim 1 \times 10^{14}\ M_{\odot}$. In particular, this is the case of our $z \sim 1$ cluster candidates that are found in previous catalogs of groups in the COSMOS field (see Section 8.6). This is clearly due to the small area of the COSMOS survey and the steepness of cluster mass function more than any detection biases of our method. Hence, we will extend our work to wider surveys (e.g. Stripe 82 of the SDSS), where we expect to have a higher chance to find more massive structures (see also Section 12.2.1).

8.10.8 The location of the FR I within the cluster

Previous work investigated the position of BCGs and radio galaxies in clusters. Ledlow & Owen (1995) found that about 90% of the radio galaxies hosted in local ($z < 0.09$) Abell clusters are located within 200 kpc from the cluster center. Furthermore, the great majority of such local radio galaxies are FR Is. Similarly, Smolčić et al. (2011) studied a sample of X-ray selected groups up to $z \simeq 1.3$. They found that low power radio galaxies ($L_{1.4\ \mathrm{GHz}} \simeq 10^{30.6-32.0}$ erg s^{-1} Hz^{-1}) are preferentially found within $0.2 \times r_{200}$ from the group center (i.e. about $\lesssim 60$ kpc).

This could also be true at our redshifts. In fact, for the six cluster candidates that are found by other authors in the fields and at the redshifts of our sources (namely 01, 03, 16, 18, 20, and 31) using different techniques (i.e. X-ray emission and overdensities based on redshift information, FGH07, Knobel et al., 2009; George et al., 2011; Knobel et al., 2012; Diener et al., 2013) we can compare the locations of our FR I beacons with the coordinates

of the cluster centers, as estimated by these authors. We find that in the cases of 01, 03 and 31 the offset is less than ~ 14 arcsec. They correspond to $\lesssim 120$ kpc at the redshifts of the overdensities. In the cases of sources 16, 18 and 20 the association between our FR I beacons and the cluster candidates found in other catalogs (Knobel et al., 2009, 2012) is less certain. This is because the offset is higher than the cases outlined above. It is about 40 arcsec for sources 18 and 20 (i.e. $\sim$300 kpc at their redshifts) and it is ~ 1 arcmin (i.e. ~ 500 kpc) for source 16. All these values statistically agree, on average, with the result reported by Ledlow & Owen (1995).

This is also consistent with the offset of $\sim$100 kpc, typically found between the optical and the X-ray cluster centroids (Dai et al., 2007). Furthermore (as pointed out in Section 3.2 and Chapter 4), at variance with FR II radio galaxies or other types of AGNs, low-redshift FR Is are typically hosted by undisturbed ellipticals or cD galaxies (Zirbel, 1996), which are often associated with the BCGs (von der Linden et al., 2007). To the best of our knowledge, the bright BCG discovered by Liu et al. (2013) at $z = 1.1$ is the most distant cD galaxy confirmed to date. Therefore, in light of the results presented here, the hosts of our FR Is could also constitute a sample of high-z cD galaxy candidates.

Concerning the BCGs, previous work found that they preferentially reside within $\lesssim 41$ kpc from the X-ray cluster center up to $z \simeq 1$ (Semler et al., 2012). However, Zitrin et al. (2012) found that the offset, if estimated from the optical cluster centroid, increases for increasing redshifts (i.e. up to ~ 14 kpc at $0.52 < z < 0.55$). A similar trend is not excluded for our cluster candidates. In fact, we find that six of our cluster candidates are detected within an annulus centered at the coordinates of the radio galaxy and an internal radius of $\gtrsim 50$ arcsec (see also Table 8.1 and related discussion in Section 8.4). Note that 50 arcsec correspond to 427 kpc at redshift $z = 1.5$. These six overdensities correspond to $32\% \pm 11\%$ of our 19 cluster candidates.[5]

The six sources are the LLRGs 26, 29, and 285 and the HLRGs 34, 37, and 226. Although the statistics is extremely poor, half of the sample of the HLRGs shows significant offsets (i.e. ≥ 50 arcsec), while a non-null offset occurs for only $\sim 20\%$ of the LLRGs. However, based on such a small sample we do not draw firm conclusions.

In order to investigate the marginal discrepancy found between the two subsamples, it would be interesting (i) to look for FR I radio galaxies in COSMOS at redshifts similar to those of the HLRGs, but with radio powers comparable with those of the LLRGs, and (ii) to search for radio galaxies with redshifts similar to those of LLRGs and radio powers comparable with

[5]Note that for this case we consider 19 clusters because for the purpose of estimating sizes of clusters and locations of the FR I beacons we exclude multiple overdensities within the same field (see Section 8.6).

those of the HLRGs. This will improve the sample statistics and will allow us to understand if the trend is due either to evolutionary properties (being the LLRGs, on average, at lower redshifts than the HLRGs) or to the difference in radio power between the LLRGs and the HLRGs.

A possibility is that such radio galaxies are hosted in underdense regions within their cluster environment. To further investigate the above scenario we visually inspected the fields of the six sources. We did not find any evidence that the non-null offsets are present because of an artificiality or a technical bias of the I09 catalog (e.g. that some sources at the redshift of the cluster candidate and in the field of the corresponding FR I are not included in the I09 catalog or that their redshifts are erroneously estimated). We also found that the galaxies in each of these fields at redshifts around that of the corresponding FR I are homogeneously distributed around the position of the radio galaxy. This means that, although these overdensities are detected with significant offsets from the location of the corresponding FR I, each radio source is still likely located around the barycentric center of the galaxies in the field, in the projected sky, and not in the outskirts of the cluster candidate.

Furthermore, our results could also imply that our cluster candidates are still encompassing a strong evolution in terms of the spatial segregation of the galaxies within the core (see e.g. Bassett et al., 2013, for a very detailed study about a $z \sim 1.6$ forming cluster).

8.10.9 A bright arc in the field of 01

In this section we discuss the serendipitous discovery of a bright arc detected with the ACS camera on board of HST in the field of the source 01, at $z_{\rm spec} = 0.88$. In Figure 8.3 we report the ACS image (Koekemoer et al., 2007) of the field of 01. The source 01 and the arc are marked in Figure with the left and the right ellipses, respectively.

The arc is clearly visible about ~ 5 arcsec westward of the pair formed by the radio galaxy host and a larger elliptical companion. Such a projected angular separation corresponds to $\sim$39 kpc at the redshift of the source. The arc is very close to the radio galaxy, and it resides within the core of the Mpc–scale overdensity associated with the source 01.

Strong lensing phenomena are expected to be originated close to the densest regions of dark matter halos. Since such a projected separation is consistent with the typical size (i.e. ~ 60 kpc, Halkola et al., 2007) of the dark matter halos of BCGs, it is likely that the arc is originated by the dark matter halo of the apparent galaxy pair.

An alternative scenario is motivated by the fact that the overdensity associated with the source 01 is a relatively compact rich group with an estimated core size of about 70 arcsec (as suggested by FGH07, George et al., 2011; Knobel et al., 2012, and in this work). Therefore, it is also possible

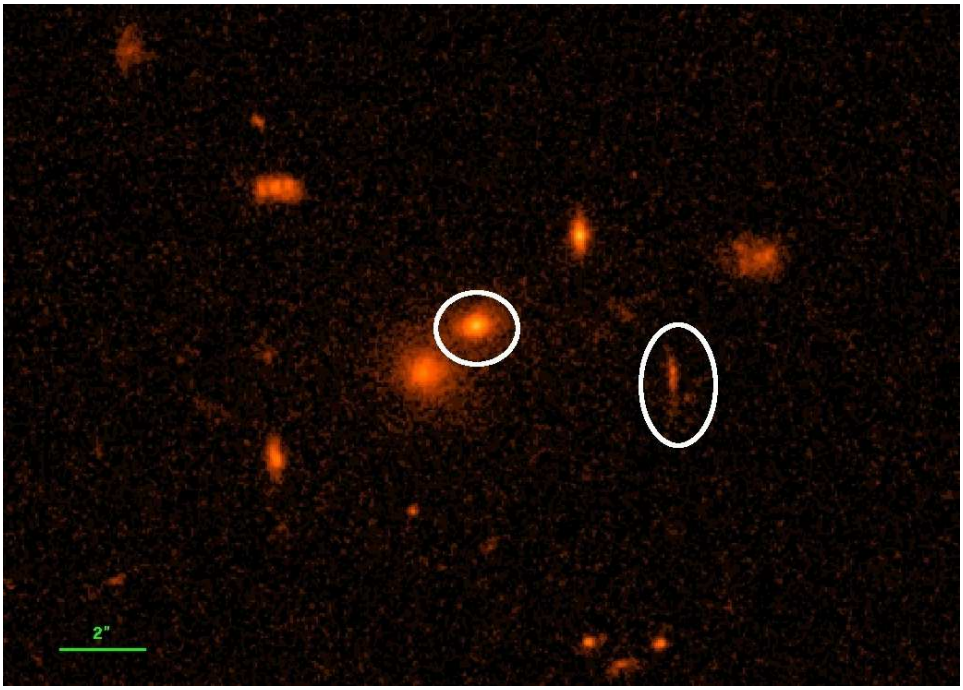

Figure 8.3: Field ($22'' \times 16''$ dimensions) of source 01 as observed by ACS on board of HST (Koekemoer et al., 2007). The galaxy host of the source 01 and the bright arc are marked with the left and right ellipses, respectively.

that the group halo itself is responsible for the observed effect. In fact, groups with intermediate masses in the range $10^{12} - 10^{14}$ $M_{\odot}$ are usually more massive than galactic halos and concentrated enough to act as lenses (More et al., 2012).

The I09 catalog reports a photometric redshift $z = 0.715$ for the arc. However such a redshift is significantly lower than that of 01. This is unexpected, since the dark matter halo should be located between the observer and the lensed object. In order to understand the discrepancy we visually inspected the COSMOS archival images of the field at different wavelengths, roughly between the i- and the u-bands. In Figure 8.4 we report four images ($10'' \times 10''$ each) of the field of the arc, that is clearly marked with a green circle in each of them.

We find that the arc is very bright from the F814W filter to the B-band, but it completely disappears in the u*-band. Therefore, we suspect that this is a u-band drop out and that the source associated with the arc is located at redshift $z \simeq 2.3$ or even higher.

While the arc clearly disappears in the u-band image, a close companion SW of the arc is clearly visible in all the four images. We suspect that, during

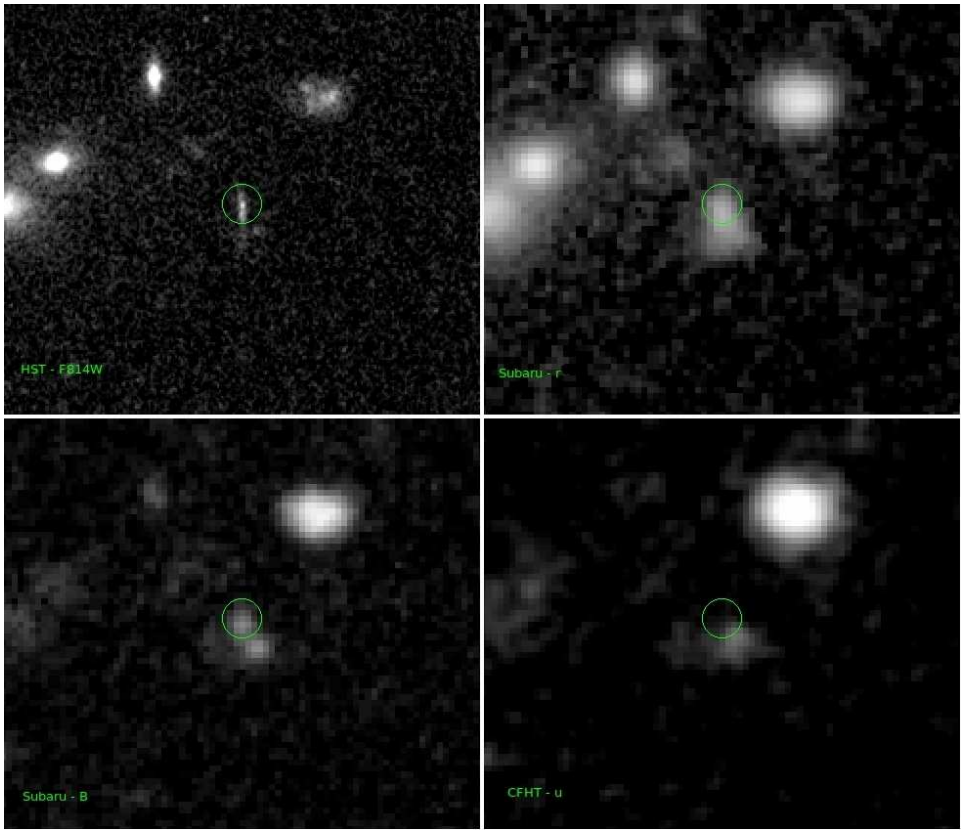

Figure 8.4: Images ($10'' \times 10''$ dimensions) of arc located in the field source 01 approximately from i- to u-bands. The arc is marked with a green circle in the center of each image. Top left: HST/ACS image (F814W filter, Koekemoer et al., 2007). Top right: *Subaru* r^+−band. Bottom left: *Subaru* B-band (Taniguchi et al., 2007). Bottom right: $u^\star$ CFHT image (Capak et al., 2007).

their automatic procedure, I09 erroneously associated with the bright arc the $u^\star$-band flux measurement that corresponds to this companion. This likely leads to an incorrect photometric redshift estimate.

Hence, our serendipitous discovery suggests that our $z \sim 1-2$ cluster finding project might also be promising for systematic studies of (strong) lensing features observed in rich groups or clusters. Our method might be complementary and would extend to higher redshifts projects that find rich groups on the basis of strong lensing signatures (e.g. Cabanac et al., 2007; Limousin et al., 2009; More et al., 2012).

One limitation of such searches is that lensing features are less likely at increasing redshifts. This is mainly because the projected number density of background objects decreases as the redshift of the lens increases. This

has so far limited the number of high redshift groups detected by means of strong lensing phenomena to $z \lesssim 1.2$. Similarly, we expect to have a better chance to observe possible occurrence of lensing phenomena for our $z \simeq 1$ cluster candidates than at higher redshifts. Therefore, our sample might not include a large number of strongly lensed objects while it includes an extremely useful number of high redshift groups.

Part III

A multiwavelength study of a homogeneous sample of bright FSRQs

Chapter 9

Introduction

The main goal of this Part III is to study statistically some physical properties of FSRQs. To achieve such a goal we investigate the multiwavelength SEDs of a complete sample of 80 FSRQs drawn at high-radio frequency, i.e. 23 GHz, from the Wilkinson Microwave Anisotropy Probe (WMAP) 7-yr catalog. The original idea behind this work was to build a large complete sample of blazars, complementary to that of Abdo et al. (2010a) that has been selected by using *Fermi Gamma-ray Space Telescope* observations in gamma-rays.

As outlined in the following we address the problems of estimating black hole masses and searching for evidence of AGN torus in the FSRQs of our sample. These analyses are key for the comprehension of the blazar physics and in particular of the active nucleus and its surrounding parsec-scale region. We refer to Sections 1.6 and 1.8 for an overview of the subjects and to Chapter 2 for a discussion about blazar sources.

In the following Chapters we estimate black hole masses for a subsample of 55 FSRQs by means of the blue-bump method introduced in Section 1.8.4 and we compare these BH mass estimates with those obtained with the independent SE method (see Section 1.8). The main goal of this study is to prove, by a direct comparison of the mass estimates obtained with the two independent methods, that the blue-bump method is a valuable alternative to the SE method to estimate black hole masses for large samples of bright AGNs (Castignani et al., 2013).

Then, we look for evidence of emission from the AGN torus in the SEDs of the FSRQs in our sample (Castignani & De Zotti, 2014). The main goal of this study is to check whether indeed FSRQs show unambiguous evidence of torus emission and, if so, to characterize its properties also in comparison with those of tori associated with radio-quiet AGNs. Note that in the case of blazars the synchrotron emission from the jet may swamp the emission from the torus, thus making our analysis more difficult.

However, we stress that FSRQs might be more promising than radio-

quiet AGNs for the proposed analyses. In fact, FSRQs have the great advantage that both tori and discs are most likely seen almost perfectly face-on, as they are expected to be almost perpendicular to the jet direction, which is closely aligned with the line-of-sight. This removes the large uncertainty plaguing estimates of both torus and disc luminosities of radio-quiet AGNs due to the fact that the inclination is generally unknown.

The present Part III is structured as follows. In Chapter 10 we introduce the blazar sample and describe the dataset adopted and the SED modeling. In Chapter 11 we describe our results. We refer to Chapter 12 for the conclusions and future work related to the project described in the present Part III.

Chapter 10

The FSRQ sample and SED modeling

In Sections 10.1, 10.2, and 10.3 of this Chapter we describe the sample selection, the photometric data used, and the SED modeling, respectively.

10.1 The blazar sample

The Wilkinson Microwave Anisotropy Probe (WMAP) satellite has provided the first all-sky survey at high radio frequencies ($\geq$ 23 GHz). At these frequencies blazars are the dominant radio-source population. We selected a complete blazar sample, flux-limited at 23 GHz (K band), drawn from the WMAP 7-yr point source catalog (Gold et al., 2011).

The basic steps in our selection procedure are the following. We adopted a flux-density limit of $F_K = 1$ Jy, corresponding to the WMAP completeness limit (Planck Collaboration XIII, 2011), and cross-matched the selected sources with the most recent version of the blazar catalog BZCAT (Massaro et al., 2013)[1]. This search yielded 251 cataloged blazars. To check whether there are additional bona fide blazars among the other WMAP sources brighter than the adopted flux density limit, we collected data on them from the NASA/IPAC Extragalactic Database (NED)[2], from the database by Trushkin (2003), and from the catalog of the Australia Telescope Compact Array (ATCA) 20 GHz survey (AT20G, Hancock et al., 2011). Sources qualify as bona fide blazars if they have i) a flat radio spectrum ($F_\nu \propto \nu^{-\alpha}$ with $\alpha \leq 0.5$), ii) high variability, and iii) compact radio morphology. Based on these criteria we added four sources to our blazar sample that satisfy the first two criteria. The third criterion is satisfied by two of them, whereas for the others no radio image is available in the NED. Our initial sample then consists of 255 blazars, 245 of which have redshift measurements.

[1] www.asdc.asi.it/bzcat/

[2] ned.ipac.caltech.edu/

One of the main goals of this work is characterizing the optical/UV bump attributed to the accretion disk. Therefore, we restricted the sample to the 105 blazars within the area covered by the Tenth Data Release[3] (DR10) of the SDSS, totaling over 14,000 square degrees of sky and providing simultaneous five-band photometry with limiting AB magnitudes at 95% completeness level u, g, r, i, and z = 22.0, 22.2, 22.2, 21.3, and 20.5, respectively (Abazajian et al., 2004). With the exception of WMAP7 # 274, these objects are in the BZCAT. Moreover, since BL Lacs generally do not show the UV bump, we dropped the 19 sources classified as BL Lacs from our sample, as well as six sources classified as blazars of uncertain type, keeping only sources classified as FSRQs. The final sample comprises 80 objects, all having spectroscopic redshift measurements.

10.2 Photometric data

For the 80 FSRQs in our sample we have collected, updated, and complemented the photometric data available on the NED, as described in the following.

10.2.1 SDSS DR10 data

SDSS counterparts of our FSRQs were searched by adopting their low-frequency radio coordinates which have uncertainties of $\simeq 1$ arcsec. Since the SDSS positional uncertainty adds very little to the error (the SDSS positional accuracy is of $\simeq 0.1$ arcsec) we have chosen a search radius of 3 arcsec. By construction, all our FSRQs have at least one SDSS counterpart within the search radius.

In many cases the SDSS/DR10 catalog gives multi-epoch photometry of the sources. We have adopted the median values and associated with them an error equal to the rms dispersion, likely due to variability, which is generally much larger than the photometric errors. The SDSS counterparts of the sources in our sample have a median and an average dereddened AB r-band magnitude of 17.67 and 17.63 mag, with an rms dispersion of 1.31 mag. Thus they are generally much brighter than the 95% SDSS magnitude limit. Only one FSRQ in the sample, WMAP7 # 314, has an r-band magnitude that is slightly fainter than that limit.

The adopted magnitudes, denoted e.g. as dered_g in the DR10 catalog, are corrected for Galactic extinction. As suggested in the DR10 tutorial[4] we have decreased the DR10 u-band magnitudes by 0.04 to bring them to the AB system.

[3] https://www.sdss3.org/dr10/

[4] www.sdss3.org/dr10/algorithms/fluxcal.php#SDSStoAB

The corrections to the magnitudes in the other bands are negligible. In principle, some additional extinction may take place within the host galaxy, but we expect it to be negligible because the jet sweeps out any intervening material along its trajectory. The correction for absorption in the IGM is described in Section 10.2.3. For the redshift range spanned by our sources it may only be relevant in the u and g bands.

The choice of the effective wavelength corresponding to each SDSS filter depends on the convolution of the filter's spectral-response function with the spectral shape of the source. We adopted the effective wavelengths reported in the SDSS tutorial[5]: 3543, 4770, 6231, 7625, and 9134 Å, for the u, g, r, i and z filters, respectively.

10.2.2 GALEX data

We looked for UV photometry for our FSRQs in the sixth data release, GR6[6], of the Galaxy Evolution Explorer (GALEX) satellite (Morrissey et al., 2007). GALEX provides near-UV (NUV, 1750–2800 Å) and far-UV (FUV, 1350–1750 Å) images down to a magnitude limit AB $\sim$ 20–21 with an estimated positional uncertainty of $\simeq 0.5$ arcsec. We adopted 1535 and 2301 Å as the effective wavelengths of the FUV and NUV filters, respectively.

Again the low-frequency radio positions of FSRQs were used and a search radius of 3.5 arcsec was adopted. At least one counterpart was found for 66 objects. Multiple counterparts were found to correspond to GALEX measurements at different epochs of the same source (i.e., differences in coordinates were within the positional errors). Such multi-epoch measurements were found for 24 of our sources. In these cases we adopted their weighted average. Whenever the S/N < 3, we adopted upper limits equal to three times the error.

The UV fluxes are very sensitive to extinction within our Galaxy and, in the case of high-z objects, to photoelectric absorption in the intergalactic medium. To correct for Galactic extinction we used the values of $E(B-V)$ given in the GR6 catalog for each source and the extinction curve by Cardelli et al. (1989), as updated by O'Donnell (1994) and normalized to $A(V) = 3.1\,E(B-V)$. The correction for absorption in the IGM is described in the next section.

10.2.3 Absorption in the intergalactic medium

Since we do not know the IGM attenuation along each line-of-sight we have used the effective optical depth $\tau_{\rm eff}(z) = -\ln[\langle\exp(-\tau)\rangle]$, averaged over all possible lines of sight. Following Haardt & Madau (2012), we computed $\tau_{\rm eff}(z)$ at the effective wavelengths of SDSS u and g filters (the effective

[5] skyserver.sdss.org/dr1/en/proj/advanced/color/sdssfilters.asp
[6] galex.stsci.edu/GR6/

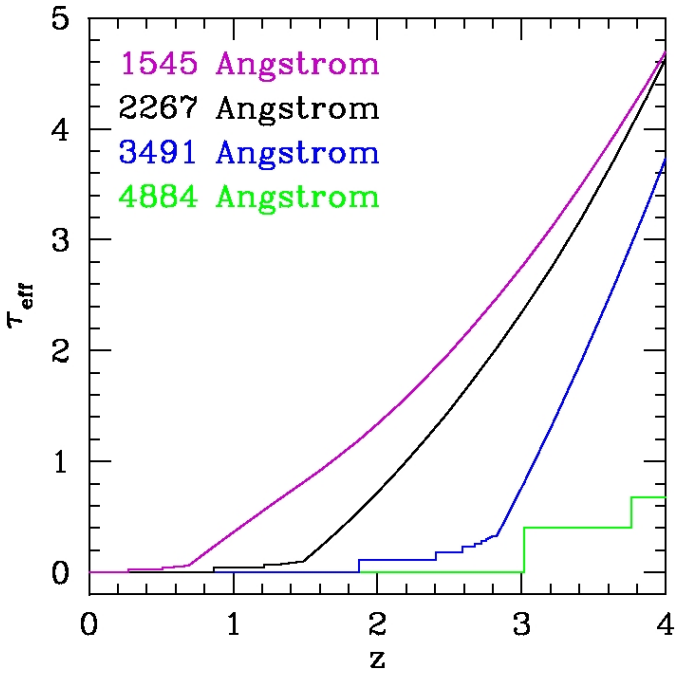

Figure 10.1: Redshift-dependent effective optical depth for IGM absorption, averaged over all lines of sight, at the effective wavelengths of SDSS g and u bands and of the GALEX NUV and FUV bands.

optical depth in the three other SDSS filters vanishes for the redshift range of interest here) and of the two GALEX filters. The results are shown in Figure 10.1 and listed in Table 10.1. The step-like features are due to Lyman series absorption. We have verified that adopting the spectral response of each filter instead of considering the single effective wavelengths results in a small (i.e. $\lesssim 10\%$) correction in the flux densities and in the smoothing of all the edges in the optical depth as a function of redshift. Details on these calculations will be presented in Madau & Haardt, in preparation.

10.2.4 X-ray data

We have found ROSAT data for 18 of the 80 FSRQs in our sample. However an inspection of the global SEDs indicates, for all of them, that X-ray data are clearly far from the fit of the blue bump in terms of the Shakura & Sunyaev (1973) accretion disk adopted in this work, and more likely related to other components, such as the synchrotron or the IC ones or the emission from a bright hot X-ray corona.

Table 10.1: Redshift-dependent effective optical depth for IGM absorption, averaged over all lines of sight, at the effective wavelengths of the GALEX NUV and FUV bands and of SDSS the g and u bands.

z	$\tau_{\rm eff}(1545\text{Å})$	$\tau_{\rm eff}(2267\text{Å})$	$\tau_{\rm eff}(3491\text{Å})$	$\tau_{\rm eff}(4884\text{Å})$
0.271	0.000	0.000	0.000	0.000
0.333	0.030	0.000	0.000	0.000
0.399	0.030	0.000	0.000	0.000
0.468	0.030	0.000	0.000	0.000
0.540	0.042	0.000	0.000	0.000
0.615	0.049	0.000	0.000	0.000
0.695	0.063	0.000	0.000	0.000
0.778	0.146	0.000	0.000	0.000
0.865	0.232	0.000	0.000	0.000
0.957	0.320	0.047	0.000	0.000
1.053	0.412	0.047	0.000	0.000
1.154	0.506	0.047	0.000	0.000
1.370	0.706	0.076	0.000	0.000
1.487	0.812	0.098	0.000	0.000
1.609	0.926	0.233	0.000	0.000
1.737	1.052	0.384	0.000	0.000
1.871	1.193	0.551	0.000	0.000
2.013	1.352	0.737	0.112	0.000
2.160	1.530	0.943	0.112	0.000
2.316	1.729	1.173	0.112	0.000
2.479	1.951	1.428	0.184	0.000
2.649	2.199	1.712	0.230	0.000
2.829	2.475	2.026	0.330	0.000
3.017	2.782	2.376	0.808	0.000
3.214	3.124	2.764	1.338	0.404
3.421	3.506	3.207	1.924	0.404
3.638	3.930	3.713	2.573	0.404
3.866	4.402	4.280	3.291	0.673
4.105	4.927	4.915	4.086	0.842
4.356	5.511	5.626	4.964	1.195
4.619	6.158	6.424	5.936	2.581
4.895	6.875	7.317	7.010	4.110
5.184	7.669	8.318	8.196	5.794

10.2.5 WISE data

We have cross-correlated our FSRQs with the AllWISE[7] source catalog, i.e. the latest version of the Wide-field Infrared Survey Explorer (WISE; Wright et al., 2010) catalog. Again, the coordinates of low radio-frequency counterparts were adopted and a search radius of 6.5 arcsec was chosen, consistent with WISE positional uncertainty[8].

WISE photometric data are provided at 3.4, 4.6, 12, and 22 μm. Hereafter we denote as $W1$, $W2$, $W3$, and $W4$ the WISE Vega magnitudes at these wavelengths, respectively. Except for WMAP7# 153, which was not detected, all the FSRQs in the sample have unambiguous WISE counterparts with signal-to-noise (S/N) ratios larger than three in the first three channels, and 75 (out of 80) were detected with $S/N > 3$ also in the fourth channel ($W4$)

In the WISE bands where S/N < 3 we have adopted an upper limit equal to three times the error. Multiple WISE sources were found within the search radius for the FSRQs WMAP7 # 46, 126, 179, 207, 274, 278, and 317. In these cases we chose the brightest WISE source as the most likely counterpart. In all cases, the other sources were at least two magnitudes dimmer.

WISE Vega magnitudes have been converted into flux densities by adopting the photometric calibrations and the color corrections for flat-spectrum sources given by Wright et al. (2010) and Jarrett et al. (2011). The color corrections are less than 1% for the $W1$, $W2$, and $W4$ filters and $\leq 8\%$ for $W3$ filter.

10.2.6 *Planck* data

In the *Planck* Early Release Compact Source Catalog (ERCSC; Planck Collaboration VII, 2011) we have found counterparts for 73 out of our 80 FSRQs; 47, 39, and 69 of them have ERCSC flux densities at 70, 44, and 30 GHz, respectively, and 64 have ERCSC flux densities at frequencies ≥ 100 GHz.

10.3 SED modeling

Of the 80 FSRQs in our sample, 55 (i.e. 69%) show clear evidence of the optical/UV bump, interpreted as the emission from a standard optically thick, geometrically thin accretion disk model (Shakura & Sunyaev, 1973). In Figure 10.2 we report the redshift distribution of all 80 FSRQs in our

[7] `http://wise2.ipac.caltech.edu/docs/release/allwise/`

[8] According to the WISE Explanatory Supplement (Cutri et al., 2013), sources with $S/N \sim 20$ have a typical rms positional uncertainty of 0.43 arcsec. Our sources generally have a much lower S/N ratio and the astrometric uncertainty scales as $(S/N)^{-1}$ (e.g. Condon et al., 1998; Ivison et al., 2007). For the typical S/N values of our sources, $S/N = 3$–5, the search radius correspond to positional errors in the range 2.3–3.8σ.

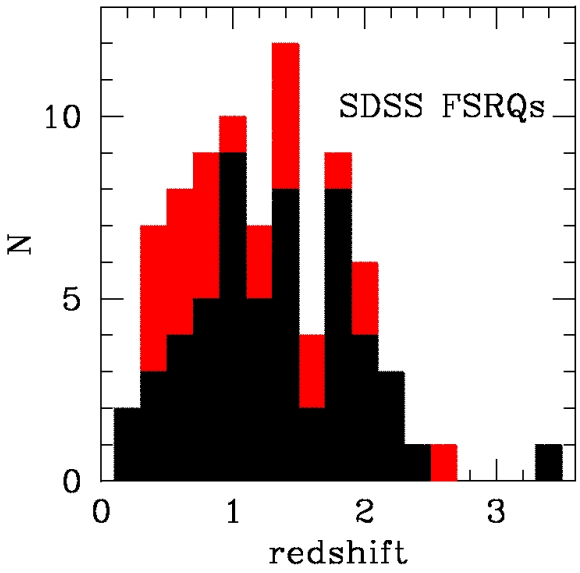

Figure 10.2: Redshift distribution of all 80 FSRQs in our sample (red) and of the subsample of 55 FSRQs with evidence of optical-UV bump (black).

sample (red histogram) along with the distribution for the subsample of 55 sources with evidence of blue bump (black histogram). The median redshifts of the two distributions are $z_{\rm median} = 1.22$ and 1.27, respectively. As illustrated by the example shown in Figure 10.3, the global SEDs are modeled by taking several additional components into account: the Doppler-boosted synchrotron continuum modeled following Donato et al. (2001); a passive elliptical host galaxy template (see, e.g., Giommi et al., 2012b); the dusty AGN torus emission based either on a type-1 QSO template (BQSO1) from the Polletta et al. (2007)[9] SWIRE template library.

The fit of the global SED was made using six free parameters. Four are those of the blazar sequence model for the synchrotron emission (the 5 GHz luminosity, the 5 GHz spectral index, the junction frequency between the low- and the high-frequency synchrotron template and the peak frequency of νL_ν, Donato et al., 2001). The remaining two parameters refer to the accretion disk model (i.e., the normalization and the peak frequency). The other components are fixed. The host galaxy template is an elliptical (Mannucci et al., 2001) with an absolute magnitude of $M_R = -23.7$, as in Giommi et al. (2012b). The normalization of the torus template was computed from that of the accretion disk emission, requiring that the torus/accretion disk luminosity ratio is equal to that of the Polletta et al. (2007) BQSO1 template.

[9] www.iasf-milano.inaf.it/∼polletta/templates/swire_templates.html

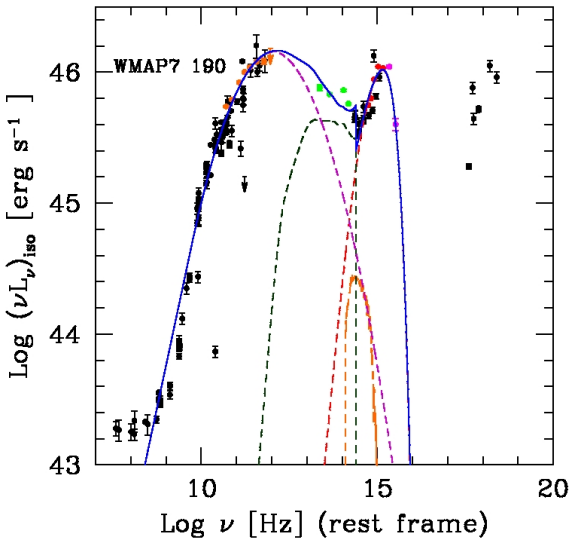

Figure 10.3: Example of an SED fit (WMAP7 # 190). Solid blue line: total SED, which includes synchrotron (Donato et al., 2001), host galaxy (Giommi et al., 2012b), disk (Shakura & Sunyaev, 1973), and torus Polletta et al. (2007) emission models; dashed violet line: synchrotron from the jet; green dashed line: torus; dashed orange line: host galaxy, taken to be a passive elliptical with $M_R = -23.7$; dashed red line: accretion disk. Orange points: *Planck* data; green: WISE data; red: SDSS data; magenta: GALEX data. Black points: data taken from the NASA/IPAC Extragalactic Database (NED). At variance with what was done to compute L_d and $\nu_{\rm peak} L_\nu(\nu_{\rm peak})$ (see text and Table 10.2), the luminosities shown here are computed assuming isotropic emission.

We stress that accurate fits of the global SEDs are beyond the scope of the work presented in this Part III, for which one of main purposes is to estimate the black hole masses by fitting the optical/UV bump with a Shakura & Sunyaev (1973) model, as discussed in the following. The consideration of the other components, fitted taking all the data we have collected into account, is mainly relevant to checking whether they may contaminate the emission from the accretion disk. In many cases, the lack of simultaneity of the measurements does not allow reliable fits of the other components. Still for the 55 objects with clear evidence of the blue bump, the data were enough either to estimate the amount of contamination or to signal points that should be better taken as upper limits to the blue bump emission.

10.3.1 The optical-UV bump

We assume a standard optically thick and geometrically thin accretion disc (Shakura & Sunyaev, 1973) and a Schwarzschild, i.e. non-rotating, black hole (see also Section 1.8.4). The thermal emission from the accretion disk is modeled as a combination of black bodies with temperatures depending on the distance, R, from the black hole (see, e.g., Frank et al., 2002). The flux density observed at a frequency ν_o is given by

$$F_\nu(\nu_o) = \nu_o^3 \frac{4\pi h_P \cos(i)}{c^2 {D_A}^2} \int_{R_\star}^{R_{\rm out}} \frac{R\, dR}{e^{h_P(1+z)\nu_o/kT(R)} - 1}, \tag{10.1}$$

where D_A is the angular diameter distance to the blazar, k the Boltzmann constant, z the redshift of the source, h_P the Planck constant, c the speed of light, and $R_\star$ and $R_{\rm out}$ are the inner and outer disk radii, respectively. Recalling Equation 1.5 the radial temperature profile, $T(R)$, is given by

$$T^4(R) = \frac{3GM_\bullet \dot{M}}{8\pi R^3 \sigma} \left(1 - \sqrt{\frac{R_\star}{R}}\right), \tag{10.2}$$

where G is the gravitational constant, $M_\bullet$ the black hole mass, $\dot{M}$ its accretion rate, σ the Stefan-Boltzmann constant, $R_\star$ the radius of the last stable orbit that, for a Schwarzschild black hole, is $R_\star = 3R_S$, $R_S = 2GM_\bullet/c^2$ being the Schwarzschild radius. The results are insensitive to the chosen value for $R_{\rm out}$ provided that $R_{\rm out} \gg R_\star$; we chose $R_{\rm out} = 100R_S$.

Since the emission of the disk is anisotropic (the flux density measured by an observer is proportional to $\cos i$), the monochromatic luminosity is related to the flux density by Calderone et al. (2013)

$$\nu_e L_\nu(\nu_e) = \frac{2\pi D_L^2 \nu_o F_\nu(\nu_o)}{\cos i}, \tag{10.3}$$

where $\nu_e = (1+z)\nu_o$ is the frequency at the emission redshift, z, and $D_L(z)$ is the luminosity distance.

The fit of the accretion disk model to the optical/UV bump for the 55 FSRQs showing it was done using only the SDSS (available for all of them) and the GALEX data (available for all but 7 of them). Using the standard minimum χ^2 technique, we obtained the values of the two free parameters, the normalization and the peak frequency, $\nu_{\rm peak}$ (in terms of νL_ν). The total disk luminosity, L_d, can then be computed integrating Equation 10.3 over frequency. The derived values of $\nu_{\rm peak} L_\nu(\nu_{\rm peak})$, L_d and $\nu_{\rm peak}$ are given in Table 10.2. The accretion rate is $\dot{M} = L_d/(\eta c^2)$ where η is the mass-to-light conversion efficiency for which we adopt the standard value $\eta = 0.1$.

WMAP ID	$\log\left(\frac{\nu_{\rm peak}}{\rm Hz}\right)$	$\log\left(\frac{\nu_{\rm peak} L_\nu(\nu_{\rm peak})}{\rm erg\,s^{-1}}\right)$	$\log\left(\frac{L_d}{\rm erg\,s^{-1}}\right)$	$\log\left(\frac{M_\bullet}{M_\odot}\right)$
9	15.52	45.62	45.90	8.53
26	15.72	46.35	46.63	8.49
27	15.29	46.00	46.26	9.18
31	15.42	46.36	46.63	9.09
39	15.32	45.37	45.64	8.80
42	15.32	45.94	46.21	9.09
89	15.42	45.32	45.59	8.57
137	15.62	46.78	47.06	8.91
150	15.33	45.81	46.07	9.01
153	15.62	46.24	46.52	8.64
155	15.39	45.81	46.08	8.88
160	15.32	46.34	46.61	9.28
166	15.32	45.69	45.96	8.96
169	15.42	45.92	46.19	8.87
173	15.42	46.49	46.77	9.17
179	15.42	45.42	45.69	8.62
182	15.57	46.05	46.33	8.64
186	15.17	46.42	46.67	9.61
190	15.15	45.72	45.96	9.30
191	15.52	46.18	46.45	8.80
195	15.39	46.10	46.37	9.04
198	15.32	45.37	45.64	8.80
203	15.52	45.21	45.48	8.32
208	15.42	46.29	46.56	9.06
220	15.27	45.99	46.25	9.20
221	15.52	46.28	46.56	8.86
224	15.36	45.93	46.20	8.99
228	15.32	45.40	45.67	8.81
232	15.52	45.12	45.39	8.27
236	15.32	44.95	45.21	8.58
250	15.35	45.97	46.24	9.04
265	15.67	45.72	46.00	8.28

278	15.17	45.97	46.23	9.39
284	15.62	45.70	45.97	8.36
295	15.92	46.24	46.52	8.04
306	15.62	45.44	45.71	8.23
307	15.22	45.78	46.04	9.20
310	15.42	45.75	46.02	8.79
311	15.31	46.21	46.47	9.25
316	15.38	46.36	46.63	9.19
317	15.42	44.78	45.05	8.30
327	15.71	46.46	46.74	8.58
402	15.42	45.92	46.19	8.87
407	15.82	46.74	47.02	8.49
412	15.40	46.87	47.14	9.40
415	15.37	45.24	45.51	8.63
417	15.32	46.55	46.82	9.39
428	15.39	46.34	46.61	9.14
430	15.67	46.66	46.93	8.75
434	15.42	45.94	46.21	8.88
452	15.38	46.32	46.59	9.16
455	15.32	45.87	46.14	9.05
458	15.52	45.21	45.49	8.32
462	15.37	46.11	46.38	9.07
470	15.52	46.03	46.30	8.73

Table 10.2: Best fit values of the big blue bump parameters.

An analysis of Equation 10.1 indicates that the main contribution to the integral comes from a region around the radius $R_{\rm peak} = (49/36)R_\star$ where the temperature profile $T(R)$ (Equation 10.2) reaches its maximum value $T_{\rm max}$. The integral over R, to compute L_d (hence $\dot{M}$), can then be approximately evaluated with the steepest-descent method. The calculation was made by setting $i = 0$. Then, introducing the value of $T_{\rm max} = T(R_{\rm peak})$ into the Wien's displacement law, $\nu_{\rm peak}/T_{\rm max} \simeq 5.879 \times 10^{10}\,{\rm Hz\,K^{-1}}$, we get an estimate of the black hole mass: $M_\bullet/10^9 M_\odot \simeq 0.46(\nu_{\rm peak}/3\times10^{15}\,{\rm Hz})^{-2}\times (\dot{M}/M_\odot\,{\rm yr}^{-1})^{1/2}$. This result shows that the estimate of $M_\bullet$ is quite sensitive to the value of $\nu_{\rm peak}$. One may then wonder whether associating it to $T_{\rm max}$ is a good enough approximation. To answer this question, we computed $M_\bullet$ by numerically solving the equation $d\log(\nu_e L_\nu(\nu_e))/d\log(\nu_e) = 0$ for all values of $\nu_{\rm peak}$ and L_d found for our sources. Remarkably, we find that the exact values of $M_\bullet$ strictly follow the dependencies on $\dot{M}$ and $\nu_{\rm peak}$ given by the approximate solution, with a coefficient lower by a factor 0.76. The black hole masses implied by the Shakura & Sunyaev (1973) model can then

be accurately computed using the simple equation

$$\frac{M_\bullet}{10^9 M_\odot} \simeq 0.35 \left(\frac{\nu_{\rm peak}}{3\times10^{15}\,{\rm Hz}}\right)^{-2} \left(\frac{\dot{M}}{M_\odot\ {\rm yr}^{-1}}\right)^{1/2}. \qquad (10.4)$$

The results for our FSRQs are reported in Table 10.2.

The statistical errors associated with $\log(\nu_{\rm peak})$ and $\dot{M}$ were computed by utilizing the standard criteria based on the χ^2 statistics (e.g., Cash, 1976), with errors estimated by adding the measurement uncertainties and the estimated spread of data points due to variability in quadrature. The uncertainties on $\log(\nu_{\rm peak})$ and on $\log(\dot{M})$ were found to be in the ranges 0.02–0.09 and 0.02–0.10, respectively, depending on the data quality. The errors on $\log(M_\bullet)$ cannot be obtained by simply summing the two contributions in quadrature because $\log(\nu_{\rm peak})$ and $\dot{M}$ are interdependent. From the distribution of $\log(M_\bullet)$ obtained varying the two quantities within their 68% confidence interval, we found uncertainties in the range 0.1–0.3.

The uncertainties on the IGM absorption correction due to variations in the effective optical depth with the line-of-sight are unknown. An insufficient correction for UV absorption leads to underestimating $\nu_{\rm peak}$ and to overestimating $M_\bullet$, while an overcorrection has the opposite effect. However, since all of our FSRQs but one (namely WMAP7 #137 that has a redshift $z = 3.4$) are at $z < 2.5$ (see Figure 10.2), the corrections for IGM absorption are relatively small. Ignoring such a correction would lead to a mean overestimate of $\log(M_\bullet)$ by 0.04 for the 18 objects with $z < 1$, of 0.09 for the 17 objects with $1 < z < 1.5$ and of 0.11 for the 13 objects at $1.5 < z < 2$. For WMAP7 #137 and for the 5 objects at $2 < z < 2.5$ the variation of $\nu_{\rm peak}$ is compensated for by that of L_d so that the average difference between corrected and uncorrected estimates is negligible.

Further uncertainties are associated with the choice of the model and of its parameters. As pointed out above, the adopted accretion disk model assumes a non-rotating BH, although the chosen value of the radiation efficiency, $\eta = 0.1$, is above the maximum efficiency for a Schwarzschild BH. However, using the Li et al. (2005) software package, Calderone et al. (2013) found that the Shakura & Sunyaev (1973) model with $R_\star = 3R_S$, as used here, mimics the SED for an optically thick, geometrically thin accretion disk around a Kerr BH quite well with a spin parameter $a \simeq 0.7$, corresponding to a maximum radiative efficiency $\eta = 0.1$. For this choice of η our BH mass estimates are therefore affected little by having neglected the general relativistic effects associated with a Kerr BH. Based on the analysis presented in Appendix A4 of Calderone et al. (2013), we find a BH mass lower by a factor of 0.6 for a pure Schwarzschild model ($a = 0$, $\eta = 0.06$), while for a maximally $a = 0.998$ rotating Kerr model with a maximum possible radiative efficiency $\eta = 0.42$, that is achieved in the case where the black hole and the accretion disc are corotating, we find a BH mass higher by a

factor of 1.75. We note, however, that the latter factor is a generous upper limit since the boundaries of the range of values of η for which Shankar et al. (2009) achieved a good match to the overall shape of the BH mass function are $0.06 \leq \eta \leq 0.15$. The effect of the choice of the inclination angle i should be minor given the model and observational indications that $i \lesssim 5°$; even if we double this value, we get $\cos(10°) = 0.985$.

Summing up in quadrature the uncertainties listed above we end up with nominal errors on $\log(M_\bullet)$ in the range 0.2–0.4. These estimates should be taken as lower limits since they do not include all the uncertainties in the theoretical accretion disk model, which are difficult to quantify.

Furthermore, we note that the photometry of the SED beyond the peak is not always available. When it is available, it is not simultaneous with the optical data determining the rising part of the SED. This represents an additional source of uncertainty, difficult to quantify, concerning the black hole mass estimates based on the optical-UV bump.

10.3.2 The clumpy AGN torus

In this section we reconsider the SEDs of all 80 FSRQs in our sample to search for evidence of clumpy AGN torus in their SEDs.

None of the 25 FSRQs without a clear evidence of optical/UV bump shows signs of torus emission in their SEDs. The absence of the optical/UV bump deprives us of an important constraint on the intensity of the torus emission that, for almost face-on tori as those of FSRQs are expected to be, cannot exceed that of the disc. Because of that, we could not obtain meaningful constraints on the torus luminosity for these objects.

For the 55 FSRQs with evidence of the bump we attempted a modeling of SEDs taking into account the different templates described above. Concerning the SED modeling, at variance with the procedure described in Section 10.3, the following modifications are applied.

Instead of the AGN template from Polletta et al. (2007), we adopt the clumpy AGN torus model by Hoenig & Kishimoto (2010) provided in the CAT3D library[10]. The following AGN torus parameter values are adopted: power law index of the radial dust cloud distribution $a = -1.5$; half opening angle of the torus $\theta_0 = 60$ degrees; mean number of clouds along an equatorial line-of-sight $N_0 = 5$; optical depth of individual clouds $\tau_V = 30$; outer radius of the torus $R_{\rm out} = 150\,{\rm pc}$; sublimation radius for a disc luminosity of $10^{46}\,{\rm erg\,s^{-1}}$, $r_{\rm sub,0} = 0.9\,{\rm pc}$. The chosen values for the model parameters are consistent with those adopted in Hoenig et al. (2011) to reproduce the mean SED of a complete sample of quasars and radio galaxies at $1.0 \leq z \leq 1.4$.

Since the data are not simultaneous the effect of variability does not allow us to accurately determine the SEDs. Therefore the fits are inevitably

[10] `http://cat3d.sungrazer.org/`

only indicative. In this situation an exploration of the parameter space is not warranted.

We note that the Polletta et al. (2007) template reproduces the SEDs of bright AGNs. However, concerning the IR part of the spectrum the emission of the host galaxy and that of the AGN torus are difficult to separate. Furthermore, the AGN optical/UV emission can be absorbed and emitted in the IR not only by the AGN torus, but also by the ISM in the host galaxy. Therefore, since the main goal of the present analysis is the characterization of the AGN torus, the Hoenig & Kishimoto (2010) AGN torus template is here adopted. Nevertheless, such a discussion does not affect the results of Section 10.3.1, where the Polletta et al. (2007) template is adopted. This is because that analysis was mainly focused on the blue bump emission.

The fit of the global SED was made using five free parameters instead of the six mentioned above. Four are those of the blazar sequence model for the synchrotron emission (the 5 GHz luminosity, the 5 GHz spectral index, the junction frequency between the low- and the high-frequency synchrotron template and the peak frequency of νL_ν; Donato et al., 2001). The remaining parameter is the normalization of the torus template. Since the routine used to compute the minimum χ^2 fit did not converge in most cases when we attempted to use more than five parameters, the other components (i.e. the host-galaxy and the optical/UV bump templates) were kept fixed. An absolute magnitude of $M_R = -23.7$ was attributed to the host galaxy, as in Giommi et al. (2012b). The normalization and the peak frequency of the accretion disc template were fixed to the values found in Section 10.3.1. We stress that accurate fits of the global SEDs are beyond the scope of this analysis whose main purpose is the characterization of the AGN torus. The consideration of the other components, fitted taking into account all the data we have collected, is mainly relevant to check whether they may contaminate the torus emission.

Statistically significant (significance level $\geq 3\sigma$, see below) signatures of a torus were found in seven FSRQs, i.e. in $\simeq 9\%$ of the 80 FSRQs in the sample or in $\simeq 13\%$ of the 55 FSRQs with evidence of the accretion disc bump. A $\sim 2\sigma$ torus detection was found for one additional object, WMAP7# 250, i.e. 3C 273. Our best fit SEDs for these objects, with the contributions of the components mentioned above, are compared with the data in Figure 10.4. Although the evidence of the torus is statistically significant the estimate of the torus luminosity is endowed with a considerable uncertainty, difficult to quantify. We remind that the data are not simultaneous, so that, due to variability, accurate fits are not physically meaningful. As clear from the Figure, the total source emission at mid-IR frequencies is much higher than that associated with the adopted host-galaxy template. Since such a template corresponds to a giant elliptical the contamination from the host galaxy around the torus peak is negligible.

For the remaining 47 FSRQs the jet emission at mid-IR frequencies

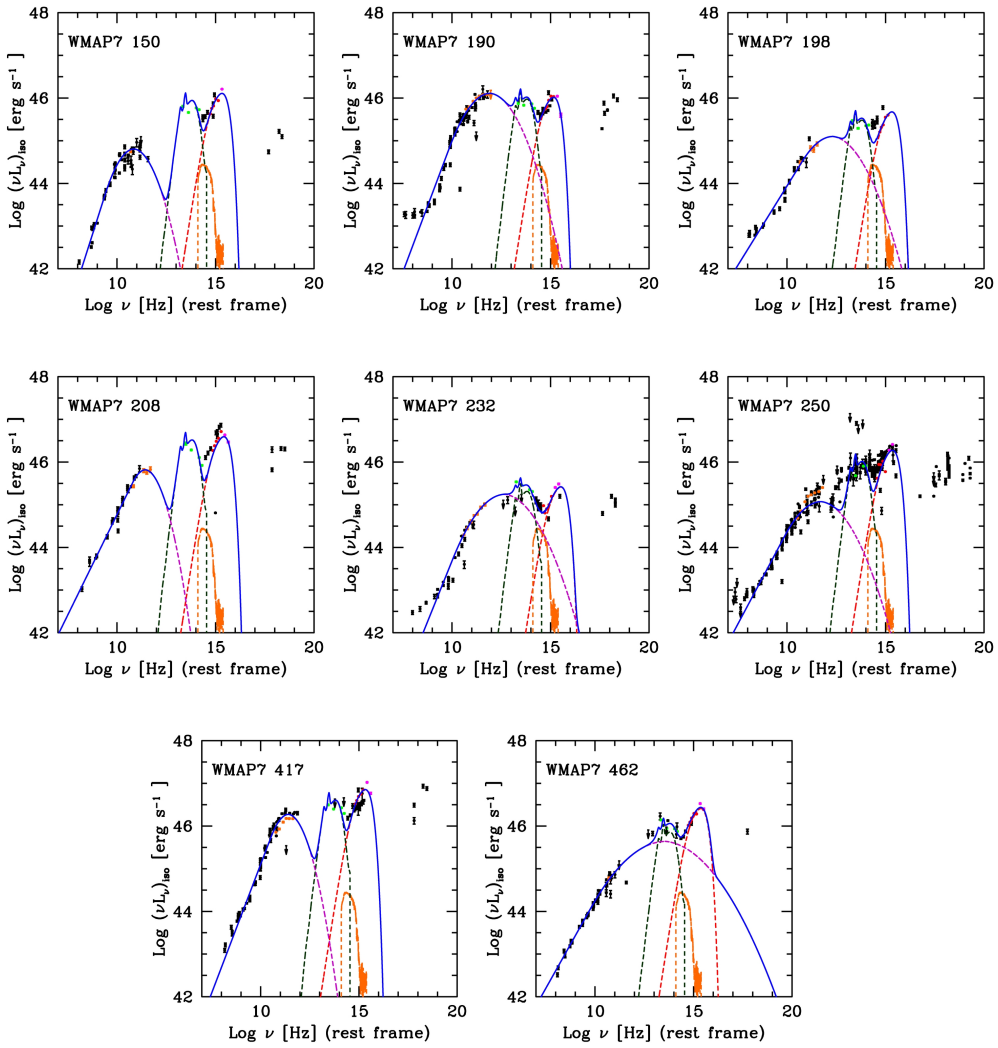

Figure 10.4: SEDs for the FSRQs with evidence (or indication) of torus emission. Solid blue line: total SED, which includes synchrotron emission (dashed violet line, Donato et al., 2001), host galaxy (dashed orange line, Giommi et al., 2012b), disc (dashed red line, Shakura & Sunyaev, 1973), and torus (dark green dashed line, Hoenig & Kishimoto, 2010) emission templates. The host galaxy was taken to be a passive elliptical with $M_R = -23.7$. Data points: *Planck* (orange); WISE (green); SDSS (red); GALEX (magenta). Black points are data taken from the NASA/IPAC Extragalactic Database (NED). Note that, at variance with what was done to compute both $L_{\rm disc}$ and $L_{\rm torus}$ (see text), the luminosities shown here are computed assuming isotropic emission.

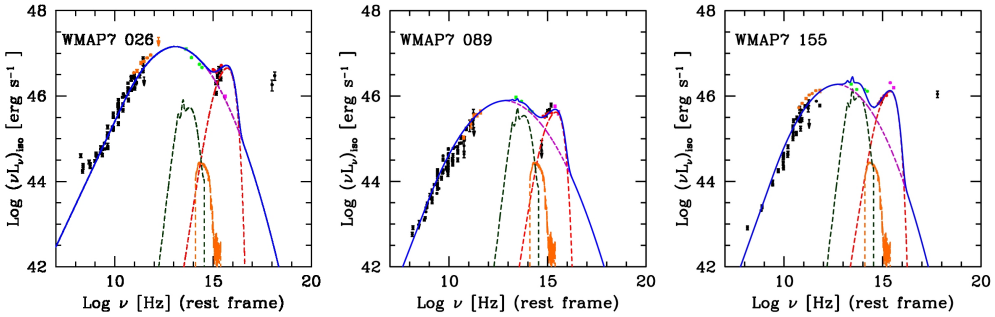

Figure 10.5: Examples of FSRQ SEDs with no evidence of torus. The same color code of Figure 10.4 is adopted. The dashed dark green lines show the upper limits to the torus component determined with the procedure described in the text.

clearly overwhelms that from the torus, if present. This prevents an estimate of the torus luminosity for the majority of our sources. Upper limits to such luminosity were derived as follows. The minimum χ^2 per degree of freedom (χ^2_ν) obtained from the fitting procedure corresponds to a negligible contribution from the torus. If χ^2_ν was $\simeq 1$ a $1\,\sigma$ upper limit to the amplitude of the torus template could be obtained gradually increasing such amplitude and redoing the fit for the other components until the minimum χ^2 increases by $\delta\chi^2 = 1$ (Cash, 1976). In our case, the minimum χ^2_ν is generally $\gg 1$ primarily because of variability and the criterion $\delta\chi^2 = 1$ is not meaningful. To overcome this problem we have applied the Cash (1976) method after having increased all the error bars by a constant factor such that $\chi^2_\nu \simeq 1$.

By the same token, the evidence of torus emission was considered to be significant if setting to zero the amplitude of the torus template increases the re-scaled minimum χ^2 by $\delta\chi^2 \geq 9$, corresponding to a significance $\geq 3\,\sigma$ for one interesting parameter (the normalization of the torus template).

For WMAP7# 153, which is missing mid-IR measurements, we have adopted $3\,\sigma$ flux density upper limits of 0.6 and 3.6 mJy, from instrumental noise alone (Wright et al., 2010), for the WISE channels $W3$ and $W4$, respectively. For channels $W1$ and $W2$ the $3\,\sigma$ limits are set by confusion noise and amount to 0.31 and 0.17 mJy, respectively (Jarrett et al., 2011). For the 4 objects detected in the $W4$ channel with S/N < 3 we have adopted an upper limit equal to three times the error.

The procedure described above yielded upper limits to the torus luminosity for 25 out of the 47 FSRQs. For the remaining 22 objects either the minimization routine did not converge (13 cases) or the result was determined by the few data points with the lowest error bars and did not look credible at visual inspection (5 cases) or the upper limits exceeded the accretion disk luminosity (4 cases). For these objects the upper limits to the

torus luminosity were obtained requiring that the torus template does not exceed both the mid-IR measurements and the disc luminosity.

Examples of SEDs which do not show evidence of torus emission are shown in Figure 10.5. The dashed green lines show the torus SED with luminosity equal to the adopted upper limit.[11]

From the SED fits of all the 55 FSRQs we have derived synchrotron, disc, and torus luminosities (or upper limits). We have taken into account that both the disc and the torus emissions are anisotropic and the result depends on their inclination, i, with respect to the plane of the sky. As argued above, the FSRQs should have $i \simeq 0$ degrees. The jet synchrotron emission is obviously also highly anisotropic but we do not have enough information to properly take the anisotropy into account; therefore we have computed the synchrotron luminosity assuming isotropic emission. This assumption has no impact on the conclusions of this work.

The disc luminosity is estimated as in Section 10.3.1. The dependence of the observed torus flux density on the inclination angle i has been derived from the CAT3D model templates reported for different values of i in the CAT3D library to obtain:

$$F_\nu(i) = F_\nu(0)\frac{0.56 + 0.88\cos i}{0.56 + 0.88} \quad . \tag{10.5}$$

The intrinsic luminosity, obtained integrating over all possible viewing angles, is thus lower by a factor of $1/(0.56 + 0.88) \simeq 0.69$ than would be obtained from the observed flux density ($i = 0$) assuming isotropic emission.

[11] Figures showing the fits to the SEDs of all 55 FSRQs are shown in Appendix B. The 22 objects without evidence of torus emission for which the χ^2 minimization did not yield meaningful upper limits are flagged with an asterisk.

Chapter 11

Blazar properties and results

In this Chapter we describe and discuss the results of our multiwavelength SED analysis for the blazars in our sample. In Sections 11.1 and 11.2 we discuss the results concerning the black hole mass estimates and the torus properties of the FSRQs in the sample, respectively.

11.1 Black hole mass estimates

11.1.1 Estimates with the single-epoch virial method

Black hole mass estimates obtained with the single-epoch virial method (SE method) are available in the literature for several FSRQs in our sample. Shaw et al. (2012) derived them for a subsample of blazars selected from the First Catalog of AGNs detected by the *Fermi* Large Area Telescope (1LAC, Abdo et al., 2010b), including 24 of our FSRQs. They considered several estimators exploiting continuum and emission line (Hβ, Mg II, C IV) measurements. We preferred the estimates based on line measurements to those obtained by using the continuum luminosity because the latter are liable to contamination from the jet's synchrotron emission. More precisely, we chose, in order of preference, estimates derived from Hβ and Mg II lines for the blazars at redshift $z < 1$ and the ones derived from the Mg II and C IV lines for the blazars at higher redshifts (see Shaw et al., 2012, for more details).

Shen et al. (2011) estimated the BH masses for a sample of quasars drawn from the SDSS-DR7 quasar catalog (Schneider et al., 2010), including 36 objects in common with our sample. Seventeen sources of our sample also belong to the Shaw et al. (2012) sample. However, although Shen et al. (2011) give measurements of line luminosities and FWHM, the fiducial BH masses they report are based on continuum rather than line luminosity. Thus we used their line data to recompute the BH masses for the 36 objects in common with our sample. Since several line measurements are present for a given source, following Shen et al. (2011) we adopted Hβ, Mg II, and

C IV line measurements for the blazars at redshifts $z < 0.7$, $0.7 \leq z < 1.9$, and $z \geq 1.9$, respectively. Concerning the 36 sources, we compare the black hole mass estimates, $M_{\bullet,\mathrm{Shen,lines}}$, based on line luminosities with the fiducial values, $M_{\bullet,\mathrm{Shen}}$, given by Shen et al. (2011), based on continuum luminosities. An average logarithmic ratio $\langle \log(M_{\bullet,\mathrm{Shen,lines}}/M_{\bullet,\mathrm{Shen}}) \rangle = -0.17$ with a rms dispersion of 0.23 is found. This suggests that indeed the continuum luminosities are maybe slightly contaminated by the optical emission from the jet, as argued by Shen et al. (2011). Our re-evaluations of the BH mass estimates of the Shen et al. (2011) blazars are in good agreement with those by Shaw et al. (2012) for the 17 blazars in common. The average logarithmic ratio of the two estimates is $\langle \log(M_{\bullet,\mathrm{Shaw}}/M_{\bullet,\mathrm{Shen,lines}}) \rangle = 0.01$, with a dispersion of 0.22. In Table 11.1 we report the available black hole mass estimates for the FSRQs in our sample from Shen et al. (2011) and Shaw et al. (2012) catalogs. Limiting to Shen et al. (2011), in the table we report the black hole masses recomputed on the basis of line measurements, as described above.

Since the analysis by Shaw et al. (2012) is focused on FSRQs, we preferred their estimates for the objects in common with Shen et al. (2011) for the comparison with the BH mass estimates obtained from the fitting of the blue bump. For the other Shen et al. (2011) blazars in our sample, we adopted our new determinations of BH masses based on line luminosities. The corresponding uncertainties were computed by applying the standard error propagation, taking measurement errors on line luminosities and FWHMs into account, as well as the errors on the coefficients of the relations between these quantities and the BH mass, as reported in Shen et al. (2011, and references therein). The latter errors are the main contributors to the global uncertainties.

Black hole mass estimates for one additional object in our sample, WMAP7 # 250, were reported by Kaspi et al. (2000) and Shang et al. (2007). We adopted the more recent estimate.

11.1.2 The factor f

The BH masses estimated with the SE method assume that the optical/UV line emission is coming mainly from the BLR, located at a radial distance R_{BLR} from the central black hole. When assuming that the BLR clouds are in virial equilibrium, $M_\bullet$ is given by Equation (1.7) in Section 1.8. There are two commonly used measures of the cloud velocity ΔV: the line FWHM and the dispersion of its Gaussian fit. We adopt the second one, $\Delta V = \sigma_{\mathrm{line}}$. R_{BLR} is estimated using empirical analytic relations with continuum or line luminosities. With these assumptions and notation for an isotropic velocity field, we have $f = 3$ (Netzer, 1990). This is, however, an oversimplified model. In practice, the value of f is empirically determined, but there is no consensus on its value (see Park et al., 2012a,b, and references therein).

WMAP ID	$\log\left(\frac{M_{\bullet,\mathrm{Shen,lines}}}{M_\odot}\right)$	$\log\left(\frac{M_{\bullet,\mathrm{Shaw}}}{M_\odot}\right)$
31	9.49 ± 0.13	—
51	—	9.22 ± 0.30^b
56	9.17 ± 0.31	—
89	—	7.74 ± 1.48^a
150	9.02 ± 0.14	—
166	8.43 ± 0.12	—
169	8.75 ± 0.12	8.70 ± 0.18^b
173	9.63 ± 0.32	—
179	9.38 ± 0.12	—
182	9.24 ± 0.13	9.14 ± 0.17^b
184	8.09 ± 0.05	—
186	9.11 ± 0.31	9.29 ± 0.53^c
187	8.88 ± 0.18	8.93 ± 0.16^b
190	9.15 ± 0.06	—
191	9.04 ± 0.13	—
194	8.36 ± 0.18	8.45 ± 0.19^b
195	8.99 ± 0.16	—
198	8.47 ± 0.15	—
203	8.64 ± 0.13	8.61 ± 0.17^b
221	8.93 ± 0.31	—
224	9.31 ± 0.13	—
228	8.95 ± 0.14	8.93 ± 0.17^b
232	8.54 ± 0.03	—
236	8.78 ± 0.13	8.14 ± 0.31^a
265	8.78 ± 0.26	9.25 ± 0.18^b
278	9.20 ± 0.13	—
284	8.58 ± 0.28	—
285	8.83 ± 0.14	—
295	8.82 ± 0.59	8.98 ± 0.24^b
306	8.65 ± 0.05	8.62 ± 0.20^a
307	9.05 ± 0.15	8.98 ± 0.16^b
310	8.72 ± 0.12	8.77 ± 0.17^b
311	9.02 ± 0.12	9.08 ± 0.16^b
316	9.09 ± 0.16	9.30 ± 0.16^b
317	—	8.61 ± 0.56^a
321	8.73 ± 0.10	8.73 ± 0.20^a
412	9.44 ± 0.31	—
426	—	8.46 ± 0.45^b
432	8.90 ± 0.12	8.70 ± 0.16^b
436	—	8.35 ± 0.40^b
452	—	8.70 ± 0.30^b
458	—	8.37 ± 0.50^a
470	9.00 ± 0.13	—

Table 11.1: SE black hole mass estimates for the FRSQs in our sample. Column description: (1) WMAP7 ID number; (2) black hole mass estimates along with their uncertainties from Shen et al. (2011), recomputed adopting line widths and fluxes; (3) black hole mass estimates along with their uncertainties from Shaw et al. (2012). The superscripts a, b, and c stand for mass estimates from Hβ, Mg II, and C IV lines, respectively. The symbol "—" is reported where the black hole mass estimate is absent. The reported errors are the nominal uncertainties estimated by means of the propagation of the errors in the measurements. They are generally smaller than the typical statistical uncertainty $\sim 0.4 - 0.5$ dex (Vestergaard & Peterson, 2006; Park et al., 2012b) associated with black hole mass estimates obtained with the SE method.

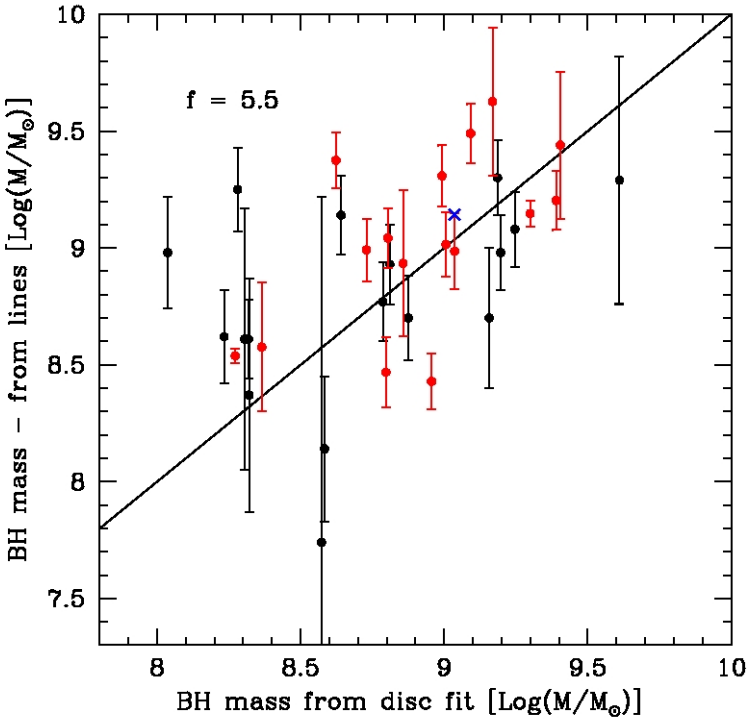

Figure 11.1: Comparison of the black hole mass estimates. Estimates with the SE method against those from fitting the accretion disk SED. The black points are from Shaw et al. (2012), the red points are our estimates using line data from Shen et al. (2011), the blue cross refers to the estimate by Shang et al. (2007) corrected as mentioned in the text. No error was reported for this estimate.

Values claimed in the literature differ by a factor of 2, from $f \simeq 2.8$ (Graham et al., 2011) to $f \simeq 5.5$ (Onken et al., 2004). For face-on objects (such as FSRQs), the average virial coefficient f may be larger than for optically selected QSOs (with random orientations) if the BLR has a flattened geometry (Decarli et al., 2011). The empirical relations used by Shen et al. (2011) and Shaw et al. (2012) implicitly assume $f = 5.5$, since this value was used, following Onken et al. (2004), in calibrating the reverberation mapping BH masses, which in turn were used as standards to calibrate SE mass estimators. Shang et al. (2007) followed a different approach by adopting $f = 3$. They also used a slightly different cosmology. We have corrected their BH mass estimate to homogenize it with the others.

11.1.3 Comparison of black hole mass estimates

Thirty-four of the 55 blazars for which we could derive the BH masses with the blue bump fitting method also have published estimates with the SE method. In Figure 11.1 we compare the results from the two methods, after having homogenized the SE estimates as described above. They are well correlated: the Spearman test yields a 99.96% (i.e. 3.5σ) significance for the correlation. The SE method with $f = 5.5$ yields, on average, slightly higher values of $M_\bullet$. We find an average $\langle \log(M_{\bullet,\mathrm{SE}}/M_{\bullet,\mathrm{blue\,bump}}) \rangle = 0.09$ with an rms dispersion of 0.40 dex. For comparison, the statistical uncertainty of the SE method is 0.4–0.5 dex (Vestergaard & Peterson, 2006; Park et al., 2012b) and the nominal errors associated with the blue-bump method are $\gtrsim 0.2$–0.4 dex (see Section 10.3). Thus the rms difference is fully accounted for by the uncertainties of the two methods. The offset between the two estimates would be removed setting $f = 4.5$, well within the range of current estimates. However, in view of the large uncertainties, reading this as an estimate of f would constitute an overinterpretation of the data. On the other hand, the consistency of the two methods strongly suggests that neither is badly off.

11.1.4 Distribution of black hole masses

In the upper panel of Figure 11.2 we report the distribution of BH masses obtained by means of the blue bump fitting for 55 of our FSRQs and the distribution for the ten additional ones for which only SE estimates are available. The estimates for the latter objects have been first homogenized as described above and then decreased by 0.09 dex to correct for the mean offset with the blue bump results. The lower panel shows, for comparison, the distribution for 1LAC blazars in the Shaw et al. (2012) sample, again decreasing the BH masses by 0.09 dex. Whenever Shaw et al. (2012) provide more than one mass estimate for a single object we made a choice abiding by the order of preference mentioned in Section 11.1.1.

The Figure shows that our 65 FSRQs are associated with very massive

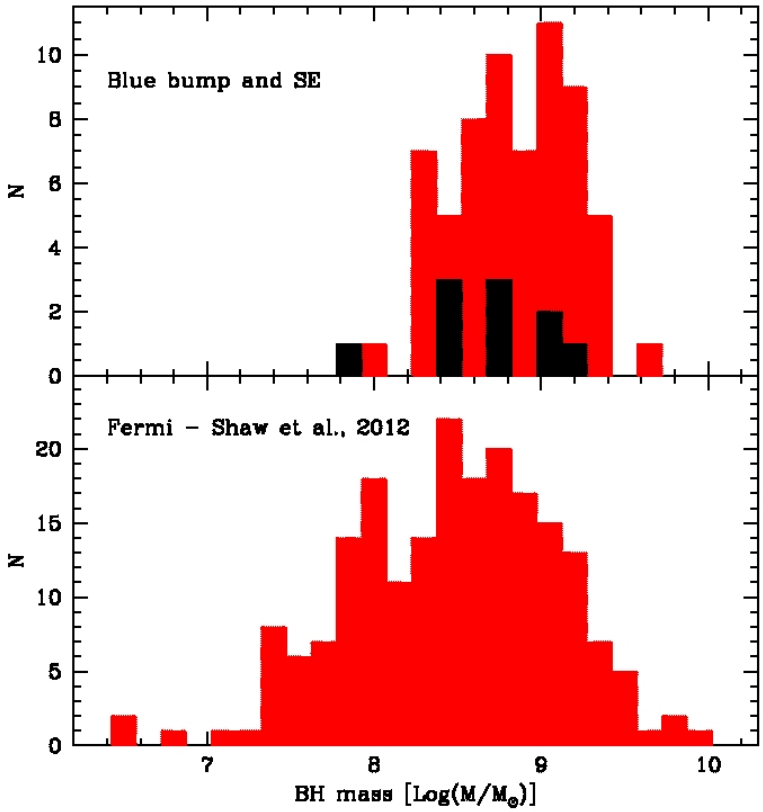

Figure 11.2: Distributions of black hole masses. The upper panel shows in red the distribution for our 55 objects having estimates via blue bump fitting and, in black, for 10 additional objects in the sample for which we have BH mass estimates via the SE method, homogenized as described above in the text and decreased by 0.09 dex to remove the mean offset with blue bump estimates. The lower panel shows the distribution for all 1LAC blazars (Shaw et al., 2012) with masses decreased by 0.09 dex.

BHs ($M_\bullet \gtrsim 10^{7.8}\,M_\odot$) with a median value of $6.8 \times 10^8\,M_\odot$. The median BH mass changes little (it becomes $7.4 \times 10^8\ M_\odot$) if we restrict ourselves to the 55 FSRQs with BH mass estimates via blue bump fitting. The decline in the distribution at lower masses may be a selection effect: we selected radio-bright objects ($S_{23\rm GHz} \geq 1\,$Jy) and the 15 (19%) FSRQs in our sample that neither show a detectable blue bump nor have SE estimates of the BH mass may well be associated with lower values of $M_\bullet$. On the other hand, our results are also consistent with the theoretical and observational studies that suggest that RLAGNs are generally associated with the most massive black holes ($M_\bullet \gtrsim 10^8\,M_\odot$, e.g., Chiaberge & Marconi, 2011). The fast decline of the distribution above $M_\bullet \simeq 10^{9.4}\,M_\odot$, which suggests some upper bound to BH masses, is more likely to be real.

The BH mass distribution of Shaw et al. (2012) blazars adds support to the conclusion that blazar BH masses either below $M_\bullet \sim 10^{7.4}\,M_\odot$ or above $M_\bullet \sim 10^{9.6}\,M_\odot$ are rare. In this context, it is worth noticing that errors in BH mass estimates tend to populate the tails of the distribution by an effect that is analogous to the Eddington bias: objects tend to move from highly populated to less populated regions. Thus in particular the highest mass tail may be overpopulated (while the effect on the low-mass tail may be swamped by selection effects).

In Figure 11.3 we report the distributions of the accretion rates (top panel) and of the Eddington ratios (bottom panel) for the 55 FSRQs in the sample for which we have estimated the BH mass fitting the blue bump of the spectrum, as reported in Table 10.2. We find a median Eddington ratio of 0.16 and a median accretion rate of $2.8\,M_\odot\,{\rm yr}^{-1}$. The few extreme values of these parameters must be taken with special caution on account of the uncertainties affecting our estimates.

The BH mass turns out to be anticorrelated with the disk peak frequency. The Spearman's test gives a probability of the null hypothesis (no correlation) $p = 6.8 \times 10^{-5}$. The anticorrelation follows from Equation 10.4 due to the weak dependence of $M_\bullet$ on the accretion rate and the limited range of $\dot{M}$ spanned by our blazars.

11.2 Color plots and torus properties

Plotkin et al. (2012) argued that statistical evidence of torus emission from AGNs can be provided by mid-IR colors. Their investigation of the WISE data for ~ 100 BL Lacs selected from the SDSS showed that even the most weakly beamed ones, whose mid-IR emission should not be completely dominated by the jet emission, have IR colors too blue for a significant contribution from the torus be present.

In Panel (a) of Figure 11.4 we show the distribution of our WMAP selected blazars of different types in the same WISE color diagram used

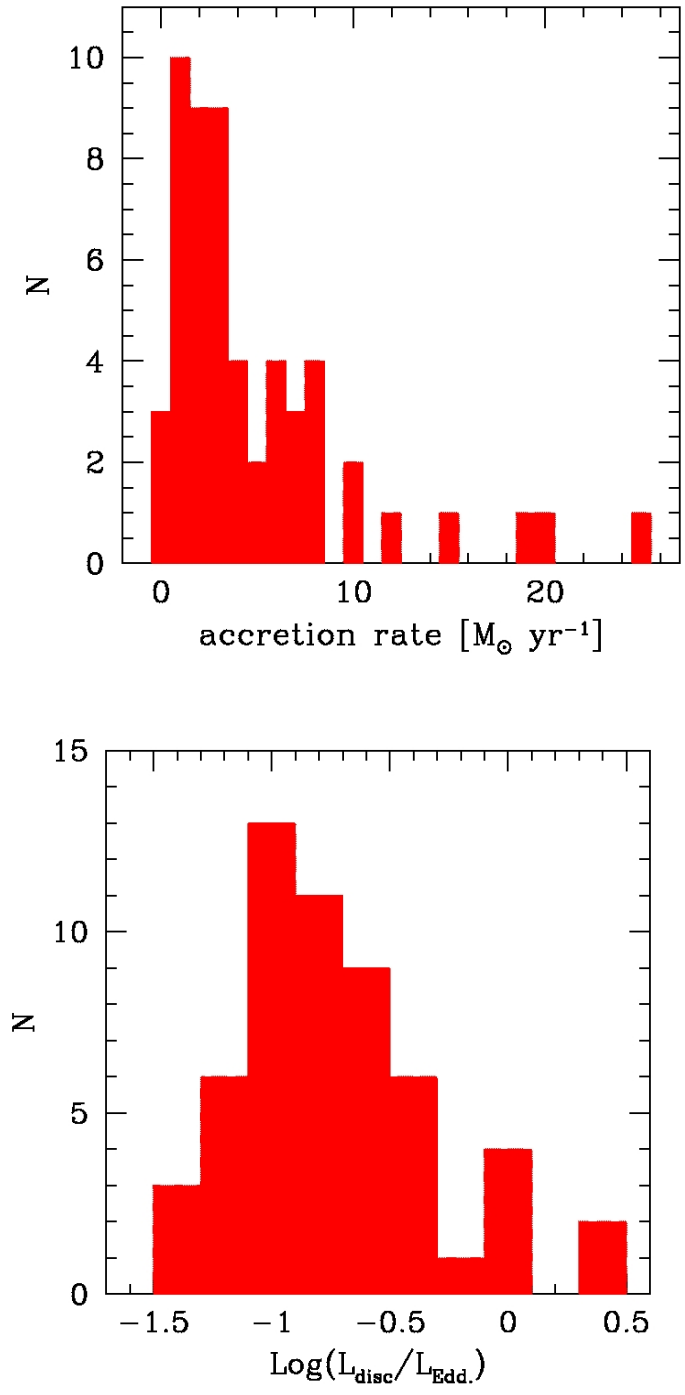

Figure 11.3: Distributions of the accretion rate (top) and of the Eddington ratio (bottom) for the our FSRQs with evidence of a blue bump.

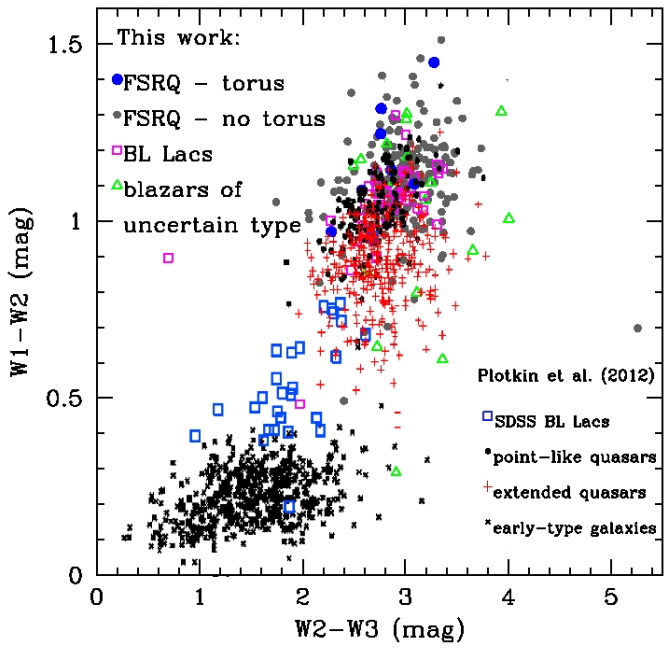

(a)

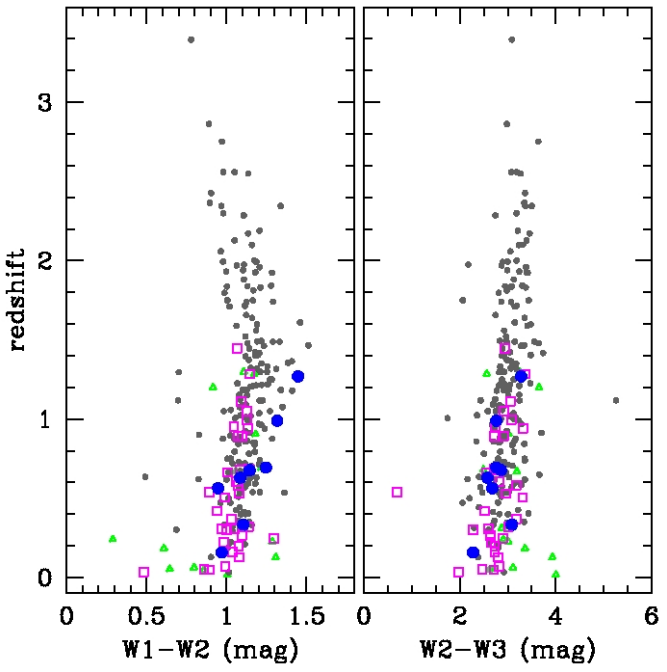

(b)

Figure 11.4: (a) mid-IR (WISE) colors of WMAP-selected blazars of different kind (filled blue circles: FSRQs with evidence of torus; gray points: FSRQs without evidence of torus; open magenta squares: BL Lacs; open green triangles: blazars of uncertain type) compared with those of sources shown in the top left panel of Figure 3 of Plotkin et al. (2012), namely SDSS BL Lacs (open blue squares), quasars with point-like (filled black circles) and extended (red + signs) morphology in SDSS imaging and early-type galaxies (black × signs). (b) WISE colors vs. redshift for WMAP-selected blazars; points have the same meaning as in the left panel.

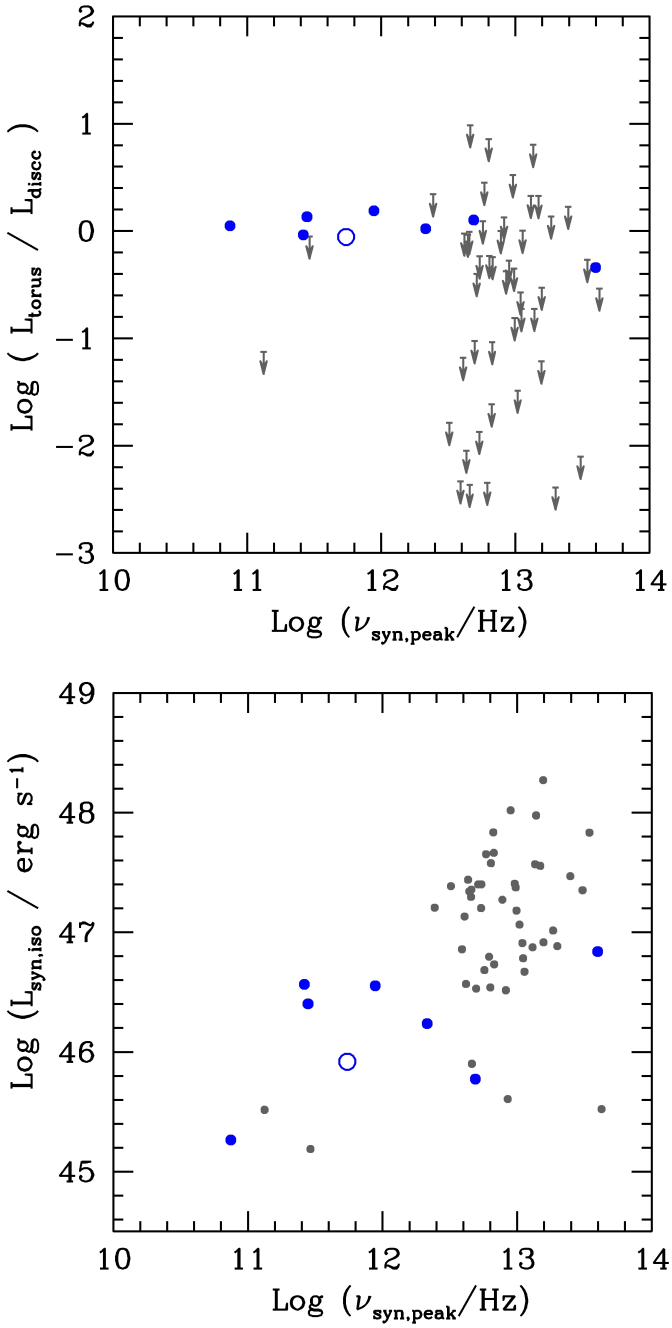

Figure 11.5: Torus to disc luminosity (top panel) and synchrotron luminosity versus synchrotron peak frequency (bottom panel) for the 55 FSRQs with evidence of blue bump. The filled blue points are the FSRQs with evidence of torus, the open blue point is WMAP7# 250, for which the presence of torus is less certain. Gray symbols refer to the FSRQs without evidence of torus; for them we show, in the left panel, the upper limits to the torus to disc luminosity ratios.

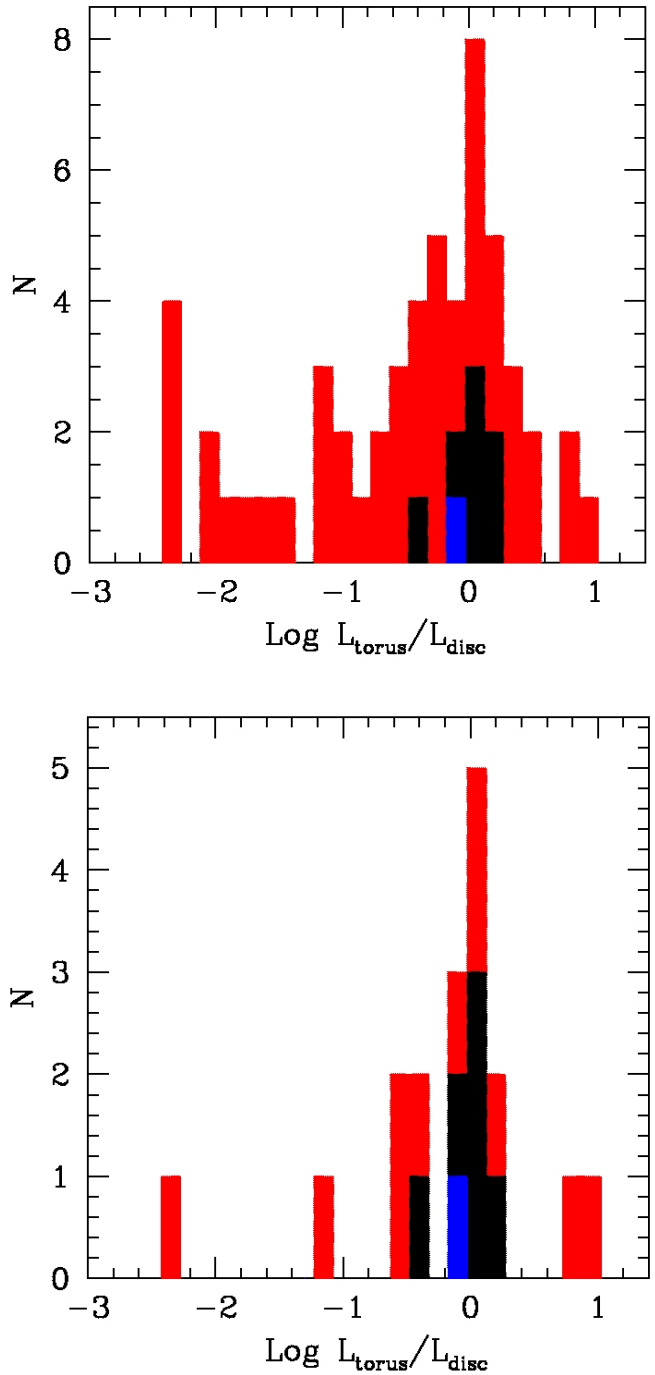

Figure 11.6: Top panel: distribution of the ratio of the torus to the disc luminosities for the 55 FSRQs with both disc and torus luminosity estimates (or upper limits). Bottom panel: distribution for the sub-sample of 18 sources located at $z \leq 1$. In both panels, the black histogram show the sources with evidence of torus, the red histogram those with only upper limits to the torus luminosity. For the latter the luminosity ratios are upper limits. The blue bar corresponds to WMAP7# 250, for which the presence of torus is less certain.

by Plotkin et al. (2012). There is no clear separation in the $(W1-W2)$–$(W2-W3)$ plane between the FSRQs with evidence of torus emission and objects of other kinds: FSRQs without evidence of torus, WMAP selected BL Lacs, WMAP blazars of unknown type. All these objects occupy the same region as SDSS quasars with point-like morphology. Hence, at variance with the findings by Plotkin et al. (2012) for their optically selected BL Lac sample, this diagram does not provide any indication on the presence or absence of torus emission in blazar SEDs.

The outlier with $W1-W2=0.7$ and $W2-W3=5.3$ is WMAP7# 376, i.e. PKS B1908-201. Its anomalous WISE colors might be due to contamination by diffuse Galactic emission, visible in the IRAS maps, that affects mostly the $W3$ channel both because of the Galactic emission spectrum and because of the poorer angular resolution.

The Figure also shows that the 28 SDSS BL Lacs at $z<0.3$ in the Plotkin et al. (2012) sample (none of which is in common with our sample) occupy, in the color-color diagram, a different region than our WMAP-selected BL Lacs, i.e. those that belong to our original sample of 255 blazars and are detected by WISE. This implies that the conclusions by Plotkin et al. (2012) do not apply to the general BL Lac population but are specific to their optical selection. The fact that the Plotkin et al. (2012) BL Lacs have colors intermediate between quasars and early-type galaxies may suggest substantial contamination from the host galaxy.

The Panel (b) of Figure 11.4 shows that the FSRQs with evidence of torus emission are all at relatively low redshift ($z<1.5$) and roughly span the same redshift range as WMAP selected BL Lacs. Since the sample is flux-limited at 23 GHz, where the emission is dominated by synchrotron, lower z objects are those with lower synchrotron luminosity. The latter is thus less likely to swamp the torus emission. This is quantified in the bottom panel of Figure 11.5 which also shows that tori are preferentially detected in FSRQs with lower synchrotron peak frequencies. The top panel of the same Figure shows that the detected tori have luminosities close to the accretion disc luminosity, i.e. are at the upper limit of the physically plausible range for face-on objects. On the whole, it appears that the torus can show up only under quite special conditions: low luminosity and preferentially low peak frequency of the beamed synchrotron emission from the jet as well as

high torus luminosity, close to that of the accretion disc. These conditions must hold at once. In other words, the lack of torus detection does not necessarily mean that blazars have weaker tori than radio-quiet AGNs with similar accretion disc luminosity. In particular, the lack of detections at $z>1.5$ for our flux limited sample does not necessarily mean that tori are weaker at high z.

In the top panel of Figure 11.6 we report the distribution of the ratios of the torus to the disc luminosities (or of upper limits to this ratio) for the 55 FSRQs with disc and torus luminosity estimates (or upper limits

in the case of tori). In the bottom panel we report the same distribution only for the sub-sample of 18 sources located at $z \leq 1$, which include six out of the seven FSRQs with evidence of torus and the uncertain case WMAP7# 250. For this subsample the median logarithmic ratio, treating upper limits as detections, is $\langle \log(L_{\rm torus}/L_{\rm disc}) \rangle = -0.02$. The median decreases to $\langle \log(L_{\rm torus}/L_{\rm disc}) \rangle = -0.24$ for the full sample.

The fraction of FSRQs with measured torus emission is too low to allow a proper use of survival analysis techniques (Feigelson & Nelson, 1985; Schmitt, 1985) to reconstruct the distribution of luminosity ratios taking the upper limits into account. Our attempt to apply anyway the Kaplan & Meyer (1958) estimator did not produce any valid estimate of the median $\langle \log(L_{\rm torus}/L_{\rm disc}) \rangle$ for the full sample. In the case of the sub-sample of the 18 FSRQs at $z \leq 1$ the estimator gave a median $\langle \log(L_{\rm torus}/L_{\rm disc}) \rangle = 0.09$ with undetermined uncertainties. As mentioned above, torus to disc luminosity ratios > 1 are unphysical.

As mentioned above, the median torus to disc luminosity ratio is biased high because only tori with luminosity close to the physical upper limit can possibly be detected against the strong dilution by the beamed jet emission. In fact the median ratios quoted above are higher than found for radio quiet quasars. For example, based on a large sample drawn from the fifth edition of the SDSS quasar catalog Calderone et al. (2012) estimated that the torus reprocesses on average $\sim 1/3$ to $\sim 1/2$ of the accretion disc luminosity. Hao et al. (2013) did not find indications of evolution with redshift of the SEDs (hence also of the torus/disc luminosity ratio) of their 407 X-ray selected AGNs. We have also looked for correlations of the torus luminosity with several physical quantities, including the black hole masses, the synchrotron properties (peak frequency, peak luminosity, total luminosity) and the disc luminosity. No significant correlation was found, not surprisingly given the poor statistics.

Chapter 12

Conclusions and future work

In the following Sections 12.1 and 12.2 we draw our conclusions and outline future work, respectively, concerning both the project on high-z galaxy clusters around radio galaxies and that on SEDs of blazars.

12.1 Summary and conclusions

12.1.1 Galaxy clusters around radio galaxies

The main goal of the project presented in Part II is to search for high redshift $z \gtrsim 1$ galaxy clusters and groups using FR I radio galaxies as beacons. We applied a newly developed method to search for overdensities around the $z \sim 1-2$ FR Is of the Chiaberge et al. (2009) sample, which has been accurately redefined in this work. The careful selection of our FR I sample and the accurate redshift estimates have also allowed us to estimate the comoving space density of sources with $L_{1.4\ \mathrm{GHz}} \simeq 10^{32.3}\,\mathrm{erg\,s^{-1}\,Hz^{-1}}$ at $z \simeq 1.1$. Previous direct observational estimates and model predictions span a quite broad range. Our result is consistent with the upper values and strengthens the case for a strong cosmological evolution of these sources (see Chapter 5).

In Chapter 6 we have described the PPM we developed to achieve the goal to search for high-z clusters. Whilst in principle general, in this work the method has been tailored to the specific properties of the $z \sim 1-2$ FR I radio galaxy sample we consider (Chiaberge et al., 2009, C09), selected within the COSMOS survey (Scoville et al., 2007a), and to the specific dataset used.

The PPM is adapted from the method proposed by Gomez et al. (1997) to search for X-ray emitting substructures within clusters in the low number count regime. Here we are similarly dealing with the problem of small number densities.

We tested the efficiency of the PPM in searching for cluster candidates against simulations (see Chapter 7). Two different approaches are adopted. i) We use two $z \sim 1$ X-ray detected clusters found in the COSMOS survey

within the Finoguenov et al. (2007) catalog. We shift them to higher redshift up to $z = 2$. We find that the PPM detects both clusters up to $z = 1.5$ and it correctly estimates both the redshift and the size of the two clusters. ii) We simulate spherically symmetric clusters of different size and richness, and we locate them at different redshifts (i.e. $z = 1.0$, 1.5, and 2.0) in the COSMOS field. We find that the PPM detects the simulated clusters within the entire redshift range considered with a statistical 1σ redshift accuracy of ~ 0.05. This is remarkably comparable to the statistical photometric redshift uncertainty of photometric redshift catalogs over the same redshift range (Mobasher et al., 2007; Ilbert et al., 2009).

Our results suggest that almost all of our simulated clusters are detected. Compact clusters (i.e. 1 Mpc comoving size) and rich clusters are more easily detected than lower richness clusters, when the cluster center coordinates are accurately known. The majority of these clusters are also detected even if the coordinates of the cluster center are known with poor accuracy (of ~ 100 arcsec). Furthermore, poor overdensities and clusters of intermediate richness are more difficult to detect in the case where the cluster coordinates are known with an accuracy of $\sim$100 arcsec. Concerning cluster sizes, we found that the PPM provides estimates with a 33% rms fractional accuracy, if the cluster center coordinates are known.

We found that our method is effective in finding clusters up to high redshift. We believe that the PPM is a valuable alternative to previously considered methods to search for high-redshift clusters based on photometric redshifts. In fact, with the inclusion of a solid positional prior and an accurate redshift sampling we overcome, at least in part, the problem of establishing whether multiple overdensity peaks in the 2-d projected density field are part of a single larger structure (Scoville et al., 2013) and, thus, identifying different structures at different redshifts.

In Chapter 8 we applied the PPM to search for high-redshift cluster candidates in the fields of our FR I. We found that the great majority of the FR Is in the sample reside in Mpc-scale rich groups or clusters. We estimated, for each cluster candidate: (i) detection significance, (ii) redshift, (iii) size, and (iv) richness.

We also compared our results with those obtained by previous work on the environments of low redshift radio galaxies, high redshift FR IIs and cluster samples at intermediate redshifts. The fraction of FR Is that are associated with cluster environments in our redshift range is consistent with what found for low redshift (i.e. $z \leq 0.25$) FR Is. However, it is significantly higher than what found for both local and high redshift FR IIs.

We applied the Kolmogorov-Smirnov (KS) test to the cumulative number distributions of galaxies in the fields of the C09 sample similarly to what was done by previous work on COSMOS (e.g. Harris, 2012). We checked that the KS test is ineffective in dealing with these types of cluster searches and the results are not conclusive. This is because shot noise fluctuations

affect the results of the KS test.

Moreover, we applied an independent method based on IR colors to search for high redshift overdensities (Papovich, 2008, P08) performing a counts-in-cell analysis. Interestingly, all of the six cluster candidates that are found with such a method, are also detected by the PPM. Vice-versa, the great majority (i.e. $\sim 70\%$) of our $z \gtrsim 1.3$ cluster candidates are not found by the P08 method. Since the P08 method is applied performing a counts-in-cell analysis, some of the clusters that are not detected by the P08 method might be populated by galaxies that are not completely segregated in the cluster core.

Spectroscopic confirmations and detailed multiwavelength observations of our cluster candidates are nevertheless required to study them in more detail, to confirm the results obtained in this work. This is especially important for our high redshift ($z \gtrsim 1.5$) cluster candidates. These would significantly increase the statistics of cluster samples at such high redshifts and might allow a more complete understanding of the ongoing processes involved in the formation and the evolution of these structures.

More in general, our results suggest that the Mpc–scale overdensities associated with the radio galaxies in our sample are similar, independently of the two subclasses considered throughout this work (i.e. the LLRGs and the HLRGs), in terms of estimated richness, mass, and size. Interestingly, on the basis of their multi-component SED fitting, Baldi et al. (2013) found that also the host galaxies of both low and high power radio galaxies in the C09 sample have homogeneous properties, in terms of UV, IR luminosities, stellar mass content, and dust temperature, independently of the subsample considered. Therefore, we can conclude that the radio galaxies in the C09 sample constitute a homogeneous population.

Furthermore, we reported the serendipitous discovery of a bright arc in the field of 01, that is at $z_{\rm spec} = 0.88$. This might suggest that the cluster associated with that source is rich and compact (as suggested by FGH07, George et al., 2011; Knobel et al., 2012, and in this work). The presence of strong and weak lensing features in our sample might be present for some of our cluster candidates.

The above results, combined with the steepness of the RLF of the radio galaxies, suggest that low power FR Is are more effective than FR IIs as beacons to search for groups and clusters at high redshifts.

Radio sources with radio powers typical of those of our FR Is are found only in $10-20\%$ of X-ray and optically selected clusters at $z \lesssim 1$ (Branchesi et al., 2006; Gralla et al., 2011). Therefore, unless this percentage dramatically changed at $z \geq 1$ we might still be missing $80-90\%$ of the entire cluster population at the redshifts of our interest. It would be interesting to blindly apply the PPM to the entire COSMOS field to robustly estimate such a total number of overdensities. This will allow us to compare that with the number counts predicted by the ΛCDM model.

Interestingly, our cluster candidates might be also studied by using the next generation telescopes such as the James Webb Space Telescope (JWST). Although the PPM is primarily introduced for the COSMOS survey, it may be applied to wide field surveys to blindly search for cluster candidates by using accurate photometric redshift information. In particular, we will also extend our work to wider surveys (e.g. Stripe 82 of the SDSS, see Section 12.2.1), where we expect to find a higher number of both FR Is ($\sim 3,000$) and cluster candidates ($\sim 2,100$) at $z \sim 1-2$. Furthermore, we will have a higher chance to find more massive structures and lensing phenomena.

Possible limitations are that the FR Is are difficult to find and that both accurate photometric redshifts and a survey depth similar or better than that of COSMOS (e.g. $I < 25$) are required. Moreover, our method will be less effective for those surveys that will provide sufficient spectroscopic high redshift information, where standard 3-D methods (e.g. correlation functions) might be more successfully applied.

Conversely, the PPM might be also applied to future wide field surveys such as LSST and *Euclid* that will provide accurate photometric redshift information (see Section 12.2.1). Another possible use of the PPM is a search for (proto)clusters at $z \gtrsim 2$, by adopting radio galaxies or other sources (e.g. Lyman break galaxies) as beacons.

12.1.2 SEDs of blazars

In Part III we have investigated the SEDs of a complete sample of FSRQs, all with measured spectroscopic redshifts, flux limited at 23 GHz, drawn from the WMAP 7-yr catalog, and located within the area covered by the SDSS DR10 catalog. The sample comprises 80 objects with 23 GHz flux ≥ 1 Jy, 55 of which (69%) have a blue bump clearly detected in the SED of the sources at optical-UV wavelengths. In this work we have studied the properties of the FSRQs in our sample focusing on the region enclosed within hundreds of parsecs from the central engine.

First we have compared black hole mass estimates we obtained fitting the blue bump with a Shakura & Sunyaev (1973) model with those obtained with the commonly used SE virial method. FSRQs are the AGN population best suited to such a comparison because there is strong evidence that their jets are highly aligned with the line-of-sight, suggesting that the accretion disk should be almost face-on, thus minimizing the uncertainty on the inclination angle that bewilders black hole mass estimates for the other AGN populations.

The mass estimates obtained from the two methods are remarkably correlated, with a significance of 99.96%. This represents the first time where such a correlation is found for a statistically significant sample of AGNs. This result was achieved through the careful blazar sample selection, SED

fitting, and black hole mass estimates, which are obtained accurately considering the standard accretion disc theory.

If the calibration factor f of the SE relation (Equation 1.7 in Section 1.8) is set to $f = 4.5$, well within the range of recent estimates, the mean logarithmic ratio of the two mass estimates is $\langle \log(M_{\bullet,\mathrm{SE}}/M_{\bullet,\mathrm{blue\,bump}}) \rangle = 0$ and its dispersion is 0.40, which is close to what is expected from uncertainties of the two methods. That the two independent methods agree so closely in spite of all the potentially large uncertainties associated with each (see Sections 1.8 and 10.3) lends strong support to both of them. However, the agreement is only statistical, and individual estimates of black-hole masses must be taken with caution.

Our results imply that the blue-bump method is a valuable alternative to the commonly used SE method to estimate black hole masses in bright AGNs such as blazars. The blue-bump method may be applied to larger samples of blazars to increase the statistics of AGNs with black hole mass estimates. In particular, future wide field optical surveys such as LSST may be used to characterize the blue-bump for larger samples of FSRQ SEDs, thus allowing an unprecedented statistically significant comparison between the SE and the blue-bump methods. We refer to Section 12.2.2 for discussion.

The distribution of black-hole masses for the 55 FSRQs in our sample with a well-detected blue bump has a median value of $7.4 \times 10^8\,M_\odot$. It declines at the low-mass end, consistent with other indications that RLAGNs are generally associated with the most massive black holes, although the decline may be, at least partly, due to the source selection. The distribution drops above $M_\bullet = 2.5 \times 10^9\,M_\odot$, implying that ultra-massive black holes associated with FSRQs must be rare.

We have also searched for evidence of dusty AGN tori from the inspection of the SEDs of the 80 blazars in our sample at NIR wavelengths. We have found evidence of torus emission for 7 objects, all included in the sub-sample of 55 sources showing the optical–UV bump interpreted as thermal emission from a standard accretion disc. An uncertain indication of torus emission was found for one additional object. For the other 47 FSRQs in the accretion disc sub-sample we have derived upper limits to the torus luminosity. Larger samples of blazars are needed to further characterize the AGN torus in blazars. Nevertheless, remarkably, ours is the first work where statistically significant evidence of AGN torus is detected in blazars.

Our analysis has also shown that the Doppler boosted synchrotron emission from the relativistic jet strongly hampers the detectability of the FSRQ torus emission. The detection was only possible for objects with torus luminosity close to the disc luminosity, which constitutes a physical upper limit to it. Even in this limiting case, the jet emission swamps that from the torus in the majority of objects unless it peaks at frequencies much lower than the mid-IR ones. This implies that the inferred ratios of torus to disc luminosity are biased high. The median values, considering upper limits as detections,

indicate $L_{\rm torus}/L_{\rm disc} \sim 1$ while studies of radio quiet quasars yield average ratios $\langle L_{\rm torus}/L_{\rm disc}\rangle \simeq 1/3$–$1/2$ (Calderone et al., 2012). On the other hand, although our poor statistics does not allow us to draw firm conclusions, our results are compatible with the FSRQ tori having the same properties as those of radio quiet quasars, consistent with the unified scenario for AGNs.

At variance with Plotkin et al. (2012), who investigated a sample of optically selected BL Lacs, we find that the WISE colors do not allow us to draw any conclusion on the presence or absence of tori associated with WMAP selected blazars. With the latter selection blazars of all types (FSRQs with and without evidence of torus, BL Lacs, blazars of unknown type) occupy the same region of the $(W1-W2)$–$(W2-W3)$ plane, and their region overlaps that of SDSS quasars with point-like morphology.

Our results prove the importance of investigating multiwavelength SEDs of bright AGNs such as blazars to understand the accretion process and estimate physical quantities such as Eddington ratios, black-hole masses, and AGN torus luminosities, that are strongly related to the activity in central region of the AGN.

12.2 Future work and perspectives

12.2.1 Galaxy clusters

In this Section we outline some of our future projects on high-z galaxy clusters. Concerning these projects a substantial part of our future work will be focused on searching for high-z galaxy clusters in surveys such as SDSS Stripe 82[1] and CFHTLS.[2] Other work will be performed in order to confirm spectroscopically our cluster candidates as well as to study the properties of galaxies in clusters at $z \sim 1-2$. We will also test and use the newly developed PPM to search for high-z galaxy clusters around radio galaxies in forthcoming surveys in view of the exploitation of *Euclid* data for high-z galaxy cluster studies.

Galaxy clusters at $z \gtrsim 1$ in SDSS Stripe 82

SDSS Stripe 82 is a $\sim$ 270 square degree survey within the SDSS. SDSS Stripe 82 overlaps with several both present and forthcoming surveys such as the large area UKIRT Infrared Deep Sky Survey (UKIDSS) in the YJHK bands (Lawrence et al., 2007), the Galaxy Evolution Explorer survey (GALEX, Morrissey et al., 2007) in UV, the Spitzer-HETDEX Exploratory Large Area (SHELA, Papovich et al., 2011) survey in IR. At longer wavelengths, the whole SDSS Stripe 82 lies within the high-radio frequency Atacama Cosmology Telescope (ACT) equatorial survey (Swetz et al., 2011) and deep

[1] `http://classic.sdss.org/legacy/stripe82.html`
[2] `http://www.cfht.hawaii.edu/Science/CFHTLS/`

VLA observations at 1.4 GHz (Hodge et al., 2011) cover 80 square degrees of SDSS Stripe 82.

First, we will use VLA and SDSS data to select a sample of $z \sim 1-2$ LLRGs, analogously to what has been done in C09 for the COSMOS survey. In fact, the depth of the SDSS images in the i-band (i = 22.69, Ivezić et al., 2007) will be sufficient to systematically search for $z \sim 1-2$ LLRGs. This search will return a sample of $\sim 3,000$ LLRGs at redshifts $z \sim 1-2$. An accurate estimation of both the photometric redshifts of the LLRGs and the photometric redshifts of all galaxies in SDSS Stripe 82 will be possible taking advantage of available and forthcoming multiwavelength photometric information.

Then, using existing and ongoing photometric redshift catalogs (e.g. Reis et al., 2012) we will apply the PPM to search for galaxy clusters in the fields of the LLRGs. Based on the results presented in Chapter 8 we expect to find ~ 700 clusters or rich groups in the exciting $z \sim 1.5-2$ redshift range. Given such a large sample of clusters, we expect that a limited number of massive clusters will be included in our sample. This is not surprising. In fact the PPM is effective to find dense environments (i.e. rich groups or clusters) that have masses below the typical $\sim 10^{14}$ $M_{\odot}$ cutoff of massive clusters (see e.g. Section 8.10.7).

Such a large sample of clusters will allow to understand better the properties of the cluster galaxy population and their changes with redshift in terms of galaxy morphologies, types, masses, colors, and star formation content. This will be especially important at $z > 1.5$, where these properties and their evolution are still debated.

Furthermore, since the field of the SDSS Stripe 82 survey is covered by the ACT survey, we are planning to apply the PPM to search for optical counterparts of the ~ 50 clusters detected by means of the SZ effect within the SDSS Stripe 82 area up to $z \sim 1.3$ (Hasselfield et al., 2013). Optical and X-ray information of the clusters (Menanteau et al., 2013) combined with SZ and X-ray scaling relations will be used to estimate the masses of the cluster candidates and, then, the completeness of the cluster samples found with the PPM as a function of the cluster mass and redshift.

Galaxy clusters at $z \gtrsim 1$ in VIPERS

In a forthcoming work (Castignani et al., in preparation) we will apply the PPM to search for high-redshift galaxy clusters and groups around LLRGs up to $z \sim 1.5$ within the VIMOS Public Extragalactic Redshift Survey (VIPERS)[3] covering 24 square degrees of the CFHTLS area.

We will draw a sample of $z \gtrsim 1$ LLRGs by means of 1.4 GHz FIRST radio fluxes. Optical counterparts will be found taking advantage of the

[3] `http://vipers.inaf.it/`

i < 22.5 photometry of the VIPERS survey. Both photometric and spectroscopic redshift information derived within the VIPERS survey will be used to search for galaxy clusters and groups in the fields of the LLRGs in our sample by means of the PPM. Then, we will combine available multi-wavelength near-infrared/optical photometry as well as galaxy stellar mass estimates available within the VIPERS survey to study the segregation of both star-forming and passively evolving galaxies within the clusters. X-ray photometry from both present and forthcoming surveys (e.g. XXL, Pierre et al., 2011) will be used to search for diffuse emission from our clusters and estimate both purity and completeness of the cluster samples by means of X-ray scaling relations.

Observations of $z \gtrsim 1$ galaxy clusters

A substantial part of our future work on clusters will take advantage of archival data. However, we are planning to write proposals to observe the cluster candidates with deeper IR and optical observations to look for any evidence (or absence) of the red sequence or a segregation of faint red objects in the fields that we might be missing by using the COSMOS catalog (Ilbert et al., 2009). In particular we will write proposals to use the FORS instrument on the Very Large Telescope (VLT) to spectroscopically confirm our best cluster candidates at $z > 1.5$.

Rest frame UV observations might also help to search for the possible presence of Lyman-α emitting regions that are commonly found in $z \gtrsim 2$ protoclusters. X-ray observations deeper than those available within the COSMOS survey will allow to search for signatures of hot plasma within the ICM (Tundo et al., 2012). All of these observations will help establishing whether our clusters are still evolving. Alternatively, they might exhibit transitional properties between those typical of high redshift ($z > 2$) Lyman-α emitter protoclusters and those associated with low redshift clusters, that show common features such as X-ray emission, red-sequence, and segregation of red objects within the core.

Color-magnitude plots

For each $z \sim 1$–2 cluster (candidate) we will explore the evolution of the red-sequence in order to constrain the scatter of the red-sequence at $z > 1$ and possibly determine at which redshift the red sequence breaks down. This is key in order to study the epoch of formation and the evolution of large red and dead elliptical galaxies. Previous work addressed the problem of the formation and evolution of the red sequence at $z \gtrsim 1.5$ (proto)clusters (e.g. Zirm et al., 2008; Zeimann et al., 2012; Tanaka et al., 2013; Fassbender et al., 2014). However, the lack of a large sample of (spectroscopically) confirmed $z > 1.5$ galaxy clusters limits our understanding of such a problem and, more

generally, of the evolution of the galaxies in clusters. Therefore, both the galaxy cluster sample presented in this work and the high-z cluster samples we expect to build in the next future will increase the statistics, thus allowing to address fully the red-sequence problem. Furthermore, the clusters associated with LLRGs are not biased in favor of having a large population of red objects, or other features that are typical of evolved clusters (e.g. evidence of SZ effect and X-ray emission). Therefore, our red-sequence study will represent a valuable alternative to previous work, which is mainly focused on X-ray or NIR selected distant clusters.[4] Preliminary results (Castignani et al., in preparation) on the high-z cluster candidates we have found in the COSMOS survey with the PPM (see Chapter 8) suggest that the color-magnitude diagrams for clusters at $z > 1.5$ obtained with ground based archival data (from CFHTLS and Subaru) seem to be sufficient to find and constrain the red-sequence in some of the highest redshift clusters.

High-z galaxy clusters around LLRGs in the *Euclid* survey

Another project concerning galaxy clusters will be focused on the exploitation and the development of the PPM to search for high-z galaxy clusters (around LLRGs) in the context of the future *Euclid* mission (Laureijs et al., 2011). We will optimize the PPM method for being used on *Euclid* data by testing it on both present and forthcoming wide field optical/IR surveys, as well as mock catalogs coming from numerical simulations and developed within the *Euclid* consortium.

Euclid is a future wide field survey primarily designed to study the nature of dark energy and dark matter taking advantage of deep NIR photometry and spectroscopy.

The project will also benefit from the radio facilities that are being developed in parallel to the *Euclid* project, in particular the Square Kilometer Array (SKA) and its precursors/pathfinders (e.g. LOw Frequency ARray - LOFAR - in Europe, Australian Square Kilometer Array Pathfinder - ASKAP - in Australia, MeerKAT in South Africa).

Euclid and SKA will start to be operational in the same period (i.e. they are expected to start in 2020) and the deep interest of joint Euclid-SKA projects is proven by a recent international conference organized in Oxford ("Synergistic Science with Euclid and the Square Kilometer Array", September 2013). The work will be performed mainly in collaboration with Christophe Benoist, Sophie Maurogordato, and Chiara Ferrari, researchers at the Observatoire de la Côte d'Azure (O.C.A.) in Nice, that are deeply involved in the *Euclid* and SKA developments.

[4] We also mention here that searches for distant galaxy clusters that are based on X-rays are highly affected by the strong dependence, $\propto (1+z)^{-4}$, of the observed surface brightness on the redshift. This represents one of the major limitations of such searches.

First, we will search for high-z LLRGs by combining existing and forthcoming radio surveys from SKA precursors and pathfinders (such as LOFAR and ASKAP) with optical data and redshift catalogs. Photometric redshifts will be provided for the *Euclid* survey by combining *Euclid* NIR photometry at YJH bands with ground based g-, r-, i-, and z-band optical photometry, down to AB magnitudes ~ 24 and ~ 25.2, at 5σ sensitivity level, for the NIR and optical bands, respectively. The expected *Euclid* survey sensitivity and redshift accuracy are comparable with those obtained for the COSMOS survey. Therefore, the PPM will be effectively applied to the *Euclid* survey to search for high-z galaxy clusters.

More specifically, by cross correlating radio (e.g., LOFAR)-optical and redshift catalogs, based on the results presented in this thesis and the steepness of the radio luminosity function, we expect to find about 3×10^7 LLRGs at $z \sim 1-2$ with specific rest frame 1.4 GHz luminosities in the range $\sim 10^{30\text{–}33}$ erg s^{-1} Hz^{-1} within the *Euclid* survey area. By using (photometric) redshift catalogs, we will apply the PPM to the fields of the LLRGs. We expect to find at least $\sim 3 \times 10^7$ clusters and rich groups at $z \sim 1-2$ down to a mass of a few 10^{13} solar masses at the time *Euclid* will be operational.

We will also work on mock catalogs from simulations developed within the *Euclid* consortium. We will apply the PPM to search for clusters and rich groups in the fields of the BCGs, for which photometric redshifts are provided in the mock catalogs. Then, we will improve the catalogs by using recipes to include LLRGs. In order to do this, we will consider the radio luminosity function of high-z LLRGs (e.g. Smolčić et al., 2009; McAlpine et al., 2013) and the fact that LLRGs are often associated with the BCGs (e.g. Best et al., 2007) and they are preferentially hosted in giant ellipticals of cD type (e.g. Donzelli et al., 2007), at least at low redshifts.

Furthermore, the collaboration with Christophe Benoist, Chiara Ferrari, and Sophie Maurogordato at O.C.A. , and with Matt Jarvis (Professor at Oxford University) will also allow us to test the PPM on existing/ongoing both optical/NIR and radio projects in which they are deeply involved, such as CFHTLS, Dark Energy Survey, VISTA Deep Extragalactic Observations (optical/NIR) and LOFAR, ASKAP, Jansky Very Large Array (radio) surveys.

In order to test our method in preparation to *Euclid* we will combine low frequency radio photometric data (e.g., from LOFAR) with optical/NIR photometry and redshift information, provided by on-going deep surveys such as SDSS Stripe 82, CFHTLS, Dark Energy Survey (DES), VISTA Hemisphere Survey (VHS) and VISTA Deep Extragalactic Observations (VIDEO) to search for optical counterparts of the radio sources, similarly to what has been done in other work (Chiaberge et al., 2009).

In particular, we will have access to DES data at g, r, i, z, and Y bands. Combining DES with VHS infrared J, H, and Ks photometry we expect to find clusters up to $z \sim 1.5$ within the $\sim 5,000$ square degrees of survey

area[5].

Furthermore, in the framework of DES and *Euclid*, Christophe Benoist is currently developing a cluster finder algorithm that performs cluster searches blindly and, analogously to the PPM, is based on photometric redshifts. We will compare the PPM with Benoist's independent method, when applied to both mock catalogs and real photometric redshift surveys, in terms of cluster detection efficiency, completeness and purity of the cluster catalogs. Combing these two methods might be extremely valuable for future high-z cluster searches.

In conclusion, our results will represent an impressive challenge for modern cosmology and present cluster search methods. Based on the results on COSMOS that are presented in this thesis, we are confident that our projects will open new perspectives in the field of statistical cosmology at unprecedented high redshift.

12.2.2 Blazars

In this Section we outline some of our future projects on blazars. We are planning to extend our multiwavelength SED analysis including (some of) the blazars that were not considered in this work, but are part of the original sample of 255 blazars drawn from the WMAP 7-yr point source catalog (Gold et al., 2011).

We will take advantage of forthcoming optical wide field surveys such as LSST. We are also planning to write proposals to obtain optical spectra of (part of) the blazars in our sample with optical telescopes such as the Telescopio Nazionale Galileo, Magellan, Hobby-Eberly, and Palomar telescopes, similarly to what has been done in previous work for blazars (Landt, 2012; Shaw et al., 2013). Optical photometric data and spectra will allow us to increase the number of blazars in our sample with black hole mass estimates obtained with the blue-bump or the SE methods.

Then, using the available black hole mass estimates, we will derive the blazar black hole mass function and will compare it with that obtained in previous work on black-hole growth and black hole mass function for AGNs and local normal galaxies (see e.g. Kelly & Merloni, 2012, for a review). The evolution of the AGN luminosity function as well as the fact that the jets of blazars are almost perfectly aligned with the line-of-sight will be taken under consideration when comparing the number densities of blazars, AGNs, and normal galaxies at different redshifts.

Furthermore, preliminary results suggest that three out of the 15 blazars (20%) at redshift $z < 0.13$ within the sample of 255 blazars are hosted in star forming galaxies, whose features are clearly visible in the SEDs. This is surprising, since blazars are expected to be hosted in bright and large

[5] `http://www.darkenergysurvey.org/survey/`

ellipticals (Scarpa et al., 2000; Nilsson et al., 2007; Giommi et al., 2012b, see also Section 2.3). Nevertheless, similarly to what has been discussed above in the case of the AGN torus, the evidence of emission from the host galaxy is expected from those low-redshift blazars for which the non-thermal emission from the jet does not overwhelm that from the host galaxy.

In order to better characterize the host galaxy in blazars we are planning to build a sample drawn at 30 GHz from the *Planck* point-source catalog (Planck Collaboration XXVIII, 2013), similarly with what has been done in the present work using the WMAP 7-yr point source catalog (Gold et al., 2011). Taking advantage of the better sensitivity of *Planck* [6] we expect to have more chances to find evidence of the host galaxy in the SEDs of the blazars we will select, at least of those at relatively low redshifts, $z < 0.13$, consistently with our preliminary results.

We will also study the Mpc-scale environments of our blazars and we will compare our results with those obtained for radio galaxies at similar redshifts. In particular we will use wide field infrared WISE photometry to search for overdensities of red objects in the fields of the blazars, similarly to what has been done in previous work (Gettings et al., 2012). This study will represent an indirect test for the RLAGN unification scheme (see also Section 2.3).

Furthermore, we will search for > 100 MeV gamma-ray emission associated with our blazars looking for counterparts in the latest catalog of AGNs detected by *Fermi* LAT (Gasparrini et al., 2012). The forthcoming catalog of AGNs detected by LAT in four years of scientific operation (Cutini et al., 2014) will be similarly used for the proposed study. X-ray (within 0.4-10 keV) counterparts of our blazars will be searched for in the 7-yr *Swift* point-source catalog (D'Elia et al., 2013). The modeling of the low- and high-frequency bumps associated with synchrotron and IC emission in the SEDs of the LAT-detected blazars, respectively, will be attempted by adopting the Donato et al. (2001) model, thus extending to higher energies what has been done in this work for the synchrotron emission only. We will estimate the BLR luminosity in those blazars where broad emission lines are reported in the literature. Then, we will search for a possible correlation between the BLR luminosity and the gamma-ray luminosity for the blazars in our sample. Such a correlation has been found in previous work for optically selected blazars (Sbarrato et al., 2012).

In conclusion, all the proposed work on blazars will open new perspectives towards a deeper understanding of the physics of accretion onto the SMBHs and the energy production in bright AGNs by means of SED modeling.

[6] The *Planck* point-source catalog is 90% complete at 30 GHz down to at 575 mJy (Planck Collaboration XXVIII, 2013).

Part IV

Appendix

Appendix A

PPM plots

In this Chapter we report all PPM plots for the fields of the sample of 32 FR I radio galaxies of this work (see Section 5.2). The PPM and the corresponding plots have been introduced and described in Chapter 6. In Figure A.1 we report the PPM plots where the significance of each overdensity is plotted. In Figures A.2 and A.3 we report the same PPM plots showing the radial cluster information concerning $r_{\rm min}$ and the fiducial cluster size $r_{\rm max}$, respectively, both estimated consistently with the PPM procedure.

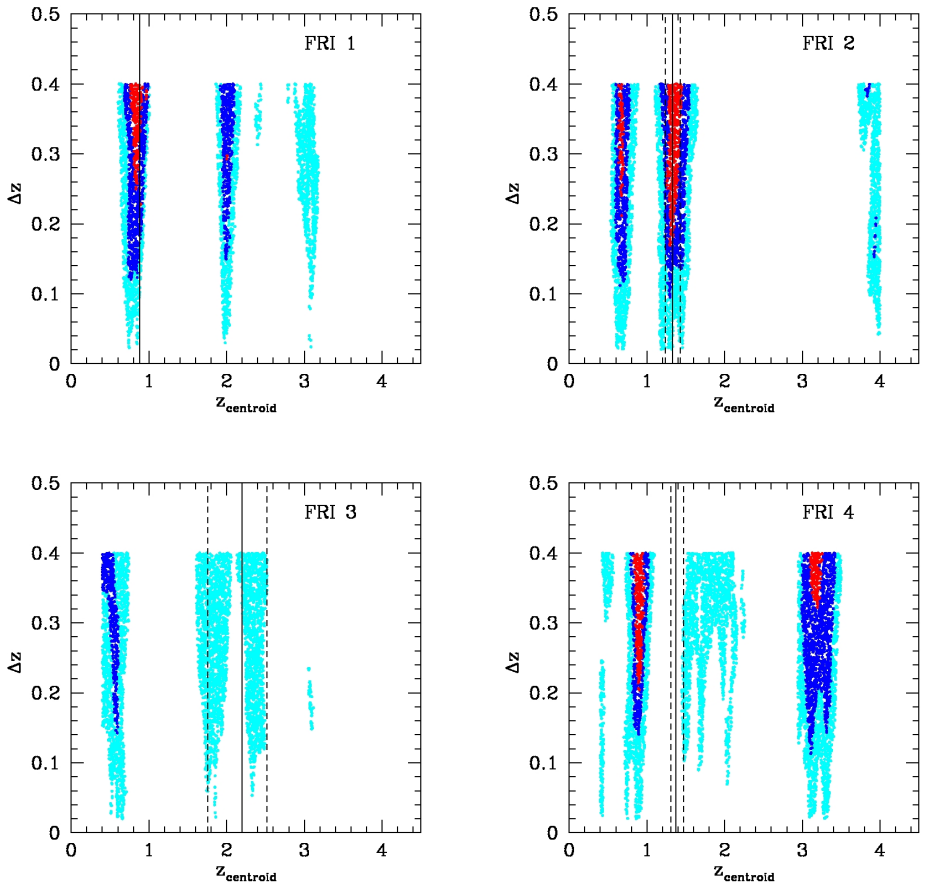

Figure A.1: PPM plots for the fields of the 32 FR I sources in our sample (see Section 5.2). The abscissa of the vertical solid line is at the redshift of the source. The vertical dashed lines show its uncertainties as given in Baldi et al. (2013). Vertical dashed lines are not reported in those case where the spectroscopic redshift of the source from zCOSMOS-bright (Lilly et al., 2007) or MAGELLAN (Trump et al., 2007) catalogs is available. Each point represents the detection significance of the number count excess for a specific choice of the values of the redshift bin Δz (within which we perform the number count) and its centroid $z_{\rm centroid}$. The detection significance is estimated as the complementary probability of the null hypothesis (i.e. no clustering) to have more than the observed number of galaxies in the field of the beacon (i.e. the FRI radio galaxy in our case), assuming Poisson statistics and the average number density estimated from the COSMOS field. We plot only the points corresponding to overdensities with a $\geq 2\sigma$ detection significance. Color code: $\geq 2\sigma$ (cyan points), $\geq 3\sigma$ (blue points), $\geq 4\sigma$ (red points). A Gaussian filter which eliminates high frequency noisy patterns is applied.

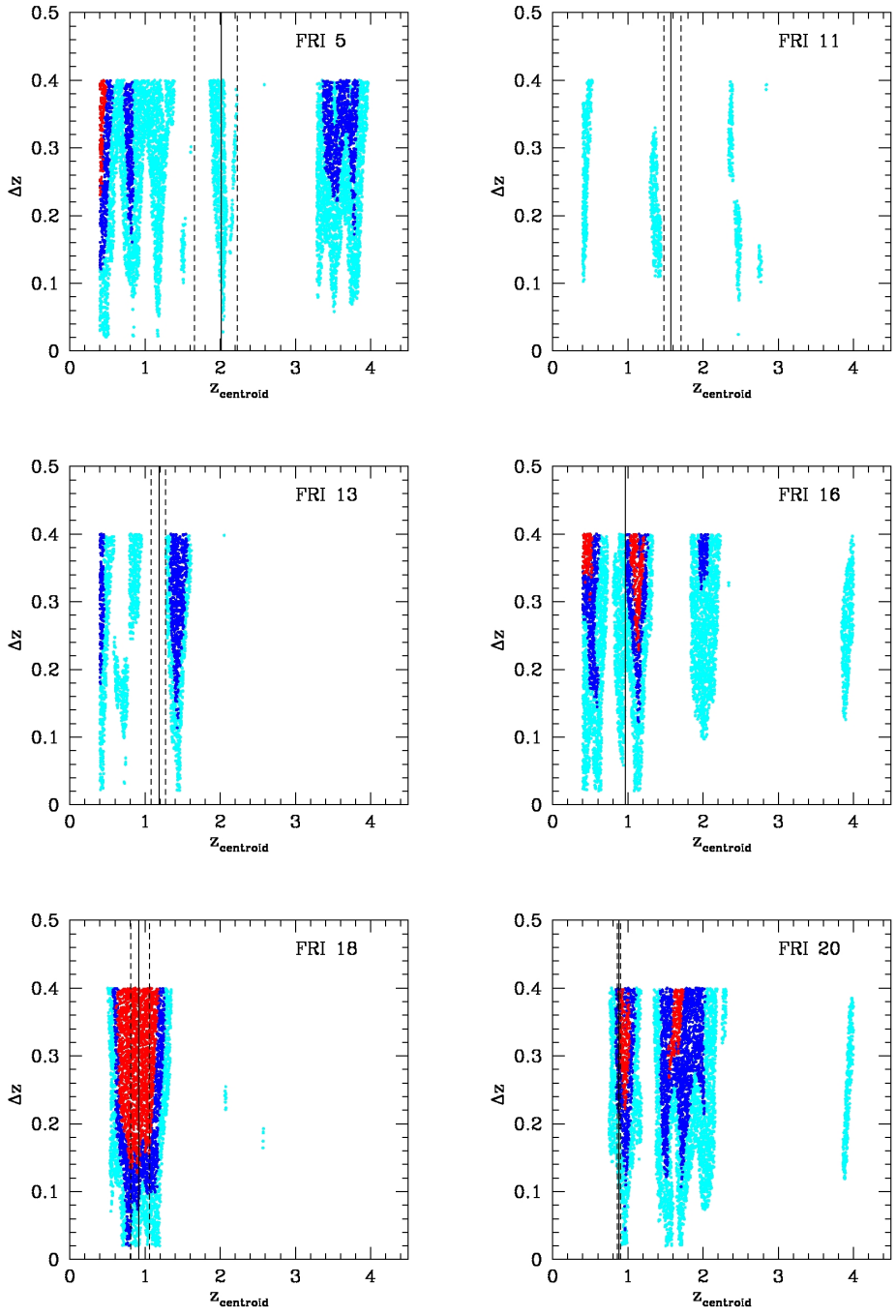

Figure A.1: Continued.

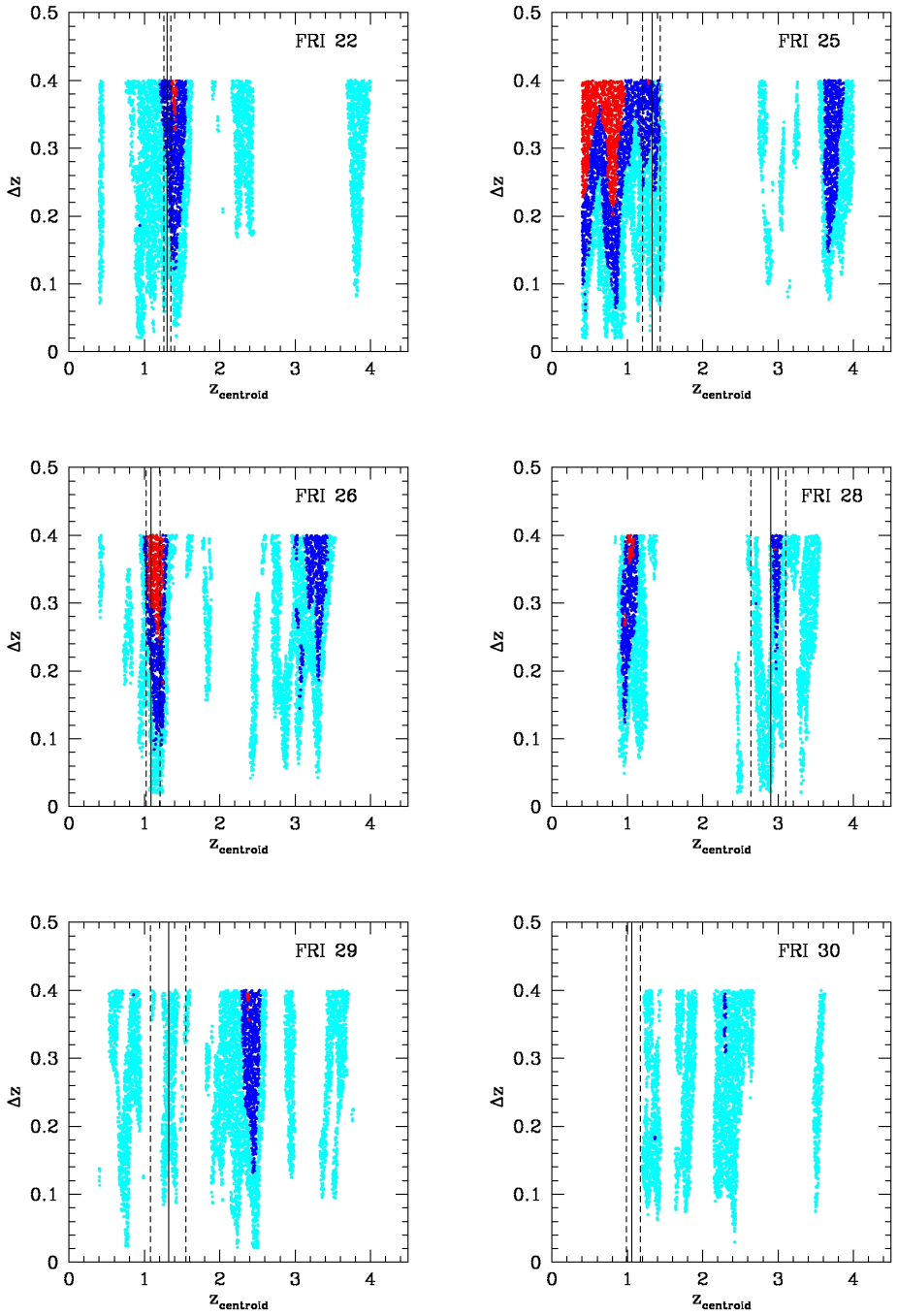

Figure A.1: Continued.

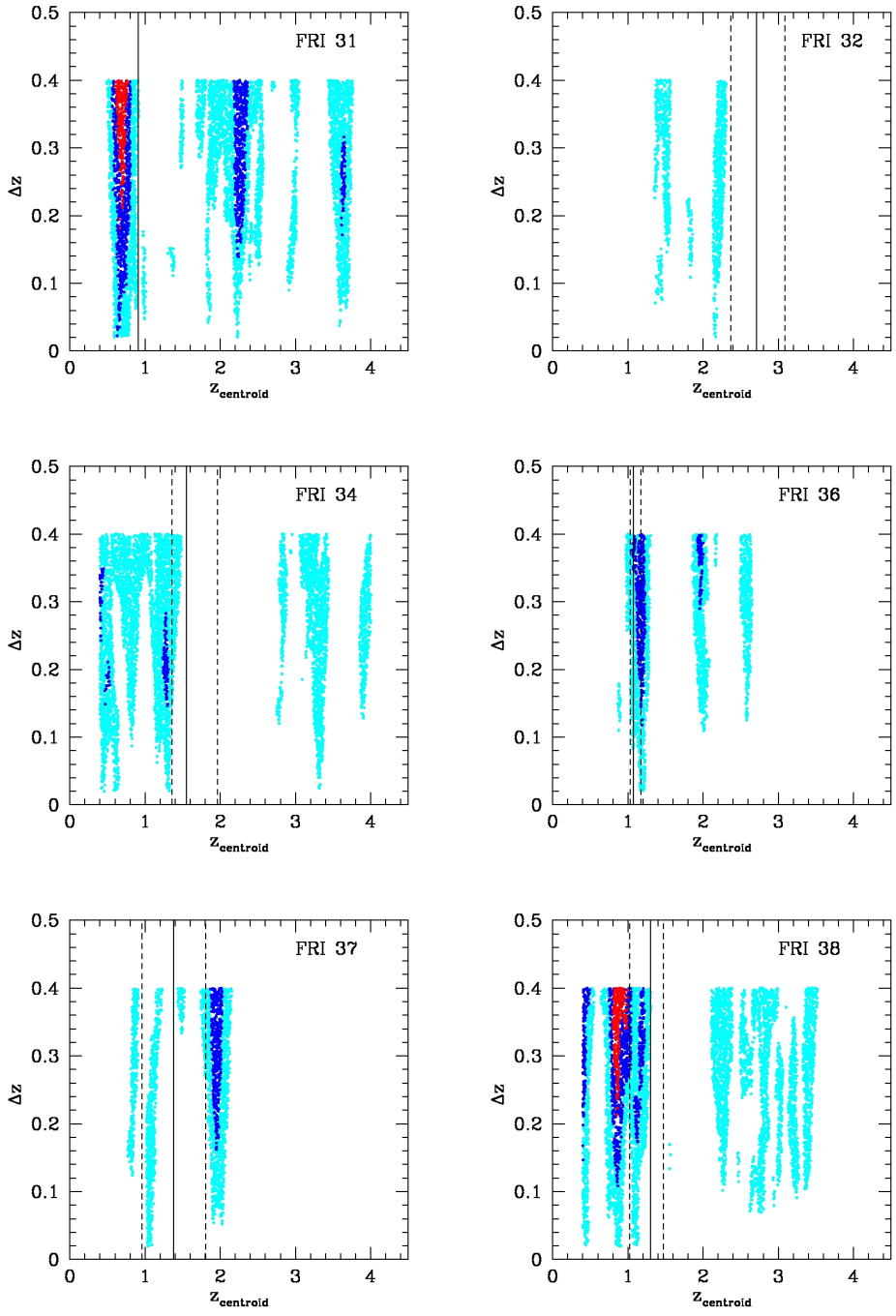

Figure A.1: Continued.

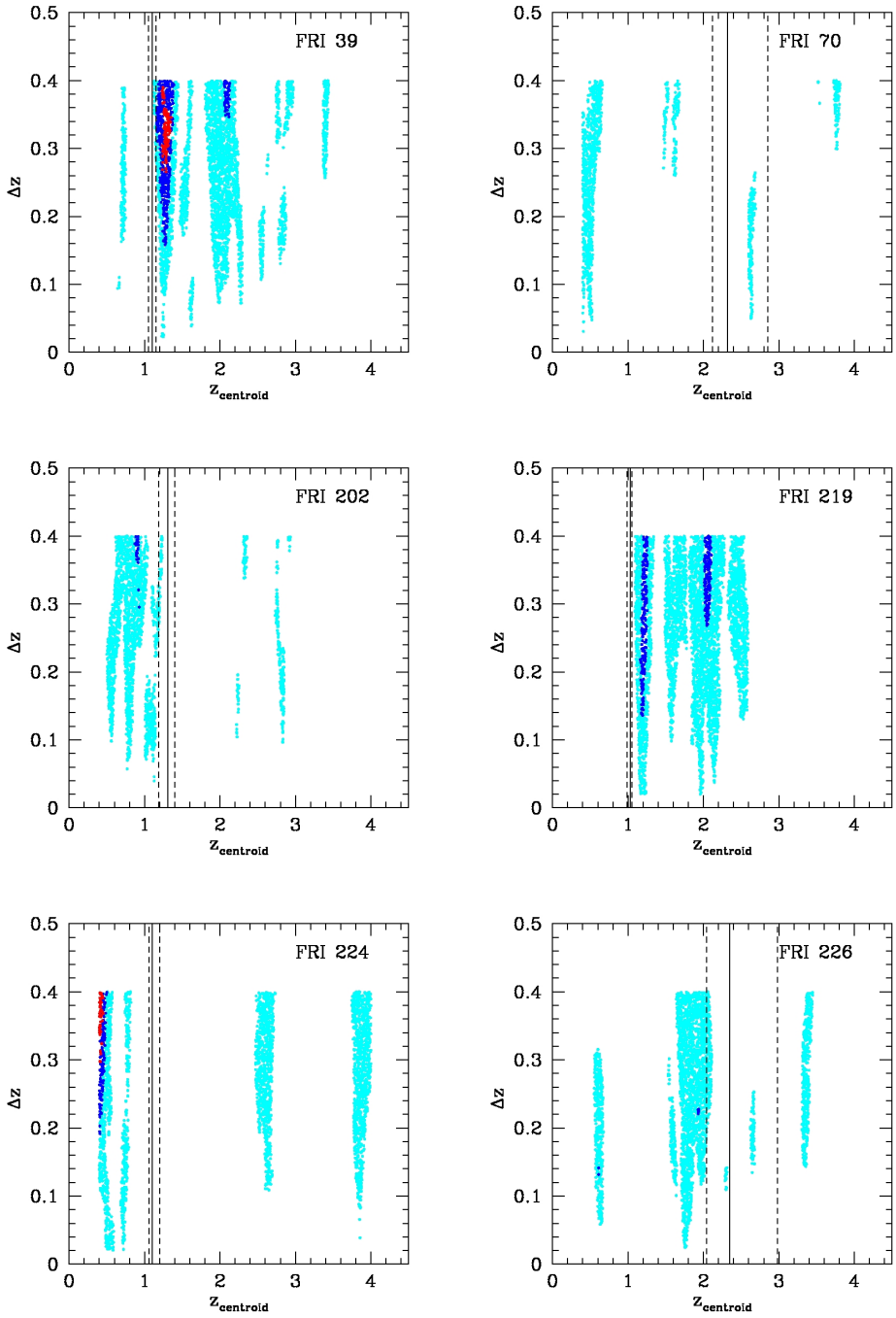

Figure A.1: Continued.

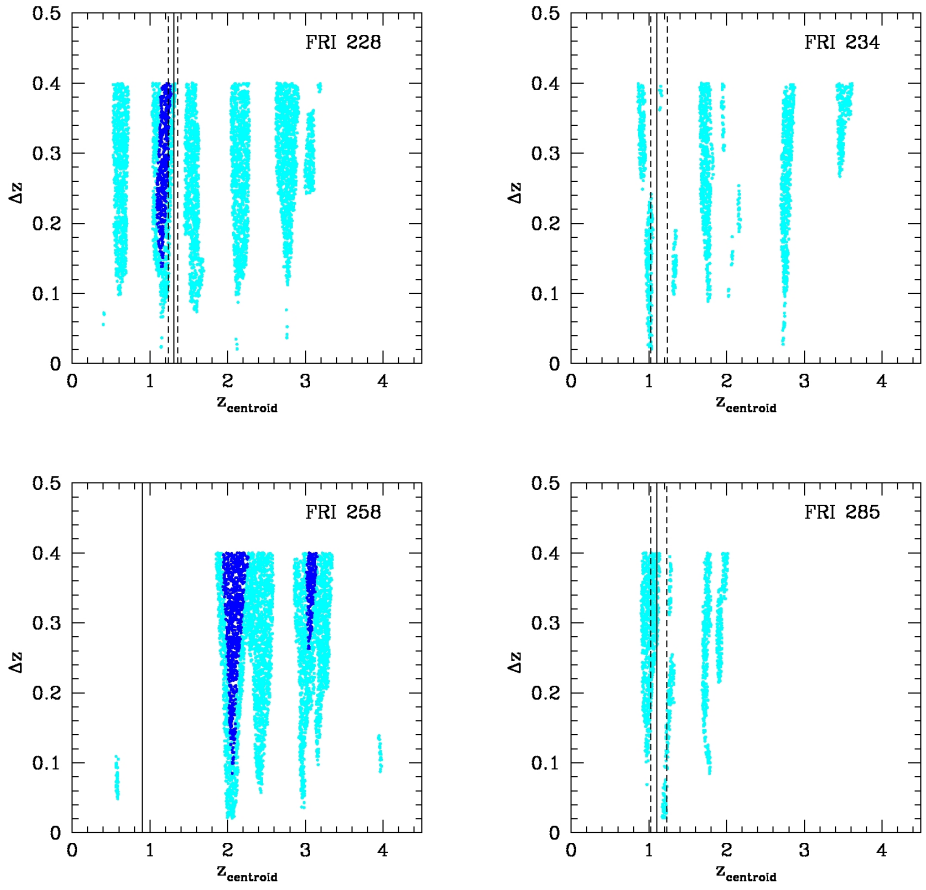

Figure A.1: Continued.

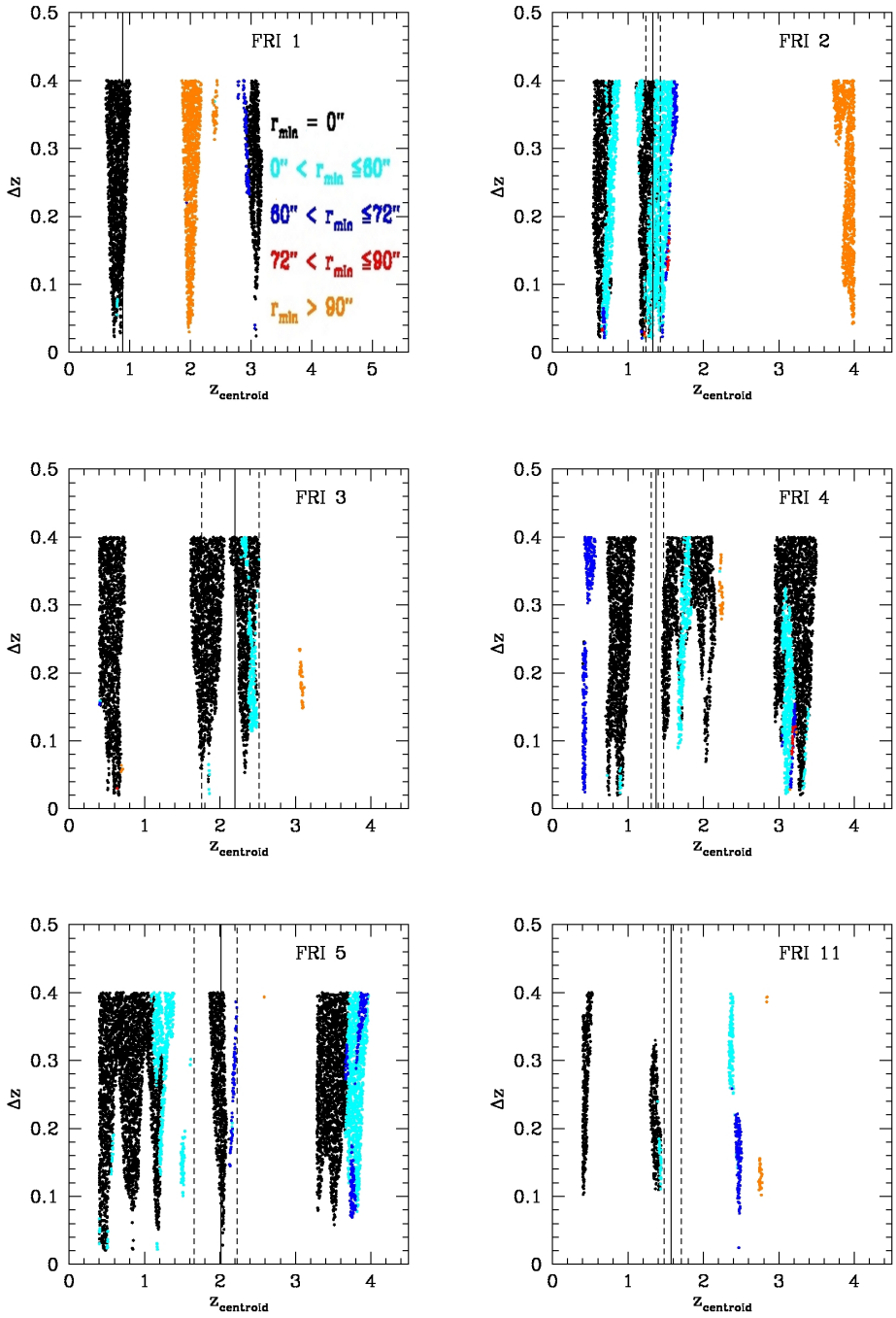

Figure A.2: PPM plots for the fields of the 32 FR I sources in our sample (see Section 5.2). The plots are the same as those in Figure A.1. Each point shows the radial cluster information concerning $r_{\rm min}$. See legend in the top left panel for information about the color code adopted. Different colors refer to different values of $r_{\rm min}$. Note that some colors may be absent in some panels.

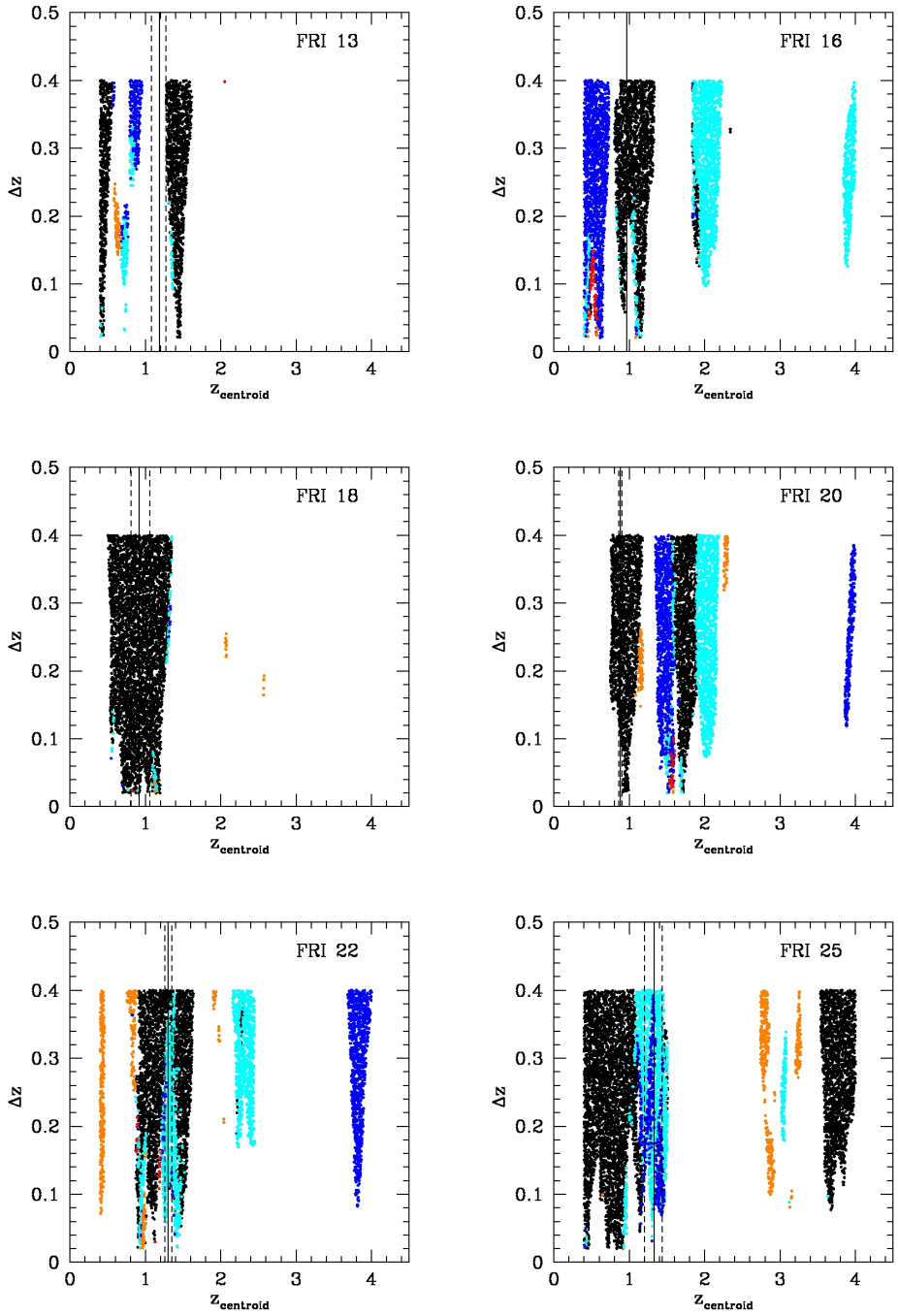

Figure A.2: Continued.

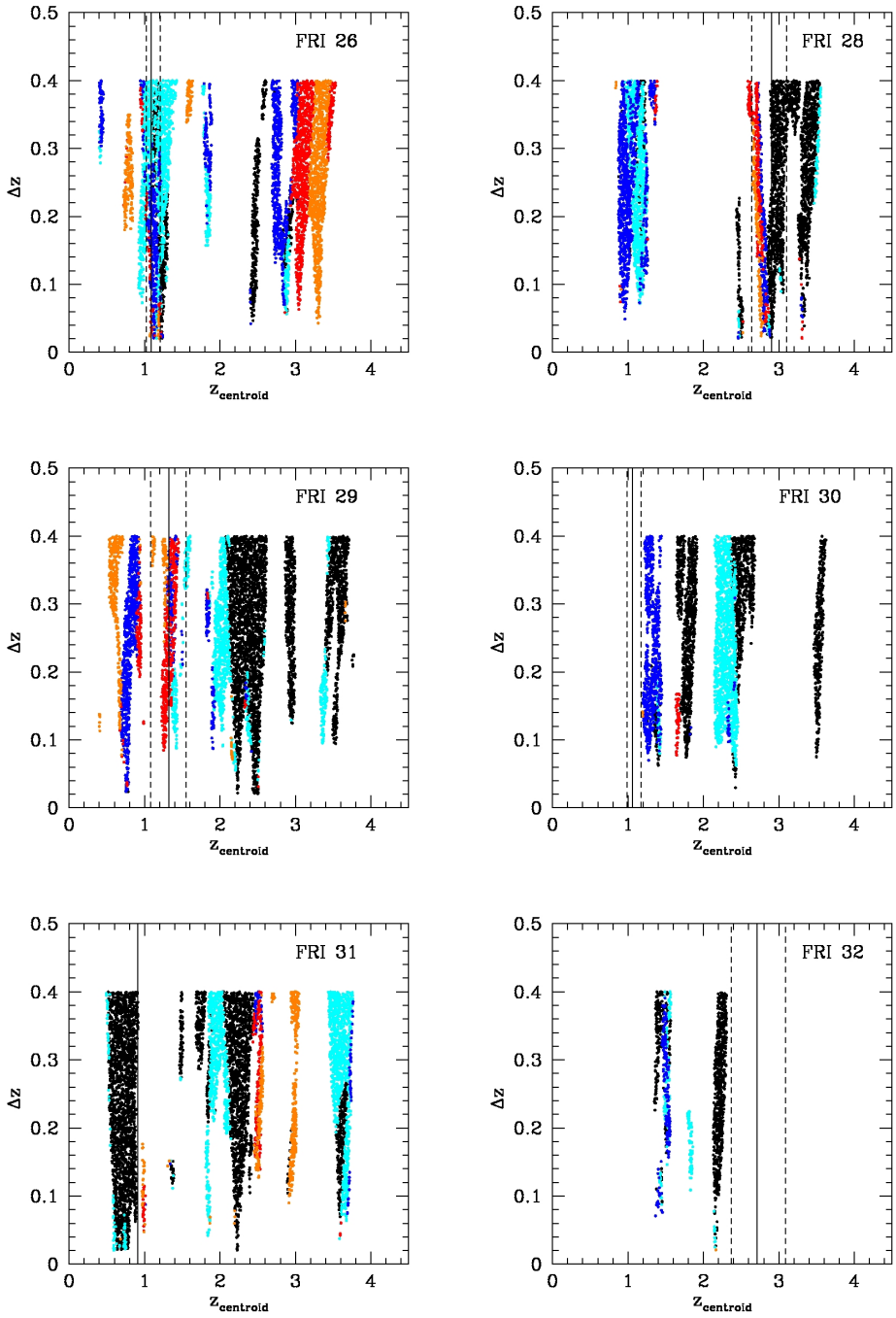

Figure A.2: Continued.

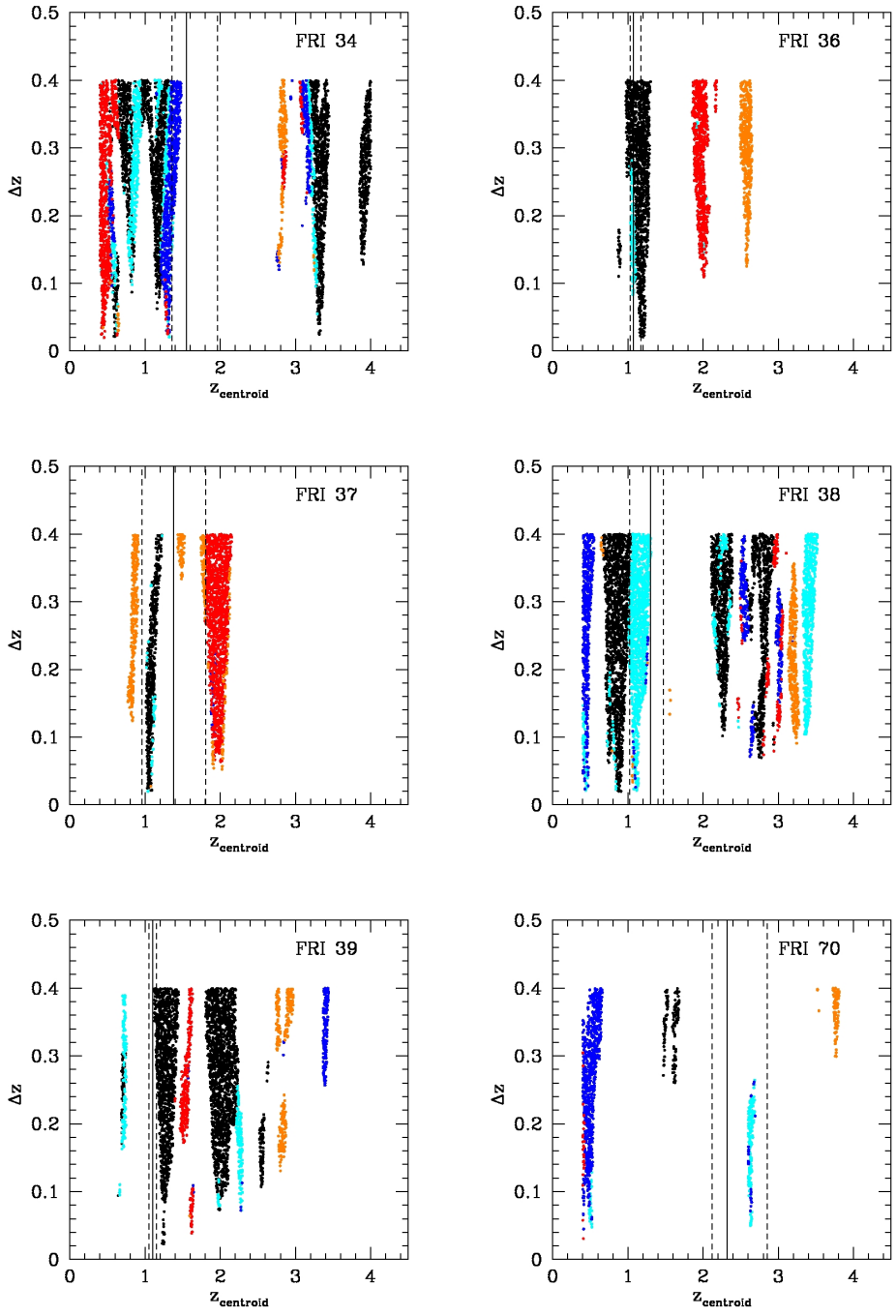

Figure A.2: Continued.

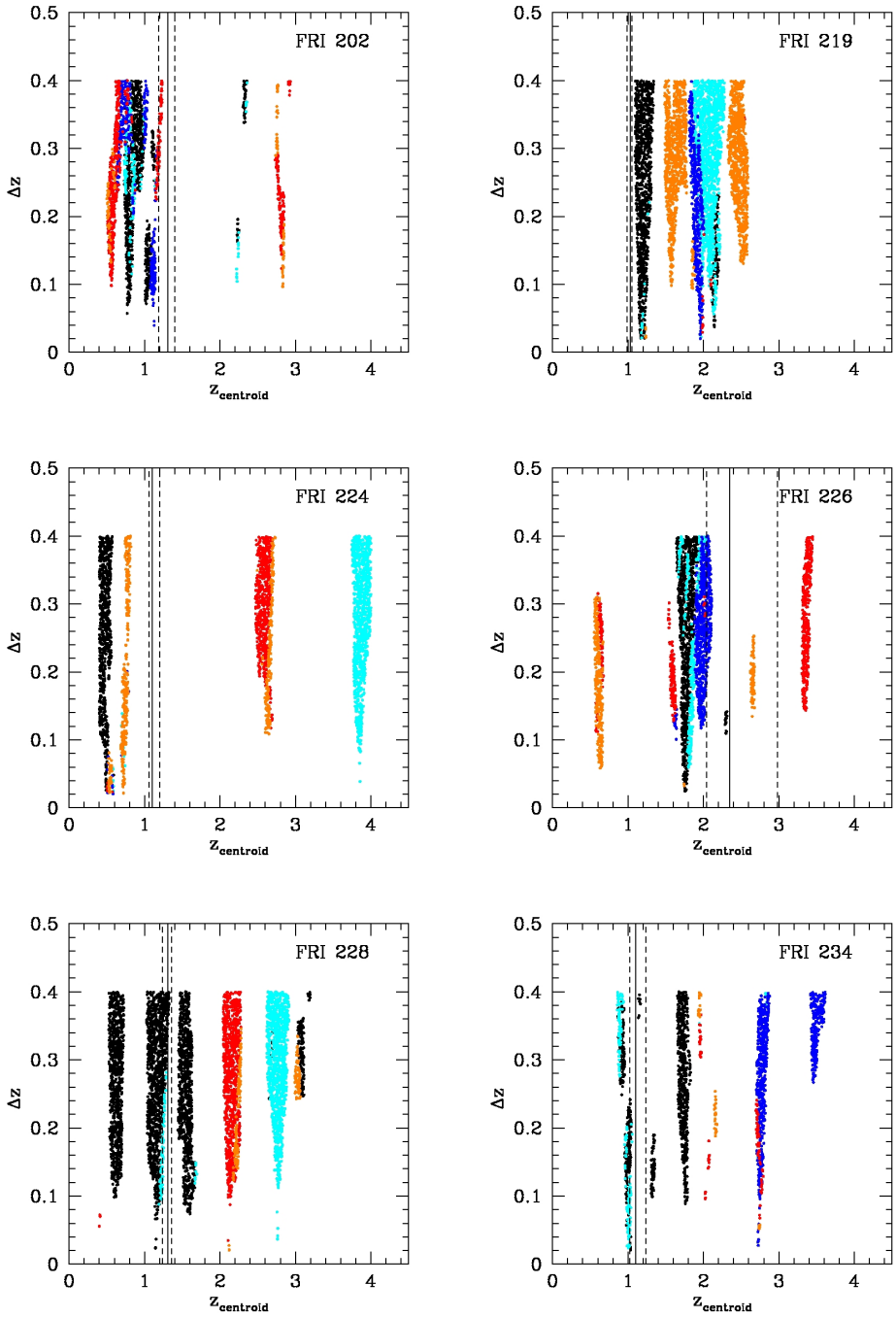

Figure A.2: Continued.

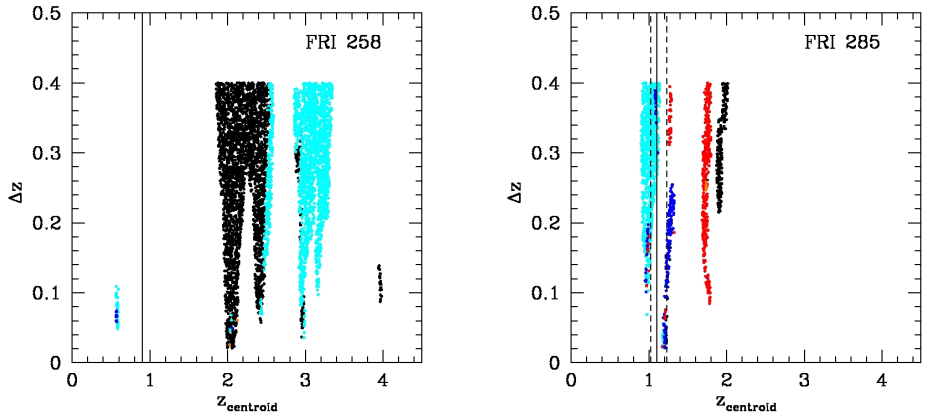

Figure A.2: Continued.

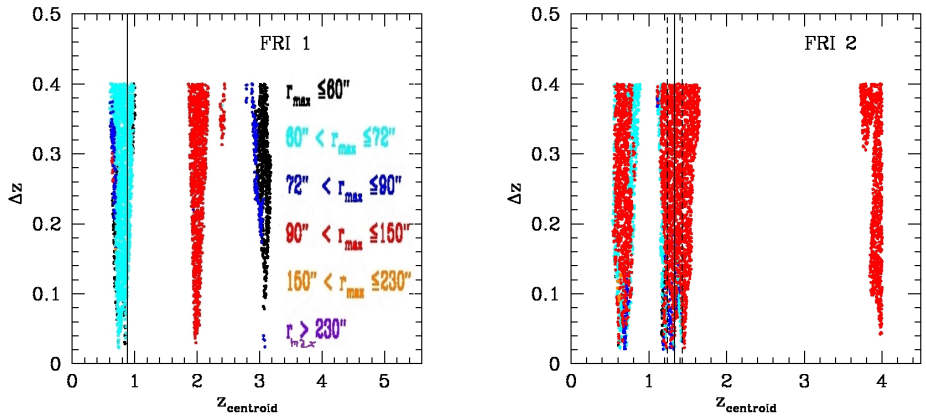

Figure A.3: PPM plots for the fields of the 32 FR I sources in our sample (see Section 5.2). The plots are the same as those in Figure A.1. Each point shows the radial cluster information concerning the fiducial cluster size $r_{\rm max}$. See legend in the left panel for information about the color code adopted. Different colors refer to different values of $r_{\rm max}$. Note that some colors may be absent in some panels.

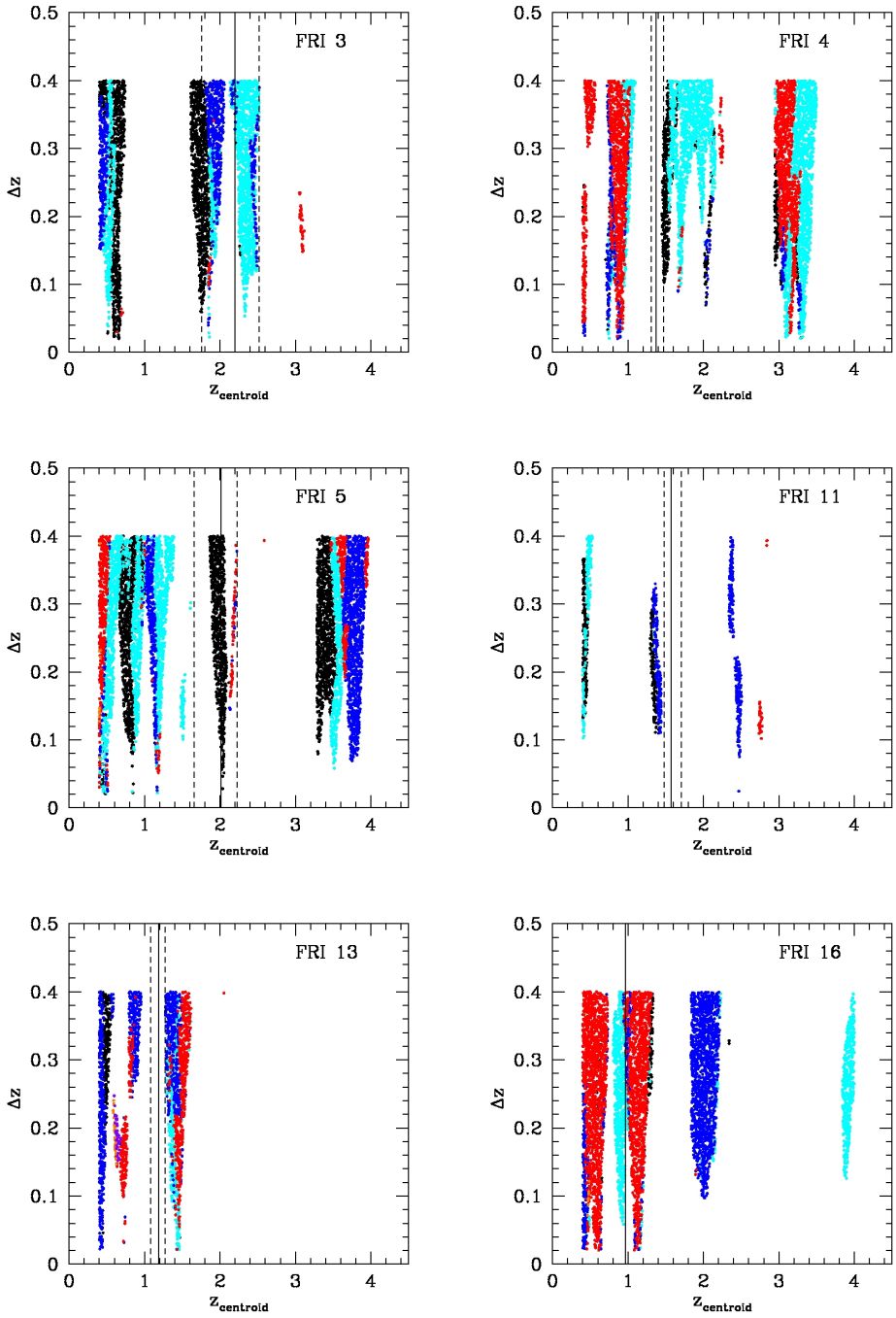

Figure A.3: Continued.

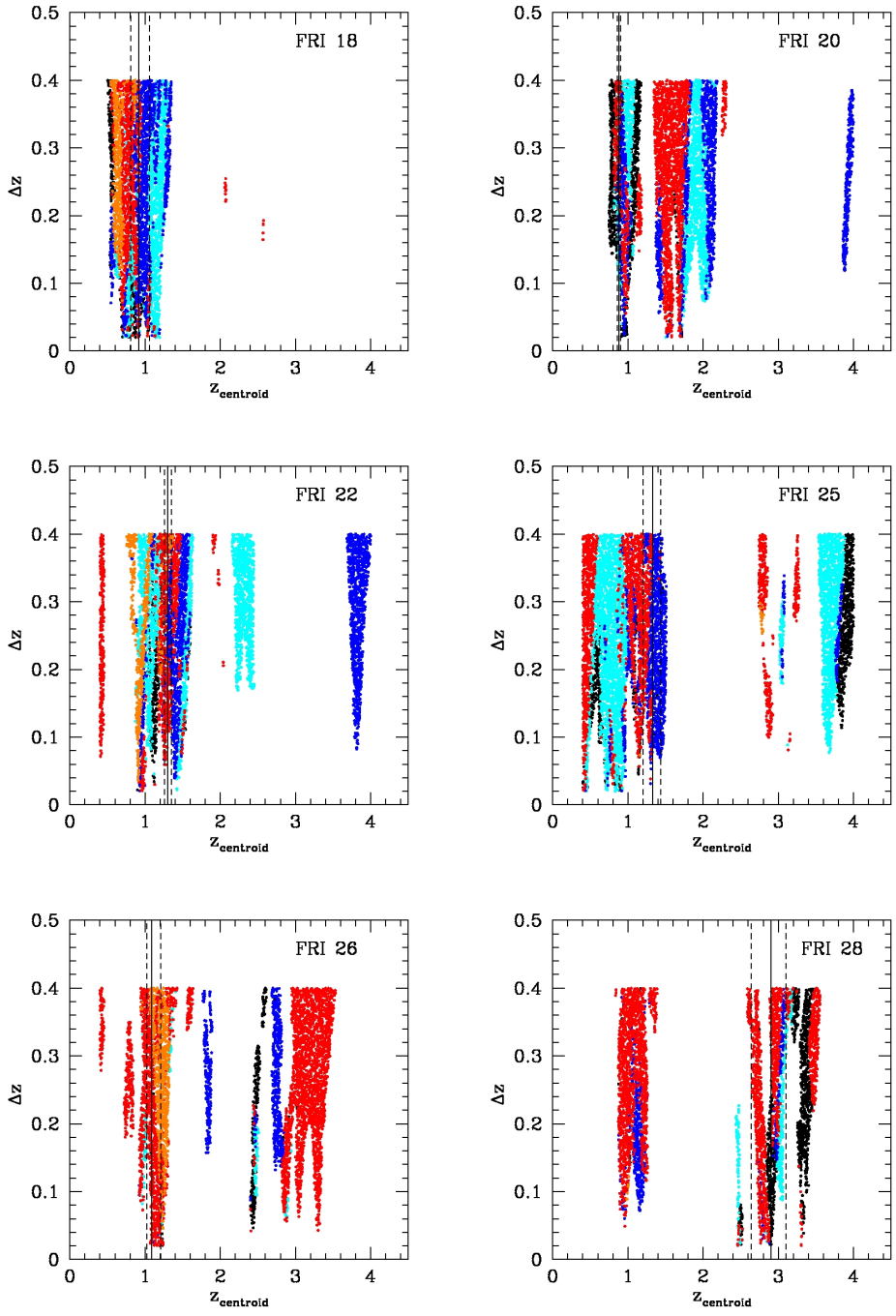

Figure A.3: Continued.

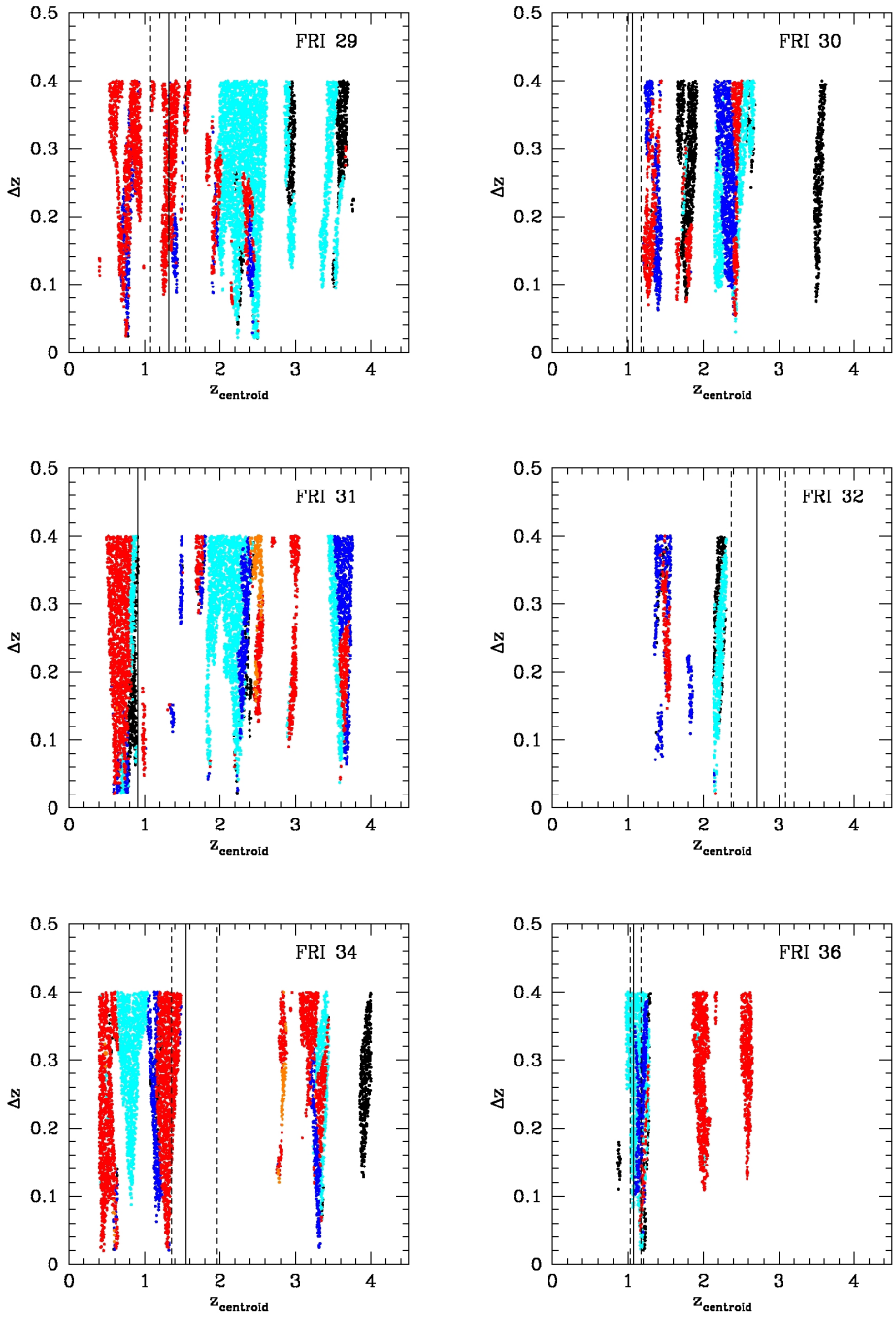

Figure A.3: Continued.

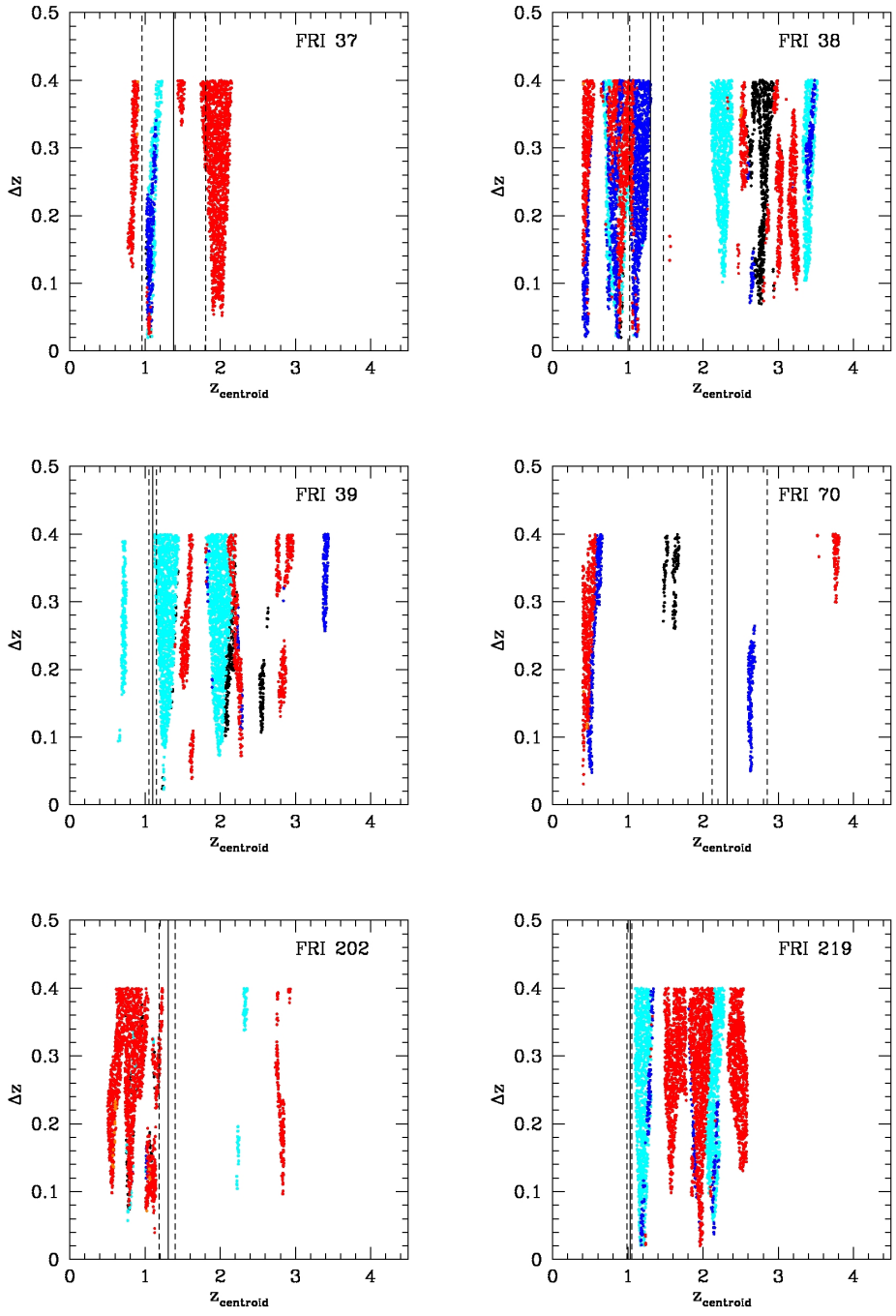

Figure A.3: Continued.

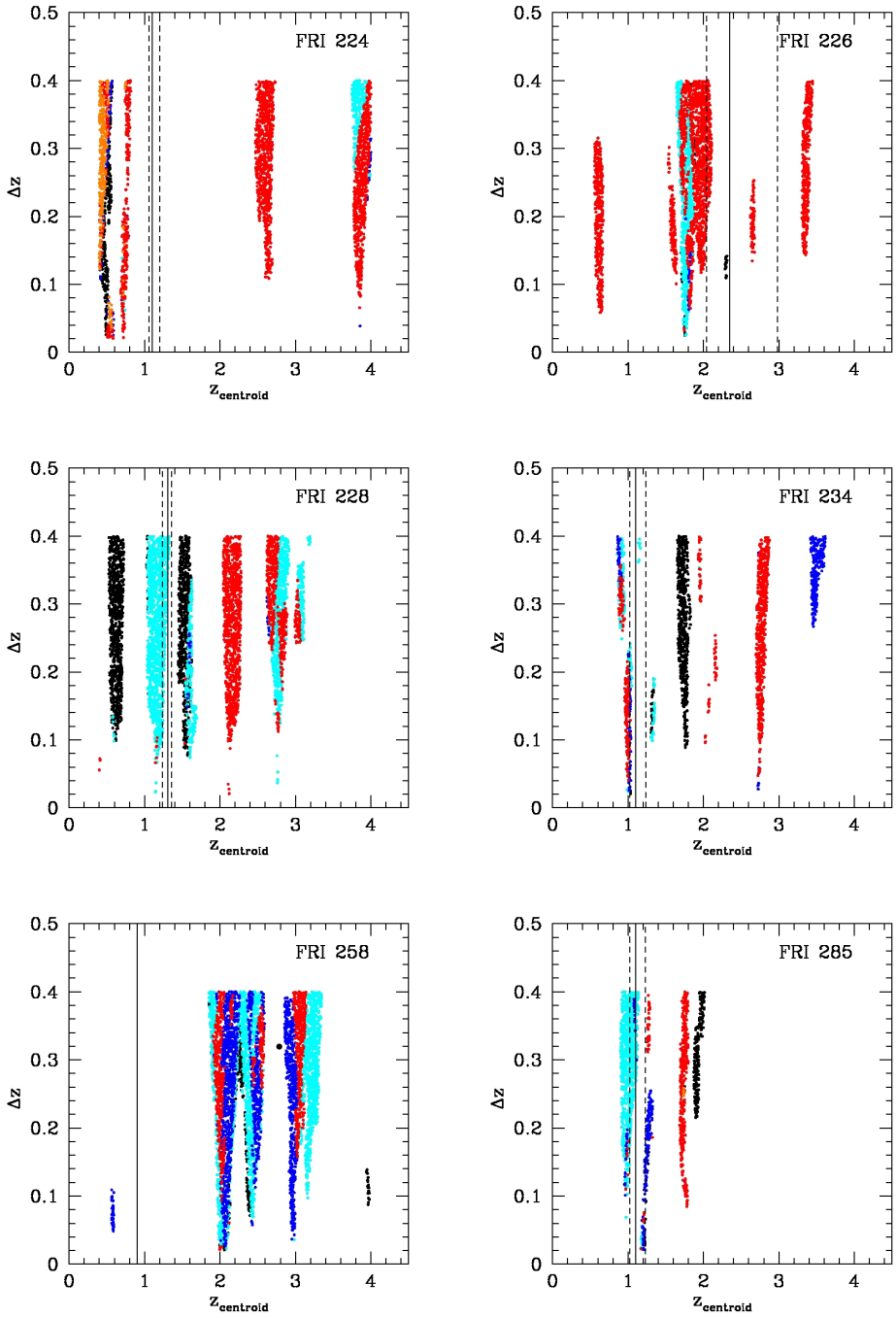

Figure A.3: Continued.

Appendix B

SEDs of FSRQs with big blue bump

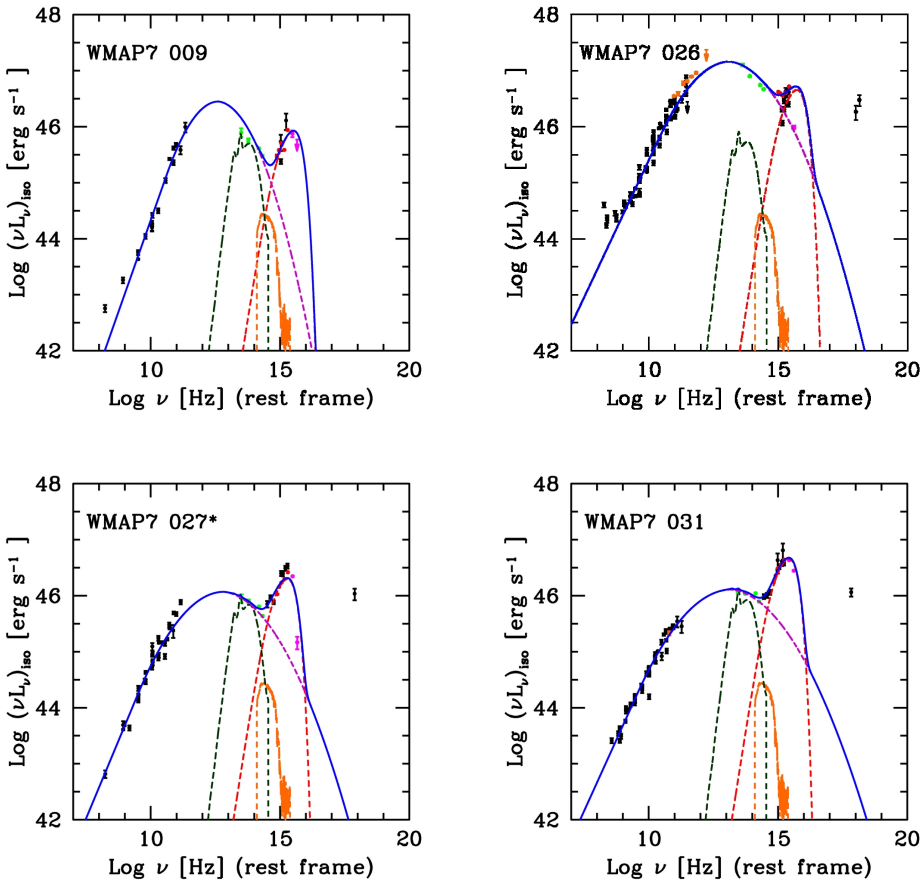

Figure B.1: SEDs for all 55 FSRQs in our sample within the SDSS area with evidence of optical/UV bump. Solid blue line: total SED, which includes synchrotron emission (dashed violet line, Donato et al., 2001), host galaxy (dashed orange line, Giommi et al., 2012b), disc (dashed red line, Shakura & Sunyaev, 1973) and torus (dark green dashed line, Hoenig & Kishimoto, 2010) emission templates. The host galaxy was taken to be a passive elliptical with $M_R = -23.7$. Data points: Planck (orange); WISE (green); SDSS (red); GALEX (magenta). Black points are data taken from the NASA/IPAC Extragalactic Database (NED). Note that, at variance with what was done to compute both $L_{\rm disc}$ and $L_{\rm torus}$ (see text), the luminosities shown here are computed assuming isotropic emission. The 22 objects without evidence of torus emission for which the χ^2 minimization did not yield meaningful upper limits are flagged with an asterisk.

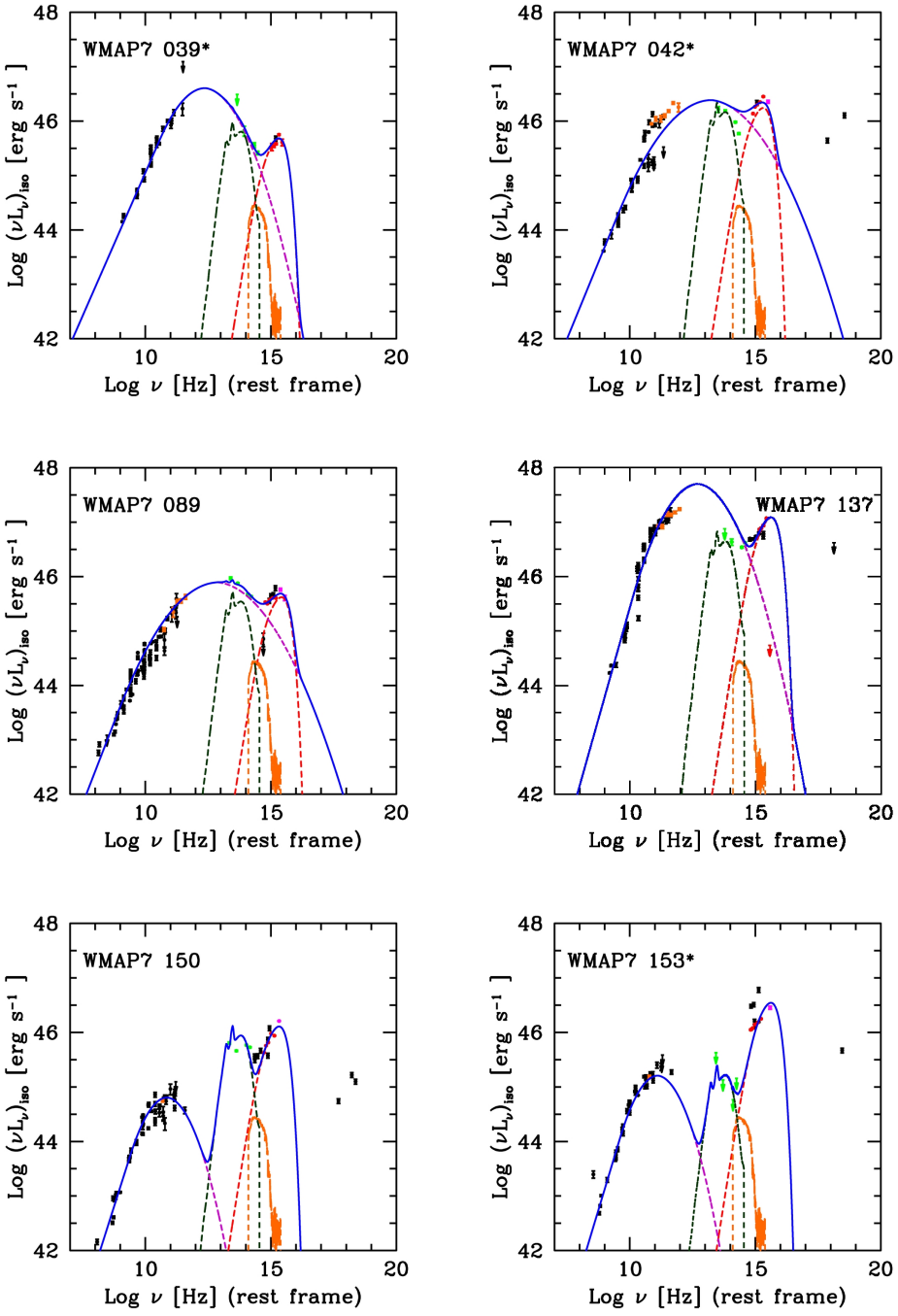

Figure B.1: Continued.

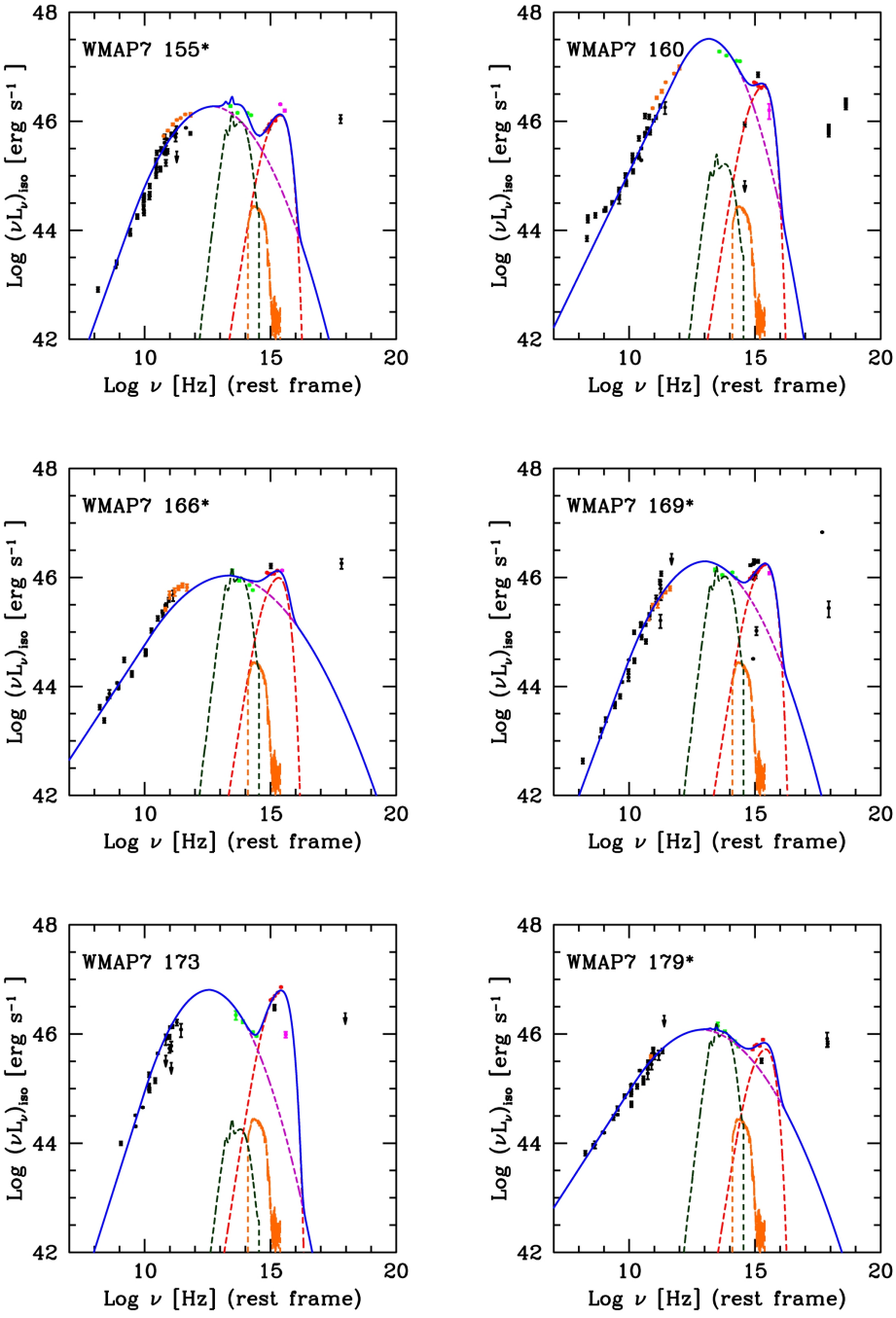

Figure B.1: Continued.

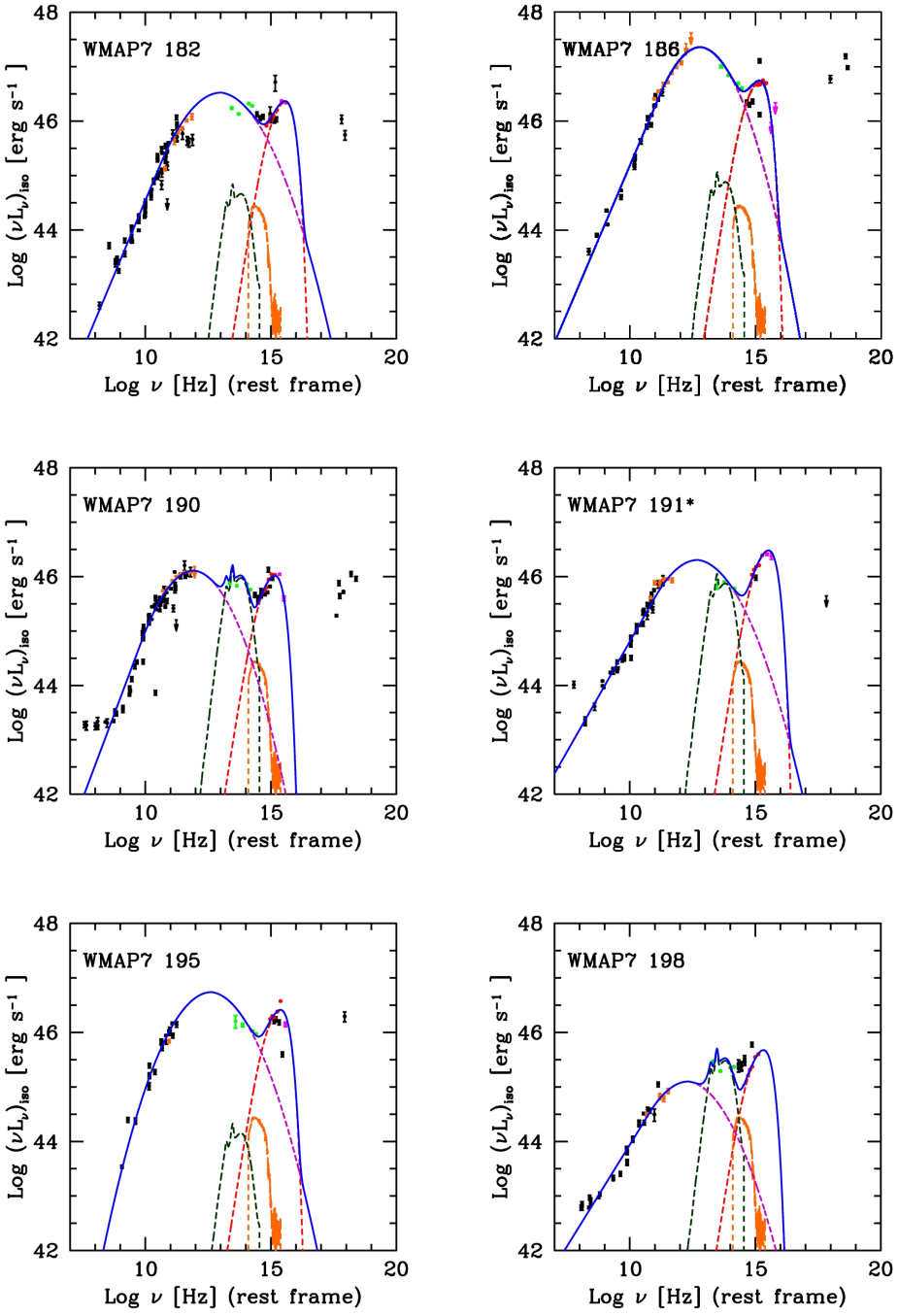

Figure B.1: Continued.

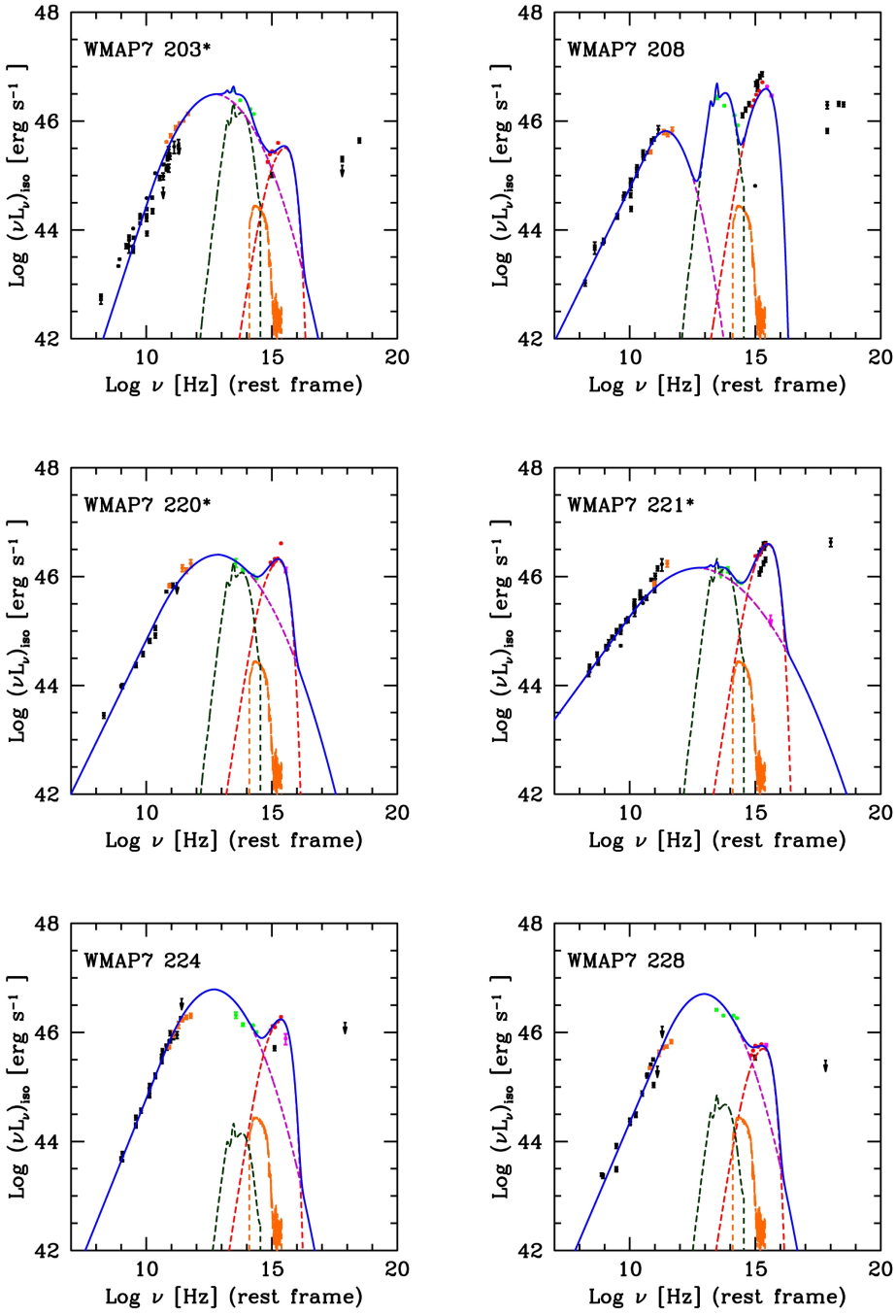

Figure B.1: Continued.

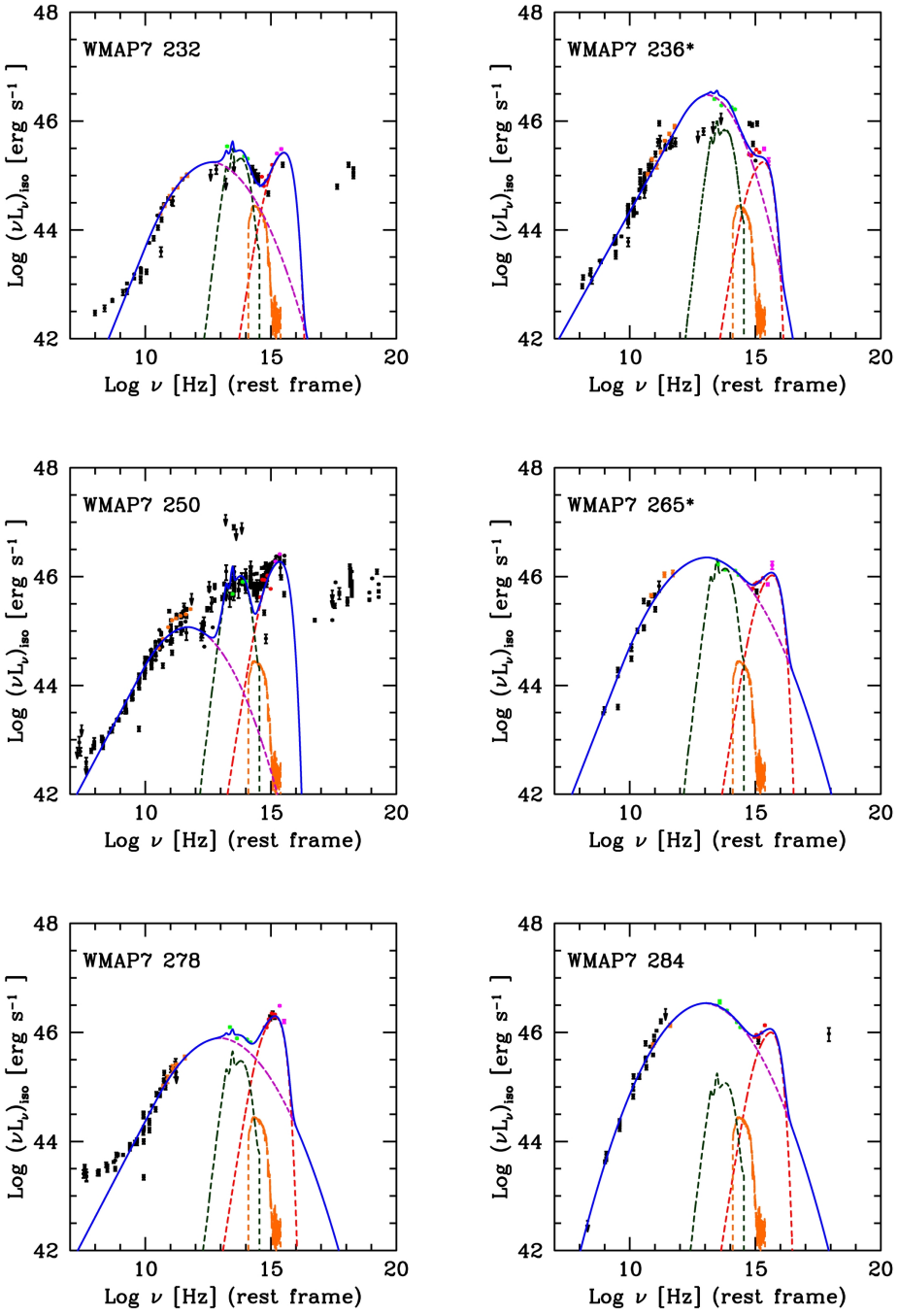

Figure B.1: Continued.

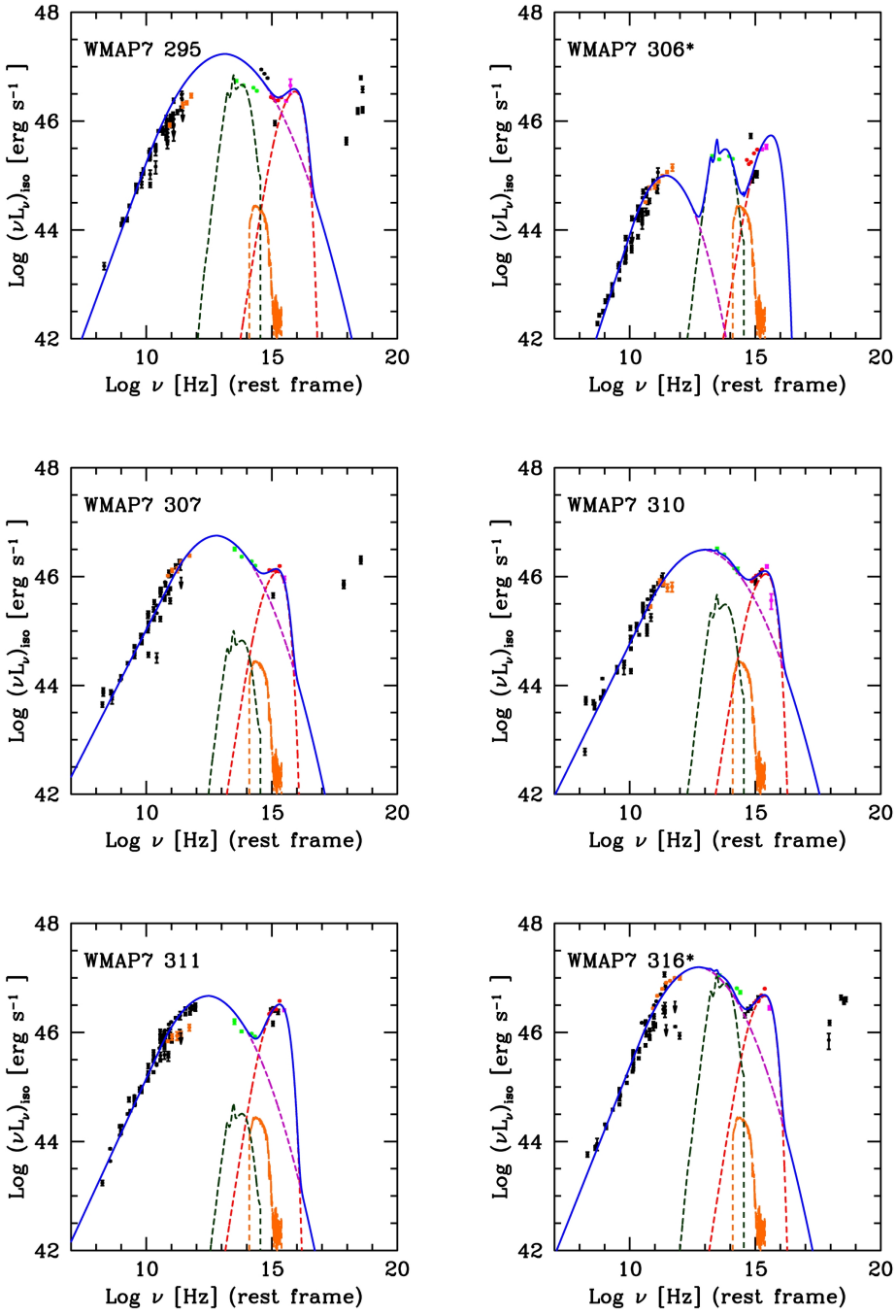

Figure B.1: Continued.

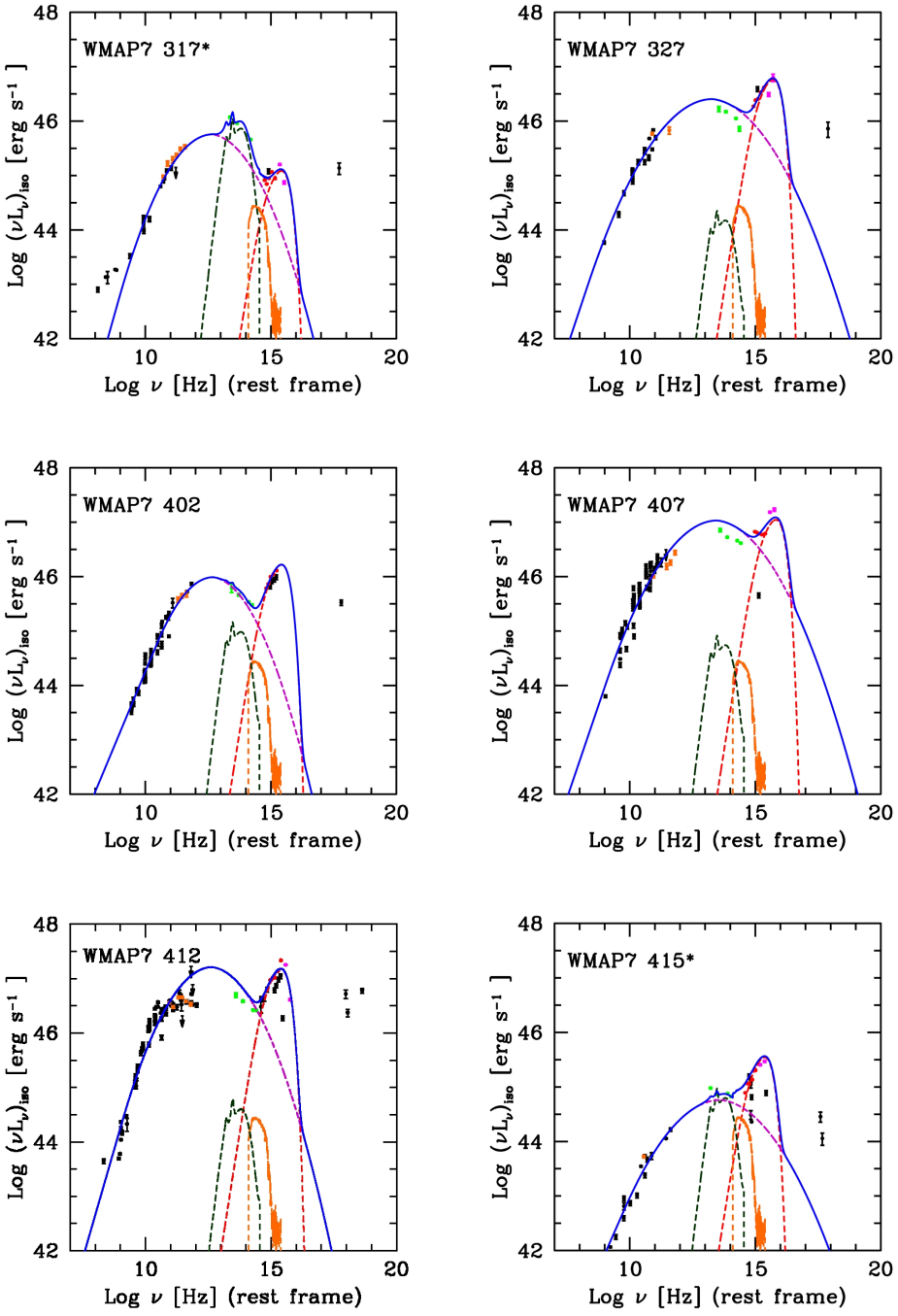

Figure B.1: Continued.

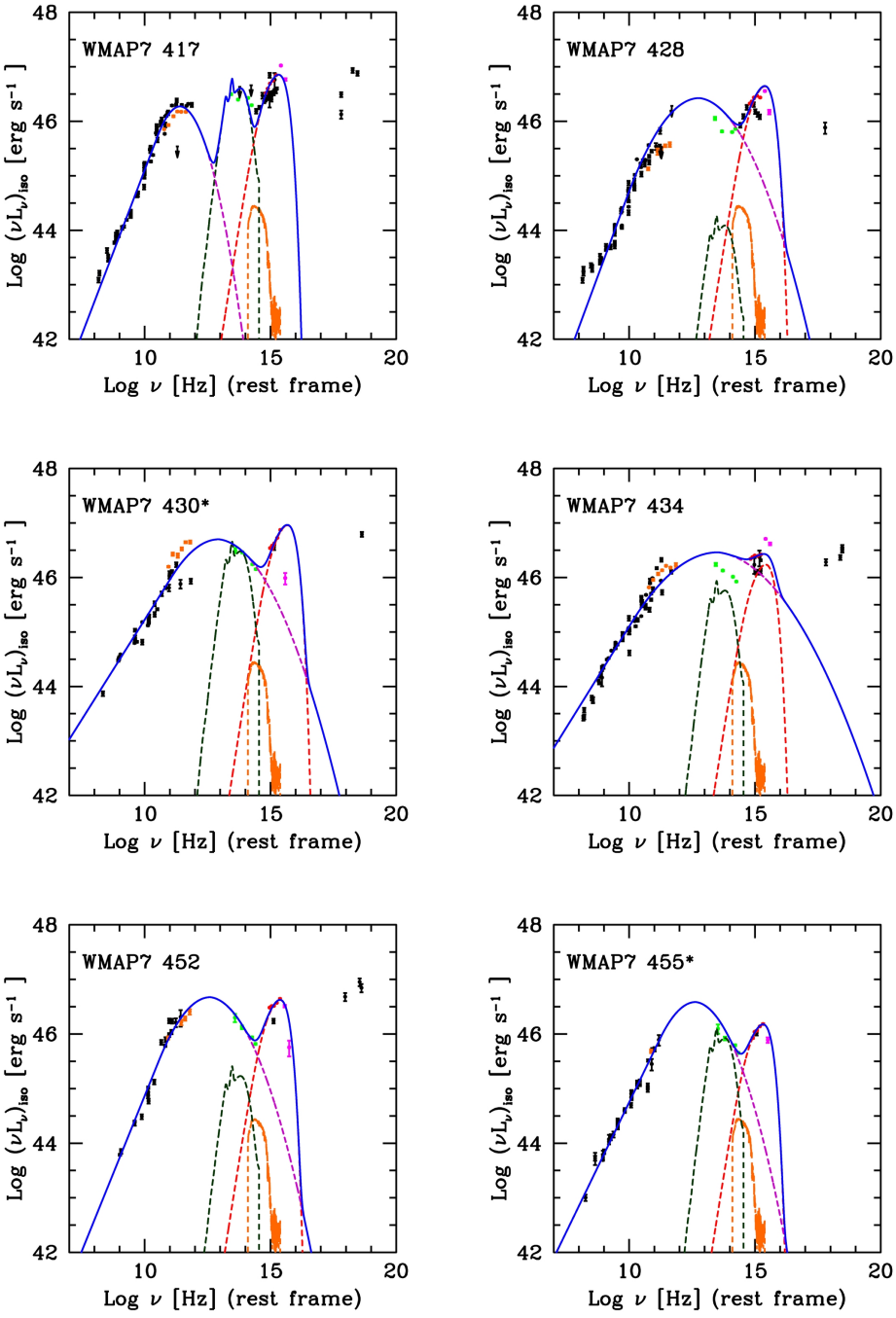

Figure B.1: Continued.

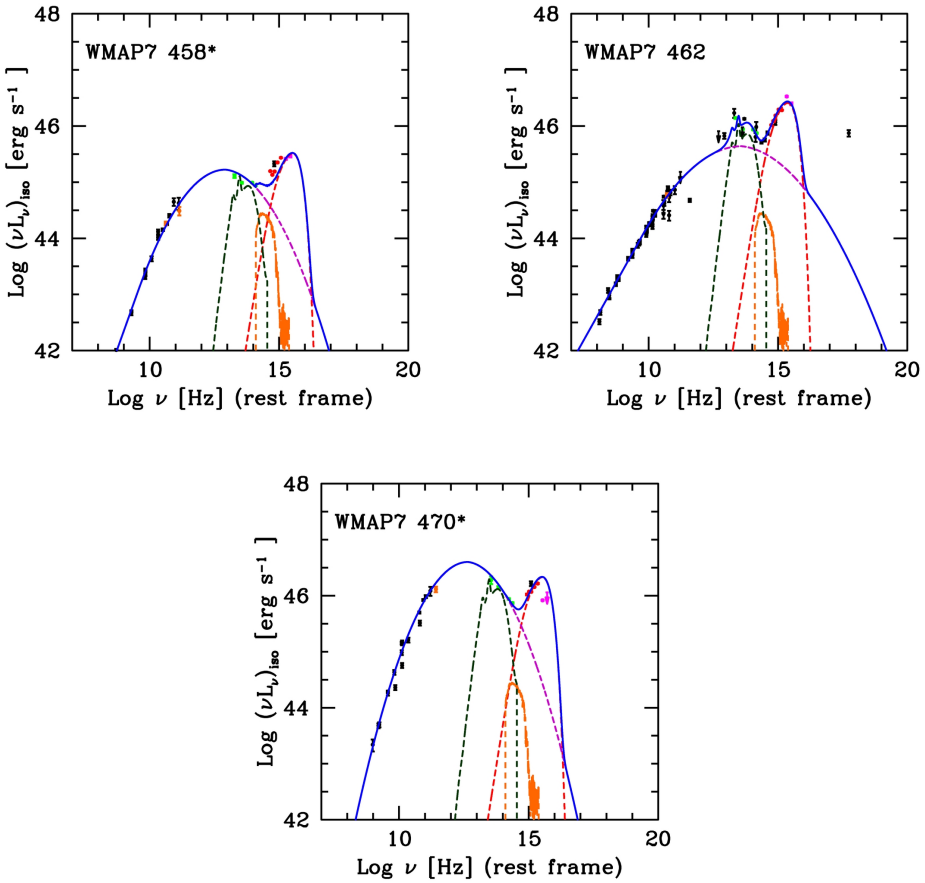

Figure B.1: Continued.

A thank-you note

Ringrazio i miei genitori, per avere avuto sempre fiducia in me, per essermi stati sempre vicino ed avermi aiutato nei momenti di difficoltà. Dedico a voi questa tesi.

Un ringraziamento speciale ad alcuni dei miei amici che mi hanno accompagnato in questa avventura.
A Daniele, per aver condiviso con me alcune tra le piú intense esperienze di vita di questi ultimi anni.
Ad Eolo, amico sempre presente nella quotidianità in questi lunghi anni del dottorato.
A Luca, per la sua amicizia antica.
Ad Alessandro ed Andrea, per le peripezie vissute assieme e le discese facili.

Bibliography

Abazajian, K., Adelman-McCarthy, J. K., Agüeros, M. A., et al., 2004, AJ, 128, 502

Abdo, A. A., Ackermann, M., Ajello, M., et al., 2009a, ApJ, 699, 976

Abdo, A. A., Ackermann, M., Ajello, M., et al., 2009b, ApJ, 707, 727

Abdo, A. A., Ackermann, M., Ajello, M., et al., 2010a, ApJ, 710, 1271

Abdo, A. A., Ackermann, M., Ajello, M., et al., 2010b, ApJ, 715, 429

Abramowicz, M. A., Czerny, B., et al., 1988, ApJ, 332, 646

Abramowicz, M. A., Fragile, P. C., 2013, LRR, 16, 1

Acciari, V. A., et al, 2009a, Science, 325, 444

Acciari, V. A., et al., ApJ, 2009b, 703, 169-178

Acero, F., Aharonian, F., Akhperjanian, A. G., et al., 2009, Science, 326, 1080

Adami, C., Durret, F., Benoist, C., Coupon, J., et al., 2010, A&A, 509, 81

Adami, C., Mazure, A., Pierre, M., et al., 2011, A&A, 526, 1

Adami, C., Durret, F., et al., 2013, A&A, 551, 20

Aharonian, F. A., 2000, New Astron., 5, 377

Aharonian F. et al., 2007, ApJ, 664, 71

Aird, J., Nandra, K., Laird, E. S., et al., 2010, MNRAS, 401, 2531

Albert, J. et al., 2007, ApJ, 669, 862

Ajello, M., Shaw, M. S., Romani, R. W., et al., 2012, ApJ, 751, 108

Ajello, M., Romani, R. W., et al., 2014, ApJ, 780, 73

Alberts, S., Pope, A., Brodwin, M., et al., 2013, MNRAS, 2563

Albeverio, S., Kondratiev, Y., and Röckner, M., 1996, CRAS, 323, 1129

Aleksić, J., Ansoldi, S., Antonelli, L. A., et al. 2014, A&A, 564, 5

Allen, S. W., Evrard, A. E., Mantz, A. B., 2011, ARA&A, 49, 409

Alonso-Herrero, A., mos Almeida, C., et al., 2011, ApJ, 736, 82

Antonucci, R., 1984, ApJ, 278, 499

Antonucci, R. R. J., & Miller, J. S., 1985, ApJ, 297, 621

Antonucci, R., 1993, ARA&A, 31, 473

Ashman, K. M., Bird, C. M., Zepf, S. E., 1994, AJ, 108, 2348

Assef, R. J., Frank, S., Grier, C. J., et al., 2012, ApJL, 753, 2

Baan, W. A., & McKee, M. R., 1985, A&A, 143, 136

Bahcall, N. A., Dong, F., et al., 2003, ApJ, 599, 814

Balbus, S. A., & Hawley, J. F., 1991, ApJ, 376, 214

Baldi, R. D., Chiaberge, M., et al., 2010, ApJ, 725, 2426

Baldi, R. D., Chiaberge, M., et al., 2013, ApJ, 762, 30 (B13)

Banerji, M., Chapman, S. C., Smail, I., et al., 2011, MNRAS, 418, 1071

Barone-Nugent, R. L., Wyithe, J. S. B., et al., arXiv1303.6109

Barthel, P. D., 1989, ApJ, 336, 606

Bassett, R., Papovich, C., et al., 2013, ApJ, 770, 58

Baum, S. A., & O'Dea, C. P., 1991, MNRAS, 250, 737

Becker, R. H., White, R. L., & Helfand, D. J., 1995, ApJ, 450, 559

Begelman, M. C., Rees, M. J., & Blandford, R. D., 1979, Nature, 279, 770

Begelman, M., et al., 1984, Rev. Mod. Phys., 56, 255

Begelman, M., et al., 1994, ApJ, 429, 57

Begelman, M. C., 1996, in Cygnus A: Study of a Radio Galaxy, eds C. L. Carilli & D. A. Harris (Cambridge: Cambridge University Press), 209

Begelman, M. C., & Li, Z.-Y., 1994, ApJ, 426, 269

Benn, C. R., Rowan-Robinson, M., McMahon, R. G., et al., 1993, MNRAS, 263, 98

Bennert, N., Jungwiert, B., et al., 2006, A&A, 459, 55

Benson, B. A., de Haan, T., Dudley, J. P., 2013, ApJ, 763, 147

Bentz, M. C., Peterson, B. M., Pogge, R. W., & Vestergaard, M., 2009, ApJL, 694, 166

Bertin, E., & Arnouts, S., 1996, A&AS, 117, 393

Best, P. N., von der Linden, A., et al., 2007, MNRAS, 379, 894

Bianchi, S., & Matt, G., 2002, A&A, 387, 76

Bianchi, S., Maiolino, R., & Risaliti, G., 2012, AdAst, 2012, 17

Bicknell, G. V., de Ruiter, H. R., et al., 1990, ApJ, 354, 98

Bicknell, G. V., 1994, ApJ, 422, 542

Bicknell, G. V., 1995, ApJS, 101, 29

Bicknell, G. V., Sutherland, R. S., et al., 2000, ApJ, 540, 678

Bird, C. M., 1994, AJ, 107, 1637

Blandford, R. D., & McKee, C. F., 1982, ApJ, 255, 419

Blandford, R. D., Rees, M. J., 1978, Pittsburqh Conference on BL Lac Objects, ed. A. M. Wolfe, p. 328. Univ. Pittsburgh Press

Blandford, R. D., & Znajek, R. L., 1977, MNRAS, 179, 433

Bloom, S. D., & Marscher, A. P., 1996, ApJ, 461, 657

Blumenthal, G., & Miley, G., 1979, A&A, 80, 13

Bode, P., Bahcall, N. A., et al., 2001, ApJ, 551, 15

Bogdán, Á, Kraft, R. P., et al., 2011, ApJ, 743, 59

Bogdanović, T., Reynolds, C. S., et al., 2009, ApJ, 704, 211

Boehringer, H., et al., 1993, MNRAS, 264, 25

Böhringer, H., Schuecker, P., Guzzo, L., et al., 2004 A&A, 425, 367

Boller, T. H., Brandt, W. N., Fabian, A. C., & Fink, H., 1997, MNRAS, 289, 393

Bolton, J. G., Stanley, G. J., Slee, O. B., 1949, Nature, 164, 101

Bonnoli, G., Ghisellini, G., Foschini, L., et al., 2011, MNRAS, 410, 368

Bott, R., 1960, Morse Theory and Its Applications to Homotopy Theory: Lectures by R. Bott. Bonn, Germany: Universität Bonn.

Böttcher, M., 2010, in proc. Fermi Meets Jansky, MPIfR, Bonn, Eds. T. Savolainan, E. Ros, R. W. Porcas, & J. A. Zensus, p. 41

Bower, G. A., et al. 1998, ApJ, 492, 111

Branchesi, M., Gioia, I. M., Fanti, C., et al., 2006 A&A, 446, 97

Brodwin, M., Stern, D., Vikhlinin, A., et al., 2011, ApJ, 732, 33

Brodwin, M., Gonzalez, A. H., Stanford, S. A., et al., 2012, ApJ, 753, 162

Brodwin, M., Stanford, S. A., Gonzalez, A. H., et al., 2013, ApJ, 779, 138

Brown, M. J. I., Webster, R. L., & Boyle, B. J., 2001, AJ, 121, 2381

Burns, J. O., AJ, 99, 14

Buttiglione, S., Capetti, A., et al., 2010, A&A, 509, A6

Cabanac, R. A., Alard, C., Dantel-Fort, M., et al. 2007, A&A, 461, 813

Calderone, G., Sbarrato, T., & Ghisellini, G., 2012, MNRAS, 425, 41

Calderone G., Ghisellini G., Colpi M., Dotti M., 2013, MNRAS, 431, 210

Capak, P., et al. 2007, ApJS, 172, 99

Capak, P. L., Riechers, D., Scoville, N. Z., et al. 2011, Nature, 470, 233

Cardelli, J. A., Clayton, G. C., & Mathis, J. S. 1989, ApJ, 345, 245

Carilli, C. L., Perley, R. A., & Harris, D. E., 1994, MNRAS, 270, 173

Casasola, V., Magrini, L., Combes, F., et al., 2013, A&A, 558, 60

Cash, W. 1976, A&A, 52, 307

Castignani, G., Castignani, G., Haardt, F., Lapi, A., et al., 2013, A&A, 560, 28

Castignani, G., Chiaberge, M., Celotti, A., & Norman, C. 2014a, ApJ, 792, 113

Castignani, G., Chiaberge, M., Celotti, A., Norman, C., & De Zotti, G., 2014b, ApJ, 792, 114

Castignani, G., & De Zotti, G., 2014, A&A, in press, arXiv:1410.2716 preprint

Castignani, G., Fritz, A., Chiaberge, M., et al., in preparation

Cavaliere, A. & Fusco-Fermiano, R., 1978, A&A, 70, 677

Cavaliere, A. & D'Elia, V., 2002, ApJ, 571, 226

Cellone, S. A., et al., 2007, MNRAS, 374, 357

Celotti, A., Ghisellini, G., & Chiaberge, M., 2001, MNRAS, 321, 1

Chambers, K. C., Miley, G. K., & van Breugel, W., 1987, Nature, 329, 604

Chiaberge, M., Capetti, A., & Celotti, A., 1999, AA, 349, 77

Chiaberge, M., 2000, PhD thesis, 2000, SISSA,`http://digitallibrary.sissa.it/handle/1963/5448`

Chiaberge, M., Tremblay, G., Capetti, A., et al., 2009, ApJ, 696, 1103 (C09)

Chiaberge, M., Capetti, A., Macchetto, F. D., et al., 2010, ApJ, 710, 107 (C10)

Chiaberge, M., & Marconi, A., 2011, MNRAS, 416, 917

Chiang, J., Fichtel, C. E., et al., 1995, ApJ , 452, 156

Chiang, Y.-K., Overzier, R., & Gebhardt, K., ApJ, 779, 127

Clearly, K., Lawrence, C. R., et al., 2007, ApJ, 660, 117

Clewley, L., Jarvis, M. J., 2004, MNRAS, 352, 909

Cohen, M. H., Ogle, P., et al., 1999, AJ, 118, 1963

Comastri, A., 2004, Review for "Supermassive Black Holes in the Distant Universe", Ed. A. J. Barger, Kluwer Academic.

Condon, J. J., Cotton, W. D., Greisen, E. W., et al. 1998, AJ, 115, 1693

Cooray, A. & Sheth, R., PhR, 372, 1

Coupon, J., Ilbert, O., Kilbinger, M., et al., 2009, A&A, 500, 981

Croom, S. M., 2011, ApJ, 736, 161

Cruddace, R., Voges, W., Böhringer, H., et al., 2002, ApJS, 140, 239

Cutini, S., Lott, B., et al., 2014, AAS, 22311508

Cutri, R.M., Wright, E.L., Conrow, T., et al., 2013, `wise2.ipac.caltech.edu/docs/release/allsky/expsup/`

D'Ammando, F., Orienti, M., Finke, J., et al., 2013, MNRAS, 436, 191

D'Ammando, F., Larsson, J., Orienti, M., et al., 2014, MNRAS, 438, 3521

Dai, B. Z. et al., 2001, AJ, 122, 2901

Dai, X., Kochanek, C. S., & Morgan, N. D., 2007, ApJ, 658, 917

Dalal, N., White, M., Bond, J. R., Shirokov, A., 2008, ApJ, 687, 12

Dallacasa, D., Fanti, C., & Fanti, R. 1993, in Jets in Extragalactic Radio Sources, ed. H.-J. Roser & K. Meisenheimer (Heidelberg: Springer), 27

Dallacasa D., Fanti C., Fanti R., Schilizzi R. T., Spencer R. E., 1995, A&A, 295, 27

Dallacasa, D., Bondi, M., Alef, W., & Mantovani, M., 1998, A&ASS, 129, 219

Dallacasa, D., Orienti, M., Fanti, C., Fanti, R., Stanghellini, C., 2013, MNRAS, 433, 147

Daly, R. A., & Guerra, E. J., 2002, AJ, 124, 1831

Davies, R. I., Thomas, J., Genzel, R., et al., 2006, ApJ, 646, 754

Davies, R., Mark, D., et al., 2012, A&A, 537, 133

Davis, D. S. & Mushotzky, R. F., 1993, AJ, 105, 409

De Breuck, C., van Breugel, W., Minniti, D., Miley, G., et al., 1999, A&A, 352, 51

De Bruyn, A. G., 1990, in Compact Steep Spectrum and GHz Peaked Spectrum Radio Sources. ed. C. Fanti, R. Fanti, C. O'Dea, & R. Schilizzi, Bologna: Istituto di Radioastronomia, p206

Decarli, R., Dotti, M., & Treves, A., 2011, MNRAS, 413, 39

D'Elia, V., Perri, M., Puccetti, S., et al., 2013, A&A, 551, 142

Della Ceca, R., et al., 1994, ApJ, 430, 533

Dermer, C. D., & Schlickeiser, R., 1993, ApJ, 416, 458

De Rosa, G., Decarli, R., Walter, F., et al., 2011, ApJ, 739, 56

De Rosa, G., Venemans, B. P., Decarli, R., et al., 2014, ApJ, 790, 145

De Young, D. S., 1993, ApJ, 405, 13

De Young, D. S., 2001, The Physics of Extragalactic Radio Sources, Chicago University Press

Diener, C., Lilly, S. J., Knobel, C., Zamorani, G., et al., 2013, ApJ, 765, 109

Donato, D., Ghisellini, G., Tagliaferri, G., & Fossati, G., 2001, A&A, 375, 739

Donnarumma, I., et al., 2009, ApJ, 691, 13

Donoso, E., Best, P. N., & Kauffmann, G., 2009, MNRAS, 392, 617

Donoso, E., Li, C., Kauffmann, G., et al., 2010, MNRAS, 407, 1078

Donzelli, C. J., Chiaberge, M., Macchetto, F. D., Madrid, J. P., Capetti, A., & Marchesini, D.s, 2007, ApJ, 667, 780

Dopita, M. A., et al., A&A, 2014, 566, 41

Drake, C. L., Bicknell, G. V., McGregor, P. J., & Dopita, M. A. 2004, AJ, 128, 969

Drouart, G., De Breuck, C., et al., 2014, A&A, 566, 53

Dunlop, J. S., Peacock, J. A., 1990, MNRAS, 247, 19

Dunlop, J. S., 2001, qhte conf., 3, arXiv:astro-ph0103238

Durret, F., Adami, C., Cappi, A., et al., 2011, A&A, 535A, 65

Ebeling H. & Wiedenmann G., 1993, Phys. Rev. E, 47, 704

Eisenhardt, P. R. M., Brodwin, M., et al., 2008, ApJ, 684, 905

Elvis, M. 1985, in Galactic and Extra-Galactic Compact X-ray Sources, Eds. Y. Tanaka & W. H. G. Lewin, p. 291

Elvis, M., Hao, H., Civano, F., et al., 2012, ApJ, 759, 6

Fabian, A. C., Guilbert, P. W., & Callanan, P. J., 1987, MNRAS, 225, 29

Fabian, A. C., 1994, ARA&A, 32, 277

Fabian, A. C., et al., 2001, MNRAS, 322, 11

Fabian, A. C., et al., 2003a, MNRAS, 341, 729

Fabian, A. C., et al., 2003b, MNRAS, 344, 43

Fabian, A. C., et al., 2005, MNRAS, 360, 20

Fabian, A. C., et al., 2006, MNRAS, 366, 417

Fabian, A. C., 2012, ARA&A, 50, 455

Falomo, R., 1996, MNRAS, 283, 241

Fan, J. H., & Lin, R., 2000, ApJ, 537, 101

Fan, X., Strauss, M. A., Becker, R. H., et al., 2006, AJ, 132, 117

Fanaroff, B. L., & Riley, J. M. 1974, MNRAS, 167, 31

Fanti, R., Fanti, C., Schilizzi, R. T., Spencer, R. E., Rendong, N., Parma, P., van Breugel, W. J. M., & Venturi, T., 1990, A&A, 231, 333

Fanti, C., & Fanti, R., 1994, in ASP Conf. Ser. 54, The Physics of Active Galaxies, ed. G. V. Bicknell, M. A. Dopita, & P. J. Quinn (San Francisco: ASP), 341

Fanti, R., & Spencer, R. E., 1995, in IAU Symp. 175, Extragalactic Radio Sources, ed. R. Ekers, C. Fanti, & L. Padrielli (Dordrecht: Kluwer), 63

Fassbender, R., Nastasi, A., Böhringer, H., et al. 2011, A&A, 527, 10

Fassbender, R., Nastasi, A., Santos, J. S., et al., 2014, A&A, 568, 5

Feigelson, E. D., & Nelson, P. I., 1985, ApJ, 293, 192

Fernández-Ontiveros, J. A., Prieto, M. A., et al., 2012, JPhCS, 372, 2006

Ferrarese, L., Ford, H. C., & Jaffe, W., 1996, ApJ, 470, 444

Ferrarese, L., & Merritt, D., 2000, ApJ, 539, 9

Ferrarese, L., & Ford, H., 2005, SSR, 116, 523

Ferrarese, L., Mould, J. R., et al., 2007, ApJ, 654, 186

Feretti, L., Giovannini, G., et al., 1998, A&A, 331, 475

Feretti, L., Dallacasa, D., et al., 1999, A&A, 344, 472

Feretti, L., & Venturi, T., 2002, Radio Galaxies and their Environment. In Mergin Processes in Galaxy Clusters, eds. L. Feretti, I. M. Gioia, & G. Giovannini. Astrophysics and Space Science Library, Volume 272, 2002, pp 163-195.

Feretti, L., & Giovannini, G., 2008. Clusters of Galaxies in the Radio. In A Pan-Chromatic View of Clusters of Galaxies and the Large-Scale Structure, ed. M. Plionis, O. Lopez-Cruz, & D. Hughes, Springer Lecture Notes in Physics [arXiv:astro-ph/0703494].

Feruglio, C., Daddi, E., Fiore, F., et al., 2011, ApJ, 729, 4

Finkelstein, S. L., Papovich, C., Giavalisco, M., et al., 2010, ApJ, 719, 1250

Finoguenov, A., Guzzo, L., Hasinger, G., et al., 2007, ApJS, 172, 182 (FGH07)

Finoguenov, A., et al., 2008, ApJ, 696, 911

Fichtel, C. E., et al., 1994, ApJ Supp., 94, 551

Foschini, L., et al., 2010, MNRAS, 408, 448

Foschini, L., Bonnoli, G., Ghisellini, G., et al., 2013, A&A, 555, 138

Foschini, L., Berton, M., Caccianiga, A., et al., 2014, submitted to A&A, arXiv1409.3716 preprint

Fossati, G., et al., 1998, MNRAS, 299, 433

Frank, J., King, A., & Raine, D. J., 2002, Accretion Power in Astrophysics, by Juhan Frank and Andrew King and Derek Raine, pp. 398. ISBN 0521620538. Cambridge, UK: Cambridge University Press, February 2002

Galametz, A., Stern, D., De Breuck, C., et al., 2012, ApJ, 749, 169

Galametz, A., Stern, D., Pentericci, L., et al., 2013, A&A, 559, 2

Gaskell, C. M., & Klimek, E. S., 2003, A&AT, 22, 661

Gasparrini, D., Cavazzuti, E., et al., 2012, AIPC, 1505, 478

Gebhardt, K., et al., 2000, ApJ, 539, 13

George, M. R., Leauthaud, A., Bundy, K., Finoguenov, A., 2011, ApJ, 742, 125

Gettings, D. P., Gonzalez, A. H., et al., 2012, ApJ, 759, 23

Ghisellini, G., Haardt, F., & Matt, G., 1994, MNRAS, 267, 743

Ghisellini, G., 1999, Astroparticle Phys., 11, 11

Ghisellini, G., & Celotti, A., 2001, A&A, 379, 1

Ghisellini, G., et al., 2009a, MNRAS, 399, 24

Ghisellini, G. et al., 2009b, MNRAS, 393, 16

Ghisellini, G., Tavecchio, F., & Ghirlanda, G., 2009c, MNRAS, 399, 2041

Ghisellini, G., 2010, Accretion and ejection in AGNs: A Global View; ASP Conference Series, Vol. 427, 2010, ed. L. Maraschi, G. Ghisellini, R. Della Ceca, and F. Tavecchio

Ghisellini, G., Della Ceca, R., Volonteri, M., et al., 2010, MNRAS, 405, 387

Ghisellini, G., Sbarrato, T., Tagliaferri, G., et al., 2014, MNRAS, 440, 111

Giavalisco, M. 2002, ARA&A, 40, 579

Giommi, P., Menna, M. T., & Padovani, P., 1999a, MNRAS, 310, 465

Giommi, P. et al., 1999b, A&A, 351, 59

Giommi, P., Padovani, P., Polenta, G., et al., 2012a, MNRAS, 420, 2899

Giommi, P., Polenta, G., Lähteenmäki, A., et al., 2012b, A&A, 541, 160

Giroletti, M., Giovannini, G., & Taylor, G. B., 2005, A&A, 441, 89

Gitti, M., O'Sullivan, E., et al., 2010, ApJ, 714, 758

Gladders, M. D., Yee, H. K. C., 2005, ApJS, 157, 1

Gobat, R., Daddi, E., Onodera, M., et al., 2011, A&A, 526, 133

Gobat, R., Strazzullo, V., Daddi, E., et al., 2013, ApJ, 776, 9

Gold, B., Odegard, N., Weiland, J. L., et al., 2011, ApJS, 192, 15

Gomez, P. L., Pinkney, J., Burns, J. O., et al., 1997, ApJ, 474, 580

Graham, A. W., Onken, C. A., Athanassoula, E., & Combes, F., 2011, MNRAS, 412, 2211

Gralla, M. B., Gladders, M. D., et al., 2011, ApJ, 734, 103

Greene, J. E., & Ho, L. C., 2005, ApJ, 630, 122

Guest, M. A., 2001, arXiv:math/0104155

Gull, S. F., & Northover, K. J. E., 1973, Nature, 244, 80

Haardt, F., & Madau, P. 2012, ApJ, 746, 125

Haggard, D., Green, P. J., et al., ApJ, 2010, 723, 2

Hailey-Dunsheath, S., Sturm, E., et al., 2012, ApJ, 755, 57

Halkola, A., Seitz, S., Pannella, M., 2007, ApJ, 656, 739

Hancock, P. J., Roberts, P., Kesteven, M. J., et al., 2011, Experimental Astronomy, 32, 147

Hao J. et al., 2010, ApJS, 191, 254

Hao, H., Elvis, M., Bongiorno, A., et al., 2013, MNRAS, 434, 3104

Hardcastle, M. J., et al., 2007, ApJL, 670, 81

Harris, D. E., & Krawczynski, H., 2002, ApJ, 565, 244

Harris, D. E., & Krawczynski, H., 2006, ARA&A, 44, 463

Harris, G. L. H., Rejkuba, M., & Harris, W. E., 2010, PASA, 27, 457

Harris, K. A., 2012, PhD thesis, arXiv1201.5746

Hasinger, G., et al. 2007, ApJS, 172, 29

Hasselfield, M., Hilton, M., Marriage, T. A., et al. 2013, JCAP, 07, 008

Hatch, N. A., Wylezalek, D., Kurk, J. D., et al., 2014, MNRAS, 445, 280

Hatziminaoglou, E., Fritz, J., Franceschini, A., et al., 2008, MNRAS, 386, 1252

Hatziminaoglou, E., Fritz, J., & Jarrett, 2009, MNRAS, 399, 1206

Heckman, T. M., O'Dea, C. P., et al., 1994, ApJ, 428, 65

Henry, J. P., Mullis, C. R., Voges, W., et al., 2006, ApJS, 162, 304

Heywood, I., Blundell, K. M., and Rawlings, S., 2007, MNRAS, 381, 1093

Hicks E. K. S., & Malkan M. A., 2008, ApJS, 174, 31

Hill, G. J., & Lilly, S. J., 1991, ApJ, 367, 1

Hilton, M., Lloyd-Davies, E., Stanford, S. A., et al., 2010, ApJ, 718, 133

Hine, R. G., & Longair, M. S., 1979, MNRAS, 188, 111

Ho, L. C., 2008, ARA&A, 46, 475

Hodge, J. A.; Becker, R. H., et al., 2011, AJ, 142, 3

Hoenig, S. F., Kishimoto, M., 2010, A&A, 523, 27

Hoenig, S. F., Leipski, C., Antonucci, R., and Haas, M., 2011, ApJ, 736, 26

Hoenig, S. F. 2013, arXiv:1301.1349

Hopkins, A. M., Mobasher, B., Cram, L., & Rowan-Robinson, M., 1998, MNRAS, 296, 839

Ilbert, O., Capak, P., Salvato, M., et al. 2009, ApJ, 690, 1236 (I09)

Ivezić, Ž, Smith, J. A., et al., 2007, AJ, 134, 973

Ivison, R. J., Greve, T. R., Dunlop, J. S., et al., 2007, MNRAS, 380, 199

Jackson, C. A., Wall, J. V., 1999, MNRAS, 304, 160

Jackson, N., & Rawlings, S. 1997, MNRAS, 286, 241

Jarrett, T. H., Cohen, M., Masci, F., et al., 2011, ApJ, 735, 112

Jee, M. J., Dawson, K. S., Hoekstra, H., Perlmutter, S., Rosati, P., et al., 2011, ApJ, 737, 59

Jelić, V. et al., 2012, MNRAS, 423, 2753

Jiang, L., Fan, X., Bian, F., et al., 2009, AJ, 138, 30

Jian, H.-Y., Lin, L., Chiueh, T., 2014, ApJ, 788, 109

John, T. L., 1988, A&A, 193, 189

Kaplan, E. L. & Meier, P., 1958, J. Amer. Statist. Assn., 53, 282, 457-481

Kaspi, S., Smith, P. S., Netzer, H., et al., 2000, ApJ, 533, 631

Kaspi, S., Maoz, D., Netzer, H., et al., 2005, ApJ, 629, 61

Kaspi, S., et al., 2007, ApJ, 659, 997

Kauffmann, G., Heckman, T. M., et al., 2003, MNRAS, 346, 1055

Kellermann, K. I., Sramek, R., et al., 1989, AJ, 98, 1195

Kellermann, K. I., et al., 1998, 115, 1295

Kelly, B. C., & Merloni, A., 2012, AdAst, id 970858

Kennicutt, R.C., Jr., ApJSS, 1992, 79, 255

King, A., 2008, NewAR, 52, 253

Knobel, C., Lilly, S. J., Iovino, A., Porciani, C., et al., 2009, ApJ, 697, 1842

Knobel, C., Lilly, S. J., Carollo, C. M., Contini, T., Kneib, J.-P., Le Fevre, O., 2012, ApJ, 755, 48

Koekemoer, A. M., et al. 2007, ApJS, 172, 196

Komissarov, S. S., 1994, MNRAS, 269, 394

Koratkar, A. P., & Gaskell, C. M., 1991, ApJL, 370, 61

Kormendy, J., & Richstone, D., 1995, ARA&A, 33, 581

Kormendy, J., & Ho, L. C., 2013, ARA&A, 51, 511

Koyama, Y., Kodama, T., Tadaki, K., et al., 2014, ApJ, 789, 18

Kravtsov, Andrey V., Borgani, Stefano, 2012, ARA&A, 50, 353

Krawczynski, H. & Treister, E., 2013, FrPhy, 8, 609

Krolik, J. H., 1999, Active Galactic Nuclei, Princeton University Press

Kuo, C. Y., Braatz, J. A., Condon, J. J., et al., 2011, ApJ, 727, 20

Landt, H., 2012, MNRAS, 423, 84

Laing, R. A., & Bridle, A. H., 1987, MNRAS, 228, 557

Laing, R., 1993, in Astrophysical Jets, ed. D. Burgarella, M. Livio, & C. P. O'Dea, Cambridge: Cambridge Univ. Press, p95

Laing, R. A., Jenkins, C. R., et al., 1994, in ASP Conf. Ser. 54, The First Stromlo Symposium: The Physics of Active Galaxies, ed. G. V. Bicknell, M. A. Dopita, & P. J. Quinn (San Francisco, CA: ASP), 201

Laor, A., 1990, MNRAS, 246, 369

Laureijs, R., Amiaux, J., Arduini, S., et al., 2011, Euclid Definition Study Report, arXiv1110.3193 preprint

Lawrence, A., Warren, S. J., Almaini, O., et al., 2007, MNRAS, 379, 1599

Lawrence, A., & Elvis, M., 2010, ApJ, 714, 561

Lazzati, D., Ghisellini, G., & Celotti, A., 1999, MNRAS, 309, 13

Leahy, D. A., & Creighton, J., 1993, MNRAS, 263, 314

Leauthaud, A., Finoguenov, A., Kneib, J.-P., et al. 2010, ApJ, 709, 97

Ledlow, M. J. & Owen, F. N., 1995, AJ, 109, 853

Ledlow, M. J. & Owen, F. N., 1996, AJ, 112, 9

Leipski, C., Antonucci, R., et al., 2009, ApJ, 701, 891

Levenson, N. A., Krolik, J. H., et al., 2002, ApJ, 573, 81

Li, L.-X., Zimmerman, E. R., Narayan, R., & McClintock, J. E., 2005, ApJS, 157, 335

Li, Z.-Y., Chiueh, T., & Begelman, M. C., 1992, ApJ, 394, 459

Lilly, S. J., Le Fèvre, O., Renzini, A., et al. 2007, ApJS, 172, 70

Limousin, M., Cabanac, R., Gavazzi, R., et al. 2009, A&A, 502, 445

Liu, F. S., Guo, Y., et al., 2013, ApJ, 769, 147

Loeb, A., & Laor, A., ApJ, 1992, 384, 115

Loken, C., et al., 1995, ApJ, 445, 80

Longair, M. S., 1966, MNRAS, 133, 421

Lusso, E., Hennawi, J. F., Comastri, A., et al., 2013, ApJ, 777, 86

Ma, X.-C., & Wang, T.-G., 2013, MNRAS, 430, 3445

Macchetto, F., Marconi, A., Axon, D. J., Capetti, A., Sparks, W., & Crane, P. 1997, ApJ, 489, 579

Madau, P., 1988, ApJ, 327, 116

Magliocchetti, M. & Brüggen, M., 2007, MNRAS, 379, 260

Majaess, D., 2010, Acta Astronomica, 60, 121

Malkan, M. A., 1983, ApJ, 268, 582

Mannheim, K., & Biermann, P. L., 1992, A&A, 253, 21

Mannucci, F., Basile, F., Poggianti, B. M., et al., 2001, MNRAS, 326, 745

Mantz, A., Allen, S. W., Rapetti, D., Ebeling, H., 2010, MNRAS, 406, 1759

Maraschi, L., Ghisellini, G., & Celotti, A., 1992, ApJ, 397, 5

Marchesini, D., Celotti, A., & Ferrarese, L., 2004, MNRAS, 351, 733

Marconi, A., Capetti, A., Axon, D. J., et al., 2001, ApJ, 549, 915

Marconi, A., & Hunt, L. K., 2003, ApJ, 589, 21

Markowitz, A. G., Krumpe, M., & Nikutta, R., 2014, MNRAS, 275

Marscher, A. P., Jorstad, S. G., et al., 2008, Nature, 452, 966

Marscher, A. P., Jorstad, S. G., et al., 2010, ApJ, 710, 126

Marshall, H. L., et al., 2002, ApJ, 564, 683

Massardi, M., Bonaldi, A., et al., 2010, MNRAS, 404, 532

Massaro, E., Giommi, P., Leto, C., et al., 2013, VizieR Online Data Catalog, 349, 50691

Matt, G., Brandt, W. N., & Fabian, A. C., 1996, MNRAS, 280, 823

Matthews, T. A., & Sandage, A. R., 1963, ApJ, 138, 30

Mattox, J. R., et al., 1997, ApJ, 476, 692

Mauch, T., Sadler, E. M., 2007, MNRAS, 375, 931

Mayo, J. H., Vernet, J., De Breuck, C., et al., 2012, A&A, 539A, 33

McAlpine, K., Jarvis, M. J., & Bonfield, D. G., 2013, MNRAS, 436, 1084

McCarthy, P. J., van Breugel, W., et al., 1987, ApJ, 321, 29

McGreer, I. D., Helfand, D. J., & White, R. L., 2009, AJ, 138, 1925

McHardy, I. 2010, in Lecture Notes in Physics, Berlin Springer Verlag, ed. T. Belloni, Vol. 794, 203, arXiv:0909.2579

McIntosh, D. H., Wagner, C., Cooper, A., et al., 2014, MNRAS, 442, 533

McLure, R. J., Kukula, M. J., et al., 1999, MNRAS, 308, 377

McNamara, B. R., & Nulsen, P. E. J., 2012, NewJPhys, 14, 055023

Mei, S., Holden, B. P., Blakeslee, J. P., et al., 2009, ApJ, 690, 42

Menanteau, F., et al., 2013, ApJ, 765, 67

Menci, N., Rosati, P., Gobat, R., et al., 2008, ApJ, 685, 863

Merloni, A., Bongiorno, A., Brusa, M., et al., 2014, MNRAS, 437, 3550

Meszaros, P., 2006, RPPh, 69, 2259

Miley, G. K., 1968, Nature, 218, 933

Miley, G. K., Perola, G. C., et al., 1972, Nature, 237, 269

Miley, G., & De Breuck, C., 2008, A&ARv, 15, 67

Milnor, J., 1963, Morse Theory, Annals of Math. Studies 51, Princeton Univ. Press.

Miyoshi, M., Moran, J., et al., 1995, Nature, 373, 127

Mobasher, B., Capak, P., Scoville, N. Z., et al. 2007, ApJS, 172, 117

Moderski, R., Sikora, M., et al., 2004, ApJ, 611, 770

Mohr, J. J., 2005, in ASP Conf. Ser. 339, Observing Dark Energy, ed. S. C. Wolf & T. R. Lauer (San Francisco, CA: ASP), 140

Molchanov, I. S. & Zuyev, S. A., 2000, Mathematics of Operation Research, 25, 485-508

More, A., Cabanac, R., More, S., et al. 2012, ApJ, 749, 38

Morrissey, P., Conrow, T., Barlow, T. A., et al., 2007, ApJS, 173, 682

Mortlock, D. J., Warren, S. J., et al., 2011, Nature, 474, 616

Mortonson, M. J., Hu, W., Huterer, D., 2011, Phys. Rev. D, 83, 023015

Mushotzky, R. F., Done, C., & Pounds, K. A., 1993, ARA&A, 31, 717

Moss, D., Seymour, N., McHardy, I. M., et al., 2007, ASPC, 380, 275

Mücke, A., & Protheroe, R. J., 2001, Astropart. Phys., 18, 593

Mücke, A., et al., 2003, Astropart. Phys., 18, 593

Muxlow, T. W. B., Richards, A. M. S., Garrington, S. T., et al., 2005, MNRAS, 358, 1159

Muzzin, A., Wilson, G., et al., 2013, ApJ, 767, 39

Nastasi, A., Fassbender, R., Böhringer, H., et al., 2011, A&A, 532, 6

Neeser, M. J., Eales, S. A, et al., 1995, ApJ, 451, 76

Netzer, H., 1990, AGN conf., 57

Newman, A. B., Ellis, R. S., Andreon, S., et al., 2014, ApJ, 788, 51

Nieppola, E., Valtaoja, E., Tornikoski, M., et al., 2008, A&A, 488, 867

Nilsson K., Valtonen, M. J., et al., 1993, ApJ, 413, 453

Nilsson, K., et al., 2007, A&A, 475, 199

Noble, A. G., Geach, J. E., van Engelen, A. J., et al., 2013, MNRAS, 436, 40

Novikov, I. D. & Thorne, K. S., 1973. In Black Holes, Les Houches, ed. C. De Witt & B. DeWitt (Gordon and Breach, New York).

O'Dea, C. P., & Owen, F. N., 1985, AJ, 90, 927

O'Dea C. P. & Owen, F. N., 1986, ApJ, 301, 841

O'Dea, C. P., Baum, S. A., & Stanghellini, C., 1991, ApJ, 380, 66

O'Dea, C. P., & Baum, S. A., 1997, AJ, 113, 148

O'Dea, C. P., 1998, PASP, 110, 493

O'Doghue, A. Q., et al., 1990, ApJS, 72, 75

O'Donnell, J. E., 1994, ApJ, 422, 158

Ogle, P., Cohen, M. H., et al., 1997, ApJ, 482, 37

Ogle, P., Whysong, D., & Antonucci, R., 2006, ApJ, 647, 161

Onken, C. A., Ferrarese, L., Merritt, D., et al., 2004, ApJ, 615, 645

Onken C. A., et al., 2007, ApJ, 670, 105

Onken, C. A., Valluri, M., Brown, J. S., et al., 2014, ApJ, 791, 37

Owen, F. N., & Rudnick, L., 1976, ApJL, 205, 1

Owen, F. N, & Laing, MNRAS, 238, 357

Owen, F. N., & White, R. A., 1991, MNRAS, 249, 164

Owen, F. N., 1993, in Jets in Extragalactic Radio Sources, ed. H. J. Röser & Meisenheimer, Berlin: Springer-Verlag, p273

Owen, F. N. & Ledlow, M. J., 1994, in ASP Conf. Ser. 54, The Physics of Active Galaxies, ed. G. V. Bicknell, M. A. Dopita, & P. J. Quinn (San Francisco, CA: ASP), 319

Owen, F. N., Dwarakanath, K. S., et al., 1996, in Energy Transport in Radio Galaxies and Quasars, eds. P. E. Hardee, A. H. Bridle, & J. A. Zensus, ASP, Conference Series, 100, 353

Paczynski, B., Acta Astron., 1978a, 28, 111

Paczynski, B., Acta Astron., 1978b, 28, 241

Padovani, P., Perlman, E. S., Landt H., Giommi P., & Perri M., 2003, ApJ, 588, 128

Papadopoulos, P. P.; Röttgering, H. J. A., et al., 2000, ApJ, 528, 626

Papovich, C., 2008, ApJ, 676, 206 (P08)

Papovich, C., Momcheva, I., Willmer, C. N. A., et al., 2010, ApJ, 716, 1503

Papovich, C. J., Gebhardt, K., Adams, J., et al., 2011, Spitzer Proposal ID no. 80100

Park, D., Kelly, B. C., Woo, J.-H., & Treu, T., 2012a, ApJS, 203, 6

Park, D., Woo, J.-H., Treu, T., et al., 2012b, ApJ, 747, 30

Parma, P., Fanti, C., Fanti, R., et al., 1987, A&A, 181, 244

Peacock, J. A., 1999, Cosmological Physics, Cambridge, UK, Cambridge Univ. Press

Pearson, T. J., Readhead, A. C., & Barthel, P. D., 1987, in Superluminal Radio Sources, ed. A. Zensus & T. Pearson, Cambridge: Cambridge University Press

Peebles P. J. E., 1980, The Large-Scale Structure of the Universe. Princeton Univ. Press, Princeton

Peebles, P. J. E., 1993, Physical Cosmology, Princeton, NJ, Princeton Univ. Press

Pentericci, L., et al., 1998, ApJ, 504, 139

Pentericci, L., et al., 1999, A&A, 341, 329

Pentericci, L., McCarthy, P. J., et al., 2001, ApJ Suppl., 135, 63

Peterson, B. M., 2001, in Advanced Lectures on the Starburst-AGN, ed. I. Aretxaga, D. Kunth, & R. Mújica (Singapore: World Scientific), 3

Peterson, B. M., 2007, ASPC, 373, 3

Pierre, M., et al., 2011, "The X-ray Universe 2008" Symposium held in Granada, Spain, 27-30 May, 2008, Published online at `http://xmm.esac.esa.int/external/xmm_science/workshops/2008symposium`, p.233

Pinkney, J., et al., ApJ, 1993, 416, 36

Pinkney, J., et al., AJ, 120, 2269

Planck Collaboration VII, 2011, A&A, 536, 7

Planck Collaboration XIII, 2011, A&A, 536, 13

Planck Collaboration XVI, 2013, arXiv:1303.5076

Planck Collaboration XX, 2013, arXiv1303.5080

Planck Collaboration XXVIII, 2013, arXiv1303.5088

Planck Collaboration XXIX, 2013, arXiv:1303.5089

Plotkin, R. M., Anderson, S. F., Brandt, W. N., et al., 2012, ApJL, 745, L27

Polletta, M., Tajer, M., Maraschi, L., et al., 2007, ApJ, 663, 81

Postman, M., Lubin, L. M., Gunn, J. E., et al., 1996, AJ, 111, 615

Prestage, R. M., & Peacock, J. A., 1988, MNRAS, 230, 131

Prescott, M. K. M., Impey, C. D., Cool, R. J., & Scoville, N. Z. 2006, ApJ, 644, 100

Prieto, M. A., Reunanen, J., Tristram, K. R. W., et al., 2010, MNRAS, 402, 724

Pringle, J. E., 1981, ARAA, 19, 137

Privault, N., 1994, Stochastics Stoch. Rep., 51, 83 109

Pursimo, T., Ojha, R., et al., 2013, ApJ, 767

Quintana, H., & Lawrie, D. G., 1982, AJ, 87, 1

Quirrenbach, A. et al., 1991, ApJ, 372, 71

Radomski, J. T., et al., 2003, ApJ, 587, 117

Ramos Almeida, C., Bessiere, P. S., Tadhunter, C., et al., 2013, MNRAS, 436, 997

Rappaport, S. A., Fregeau, J. M., & Spruit, H. C., 2004, ApJ, 606, 436

Readhead, A. C. S., Taylor, G. B., et al., 1996a, ApJ, 460, 612

Readhead, A. C. S., Taylor, G. B., et al., 1996b, ApJ, 460, 634

Rees, M. J., 1978, MNRAS, 184, 61

Reichardt, C. L., Stalder, B., et al., 2013, ApJ, 763, 127

Reiprich, T. H., Böhringer, H., 1999, in Diffuse Thermal and Relativistic Plasma in Galaxy Clusters, ed. H. Böhringer, L. Ferretti, & P. Schuecker (Garching:MPE), 157

Reis, R. R. R., Soares-Santos, M., et al., 2012, ApJ, 747, 59

Rekola, R., Richer, M. G., et al., 2005, MNRAS, 361, 330

Reuland, M., van Breugel W, et al., 2003, ApJ, 592, 755

Reuland, M., Röttgering, H., et al., 2004, MNRAS, 353, 377

Rigby, E. E., Best, P. N., & Snellen, I. A. G., 2008, MNRAS, 385, 310

Rigby, E. E., Hatch, N. A., et al., 2014, MNRAS, 437, 1882

Risaliti, G., Maiolino, R., & Salvati, M., 1999, ApJ, 522, 157

Risaliti, G., Elvis, M., & Nicastro, F., 2002, ApJ, 571, 234

Risaliti, G., Elvis, M., et al., 2005, ApJ, 623, 93

Roettiger, K., Burns, J. O., & Loken, C., 1996, ApJ, 473, 651

Romero, G., et al., 1999, ApJS, 135, 477

Romero, G., et al., 2000, A&A, 360, 47

Romero, G. E., et al., 2002, A&A, 390, 431

Rosati, P., Borgani, S., Norman, C., 2002, ARA&A, 40, 539

Rosati, P., Tozzi, P., Gobat, R., et al., 2009, A&A, 508, 583

Roseboom, I. G., Lawrence, A., Elvis, M., et al., 2013, MNRAS, 429, 1494

Rozo, E., Wechsler, R. H., Rykoff, E. S., et al., 2010, ApJ, 708, 645

Rudnick, G. H., Tran, K.-V., Papovich, C., et al., 2012, ApJ, 755, 14

Rybicki, G. B., & Lightman, A. P., 1979, Radiative processes in astrophysics, ed. Wiley

Sadler, E. M., Cannon, R. D., Mauch, T., Hancock, P. J., 2007, MNRAS, 381, 211

Sahu, S., Zhang, B., & Fraija, N., PhRvD, 85, 3012

Saikia, D. J., 1988, in Active Galactic Nuclei, ed. H. R. Miller & P. J. Wiita (Berlin: Springer), 317

Saikia, D. J., Jeyakumar, S., et al., 1995, MNRAS, 276, 1215

Sanders, D. B., Salvato, M., Aussel, H., et al., 2007, ApJS, 172, 86

Sani, E., Davies, R., et al., 2012, MNRAS, 424, 1963

Santos, J. S., Rosati, P., Gobat, R., et al., 2009, A&A, 501, 49

Santos, J. S., Fassbender, R., Nastasi, A., et al. 2011, A&A, 531, 15

Santos, J. S., Altieri, B., Popesso, 2013, MNRAS, 433, 1287

Sarazin, C. L., Baum, S. A., & O'Dea, C. P., 1995, ApJ, 451, 125

Sarazin, C. L., 1997, ASPC, 116, 375

Sarazin, C. L., Irwin, J. A., & Bregman, J. N., 2001, ApJ, 556, 533

Savolainen, T., Homan, D. C., et al., 2010, A&A, 512, 24

Sazonov, S., Willner, S. P., et al., ApJ, 757, 181

Sbarrato, T., Ghisellini, G., et al., 2012, MNRAS, 421, 1764

Sbarrato, T., Tagliaferri, G., Ghisellini, G., et al., 2013a, ApJ, 777, 147

Sbarrato, T., Ghisellini, G., Nardini, M., et al., 2013b, MNRAS, 433, 2182

Scarpa, R., et al., 2000, ApJ, 532, 740

Scarpa, R., & Urry, C. M., 2001, ApJ, 556, 749

Schinnerer, E., et al. 2007, ApJS, 172, 46

Schmidt, M., 1968, ApJ, 151, 393

Schmitt, J. H. M. M., 1985, ApJ, 293, 178

Schneider, D. P., Richards, G. T., Hall, P. B., et al., 2010, AJ, 139, 2360

Scoville, N., et al. 2007a, ApJS, 172, 1

Scoville, N., et al. 2007b, ApJS, 172, 150

Scoville, N.; Arnouts, S.; Aussel, H. et al., 2013, ApJS, 206, 3

Semler, D. R., et al., 2012, ApJ, 761, 183

Seymour, N., McHardy, I. M., & Gunn, K. F., 2004, MNRAS, 352, 131

Seymour, N., Stern, D., et al., 2007, ApJS, 171, 353

Shakura, N. I., & Sunyaev, R. A., 1973, A&A, 24, 337

Shang, Z., Wills, B. J., Wills, D., & Brotherton, M. S., 2007, AJ, 134, 294

Shankar, F., Weinberg, D. H., & Miralda-Escudé, J., 2009, ApJ, 690, 20

Shaw, M. S., Romani, R. W., Cotter, G., et al., 2012, ApJ, 748, 49

Shaw, M. S., Romani, R. W., Cotter, G., et al., 2013, ApJ, 764, 135

Shen, Y., Richards, G. T., Strauss, M. A., et al., 2011, ApJS, 194, 45

Shen, Y., 2013, BASI, 41, 61

Shen, Y., Brandt, W. N., Dawson, K. S., et al., 2014, ApJ submitted, arXiv:1408.5970

Sheth, R. K., 2007, MNRAS, 378, 709

Sheth, R. K., Tormen, G., 2004, MNRAS, 350, 1385

Sikora, M., et al., 1994, ApJ, 421, 153

Sikora, M., 2001, ASPC, 227, 95

Simpson, C., & Rawlings, S., 2002, MNRAS, 334, 511

Simpson, C., Rawlings, S., et al., 2012, MNRAS, 421, 3060

Smith, H., & Hoffleit, D., 1963, Nature, 198, 650

Smith, E. P., & Heckman, T. M. 1990, ApJ, 348, 38

Smolčić, V., Zamorani, G., Schinnerer, E., et al., 2009, ApJ, 696, 24

Smolčić, V., Finoguenov, A., et al., MNRAS, 416, 31

Snellen, I. A. G., Schilizzi, R. T., Miley, G. K., de Bruyn, A. G., et al., 2000, MNRAS, 319, 445

Snellen, I. A. G. & Best, P. N., 2001, MNRAS, 328, 897

Soares-Santos, M., de Carvalho, R. R., et al., 2011, ApJ, 727, 45

Soldi, S., Beckmann, V., Baumgartner, W. H., et al., 2014, A&A, 563, 57

Spitler, L. R., et al., 2012, ApJ, 748, 21

Spruit, H. C., & Taam, R. E., 1993, ApJ, 402, 593

Stanford, S. A., Brodwin, M., Gonzalez, A. H., et al., 2012, ApJ, 753, 164

Stanghellini, C., Bondi, M., et al., 1997, A&A, 318, 376

Steidel, C. C., Adelberger, K. L., Shapley, A. E., et al., 2000, ApJ, 532, 170

Steidel, C. C.; Shapley, A. E., 2004, ApJ, 604, 534

Stern, D., & Spinrad, H., 1999, PASP, 111, 1475

Stone, J. M., & Balbus, S. A., ApJ, 1996, 463, 656

Strazzullo, V., Rosati, P., Pannella, M., et al., 2010, A&A, 524, 17

Strazzullo, V., Gobat, R., Daddi, E., et al., 2013, ApJ, 772, 118

Šuhada, R., Song, J., Böhringer, H., et al., 2012, A&A, 537A, 39

Sunyaev & Zel'dovich, 1970, CoASP, 2, 66

Sunyaev & Zel'dovich, 1972, CoASP, 4, 173

Swetz, D. S., Ade, P. A. R., Amiri, M., et al., 2011, ApJS, 194, 41

Szuszkiewicz, E., Malkan, M. A., & Abramowicz, M. A., 1996, ApJ, 458, 474

Tadhunter, C., et al. 2007, ApJ, 661, 13

Tanaka, M., Finoguenov, A., Mirkazemi, M., et al., 2013, PASJ, 65, 17

Taniguchi, Y., et al. 2007, ApJS, 172, 9

Tavecchio, F., Maraschi, L., et al., 2000, ApJ, 544, 23

Thorne, K. S., 1974, ApJ, 191, 507

Tielens, A. G. G. M., Miley G. K., & Willis, A. G., 1979, A&A Suppl., 35, 153

Tinker, J., Kravtsov, A. V., Klypin, A., et al., 2008, ApJ, 688, 709

Tinti, S., & De Zotti, G., 2006, A&A, 445, 889

Trenti, M., Bradley, L. D., Stiavelli, M., et al., 2012, ApJ, 746, 55

Toshikawa, J., Kashikawa, N., et al., 2014, ApJ, 792, 15

Tozzi, P., Santos, J. S., Nonino, M., Rosati, P., 2013, A&A, 551, 45

Trakhtenbrot, B., & Netzer, H., 2012, MNRAS, 427, 3081

Trump, J. R., Impey, C. D., McCarthy, P. J., et al. 2007, ApJS, 172, 383

Trushkin, S. A., 2003, Bulletin of the Special Astrophysics Observatory, 55, 90

Tundo, E., Tozzi, P., & Chiaberge, M. 2012, MNRAS, 420, 187

Ulrich, M., et al., 1997, ARA&A, 35, 445

Urry, M. & Padovani, P, 1995, PASP, 107, 803

Urry, C. M., 1999, Astropart. Phys., 11, 159

Valencia-S., M., Busch, G., et al., 2014, IAUS, 304, 274

Vallée, J. P., et al., 1981, ApJ, 250, 66

Venemans, B. P., Röttgering, H. J. A., Miley, G. K., et al. 2007, A&A, 461, 823

Venturi, T., Castaldini, C., Cotton, W. D., et al., 1995, ApJ, 454, 735

Véron-Cetty, M. P.; Véron, P., 2000, A&ARv, 10, 81

Vestergaard, M., & Peterson, B. M., 2006, ApJ, 641, 689

Vikhlinin, A., Kravtsov, A. V., Burenin, R. A., Ebeling, H., Forman, W. R., et al., 2009, ApJ, 692, 1060

von der Linden, A., Best, P. N.; Kauffmann, G., 2007, MNRAS, 379, 867

van Breugel, W., De Breuck, C., et al., 1999, ApJ, 518, 61

van Ojik R., Röttgering, H. J., et al., 1997, A&A, 317, 358

Vercellone, S. et al., 2010, ApJ, 712, 405

Vietri, M., 2008, Foundations of High-Energy Astrophysics, University of Chicago Press, Chicago

Wald, R. M., 1984, General Relativity, Univ. of Chicago Press

Wall, J. V., 1980, Phil. Trans. R. Soc., 296, 367

Wandel, A., & Petrosian, V., 1988, ApJ, 329, 11

Weinberg, D. H., Mortonson, M., Eisenstein, D., Hirata, C., et al., 2013, PhR, 530, 87

Webb, W. & Malkan, M., 2000, ApJ, 540, 652

Wen, Z. L. & Han, J. L., 2011, ApJ, 734, 68

Wehrle, A. E., 1998, ApJ, 497, 178

Willett, K., Nelson, T., & Fortson, L., 2012, AIPC, 1505, 558

Willott, C. J., Rawlings, S., et al., 2001, MNRAS, 322, 536

Willott, C. J., Delorme, P., et al. 2010, AJ, 139, 906

Wills, B. J., Netzer, H., & Wills, D., 1985, ApJ, 288, 94

Wilson, A. S., & Colbert, E. J. M., 1995, ApJ, 438, 62

Windhorst, R. A., Miley, G. K., Owen, F. N., et al., 1985, ApJ, 289, 494

Wing, J. D. ,& Blanton, E. L., 2011, AJ, 141, 88

Witten, E., 1982, Supersymmetry and Morse theory, JDGeo, 17, 661.

Worpel, H., Brown, M. J. I., et al., 2013, ApJ, 772, 64

Wright, E. L., Eisenhardt, P. R. M., Mainzer, A. K., et al., 2010, AJ, 140, 1868

Wu, X.-B., Wang, R., Kong, M. Z., Liu, F. K., & Han, J. L., 2004, A&A, 424, 793

Wurster, J., & Thacker, R. J., 2013, MNRAS, 431, 539

Wurtz, R., Ellingson, E., et al., 1993, AJ, 106, 869

Wurtz, R., Stocke, J. T., et al., 1997, ApJ, 480, 547

Wylezalek, D., Galametz, A., Stern, D., 2013a, ApJ, 769, 79

Wylezalek, D., Vernet, J., et al., 2013b, MNRAS, 428, 3206

Xie G. Z., et al., 2001, ApJ, 548, 200

Xie G. Z. et al., 2004, MNRAS, 348, 831

Yi, W.-M., Wang, F., et al., 2014, ApJL in press, arXiv1410.2689 preprint

York, D. G. et al., 2000, AJ, 120, 1579

Young, M., Brandt, W. N., et al., 2012, ApJ, 748, 124

Yuan, T.-T., Nanayakkara, T., Kacprzak, G. G., et al., 2014, ApJ Letters in press, arXiv1410.0690 preprint

Zatloukal, M., Röser, H.-J., Wolf, C., Hippelein, H., & Falter, S., 2007, A&A, 474, 5Z

Zeimann, G., Stanford, S. A., et al., 2012, ApJ, 756, 115

Zeimann, G., Stanford, S. A., Brodwin, M., et al., 2013, ApJ, 779, 137

Zirbel, E. L. 1996, ApJ, 473, 713

Zirbel, E. L., 1997, ApJ, 476, 489

Zirbel, E. L. & Baum, S. A., 1998, ApJS, 114, 177

Zirm, A. W., Stanford, S. A., Postman, M., Overzier, R. A., et al., 2008, ApJ, 680, 224

Zitrin, A., Bartelmann, M., et al., 2012, MNRAS, 426, 2944